

Quantifying Emissions of Carbon Dioxide and Methane in Central and Eastern Africa Through High Frequency Measurements and Inverse Modeling

By

Jimmy Gasore

B.S. Physics

National University of Rwanda, 2007

Submitted to the Department of Earth Atmospheric and Planetary Sciences in Partial Fulfillment of the Requirements for the Degree of

Doctor of Philosophy in Atmospheric Sciences

at the

MASSACHUSETTS INSTITUTE OF TECHNOLOGY

February 2018

© 2018 Massachusetts Institute of Technology. All rights reserved

Signature of Author.....

Department of Earth, Atmospheric and Planetary Sciences
September, 2017

Certified by

Ronald G. Prinn
TEPCO Professor of Atmospheric Science

Accepted by

Robert D. Van Der Hilst
Schlumberger Professor of Earth and Planetary Sciences
Head, Department of Earth Atmospheric and Planetary Sciences

Quantifying Emissions of Carbon Dioxide and Methane in Central and Eastern Africa Through High Frequency Measurements and Inverse Modeling

by

Jimmy Gasore

Submitted to the Department of Earth, Atmospheric and Planetary Sciences on September 18, 2017 in partial fulfillment of the requirements for the degree of Doctor of Philosophy in Atmospheric Sciences

Abstract

Carbon dioxide (CO₂) and methane (CH₄) are the main greenhouse gases, contributing about 81% of the total human induced radiative forcing. Sufficient observations exist to quantify the global budget of carbon dioxide and methane which is necessary for calculating the resulting radiative forcing. Still, more observations are needed to constrain their time evolution and regional budgets which are needed for climate change mitigation policies. Atmospheric observations are particularly scarce on the African continent, despite Africa's significant CO₂ emissions from agriculture, biomass burning and land use changes, as well as methane emissions from wetlands. There are very few low frequency flask measurements due to limited logistics and there is no land based station at all in equatorial Africa. Satellite observations can only provide an incomplete record due to frequent clouds and aerosol in the equatorial belt.

We have set up a high-frequency in-situ greenhouse gases monitoring station in North West Rwanda at Mount Mugogo. The station is intended to be a long-term station, hence, filling the gap of current lack of measurements in Equatorial Africa. The station is part of the Advanced Global Atmospheric Gases Experiment (AGAGE) and follows its calibration protocols and operational standards, therefore, providing data of internationally recognized quality standards. We have found that massive regional scale biomass burning largely drives the bi-model seasonal cycle of carbon dioxide, carbon monoxide and black carbon with the burning following the shift of the inter-tropical convergence zone. The seasonal cycle of methane is largely driven by the inter-hemispheric gradient, where methane-rich northern hemisphere air masses are advected to the station during the northern winter.

We have used the Reversible Jump Markov Chain Monte Carlo methods to estimate optimized methane and carbon dioxide emissions in the Central and East African region. We have found that the region emitted about 25 Tg of CH₄ and 139 Tg of CO₂ in 2016.

Thesis supervisor: Ronald G. Prinn

Title: TEPCO Professor of Atmospheric Science

Acknowledgement

I hereby express my sincere gratitude to my advisor Prof. Ron Prinn, his guidance, motivation and support have been invaluable throughout this program. I would also like to thank members of my thesis committee, Prof. Susan Solomon, Prof. Shuhei Ono and Dr. Matt Rigby for insightful comments, advice and guidance.

My sincere thanks go to Dr. Mark Lunt and all members of the Atmospheric chemistry group, the University of Bristol, UK. They provided software code and support for the inverse method used in this work.

Financial support has come from NASA grant to MIT for the Advanced Global Atmospheric Gases Experiment. Additional funds were provided by the Center for Global Change Science and the Martin Family Society of Fellows for Sustainability.

I am also grateful to the Government of Rwanda, the Ministry of Education for providing infrastructures, staff and technical support to set up and run the climate station at Mt. Mugogo.

I take opportunity to express gratitude to generous donors to MIT who supported the building and installation of all instruments used in this thesis.

I would like to thank former and current members of the technical team at Mugogo station for their contribution to the success of this project.

Last but not least, I would like to thank my wife Alice and my sons Rwema and Kirenga, without their emotional support and patience, I would not have gone this far.

Contents

Acronyms	10
1 Introduction	13
1.1 Problem statement	15
1.1.1 CO_2 and CH_4 measurement in Africa	15
1.1.2 Goals of the current project	18
1.2 Rationale	18
1.3 Budgets of carbon dioxide and methane	19
1.3.1 Global and Regional Budgets of Carbon Dioxide	19
1.3.2 Global and regional budgets of methane	19
1.3.3 Method for estimation of sources and sinks of CO_2 and CH_4	21
1.4 Site selection and characterization	23
1.4.1 Geography and climate of Rwanda	23
1.4.2 Site selection	24
2 Field Set up and Instrumentation	27
2.1 Description of the field site	28
2.2 Picarro G2401 for high frequency measurement of carbon dioxide, methane and carbon monoxide	29
2.2.1 Earth Networks sampling and drying unit	29
2.2.2 Site setup and calibration	33
2.3 Black carbon, weather and other measurements at Mt. Mugogo	39
3 The Lagrangian Particle Dispersion Model: NAME	41
3.1 Model formulation	41
3.2 Model setup and Meteorology	43
4 Trans-dimensional Markov Chain Monte Carlo Inversion	51
4.1 Bayesian approach to inverse problem	51
4.2 Markov Chain Monte Carlo Method	52
4.2.1 Monte Carlo Integration	52
4.2.2 Markov Chains	53
4.2.3 The Metropolis-Hastings Algorithm	53
4.3 Trans-Dimensional Markov Chain Monte Carlo Methods	54
4.3.1 Basis functions	55

4.3.2	Acceptance probability for the Trans-dimensional Markov Chain Monte Carlo (TDMCMC)	56
4.3.3	Prior distribution	57
4.3.4	Likelihood function	58
4.3.5	Proposal distributions and acceptance probabilities	59
4.4	Implementation of the RJMCMC	63
4.4.1	List of parameters used in the inversion	63
4.4.2	Data filtering using NAME model	63
5	Data Presentation and Analysis	64
5.1	Time series of measured mole fractions and black carbon concentrations . . .	64
5.1.1	Seasonal cycles	67
5.2	Diurnal cycles of CO_2 and CH_4	73
5.3	Weather data	75
5.4	Correlations between species	79
5.4.1	Mixing ratio correlations between black carbon and carbon monoxide	79
5.4.2	Correlation between carbon monoxide and methane mole fractions . .	80
5.4.3	Correlation between carbon monoxide and carbon dioxide mole fractions	82
5.4.4	Methane mole fractions dependence on wind direction	84
5.4.5	Carbon dioxide mole fractions dependence on wind direction	86
6	Methane inversion	88
6.1	Inversion prior	88
6.1.1	CarbonTracker-CH4	88
6.2	Inversion setup	90
6.2.1	Inversion domain and sub-domain	90
6.2.2	Boundary Conditions	91
6.2.3	Inversion parameters	92
6.3	CH_4 inversion results	93
6.3.1	Uncertainty reduction maps	93
6.3.2	Posterior emission maps	94
6.3.3	Scaling factors and country totals	94
6.3.4	Forward run with optimized methane emissions	95
6.3.5	Summary of methane inversion results	97
7	Carbon dioxide inversion	99
7.1	Inversion prior	99
7.1.1	Inversion domain and boundary conditions	100
7.1.2	Modeling the diurnal cycle of CO_2	101
7.2	CO_2 inversion results	101
7.2.1	Uncertainty reduction map and footprints	101
7.2.2	Prior and posterior emissions	102
7.2.3	Emissions scaling factors and country totals	103

7.2.4	Forward run with optimized CO_2 emissions	104
7.2.5	Summary of CO_2 inversion	105
Conclusions and way forward		107
	Conclusions	107
	Limitations and future research	108
Appendices		109
A	CH_4 Inversion results	110
B	CO_2 Inversion results	146

List of Figures

1.1	Estimated CO_2 emissions compared to IPCC scenarios	14
1.2	location of WDCGG ground stations	16
1.3	Location of TCCON sites	17
1.4	Typical GOSAT monthly mean column	17
1.5	Sources and sinks of atmospheric methane	20
1.6	Zonal mean flux of methane	21
1.7	Rwanda rainfall and temperature	24
1.8	Back trajectories for Mugogo station	25
2.1	Picture of the laboratory building at Mt. Mugogo	28
2.2	View of Mount Mugogo	28
2.3	Picarro G2401	29
2.4	Earth Networks sampling and drying unit	31
2.5	Water vapor mixing ratios, dry vs humid sample air	32
2.6	Comparing the amount of water correction, dry vs humid air	32
2.7	CO_2 mole fractions time series and corresponding calibration tanks	33
2.8	Data time series and calibration tanks for CH_4 and CO_2	34
2.9	Standard deviation of calibration sessions, CO_2	34
2.10	Standard deviations of calibration sessions, CH_4	35
2.11	Standard deviations of calibration sessions, CO	35
2.12	Normalized instrument responses, for calibrations tanks	36
2.13	Instrument sensitivity, CO_2	36
2.14	Instrument sensitivity, CH_4	37
2.15	Instrument sensitivity, CO	38
2.16	Two points calibration minus one point calibration for CO_2 and CH_4	39
2.17	Other instruments present at the station	40

3.1	NAME model domain	43
3.2	Mugogo meteorology, Dec-Jan-Feb	45
3.3	Mugogo meteorology Mar-Apr-May	45
3.4	Mugogo meteorology Jun-Jul-Aug	46
3.5	Mugogo meteorology Sep-Oct-Nov.	46
3.6	Footprint and wind streamlines, February	47
3.7	Footprint and wind streamlines, April	48
3.8	Footprint and wind streamlines, July	49
3.9	Footprint and wind streamlines, October	50
4.1	Voronoi diagrams	56
5.1	CO_2 time series for Mugogo station	65
5.2	Time series of measured CH_4 mole fractions at Mugogo	65
5.3	Time series of measured CO at Mugogo from June 2015 to February 2017	66
5.4	Black carbon fossil fuel biomass burning ratio	66
5.5	ITCZ location from meridional wind and surface pressure	67
5.6	Vegetation health index and open fires, February	68
5.7	Vegetation health index and fires, August 2016	68
5.8	Zonal mean methane, GlobalView	70
5.9	Zonal mean CO_2 , GlobalView	71
5.10	Time series of closest NOAA stations	72
5.11	Location of closest NOAA sites and the ITCZ	73
5.12	Diurnal cycle of CO_2	74
5.13	Diurnal cycle of methane	75
5.14	measured Mugogo meteorology	76
5.15	Mugogo winds for Dec-Jan-Feb.	77
5.16	Mugogo winds for Mar-Apr-May	77
5.17	Mugogo winds, Jun-Jul-Aug	78
5.18	Mugogo winds for Sep-Oct-Nov	78
5.19	Daily mean carbon monoxide (blue) and black carbon (red) for 2016	79
5.20	CO and BC correlation,Dec-Jan-Feb and Mar-Apr-May	80
5.21	CO and BC correlation,Jun-Jul-Aug and Sept-Oct-Nov	80
5.22	CO and CH_4 correlation, Dec-Jan-Feb and Mar-Apr-May	81
5.23	CO and CH_4 correlation, Jun-Jul-Aug and Sept-Oct-Nov	82
5.24	CO and CO_2 correlation,Dec-Jan-Feb and Mar-Apr-May	82
5.25	CO and CO_2 correlation, Jun-Jul-Aug and Sep-Oct-Nov	83
5.26	Methane rose plot overlaid on a map	84
5.27	Monthly methane rose plots	85
5.28	Monthly CO_2 rose plots	87
6.1	Prior emissions fluxes of methane	90
6.2	NAME domain and subdomain	91

6.3	Scaling factors for boundary conditions	92
6.4	Uncertainty reduction map, methane February 2016	93
6.5	Methane prior and posterior emissions fluxes, February	94
6.6	Scaling map and country totals, February	95
6.7	Time series of optimized mole fractions	96
6.8	time series of optimized mole fractions, October	97
6.9	Monthly methane emissions for the subdomain	98
6.10	Country's prior and posterior emissions estimated for the year 2016	98
7.1	CO_2 Uncertainty reduction map and footprint	102
7.2	CO_2 prior (a) and posterior (b) emissions for February 2016	103
7.3	CO_2 scaling map and country totals	103
7.4	CO_2 optimized mole fractions, March	104
7.5	CO_2 optimized mole fractions, October	105
7.6	Net prior and posterior CO_2 emissions fluxes by country for 2016	106
7.7	Net prior and posterior CO_2 monthly emissions fluxes within the inversion subdomain	106

Acronyms

R_A autotrophic respiration. 99, 101

R_E total ecosystem respiration. 99

R_H heterotrophic respiration. 99, 101

3-D three-dimensional. 41

AERO2k Global Aircraft Emissions data project for climate change impacts evaluation. 100

AGAGE Advanced Global Atmospheric Gases Experiment. 18, 38, 107

AR5 the fifth assessment report. 19

BC black carbon. 39, 79

BP British Petroleum. 100

CARMA CARbon Monitoring and Action. 100

CASA Carnegie-Ames Stanford Approach. 89, 99, 100

CDIAC Carbon Dioxide Information Analysis Center. 100

CRDS Cavity Ring-Down Spectrometry. 29–31, 35, 38

DMSP U. S. Airforce Defense Meteorological Satellite Project. 100

EC Environment Canada. 89

ECMWF European Center for Medium range Weather Forecast. 89, 99

EDGAR Emissions Database for Global Atmospheric Research. 13, 89, 100

ESRL Earth System Research Laboratory. 15, 89, 100

GAW global atmosphere watch. 15, 30, 31

GC Gas Chromatography. 38

GC/MS Gas Chromatography-Mass Spectrometry. 38

GEIA Global Emissions Inventory Activity. 14

GFED Global Fire Emission Database. 89

GFED4.1 Fourth-generation Global Fire Emission Database. 99

GFED_CMS Global Fire Emission Database from NASA Carbon Monitoring System. 99

GHG greenhouse gase. 13, 21, 22

GMD Global Monitoring Division. 107

GOSAT Greenhouse gases Observing SATellite. 16, 17

GPP Gross Primary Production. 99, 101

HYSPLIT Hybrid Single Particle Lagrangian Integrated Trajectory Model. 25

IPCC intergovernmental panel on climate change. 13, 14, 19, 21

IPD inter-polar difference. 20

ITCZ inter tropical convergence zone. 17, 67, 71, 73, 106, 107

LPDM Lagrangian Particle Dispersion Model. 41

M-H Metropolis-Hastings. 53, 54, 56, 59, 90

MCMC Markov Chain Monte Carlo. 55, 62

MERRA Modern-Era Retrospective Analysis for Research and Application. 99

MODIS Moderate Resolution Imaging Spectroradiometer. 89

NAME Numerical Atmospheric dispersion Modeling Environment version 3. 41, 43–46, 67, 90, 99–101

NCEP National Centers for Environmental Prediction. 25

NDVI Normalized difference Vegetation Index. 99

NEE Net Ecosystem Exchange. 99, 101

NOAA National Oceanic and Atmospheric Administration. 15, 19, 23, 25, 33, 69–73, 88, 89, 91, 100, 107, 108

NPP Net Primary Production. 99

NPP National Polar-orbiting partnership. 69

NWP numerical weather prediction. 41

OCO-2 Orbiting Carbon Observatory 2. 16

ODIAC Open-source Data Inventory of Anthropogenic CO_2 . 100

PDF probability density function. 58, 60, 61

RCP representative concentration pathways. 13, 14

RJMCMC reversible-jump Markov Chain Monte Carlo. 6, 55, 63, 88, 99

SCIAMACHY Scanning Imaging Absorption Spectrometer for Atmospheric Cartography. 16, 23, 89

SIO scripps institution of oceanography, university of california, san diego. 19

SRES special report on emission scenarios. 14

STAR Satellite Applications and Research. 69

TCCON Total Carbon Column Network. 17

TDMCMC Trans-dimensional Markov Chain Monte Carlo. 6, 55, 56, 58, 90, 92, 100

TM5 Tracer Model, version 5. 88, 89, 100

UMD University of Maryland. 69

UNFCCC UN Framework Convention on Climate Change. 13

UPS Uninterruptible Power Supply. 28, 38

VIIRS Visible Infrared Imaging Radiometer Suites. 69

WDCGG World Data Center for Greenhouse Gases. 15, 16

WMO World Meteorological Organization. 15, 30, 39

Chapter 1

Introduction

Since the beginning of the industrial revolution, human activities have led to an increase of atmospheric concentrations of most greenhouse gases (GHGs), and the resultant human-induced radiative forcing of the Earth's climate is largely due to the increase in these concentrations. Carbon dioxide (CO_2) and methane (CH_4) are the most radiatively important anthropogenic greenhouse gases; together they contribute to about 81% of the total radiative forcing of well-mixed greenhouse gases [IPCC:WGI 2013, Table 8.2]

Observed emissions trends have been consistently tracking the intergovernmental panel on climate change (IPCC)'s emissions scenarios that lead to the highest temperature increases [Peters, Andrew, et al. 2013; Le Quéré et al. 2009; Raupach et al. 2007], Figure 1.1 [Peters, Andrew, et al. 2013] shows the estimate of observed CO_2 emissions compared to the four generations of intergovernmental panel on climate change (IPCC) scenarios. Interestingly, the observed emissions are out of the range of the most recent IPCC representative concentration pathways (RCP) scenarios, and this suggests that the upper end of possible emissions pathways might need to be readjusted to accommodate even higher emissions in the future. But, more importantly, Figure 1.1 emphasizes the urgent need for an immediate and sustained global mitigation strategy.

Diagnostic studies, commonly called 'top down' methods, which use direct atmospheric measurements lead to independent emissions estimates [Prinn 2000; Weiss et al. 2011; Dlugokencky, Nisbet, et al. 2011; Nisbet et al. 2010] that can be used to better understand responses of climate to emissions and to validate emissions declarations under the UN Framework Convention on Climate Change (UNFCCC).

The accuracy of emission declarations is mixed. Bergamaschi, Krol, et al. [2005] used an atmospheric transport model with observed CH_4 mole fractions to estimate national-level emissions for Europe. They found that emissions reported by some nations to the UNFCCC were underestimated by 50-90% compared to model inversions. Kort et al. [2008] used a Lagrangian particle dispersion model with aircraft measurement of CH_4 and found that North American inventories compiled by the Emissions Database for Global Atmospheric Research

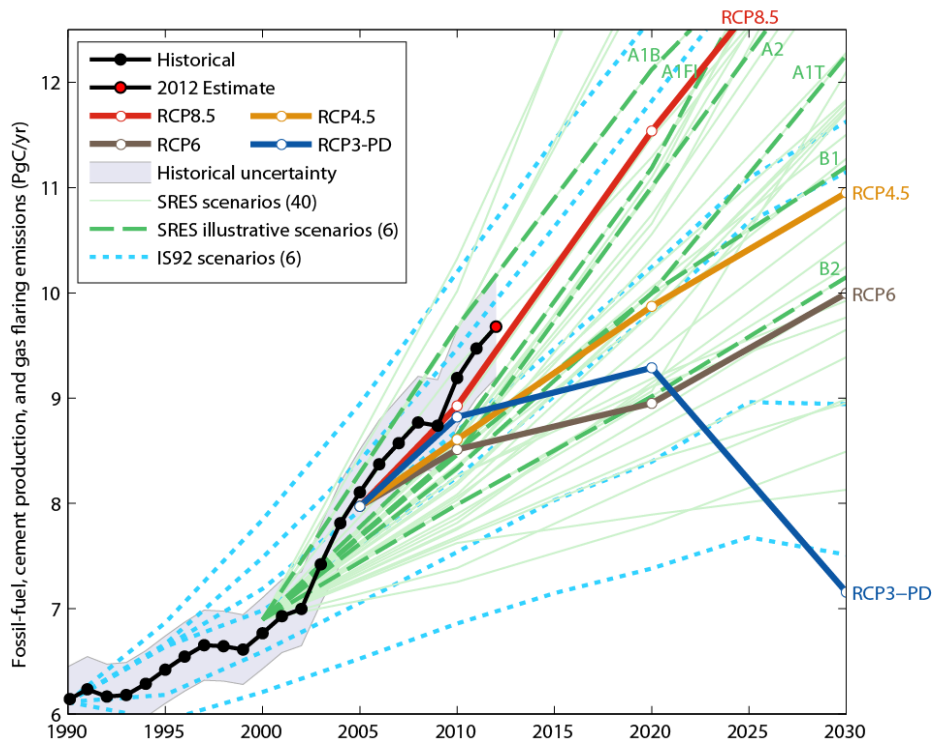


Figure 1.1: Estimated CO_2 emissions over the past three decades compared with IPCC special report on emission scenarios (SRES) and representative concentration pathways (RCP) scenarios. Only IS92-E, IS92-F and SRES A1B exceed the observed emissions [Peters, Andrew, et al. 2013]

(EDGAR) and Global Emissions Inventory Activity (GEIA) are reasonably consistent with observations, at least for the limited temporal and spatial extent of their study.

Current observational networks are suitable to constrain emissions at large scales [Nisbet et al. 2010; IPCC:WGI 2013] but not at regional to national scales necessary to verify emissions reductions. This is particularly true in the tropics where there is virtually no long-term land-based time series of concentrations [Dlugokencky, Nisbet, et al. 2011]. The lack of accurate meteorological data, particularly in Africa, constitutes an additional limitation to top down estimation of regional emissions and sinks of CO_2 and CH_4 .

The objective of this study is to provide significantly more accurate estimations of CO_2 and CH_4 sources and sinks in Central and Eastern Africa through a new high frequency greenhouse monitoring station and a new method for objective quantification of model uncertainties in inverse modeling.

1.1 Problem statement

The role of the tropics in the global carbon budget is becoming more apparent and is likely to be central in the coming decades. This is due to the significant share of carbon emissions from agriculture, biomass burning and other land use change, which is, in fact, the most uncertain term in the global CO_2 budget [Houghton et al. 2012]. Furthermore, the tropics played a central role in the recent increase of atmospheric methane [Rigby et al. 2008; Dlugokencky, Bruhwiler, et al. 2009; Bousquet, Ringeval, et al. 2011].

This section reviews the status of observational networks in Africa including ground-based and satellite observations, highlighting the urgent need for high frequency ground-based observations.

1.1.1 CO_2 and CH_4 measurement in Africa

1.1.1.1 Ground-based observations

Atmospheric measurements are mostly made by developed countries and where logistics make them feasible. This results in large gaps in sampling. In particular, there are only a few stations measuring CH_4 and CO_2 in the tropics, and virtually no long-term interior land-based time series [Dlugokencky, Nisbet, et al. 2011]. Figure 1.2 shows the distribution of stations that contribute to World Data Center for Greenhouse Gases (WDCGG) of World Meteorological Organization (WMO) global atmosphere watch (GAW) program [GAW November, 2013]. Only two low frequency flask stations, operated by National Oceanic and Atmospheric Administration (NOAA)/Earth System Research Laboratory (ESRL), are located on the entire African continent, and there is currently no station in equatorial Africa (The Mount Kenya station shown on the map stopped operating in June 2011) [NOAA/ESRL/GMD November, 2013]).

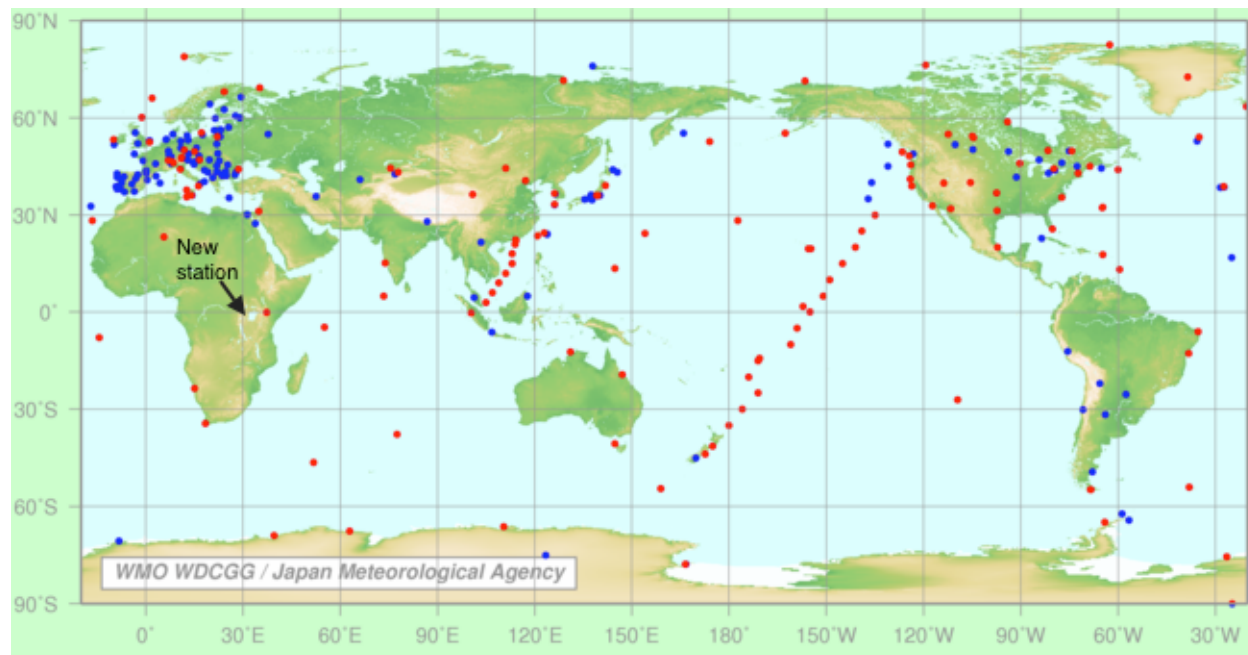


Figure 1.2: Distribution of fixed stations that contribute data to the WDCGG The red symbol denotes that the data from the station have been updated in the last 365 days prior to this report [GAW November, 2013]

1.1.1.2 Satellite observations

Satellite data complement ground-based observations due to their wider geographical coverage. Satellites are particularly valuable in tropical latitudes where long term *in situ* data are scarce. In a recent CO_2 fluxes estimation, Maksyutov et al. [2013] have found that including Greenhouse gases Observing SATellite (GOSAT) column-averaged mole fractions reduced uncertainty in estimated fluxes in the tropics by 60% compared to ground-based observations only. A similar study [Fraser et al. 2013] for CH_4 found at least twice the error reduction using Greenhouse gases Observing SATellite (GOSAT) plus surface measurements compared to the surface network only. Bergamaschi, Houweling, et al. [2013] have found that addition of Scanning Imaging Absorption Spectrometer for Atmospheric Cartography (SCIAMACHY) column averages produces more reasonable spatial distributions of emissions in the tropics. However, after the retirement of SCIAMACHY, GOSAT and the Orbiting Carbon Observatory 2 (OCO-2) are currently the only available satellites for CO_2 and CH_4 column data.

The usefulness of satellite data relies on the existence of ground-based validation and calibration networks. Relying on reflected sunlight and ground infrared emissions, GOSAT retrievals are highly affected by aerosol and clouds and have been associated with large biases. In a preliminary validation of GOSAT retrievals, Morino et al. [2011] have found a negative

bias of 8.85 ± 4.75 ppm and 20.4 ± 18.9 ppb respectively for CO_2 and CH_4 and Yoshida et al. [2012] have also found a time-dependent degradation of GOSAT's radiometric sensor. Although a correction has been applied, this still suggests a need for regular validation and calibration of satellite data.

Figure 1.3 shows the stations location for the Total Carbon Column Network (TCCON) [Wunch et al. 2011], which is currently used to validate and calibrate GOSAT retrievals. TCCON has only a handful of stations and a single station in the tropics. This is a severe limitation, given high cloud fractions and aerosol loading found in the tropics. There is therefore an urgent need for much high accuracy *in situ* time series from the tropics [Dlugokencky, Nisbet, et al. 2011]. In addition, the frequent cloud cover in equatorial regions, makes it difficult for the satellite to 'see' the equatorial atmosphere, which leads to under-sampling those regions. The maps of typical monthly average CO_2 columns are represented in Figure 1.4 for July 2009 and January 2010. A large gap in equatorial regions is due to elevated aerosol loading and cloud fraction corresponding to the approximate location of the inter tropical convergence zone (ITCZ), while the data gap in the northern hemisphere winter is due to the high surface albedo.

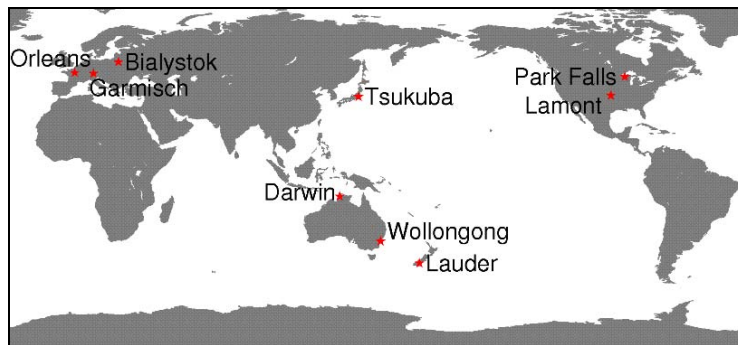


Figure 1.3: Ground based Total Carbon Column Network (TCCON) sites used for GOSAT product validation [Morino et al. 2011]

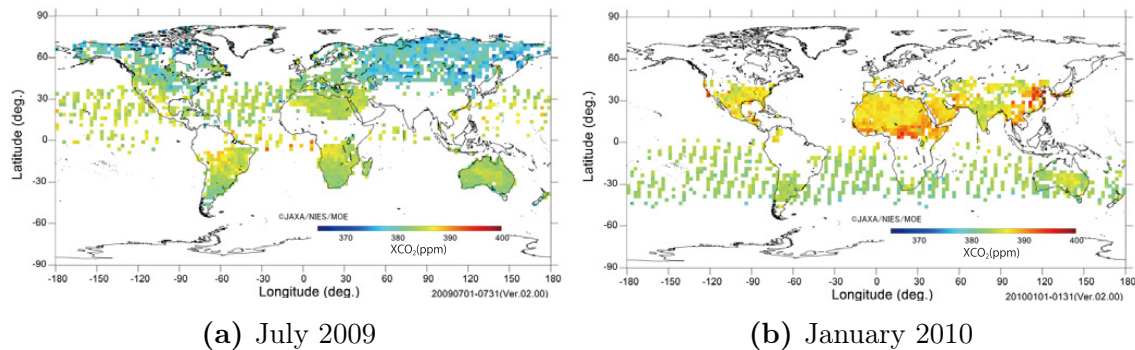


Figure 1.4: Typical monthly average CO_2 columns from GOSAT [GOSAT leaflet, GOSAT Project 2013]

1.1.2 Goals of the current project

This study aims at improving the accuracy of regional estimates of CO_2 and CH_4 fluxes in Central and Eastern Africa in two complementary approaches. First, we have established a high frequency high precision greenhouse gases monitoring site in Rwanda, which measures multiple greenhouse gases including CO_2 , CH_4 , CO and meteorological parameters. The measured parameters are detailed in chapter 2. The new site located at Mount Mugogo ($1^{\circ}35.175 S$, $29^{\circ}33.941 E$), follows the protocols and calibration standards of the Advanced Global Atmospheric Gases Experiment (AGAGE) [AGAGE, Prinn, Weiss, et al. 2000] and is joining the AGAGE global network. The location of the new station is shown by a black dot and arrow in the map of Figure 1.2.

Second, we have used the high frequency data from the new station to optimally estimate the surface fluxes of CO_2 and CH_4 in Eastern and Central Africa. The optimized emissions provide improved knowledge and understanding of the drivers of the carbon cycle in this region.

1.2 Rationale

The station in Rwanda is the only high frequency greenhouse monitoring station on the African continent. This station is being integrated in the AGAGE network, to provide a new long term series of measurements added to the present AGAGE research project. The high frequency mixing ratios combined with meteorological data, allowed the detection of changing surface fluxes or processes from all the surrounding regions sampled due to the shifting wind patterns, and has allowed the discrimination of local versus remote pollution sources. The newly established station has been a valuable resource not only for this study but also for the scientific community seeking to estimate regional and global fluxes of CO_2 and CH_4 .

We have produced the first comprehensive regional observation-based optimal estimates of net surface fluxes of equatorial African CO_2 and CH_4 . The estimated fluxes constitute additional data for comparison and cross-checking global inversion studies, for calibration of ecosystem models, and for regional emissions verification.

The regional climate of Eastern and Central Africa where a very dry season alternates with a heavy rainy season has provided a unique opportunity to qualitatively assess the response of ecosystem CO_2 sources and sinks and wetland methane emissions to different meteorological conditions. Therefore, we have, at least partially, contributed to the currently unresolved question of the role of this region in the global CO_2 cycle [IPCC:WGI 2013], and the potential drivers of the recent global methane increase as discussed in section 6.3.

1.3 Budgets of carbon dioxide and methane

1.3.1 Global and Regional Budgets of Carbon Dioxide

The fifth assessment report (AR5) of the IPCC has concluded that the tropospheric mixing ratio of CO_2 was 390.5ppm in 2011[IPCC:WGI 2013, table 2.1] while the most recent estimate of tropospheric CO_2 mole fractions from NOAA is 406.36 ppm . This is a well constrained quantity with the 90% confidence interval uncertainties of 0.07% and 0.04% respectively for estimates from scripps institution of oceanography, university of california, san diego (SIO) and NOAA.

The partition of global CO_2 emissions into different sources and sinks is relatively well constrained by observations. The largest source of net CO_2 emissions is fossil fuel combustion with a 1750-2011 cumulative estimate of 365 ± 30 PgC, while the most uncertain term in the global carbon budget is the land-to-atmosphere flux with the 1750-2011 cumulative estimate of 30 ± 45 PgC, that has 150% uncertainty (90% confidence interval)[IPCC:WGI 2013; Houghton et al. 2012; Ballantyne et al. 2012].

Current observational networks are sufficient to quantify global annual mean burdens of CO_2 , but they are not sufficient for accurately estimating regional scale net emissions and their evolution with time. This is particularly the case for land-to-atmosphere CO_2 fluxes. The results from atmospheric CO_2 inversions, terrestrial ecosystem models and forest inventories consistently show that there is a large net CO_2 sink in the northern extra-tropics, with no robust conclusion in the tropics due to the very limited availability of observations [IPCC:WGI 2013, AR5, p.165].

1.3.2 Global and regional budgets of methane

Methane is an attractive target for short term reduction in greenhouse gas induced warming. The short lifetime and high global warming potential relative to CO_2 mean that the benefits of emissions reductions manifest in short term. Investment in methane abatement is relatively cheap [Dlugokencky, Nisbet, et al. 2011] and would, therefore, buy time for development of cheaper CO_2 mitigation technologies.

Methane is emitted to the atmosphere by natural (wetlands, oceans, wild animals, termites, wild fires) and anthropogenic (fossil fuel exploitation, domestic ruminants, rice cultivation, waste decomposition, biomass burning) sources. Both natural and anthropogenic sources have approximately equal contributions to atmospheric CH_4 . Figure 1.5a [adapted from: Global Carbon Project(2013) Methane budget and trends 2013; Kirschke et al. 2013] illustrates that wetland emissions are the single largest source of CH_4 in the atmosphere. As indicated by Figure 1.5b, the relative magnitude of removal processes of atmospheric methane; the major removal mechanism is the reaction of CH_4 with the hydroxyl radical (OH) in the troposphere.

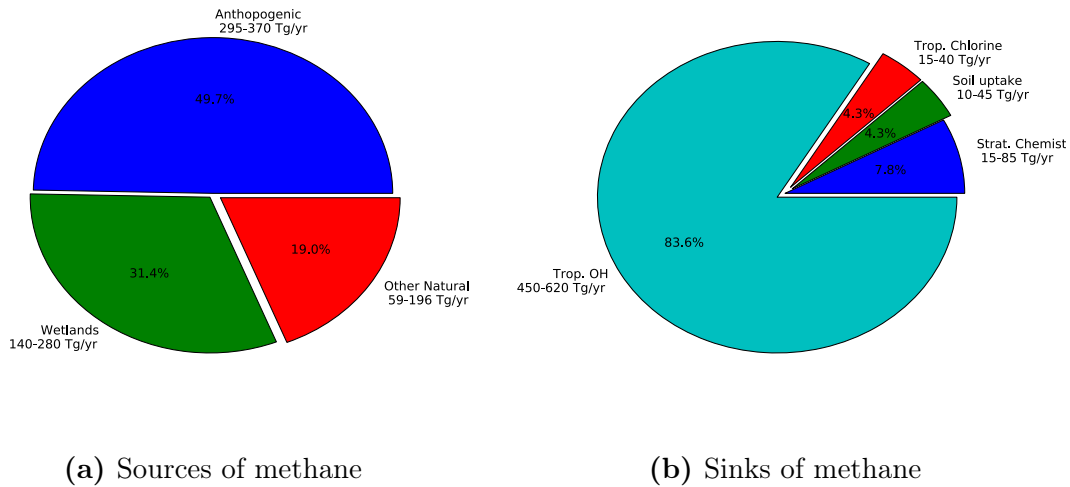


Figure 1.5: Sources and sinks of atmospheric methane [adapted from: Global Carbon Project(2013) Methane budget and trends 2013; Kirschke et al. 2013]

Additional minor removal pathways include reaction with atomic chlorine in the marine boundary layer [Dlugokencky, Nisbet, et al. 2011; Kirschke et al. 2013] soil uptake and stratospheric sinks which include reaction with Cl, OH and $O(^1D)$.

Since the beginning of the industrial era, atmospheric methane concentrations have increased from 733 ppb to 1803 ppb in 2011 [IPCC:WGI 2013]. Atmospheric CH_4 concentrations were relatively stable from 1990 to 2006. Several possible scenarios have been proposed to explain this near-cessation of methane growth rate: Simpson et al. [2012] and Chen et al. [2006] have suggested a reduction of anthropogenic emitting activities such as coal and gas industry and animal husbandry especially in the former Soviet Union; Bousquet, Ciais, et al. [2006] and Chen et al. [2006] have proposed a compensation between increasing anthropogenic emissions and decreasing wetlands emissions; while a significant [Rigby et al. 2008] or small [Montzka et al. 2011] increase in OH concentrations (i.e. increase in sink) have been proposed.

Dlugokencky, Nisbet, et al. [2011] have found that the difference between northern ($53 - 90^\circ N$) and southern ($53 - 90^\circ S$) annual mean CH_4 mole fractions, referred to as the inter-polar difference (IPD) was decreasing from 1991 to 1992 and has not yet recovered. The decreasing IPD suggests that the recent post (2006) methane increase was not driven by a source in northern high latitudes. Analysis of $\delta^{13}C$ in CH_4 and CO mole fractions [Dlugokencky, Nisbet, et al. 2011], and tropical precipitation patterns suggest that these increases were driven by higher than average precipitation in the tropics [IPCC:WGI 2013].

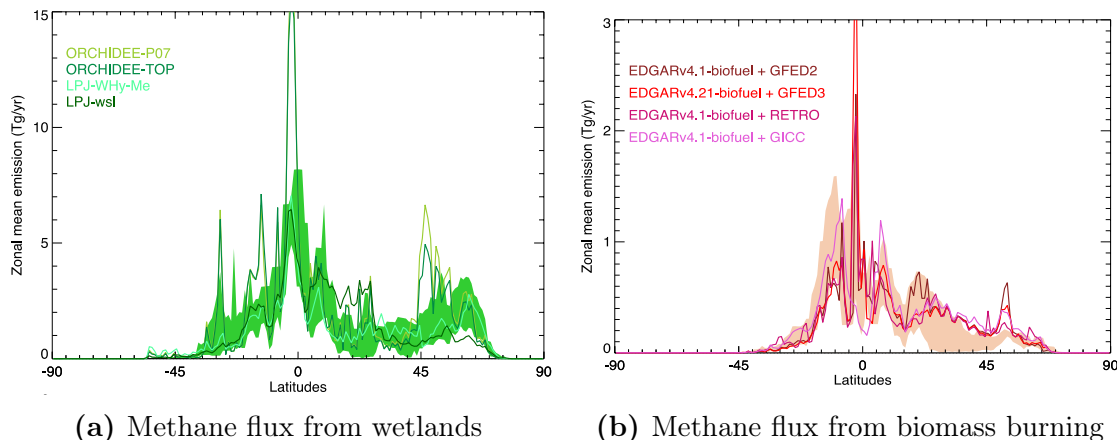


Figure 1.6: Zonal mean flux of CH_4 from wetlands and biomass burning [Kirschke et al. 2013, Supplementary information]

Methane fluxes from tropics play an important role in the global methane budget and inter-annual variability; Figure 1.6 from Kirschke et al. [2013] shows the zonal mean flux of CH_4 from wetlands and biomass burning, which shows that the largest fluxes of CH_4 are located in the tropics. In addition, the largest CH_4 sink is also in the tropics due to the strong tropical sunlight producing OH. Despite the important role of the tropics in the CH_4 budget, there are only a handful of sites measuring CH_4 at high frequency (e. g. hourly) and virtually no long-term interior land-based time series [Dlugokencky, Nisbet, et al. 2011]. The available satellite tropical data are of limited usefulness if not validated by much higher accuracy *in situ* measurements in the tropics.

1.3.3 Method for estimation of sources and sinks of CO_2 and CH_4

1.3.3.1 Bottom up methods

Current emissions reduction legislation relies upon accounting methods for calculating emissions inventories of industrial and biogenic greenhouse gases at their sources, and this approach is generally called ‘bottom-up’ reporting. IPCC has developed detailed guidelines [IPCC 2006] for emissions inventories and reporting. The IPCC approach is to combine information on the extent to which human activities take place (called *activity data* or AD) with the coefficients quantifying the emissions or removals per unit of activity (called *emission factor* EF). The basic equation is therefore:

$$Emissions = AD \times EF \tag{1.1}$$

Other ‘bottom-up’ GHG emissions estimations include global extrapolation of direct flux (or proxy flux) measurements, where local exchange fluxes are measured from different source types and extrapolated to regional or global scales, thus enabling quantification of the flux

budgets, under the assumption that the study sites are representative of those scales. The challenge for this method is the typically large heterogeneity of surface fluxes depending on the type, extent and state of the considered ecosystem.

Process models are additional ‘bottom-up’ methods which seek to represent the actual physical and biological process that produce a considered greenhouse gas [e.g. Saikawa et al. 2013]. This approach suffers from modeling uncertainties, especially those equations and parameters linking climate variables to actual fluxes .

Bottom-up GHG estimates often tend to differ significantly from those deduced from observations and inverse modeling. But these methods usually do better than inverse methods in attributing emissions to different source types [e.g. Kirschke et al. 2013].

1.3.3.2 Top down methods

The Bayesian setting for inverse problems offers a rigorous foundation for inference from noisy data and uncertain forward models. It is a natural mechanism for incorporating both prior information, and quantitative assessments of uncertainty into the inferred results (a detailed formulation of the Bayesian inverse problem is provided in section 4.1). In the Bayesian inference, the condition for optimality is often expressed by the need to minimize the “cost” or “objective” function. Different Bayesian methods differ mostly in the way they minimize the cost function: sequential data assimilation like Kalman filters, iterative minimization like variational methods and sampling methods like Markov Chain Monte Carlo methods. The latter method is usually the most general and flexible method for complex high-dimensional problems [Marzouk et al. 2007; Miller et al. 2013]. The following paragraphs briefly review common methods used in Bayesian inference and some example applications in atmospheric sciences.

General approach: Stochastic filtering

The Kalman Filter(KF): The Kalman filter [Kalman 1960] is an optimal sequential data assimilation method for a system driven by linear dynamics and involving measurement processes with Gaussian errors. The KF, therefore, provides an unbiased, minimum variance estimate of the state of the system from noisy measurements. A Kalman smoother uses past and future (relative to a given time) observations to update the priors. Fixed-lag Kalman filter/smoother use a fixed time window of observations to recursively update the priors. Fixed-lags are particularly useful in application to the atmosphere because a pulse in emissions at a given location and time gradually decays within a few months. Rigby et al. [2008] have used a Kalman filter together with a 12-box model to investigate the possible drivers a renewed growth of atmospheric methane [see also, Chen et al. 2006, for KF application to methane in a 3D model]. Maksyutov et al. [2013] have used a 3-months

window fixed-lag Kalman smoother to estimate regional CO_2 emissions from GOSAT satellite column data [see also, Bruhwiler et al. 2005, for details on the fixed-lag Kalman smoother].

The Extended Kalman Filter (EKF): For nonlinear systems, a linearization process can be used to approximate the nonlinear dynamics, thus applying the Kalman filter on the approximate model. The linearized models are often obtained by a first-order Taylor approximation or by Tangent linear models. The resulting filter is known as the Extended Kalman Filter [Chui et al. 1991]

Variational data assimilation is used for nonlinear models for an iterative minimization of the cost function. Bergamaschi, Houweling, et al. [2013] have used 4-dimensional variational data assimilation to optimally estimate the surface fluxes of methane using SCIAMACHY satellite retrievals and NOAA surface observations.

Ensemble Kalman Filter (EnKF): The ensemble Kalman filter [Burgers et al. 1998] aims at resolving some of the drawbacks of the extended Kalman filter. The EnKF is based on forecasting the error statistics using Monte Carlo sampling. The major drawback of the EnKF is the large number of model runs necessary to properly approximate the model state statistics.

Markov Chain Monte Carlo (MCMC): MCMC algorithms make it possible to generate realizations of the unknown quantity from high-dimensional probability density functions. MCMC methods can be applied in the Bayesian inference for inverse problems as an efficient method for calculating multidimensional integrals needed to extract information from the *a posteriori* probability density function. This method relies on the generation of conditional realizations: each realization is a guess of the unknown that should represent a random draw from the posterior probability distribution. The algorithms create a new realization based only on the previous one. Miller et al. [2013] have used synthetic methane data for the US in order to compare various methods used in inverse flux estimation. They have found that MCMC implementations produce the most realistic best estimate, conditional realizations and uncertainty bounds. MCMC methods are discussed in section 4.2 while transdimensional MCMC methods are discussed in section 4.3.

1.4 Site selection and characterization

1.4.1 Geography and climate of Rwanda

Rwanda is a landlocked country in Central/Eastern Africa bordered by Uganda to the North, Burundi to the South, Tanzania to the East and the Democratic Republic of the Congo to the West. With 26 338 km², Rwanda is the fourth smallest country on the African mainland.

Rwanda is mostly high altitude with the lowest point at 950 m above sea level in the South West. The central and western parts of Rwanda are dominated by mountains which are part of the Albertine branch of the East African Rift, and in this region the altitude ranges between 1500 to 2500 m above sea level, with the highest point found at the summit of the volcano Karisimbi at 4507 m. The eastern part of Rwanda is savannas and plains which are generally around 1400 m above sea level.

Despite being in the tropical belt, Rwanda experiences a temperate tropical highland climate as a result of high elevations. The daily average minimum temperature varies between 10 °C to 16 °C and the average maximum temperature between 20 °C to 28 °C [Mendelsohn et al. 2016; Vital Signs 2016]. The temperature varies across different regions due to the elevation changes, but it is fairly constant around the year for a specific location. The mountainous North West is generally cooler than the low-lying eastern part of the country.

Rwanda experiences a bimodal pattern of rainfall, which is primarily driven by the progression of the Inter-Tropical Convergence Zone (ITCZ). The two rainy seasons of March-April-May and October-November-December alternate with two dry seasons of January-February and June-July-August-September.

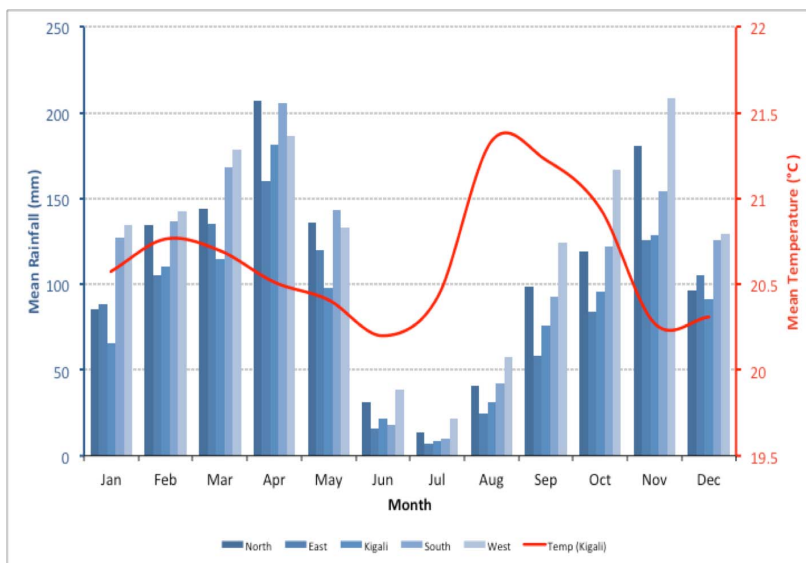


Figure 1.7: Monthly average rainfall for different regions of Rwanda (vertical bars) and monthly average temperature (red curve) at Kigali airport [McSweeney 2011]

1.4.2 Site selection

Mount Mugogo is located in the Northern province of Rwanda. The site is located at latitude 1°35.175 South, longitude 29°33.941 East and altitude 2590 m above sea level. Mount

Mugogo was primarily selected for its ability to sample air masses from a wide area of tropical Africa and a wide range of altitudes. Figure 1.8 depicts the 7-day back trajectories of air masses arriving at Mount Mugogo during the year 2008 [Prinn, Huang, et al. 2011]. Trajectories are computed by the NOAA Hybrid Single Particle Lagrangian Integrated Trajectory Model (HYSPLIT) using National Centers for Environmental Prediction (NCEP) reanalysis meteorology.

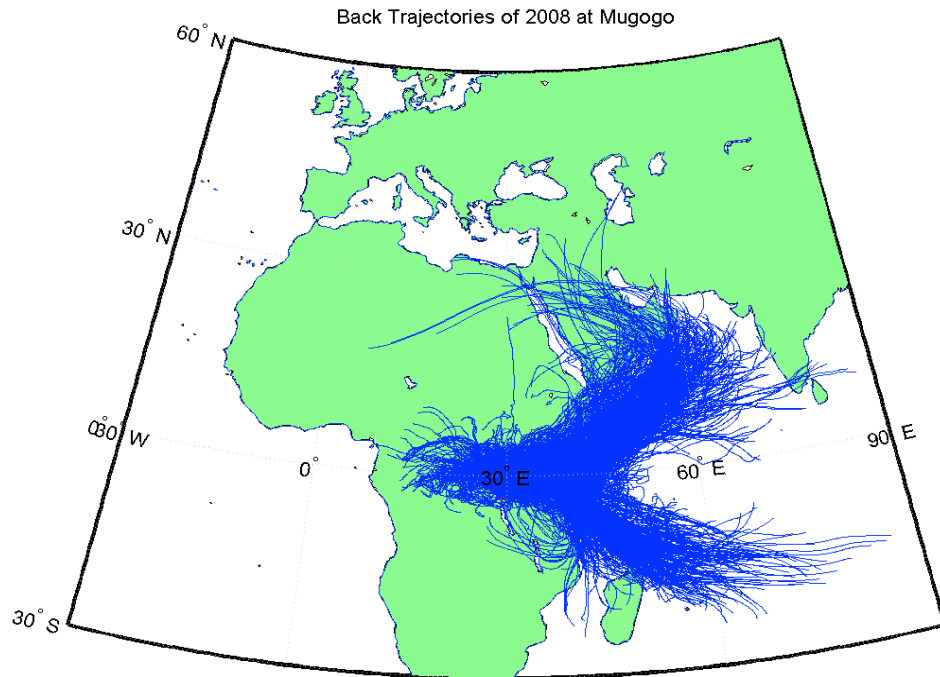


Figure 1.8: Back trajectories of air mass coming to Mount Mugogo for the year 2008[Prinn, Huang, et al. 2011]

Back trajectories were calculated every six hours and each trajectory was run for 7 days backward in time. The trajectories of air masses sampled at Mugogo stretch Northeast as far as Saudi Arabia and the Indian West Coast. In the South East direction the air masses sampled at Mugogo come from as far as Madagascar. The air masses from the East of Mugogo travel over the East African region characterized by a high population density, urban areas and intense agricultural activities. On the western side of Mugogo, air parcels come mainly from the equatorial forests in the Democratic Republic of Congo and Central African Republic.

The low infrastructure costs and accessibility of Mount Mugogo also motivated the choice of this site. Mount Mugogo was already equipped with two telecommunication towers, power

supply, back-up power supply and an existing building suitable for a field laboratory.

Mount Mugogo is located in a rural area at about 70 km away from the capital city of Rwanda, Kigali and 13 km away from the nearest town of Musanze. Depending on wind and boundary layer height, measurements taken at Mount Mugogo may be occasionally influenced by local sources including emissions from the nearby city and wood fires from small rural settlements around Mugogo.

Chapter 2

Field Set up and Instrumentation

One of the main goals of this project was to setup a station that measures greenhouse gases in North West Rwanda to continuously monitor carbon dioxide, methane and other trace gases.

This chapter describes the field site and the instrument used. This chapter also provides technical descriptions of our approach to minimizing water vapor interference as well as the precision, drift and linearity of the instrument . The last section is an overview of other instruments that were also installed at our field site.

We have found that the instrument has very good precision, comparable to the values reported in literature for similar instruments. Furthermore, the instrument was stable with no measurable drift during the course of this work.

2.1 Description of the field site

The climate observatory station is housed in a small three-room building at the summit of mount Mugogo. On the same summit there is a 50-meter tall tower which hosts the instrument inlets as well as Radio, TV and mobile communication equipment. There is also another smaller tower used by telecommunication companies.

The station is powered by mainline 240 V power from national grid, with a backup automatic diesel generator conveniently located at 300 meters below and away from the station. Instruments in the laboratory are powered through an Uninterruptible Power Supply (UPS).



Figure 2.2: View of Mount Mugogo



Figure 2.1: Laboratory building for the station. The tall tower is in the background and the smaller tower in the foreground

2.2 Picarro G2401 for high frequency measurement of carbon dioxide, methane and carbon monoxide

The main instrument for this work is the Picarro G2401 which measures CO_2 , CH_4 , carbon monoxide (CO) and water vapor (H_2O).

This is an optical instrument which uses Cavity Ring-Down Spectrometry (CRDS) to accurately measure mole fractions of CO_2 , CH_4 , CO and water vapor (which is also used to correct for H_2O interference with CO_2 and CH_4). The G2401 attributes are reviewed below [Yver Kwok et al. 2015; Rella et al. 2013; Picarro 2016]:

1. The measurement cell is a low-loss (mirror reflectivity of 99.995 %) optical resonant cavity consisting of three highly reflective mirrors. The optical cavity serves as a compact flow cell with volume less than 10 cm^3 and effective optical path length of 15 to 20 km
2. When a pulse of laser light is introduced into the cavity, it is reflected multiple times and partially transmitted through the mirrors. A photosensitive detector located behind one of the mirrors detects the transmitted light and monitors the decay (ring-down) time of the laser light. The decay time depends on the cavity loss as well as the amount of absorbing gases inside the cavity.
3. The concentration of the absorbing gas inside the cavity is estimated by comparing the ring down time of an empty cavity (with no absorbing gas) to the cavity containing the gas. An empty cavity is achieved by alternatively tuning the laser to different wavelengths where the gas absorbs light and then to wavelengths where the gas does not absorb light.

The cavity ring down spectroscopy which is a relatively new technology [Crosson 2008] has gained global attention [Yver Kwok et al. 2015; Andrews et al. 2014] in greenhouse gas field measurements because it provides multiple advantages compared to gas chromatography systems and nondispersive infrared sensors. Some of the advantages of cavity ring down systems include low maintenance and consumables, linearity and stability robustness and easy deployment.

2.2.1 Earth Networks sampling and drying unit

The atmospheric water vapor concentration affects measurements of CO_2 and CH_4 mainly in two ways: *dilution* and *spectral line broadening*.



Figure 2.3: Picarro G2401

Dilution effect: The dilution effect is the change of the mole fractions of atmospheric trace gases due to the variation in the humidity. Increasing humidity adds additional water vapor to the air thus decreasing the mole fractions of other gases. Similarly, when the air becomes dryer, the mole fractions of CO_2 and CH_4 will be enhanced due to water vapor molecules that have been removed from the air.

Spectral broadening effect: This is an effect by which thermal vibrations and random collisions of the target molecule with surrounding molecules cause the broadening of the spectral line. This Lorentzian broadening is parameterized by the line broadening parameter γ which is proportional to the pressure and the compositions of the background gas mixture and is, therefore, affected by the presence or absence of water vapor.

Water vapor can vary very rapidly geographically and in time, which causes variability in mole fractions of CO_2 and CH_4 . The variability due to change in humidity can potentially mask the smaller variability in mole fractions of CO_2 and CH_4 that are due to surface-atmosphere exchanges [Rella et al. 2013]. Consequently, mole fractions of CO_2 and CH_4 are meaningful only when they are reported relative to dry air conditions.

The Global Atmospheric Watch program of the World Meteorological Organization (WMO/GAW) has set an inter-laboratory compatibility goal of ± 0.1 ppm and ± 0.05 ppm for CO_2 in Northern and Southern Hemispheres respectively and an inter-laboratory compatibility goal of ± 2 ppb for methane [WMO 2011, Table 1]. Traditionally to achieve this WMO requirements using non-dispersive infrared spectroscopy for carbon dioxide and gas chromatography for methane, measurement has to be taken from a dry sample; for example a water vapor mole fraction of 500 ppm (dew point of -32°C at 1 bar) causes a dilution bias of -0.2 ppm for lower CO_2 readings [Rella et al. 2013].

Drying systems come with several disadvantages among others: they add cost and complexity to the sampling system, they use consumables that need periodic replacement and most of them require periodic human intervention for proper operation.

Cavity ring down spectroscopy based analyzers allow accurate and precise measurements of dry mole fractions of carbon dioxide and methane by measuring water vapor and using experimentally derived water vapor correction algorithms.

Yver Kwok et al. [2015] have conducted a thorough testing of Picarro CRDS analyzers using 62 Picarro CRDS instruments, 47 instruments in the laboratory and 15 instruments in the field for a period of five years, their recommendations which are echoed by Picarro's own study [Rella et al. 2013] are summarized below:

- for water vapor mixing ratios below 1% the Picarro CRDS analyzers are well within the GAW compatibility goals, even if all instruments use the same water correction factors.

- When an instrument-specific correction factors are used, the water vapor mixing ratio ranges can be extended to 2%
- If correction factors are determined periodically over time, the water vapor mixing ratio ranges can be extend to 4%

For our station located around 1.5°S, water vapor concentration above 2% are expected to be common during the rainy seasons. We address this issue using the Earth networks sampling and drying module (Figure 2.4), Figure 2.5 shows the water vapor mixing ratio measured by the Picarro G2401 before February 2016 when the station has not yet acquired the Earth Network dryer, and from February 2016 when the sample air was dried, the corresponding percentage corrections for CO_2 and CH_4 are presented in Figure 2.6. During the short rain season of October, November and December; water vapor mixing ratios were consistently greater than 2%. Worth noting is that the measured water vapor mixing ratio before February 2016 does not represent the whole picture because the short dry season of January to March and the long rain season of March to June are not represented. To stay in the GAW compatibility goals, periodic calculation of water vapor correction coefficients would, therefore, be required for our station. H_2O corrections coefficients experiments are difficult to perform especially for our field work which is located in a remote region.

A more attractive alternative to periodic determination of water vapor correction coefficients has been implemented by Earth Networks Inc. which operates a commercial meteorological observing system including greenhouse gas monitoring [Welp et al. 2013]. In this approach, a simple but effective drying technique is used with residual water vapor mixing ratio generally close to 0.2% (0.1% for our case) . With water vapor mixing ratio of 0.2% or less the Picarro CRDS analyzer is guaranteed to provide accurate dry mole fractions of carbon dioxide and methane during the lifetime of the instrument. The Earth Network sampling and drying unit uses a nafion dryer that is purged by reusing the sample gas that has been partially dried passing through the inner nafion membrane, and, therefore, the Earth Network sampling and drying unit does not use consumables that need to be replaced.



Figure 2.4: Earth Networks sampling and drying unit

During this study we have used the Picarro G2401 without Earth network sampling and drying unit from June 2015 to end of January 2016. From February 2016 ongoing, the station uses the Earth Networks unit.

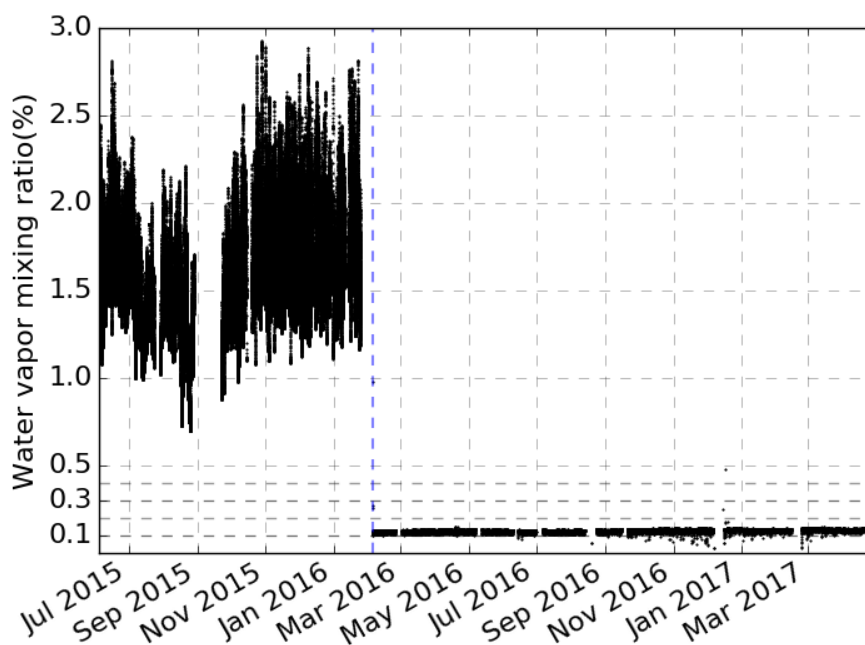
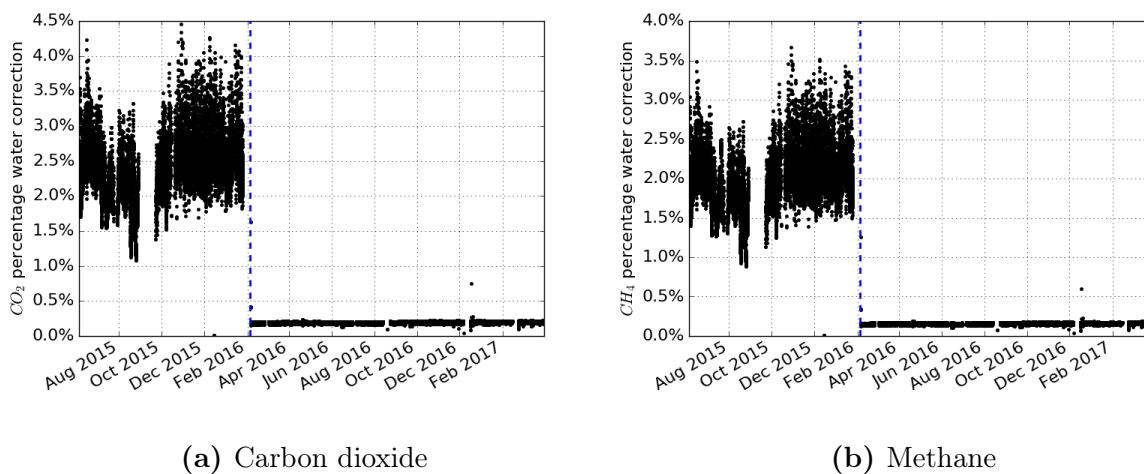


Figure 2.5: Measured water vapor mixing ratio in humid air (up to January 2016) and in dry air (from February 2016), the vertical line indicates the start of drying



(a) Carbon dioxide

(b) Methane

Figure 2.6: Percentage water corrections (dry - wet)/dry. The vertical line indicates when we started drying the sample

2.2.2 Site setup and calibration

The air sample inlet which is a stainless steel inverted cup, is located at 40 m above the ground on the tower. A synflex tubing connects the inlet to the Earth Network sampling and drying module in the laboratory, where all connections are stainless steel $\frac{1}{8}$ inch diameter. A VICI[®] Valco multiposition valve inside the sampling module follows a pre-programmed sequence of ambient air and calibration tanks.

In the context of calibration, we will use the term *instrument response* with symbol r , to mean the mole fractions output by instrument before a calibration is applied, while *mole fractions* with symbol χ will be used for calibrated mole fractions.

2.2.2.1 Calibration tanks

We have used three calibration tanks filled by NOAA in aluminum AL-150 cylinders. The serial numbers of the calibration tanks are listed in Table 2.1 along with the mole fractions of CO_2 , CH_4 and CO .

Table 2.1: Serial numbers and composition of calibration tanks used in this project. Values marked with a '*' are measured values calibrated with the two other tanks

	CC114957	CB10893	CB10203
CO_2	389.32 ± 0.01 ppm	419.34 ± 0.00 ppm	230.20^* ppm
CH_4	1946.16 ± 0.09 ppb	1888.12 ± 0.26 ppb	1074.94^* ppb
CO	136.58 ± 0.04 ppb	240.64 ± 0.38 ppb	91.26 ± 0.15 ppb

The mole fractions for CO_2 and CH_4 were not reported by NOAA for the tank CB10203 because it was specifically targeted to cover the low range of carbon monoxide mole fractions. This resulted in far too low mole fractions for CO_2 and CH_4 relative to ambient levels. Still, the CB10203 calibration tank has been useful in assessment of the instrument drift and linearity.

Due to logistical reasons, the tank CC114957 which is near ambient for CO_2 and CH_4 was only available from August 2016, for other tanks, calibrations started in October 2015 while measurement started in June 2015. We have, therefore, used one point calibration for CO_2 and CH_4 before August 2016 and two points calibration afterwards. The implication of this is discussed in section 2.2.2.5. Data time series and corresponding measurements of calibration tanks are presented in Figure 2.7 for

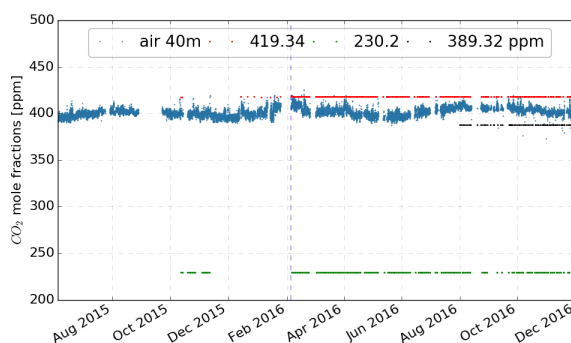


Figure 2.7: CO_2 mole fractions time series and corresponding calibration tanks

CO_2 and Figure 2.8 for methane and carbon monoxide.

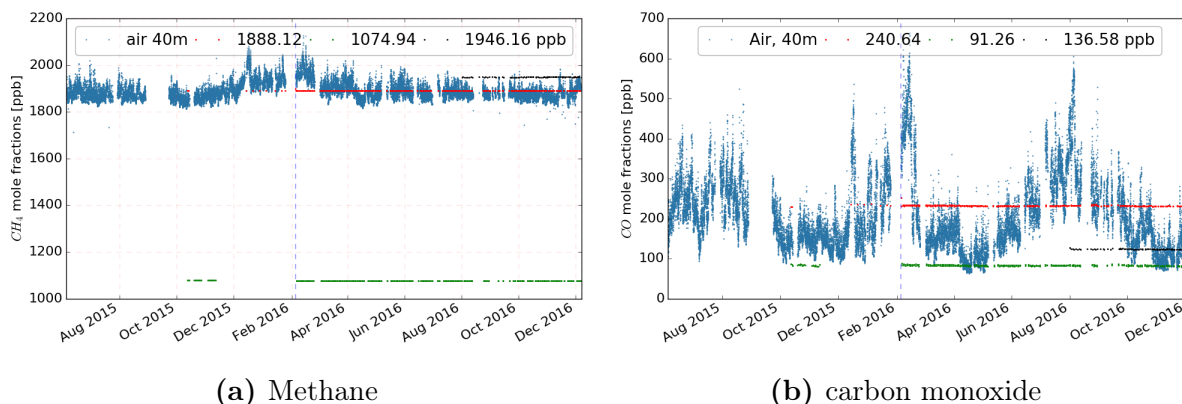


Figure 2.8: Data time series and calibration tanks for CH_4 and CO_2

2.2.2.2 Repeatability

Repeatability allows to understand the smallest mole fractions that can be resolved by an instrument, which is an indicator of the instrument’s precision. We have assessed repeatability by taking the standard deviation of each calibration session for each calibration tank. Calibration sessions, which last twenty minutes, were done every other day for each tank, but data corresponding to the transient period of the first ten minutes were automatically rejected.

We have found an average repeatability of 0.02 ppm for CO_2 , 0.20 ppb for CH_4 and 7.2 ppb for CO , these values are similar to those found by Yver Kwok et al. [2015, Table 1] for the Picarro G2401 models. Histograms of standard deviations of ten minutes calibration sessions are shown in Figure 2.9 for CO_2 , Figure 2.10 for CH_4 and Figure 2.11 for CO .

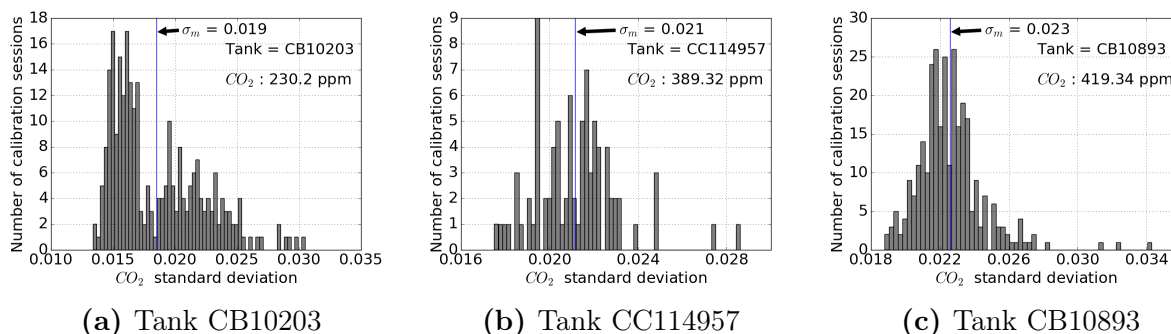


Figure 2.9: Histograms of standard deviations of 10 minutes calibration sessions for CO_2 for each calibration tank

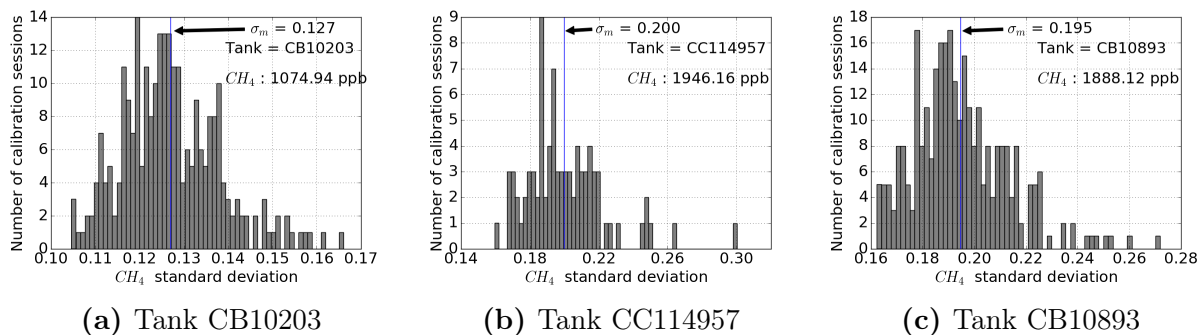


Figure 2.10: Histograms of standard deviations of 10 minutes calibration sessions for CH_4 for each calibration tank

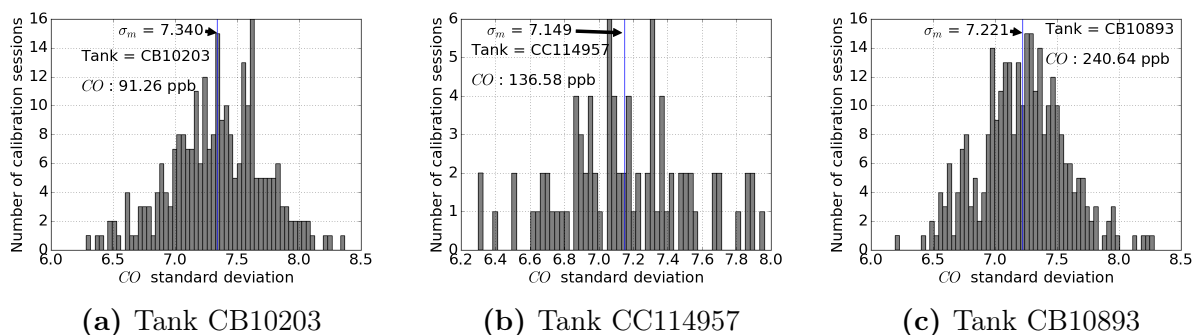
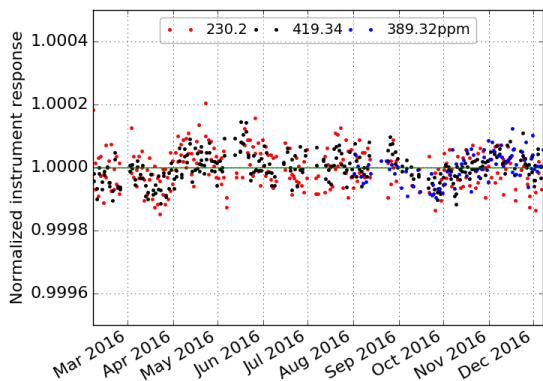


Figure 2.11: Histograms of standard deviations of 10 minutes calibration sessions for CO for each calibration tank

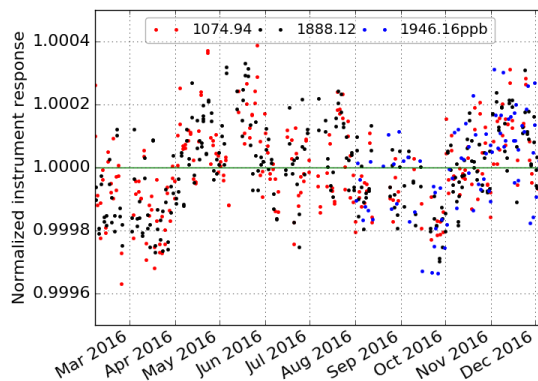
2.2.2.3 Instrument drift

The drift in measurements characterizes a slow and gradual change in the instrument response over time. This might be caused by a change in the precision of the lasers, mirrors reflectivity etc. The CRDS estimates the mixing ratios by comparing the ring-down time of the cavity containing the absorber gas to an empty cavity, which is achieved by tuning the lasers to frequencies at which the analyte does not absorb. By continuously taking the ratios of the ring-down times not their absolute values, the instrument becomes less sensitive to small change in the cavity parameters because both ring-down times are measured within the same hardware environment.

The time and pressure dependent drifts are minimized by actively and precisely controlling the cavity pressure and cavity temperature. Therefore, there is no significant drift expected from the Picarro CRDS instrument for the timeframe of this study. This expectation is confirmed by Figure 2.12 where instrument responses normalized by their mean values for CO_2 and CH_4 are plotted as a function of time for all calibrations tanks.



(a) carbon dioxide

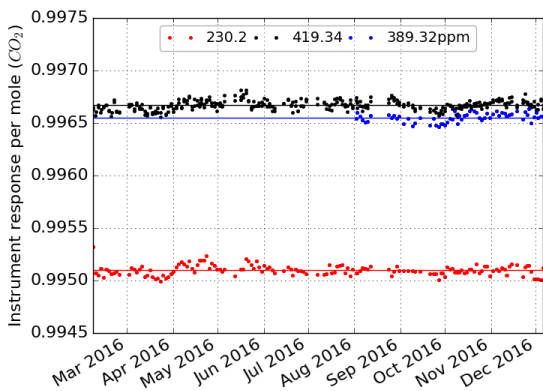


(b) methane

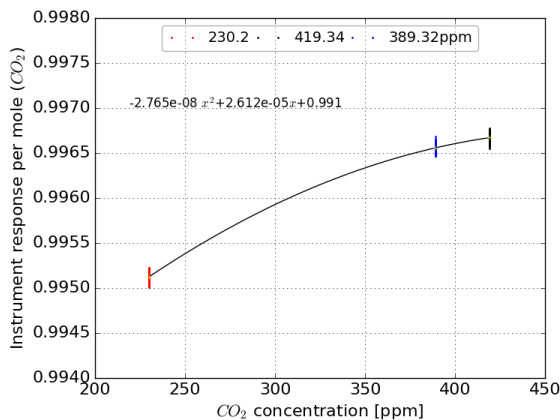
Figure 2.12: Instrument responses normalized by their mean for CO_2 and CH_4 for the three calibration tanks

2.2.2.4 Instrument linearity

Non-linearities arise when the sensitivity of the instrument depends on the concentration of the analyte. The sensitivities of our Picarro G2401 are shown as function of time and mole fractions for CO_2 (Figure 2.13), CH_4 (Figure 2.14) and CO (Figure 2.15). For a linear instrument the sensitivity which is the instrument response per mole would be the same across all concentration range, implying that data points would overlap in Figure 2.13a (and Figure 2.14a, Figure 2.15a) and make an horizontal line in Figure 2.13b (and Figure 2.14b, Figure 2.15b).



(a)



(b)

Figure 2.13: Instrument sensitivity as a function of time (a) and as a function of CO_2 mole fractions (b)

We have found a slope of 0.012% for CO_2 over the range of 389.32–419.34 ppm (black and blue dots in Figure 2.13) which is relevant for ambient CO_2 monitoring and a slope of 0.0016% for the near ambient range of 1888.12–1946.16 ppb for CH_4 . The slope for CO_2 and CH_4 are very small, corresponding to a correction of $0.012\% \times (419.34 - 389.32)$ or 0.004 ppm for CO_2 and similarly, 0.0009 ppb for methane, which does not justify the cost of purchasing another calibration tanks to correct for non-linearities. We have, therefore, considered our instrument linear for ambient CO_2 and CH_4 monitoring for the duration of this study. A slope of 6.9% exists for carbon monoxide in the range of 91.26–240.64 ppb, a nonlinear correction would be needed for CO data either by applying a slope or using the quadratic equation shown in Figure 2.15b.

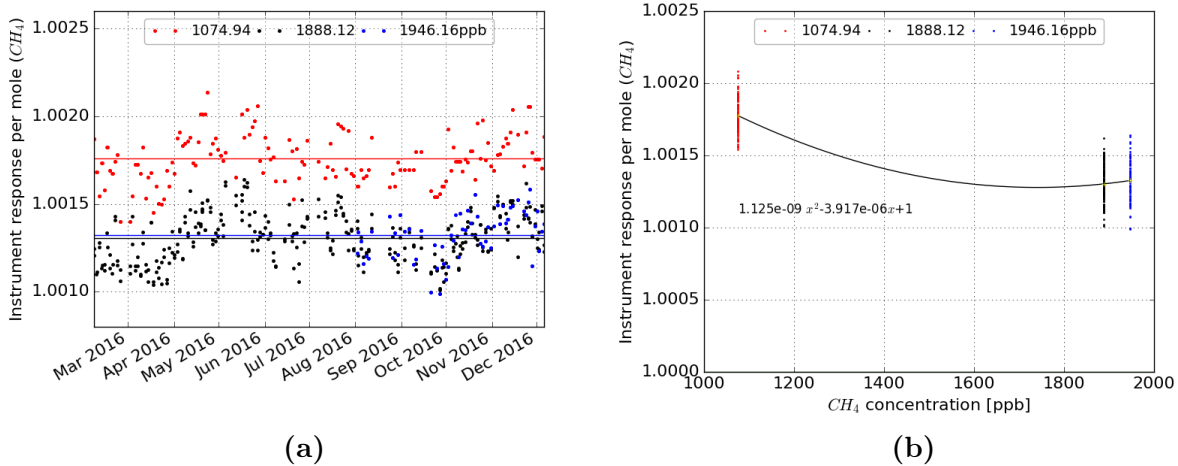


Figure 2.14: Instrument sensitivity as a function of time (a) and as a function of CH_4 mole fractions (b)

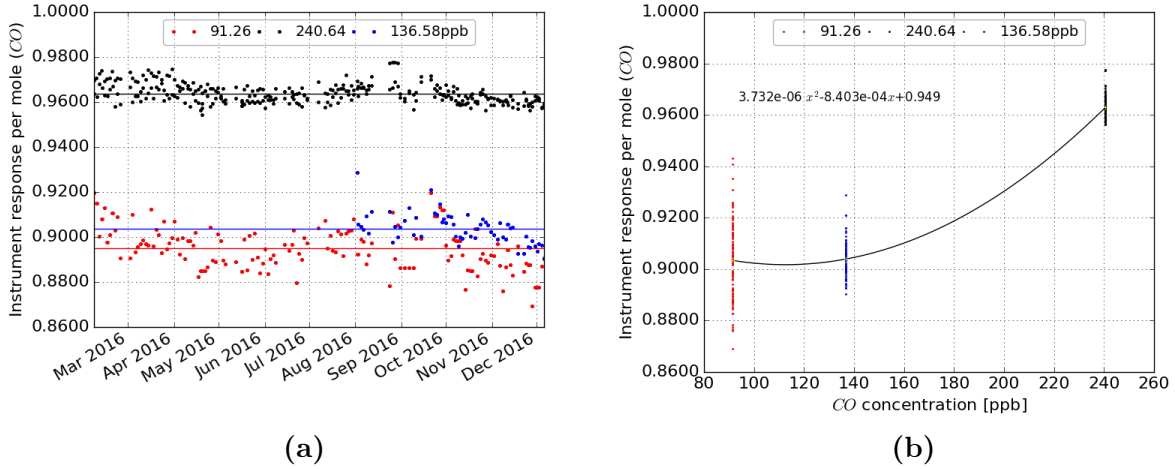


Figure 2.15: Instrument sensitivity as a function of time (a) and as a function of CO mole fractions (b)

2.2.2.5 Calibration

GCWERKS[®] software: GCWERKS [Peter Salameh 2016] is a software used across all AGAGE stations which controls individual parts of instruments including Gas Chromatography (GC), Gas Chromatography-Mass Spectrometry (GC/MS), CRDS and even UPS. GCWERKS[®] controls calibration sequences, drift and non-linearity corrections with remote access, remote backup and extensive plotting and reporting capabilities. The Picarro G2401 used for this project was also controlled by GCWERKS[®].

We have been running a calibration sequence for each calibration tank every other day. Due to logistic reason the second calibration tank for CO_2 and CH_4 was not available until August 1st, 2016. Before that we have been doing one point calibration expressed as follow,

$$\chi = \frac{\chi_{std}}{r_{std}} r_{air} \quad (2.1)$$

where χ are calibrated mole fractions and r_{air} are dry mole fractions reported by the instrument. χ_{std} and r_{std} are actual mole fractions and instrument response for the standard tanks, respectively.

After August 1, 2016 we have been using two points calibration with slope m expressed as Equation 2.2 and offset b expressed as in Equation 2.3.

$$m = \frac{\chi_{std2} - \chi_{std1}}{r_{std2} - r_{std1}} \quad (2.2)$$

$$b = \chi_{std1} - m \times r_{std1} \quad (2.3)$$

In order to understand the error margin caused by using one point calibration instead of two points calibration, we have made a comparison of both for the period where we had two calibration standards, as shown in Figure 2.16, we have found a mean underestimation of 0.020 ± 0.009 ppm for CO_2 and 0.02 ± 0.11 ppb for methane when using one point calibration only, these values are still well below the WMO goals of 0.05 ppm for CO_2 and 2.0 ppb for CH_4 . In addition, for the context of this project goal of inverse emissions estimation, the calibration error margins are very small compared to other potential source of uncertainties, including modeling and aggregation errors.

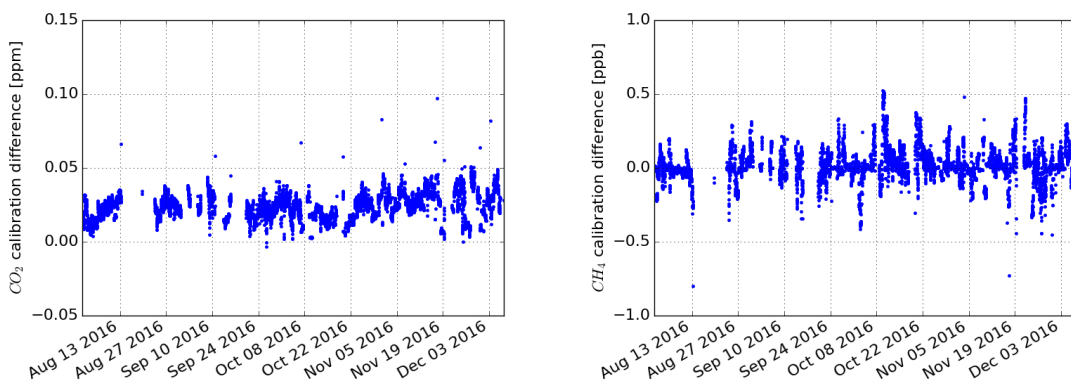


Figure 2.16: Two points calibration minus one point calibration for CO_2 and CH_4

2.3 Black carbon, weather and other measurements at Mt. Mugogo

Black carbon has been continuously monitored by a 7-wavelength Aethalometer[®] model AE33 supplied by MAGEE Scientific pictured in Figure 2.17a this instrument provides real time (one minute time average) concentrations of black carbon (BC) using the absorption over the 7 wavelengths (350–950 nm). The Aethalometer[®] also calculates the fraction of biomass burning which has higher absorption at lower wavelengths compared to fossil fuel BC which has equal absorption efficiency across all wavelengths [Sandradewi et al. 2008].

Weather parameters, are measured by two weather stations, one is a WXT520 Vaisala automatic weather station (Figure 2.17g) and, from February 2016, another weather station was provided with the Earth Networks sampling module (Figure 2.17f).

Other instruments include the Picarro G5105 (Figure 2.17b) and its Earth Networks module (Figure 2.17c) for nitrous oxide N_2O measurements, The Teledyne T400 (Figure 2.17e) ozone analyzer and a Licor L-200 pyranometer (Figure 2.17d) which measures solar radiation intensity.

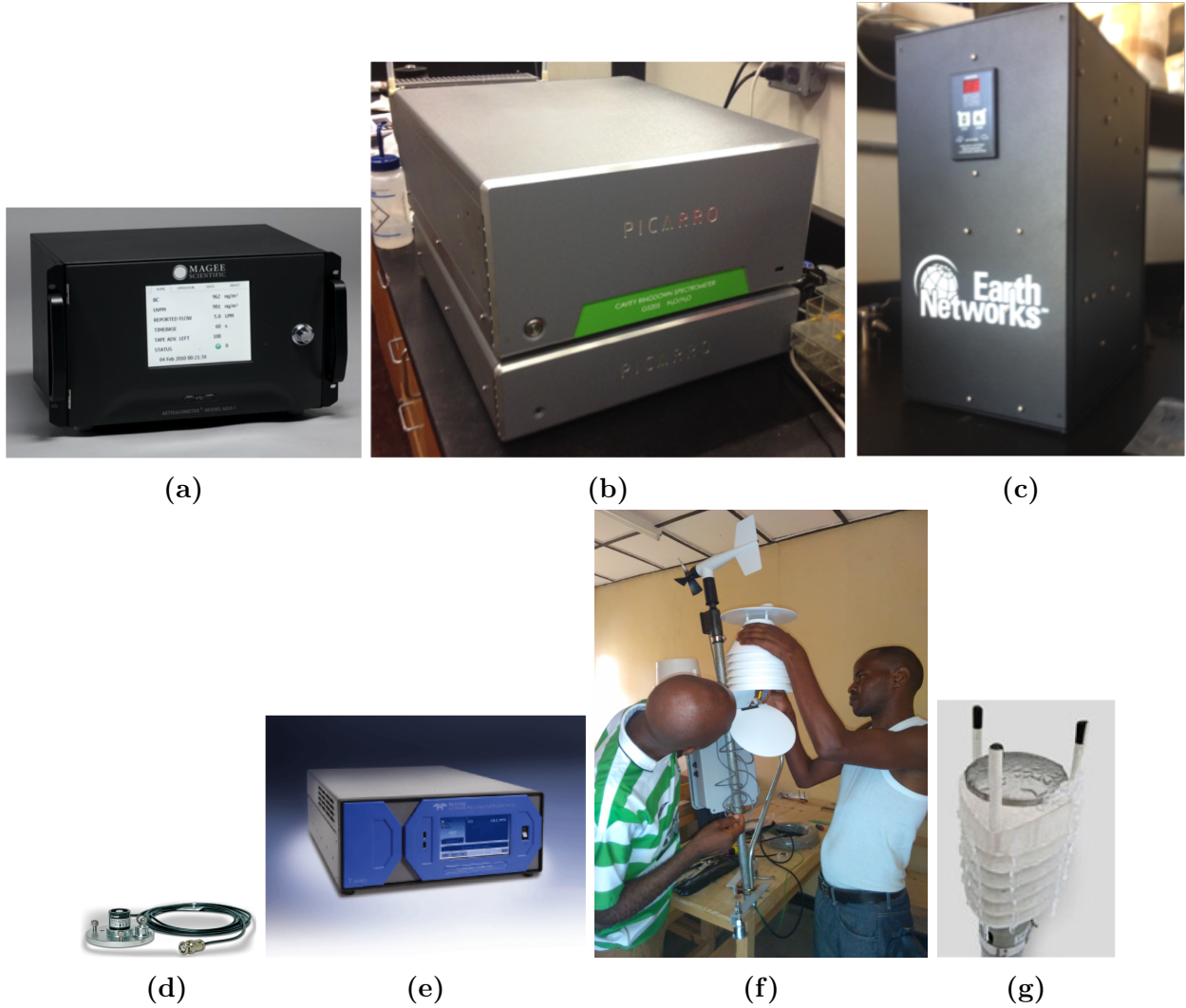


Figure 2.17: Other instruments present at the station include the Aethalomer (a), the Picarro G5105 (b) and its corresponding Earth Networks module (c), the Pyranometer (d), ozone analyzer(e), the Earth Networks weather station (f) and the Vaisala weather station (g)

Chapter 3

The Lagrangian Particle Dispersion Model: NAME

The particle dispersion modeling was used to quantify the sensitivity of mole fractions measured at Mount Mugogo station to various potential emission sources location. Here we present the Lagrangian particle dispersion model used in this study, the model parameterization of turbulence and specific parameters that were set for this work. We have also compared the wind speed and directions measured at the station to the reanalysis meteorology interpolated at the station location. We have found that the reanalysis meteorology was unable to accurately simulate the wind speed and directions measured at the station; a conclusion expected at this mountainous location. The footprints and winds streamlines shows that the model accurately reproduce the large scale circulation expected in the region.

3.1 Model formulation

In a Lagrangian Particle Dispersion Model (LPDM), transport and diffusion of air tracers is described by trajectories of a large number of ‘particles’, which are abstraction to infinitesimally small air parcels. In present work, we have use the UK Met Office’s Numerical Atmospheric dispersion Modeling Environment version 3 (NAME).

In the NAME model formulation, trajectories are calculated by following the movement of particles from release points forward in time, or from receptor points (measurement sites) backward in time, along a three dimensional grid. The particles carry the mass, physical and chemical properties of the tracers being simulated, and those properties evolve over time due to chemical transformation, dry and wet deposition and radioactive decay.

Particle dispersion within NAME largely follows the wind, which is provided by three-dimensional (3-D) wind fields and other meteorological parameters supplied by the numerical weather prediction (NWP) model. Atmospheric turbulence is simulated with a random walk technique. Particles are advected in each time step following the equation 3.1 [Morrison et al.

$$\mathbf{X}_{t+\Delta t} = \mathbf{X}_t + [\mathbf{u}(\mathbf{X}_t) + \mathbf{u}'(\mathbf{X}_t) + \mathbf{u}_l'(\mathbf{X}_t)]\Delta t \quad (3.1)$$

Here \mathbf{X} are particle position vectors, $\mathbf{u}(\mathbf{X})$ are the mean ambient winds interpolated to the particle position, $\mathbf{u}'(\mathbf{X})$ are the turbulent velocity components, $\mathbf{u}_l'(\mathbf{X})$ are the low frequency meander vectors and Δt is the time step. A random walk technique is used to simulate wind meander and dispersion due to atmospheric turbulence. Profile of turbulence are estimated by empirical fit to the observed data for stable and unstable (e.g. convective) conditions. For stable conditions, horizontal velocity variance σ_u^2 profile is expressed as equation 3.2 and the vertical velocity variance σ_w^2 is given in equation 3.3

$$\sigma_u^2 = \left[2.0u_* \left(1 - \frac{z}{z_i} \right)^{\frac{3}{4}} \right]^2, \quad (3.2)$$

$$\sigma_w^2 = \left[1.3u_* \left(1 - \frac{z}{z_i} \right)^{\frac{3}{4}} \right]^2, \quad (3.3)$$

where u_* is the friction velocity, z_i is the boundary layer depth and z is the height above ground. In unstable conditions, the turbulence parameters are expressed as

$$\begin{aligned} \sigma_u^2 &= 0.4w_*^2 + 4.0u_*^2 \left(1 - \frac{z}{z_i} \right)^{\frac{3}{2}}, \\ \sigma_w^2 &= 1.2w_*^2 \left(\frac{z}{z_i} \right)^{\frac{2}{3}} \left(1 - \frac{z}{z_i} \right) + 1.69u_*^2 \left(1 - \frac{z}{z_i} \right)^{\frac{3}{2}}. \end{aligned} \quad (3.4)$$

The convective velocity scale is given by,

$$w_* = u_* \left(\frac{z_i}{0.4|L|} \right)^{\frac{1}{3}}, \quad (3.5)$$

where L is the Obukhov length which is the height at which turbulence is generated more by buoyancy than by wind shear. For both stable and unstable conditions, turbulence profiles are set to converge to a small values in the free troposphere with a fixed standard deviation ($\sigma_u = 0.25 \text{ m s}^{-1}$ and $\sigma_w = 0.1 \text{ m s}^{-1}$).

Turbulence terms in the advection scheme of equation 3.1 are shown in equations 3.6 and 3.7, where τ_u and τ_w are horizontal and vertical lagrangian timescales respectively and r_t is

a random value of zero mean and unit variance [Ganesan 2013].

$$\mathbf{u}'_{t+\Delta T} = \mathbf{u}'_t \left(1 - \frac{\Delta t}{\tau_u}\right) + \left(\frac{2\sigma_u^2 \Delta t}{\tau_u}\right)^{1/2} r_t \quad (3.6)$$

$$\mathbf{w}_{t+\Delta t} = \mathbf{w}_t \left(1 - \frac{\Delta t}{\tau_w}\right) + \left(\frac{2\sigma_w^2 \Delta t}{\tau_w}\right)^{1/2} r_t + \frac{\Delta t}{\sigma_w} \frac{\partial \sigma_w}{\sigma_w \partial z} \quad (3.7)$$

The first terms of the right-hand side of equations 3.6 and 3.7 express ‘memory’ of the previous step, the second terms represent random perturbations and the third right-hand term of equation 3.7 is needed due to the fact that vertical velocity variance can vary rapidly with height compared to slow variation in the horizontal velocity variance which makes this term negligible for horizontal turbulence.

3.2 Model setup and Meteorology

The NAME model was driven by archived meteorological fields from the UK Met Office’s global unified model. The model has a resolution of 0.352° longitude and 0.234° latitude, 59 vertical levels and three-hourly temporal resolution.

The computational domain extends from -15° to 55° longitude and -40° to 18° latitude as show in Figure 3.1.

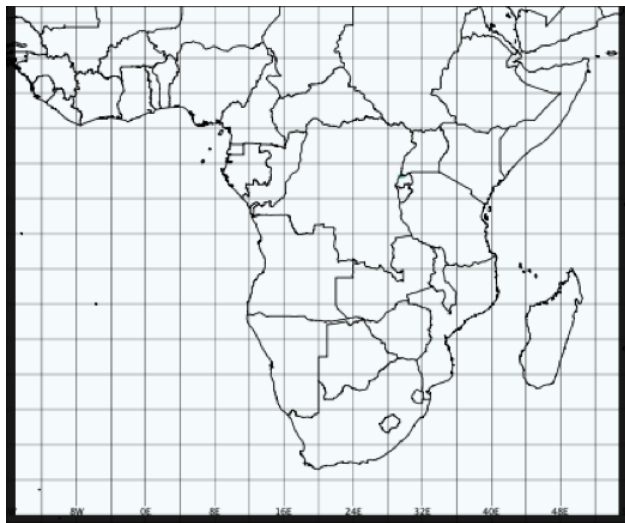


Figure 3.1: NAME model domain, a geographic region for which the footprints were calculated

Inert particles were continuously released from a 40 m column centered at 300 meters above ground level, at a rate of 20000 particles per hour and a mass of 1.0 g s^{-1} . We have chosen 300 m above ground because the altitude of the Mugogo location in NAME is 2117 m above sea level, while the actual altitude at Mugogo is 2507 m above sea level, the chosen release height allows the particles to be released at a height close to the realistic altitude. Particles were tracked back in time for 30 days, a period they are expected to have reached down to the boundary layer or exited the domain. The coordinates of locations where particles reach the boundary layer are recorded as potential sources of emissions and coordinates of points where particles exit the modeling domain are recorded for calculation of the influence of emissions coming from outside the domain.

By using inert particles we assume that the chemical loss is negligible for the long lived greenhouse gases we are modeling. Manning et al. [2011] have estimated that, at ambient OH levels, CH_4 chemical loss by OH oxidation is close to 0.7% for the 12 days period of their study. We expect higher chemical loss due to the tropical location of our domain where OH levels are higher and considering our longer modeling time, but still the CH_4 chemical loss should stay below a few percent, which is potentially smaller than other expected sources of uncertainty in a typical modeling system like ours, including model representation of topography, convection, boundary layer height etc.

We have compared the wind speed and directions from the UK Met Office's global unified model at the location of Mt. Mugogo with the wind speed and directions measured at the station, and the wind roses are plotted in Figure 3.2, Figure 3.3, Figure 3.4 and Figure 3.5 for the December-January-February, March-April-May, June-July-August and September-October-November seasons respectively. The wind directions from the global unified model do not agree with those measured at the stations. We would not expect a global model to capture the local circulation at Mount Mugogo especially because the local meteorology is likely driven by the unique hilly topography of the region and the nearby lake.

Figure 3.6, Figure 3.7, Figure 3.8 and Figure 3.9 present sample calculated air histories from the NAME model overlaid to the winds streamlines from the UK Met Office's global unified model. The footprints agree well with the expected synoptic circulation at the location of Mt. Mugogo. We notice that from the unified model perspective; a small anti-cyclonic circulation sets up around the station, where the wind seems to go around volcanic mountains. Still, we expect that the uncertainty due to the meteorology is the main source of uncertainty in our work, given the scarcity of ground meteorological data from Africa that feed into global numerical weather prediction models.

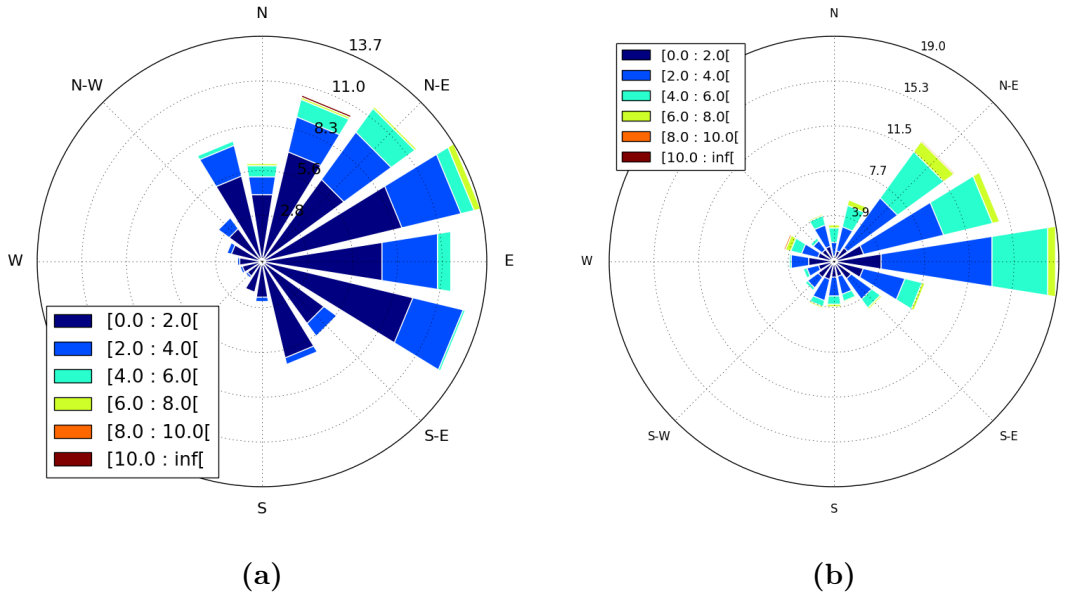


Figure 3.2: Wind roses comparing wind speed and direction for the meteorology used in the NAME model (a), and the wind speeds and directions measured at Mugogo (b), during the Dec-Jan-Feb season.

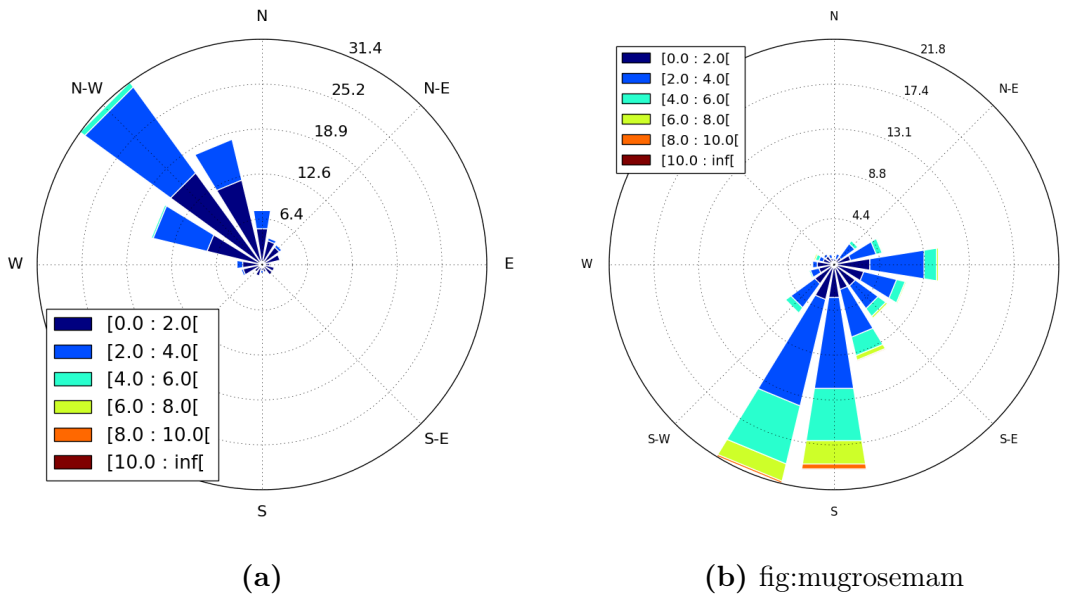


Figure 3.3: Wind roses comparing wind speed and direction for the meteorology used in the NAME model (a), and the wind speeds and directions measured at Mugogo (b), during the Mar-Apr-May season.

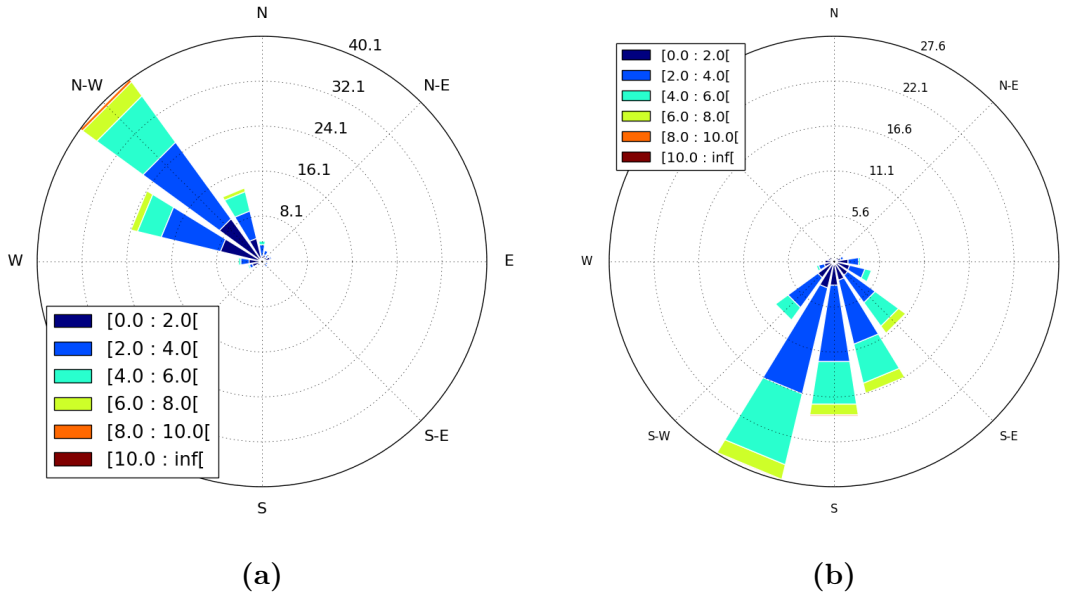


Figure 3.4: Wind roses comparing wind speed and direction for the meteorology used in the NAME model (a), and the wind speeds and directions measured at Mugogo (b), during the Jun-Jul-Aug season.

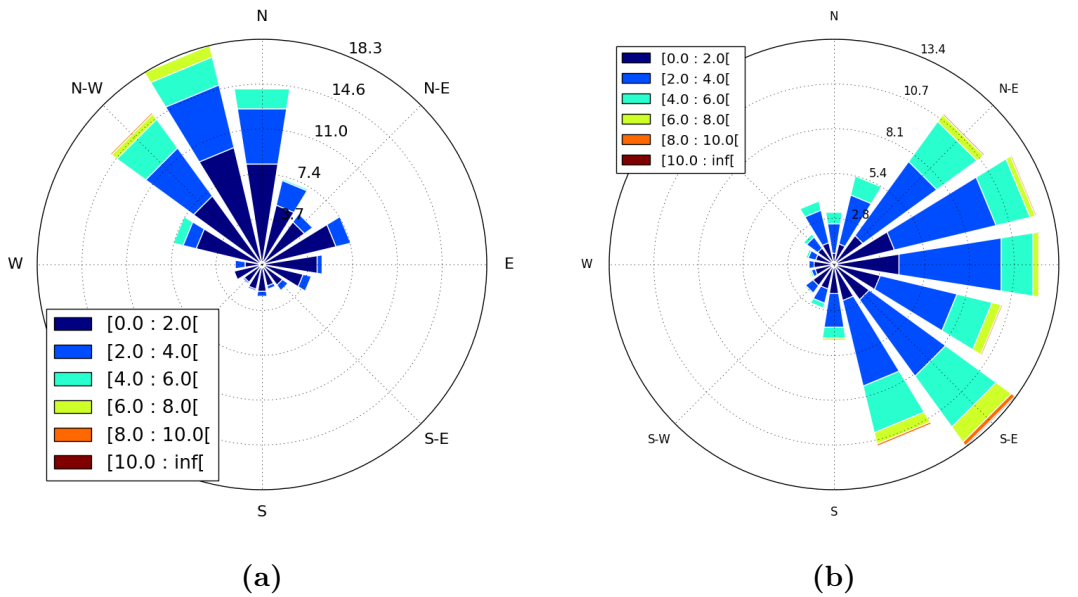


Figure 3.5: Wind roses comparing wind speed and direction for the meteorology used in the NAME model (a), and the wind speeds and directions measured at Mugogo (b), during the Sep-Oct-Nov season.

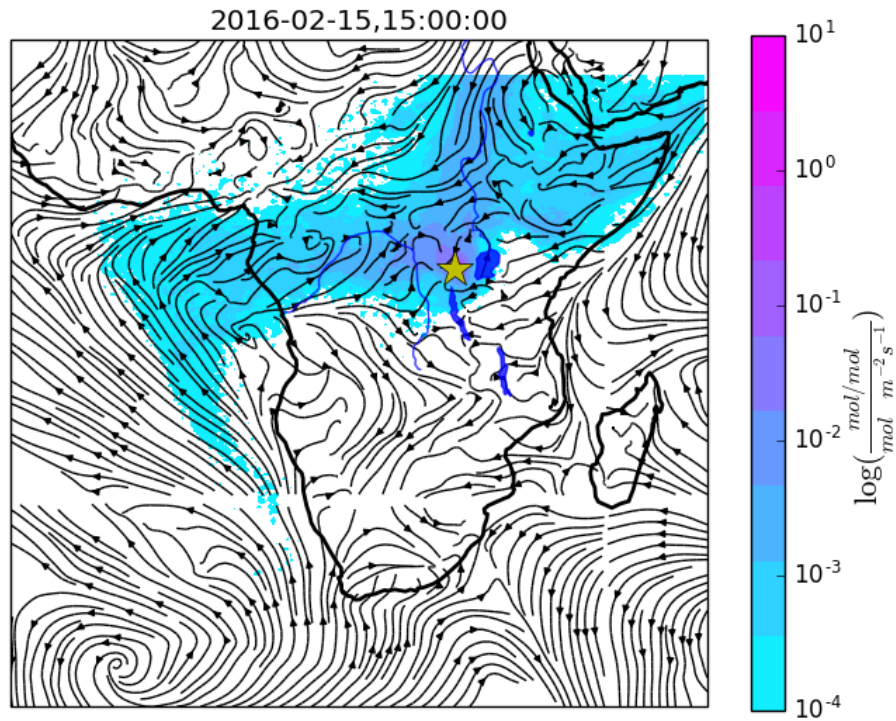


Figure 3.6: A NAME footprint overlaid with wind speed streamlines for February 15,2016 at 15:00:00. Footprints indicate the potential source of air masses arriving at the station for a specific time. Streamlines provide information on the general circulation, long lines indicate high wind speed, arrows indicate the direction of the flow. A yellow star marks the location of the station (The subtle horizontal and vertical discontinuities in the South and East are due to the merging of four separate blocks of the unified model (PT6, PT7, PT10, PT11) to make this image)

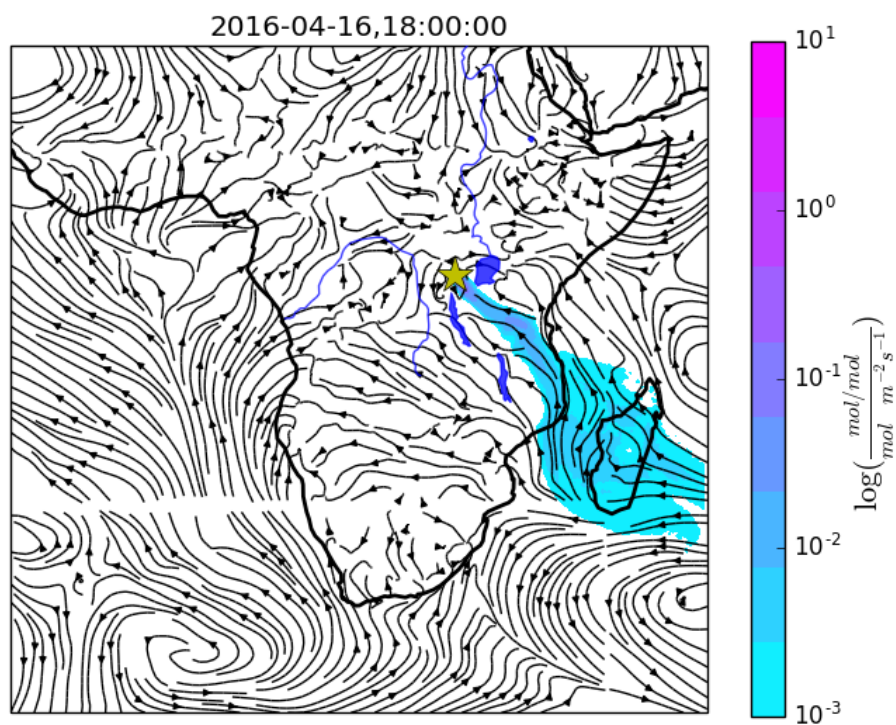


Figure 3.7: A NAME footprint overlaid with wind speed streamlines for April 16,2016 at 18:00:00. Footprints indicate the potential source of air masses arriving at the station for a specific time. Streamlines provide information on the general circulation, long lines indicate high wind speed, arrows indicate the direction of the flow. A yellow star marks the location of the station (The subtle horizontal and vertical discontinuities in the South and East are due to the merging of four separate blocks of the unified model (PT6, PT7, PT10, PT11) to make this image)

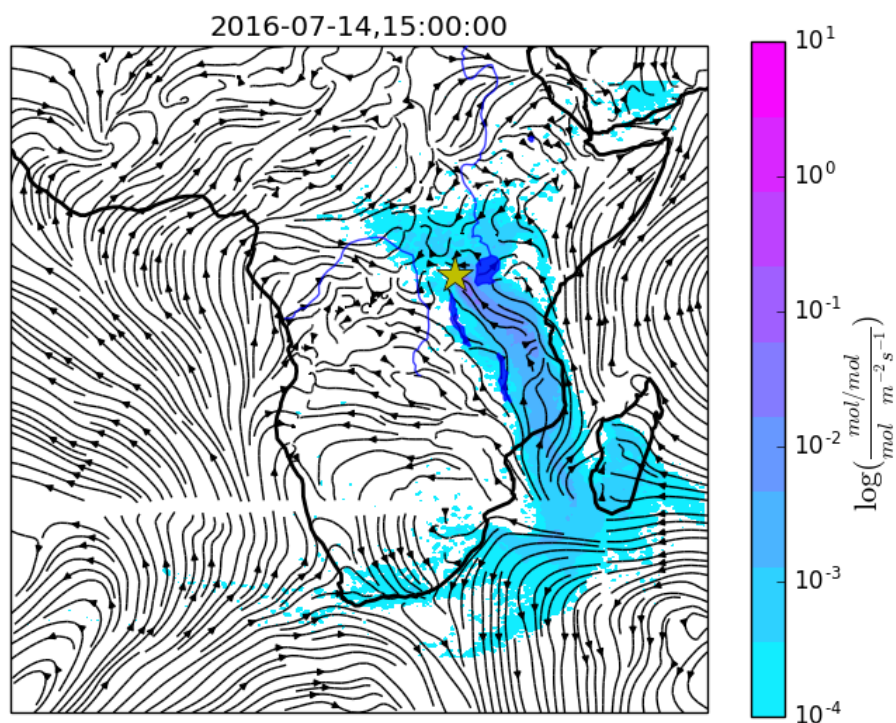


Figure 3.8: A NAME footprint overlaid with wind speed streamlines for July 14,2016 at 15:00:00. Footprints indicate the potential source of air masses arriving at the station for a specific time. Streamlines provide information on the general circulation, long lines indicate high wind speed, arrows indicate the direction of the flow. A yellow star marks the location of the station (The subtle horizontal and vertical discontinuities in the South and East are due to the merging of four separate blocks of the unified model (PT6, PT7, PT10, PT11) to make this image)

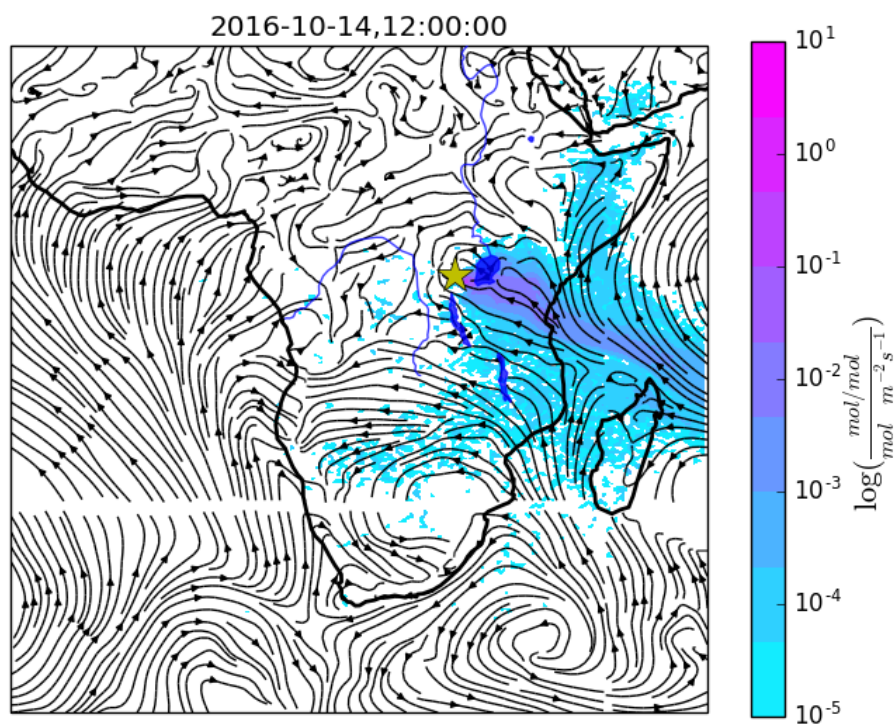


Figure 3.9: A NAME footprint overlaid with wind speed streamlines for October 14,2016 at 12:00:00. Footprints indicate the potential source of air masses arriving at the station for a specific time. Streamlines provide information on the general circulation, long lines indicate high wind speed, arrows indicate the direction of the flow. A yellow star marks the location of the station (The subtle horizontal and vertical discontinuities in the South and East are due to the merging of four separate blocks of the unified model (PT6, PT7, PT10, PT11) to make this image)

Chapter 4

Trans-dimensional Markov Chain Monte Carlo Inversion

Estimating surface fluxes of atmospheric trace constituents is a common problem in atmospheric sciences, which seeks to find the best way to combine the observed atmospheric mixing ratios, the known physical relationship between the sources and the observation usually expressed in form of chemical transport models and the already existing prior information about the emissions which generally comes from bottom up methods, process models or expert knowledge.

This chapter outlines the details of Monte Carlo and Markov Chain Monte Carlo solution to inverse problem and the problem of subjective versus objective determination of basis functions. The trans-dimensional reversible-jump Markov Chain Monte Carlo is introduced as an objective approach to determining basis functions, the mathematical representation of basis functions and various probability distributions for the prior, the likelihood proposal distribution and acceptance probability are presented.

4.1 Bayesian approach to inverse problem

Bayesian formalism provides a mechanism for learning from incomplete and noisy data, characterized by probability density functions, and heterogeneous sources of information typical to atmospheric sciences problems.

The prior information of emissions and other parameters which is represented by the probability density function $\rho(x)$ is updated by the observations $\rho(y/x)$ to the posterior probability of parameters given the observations $\rho(x|y)$ following the Bayes' rule expressed by,

$$posterior = \frac{likelihood \times prior}{evidence}$$

$$\rho(x|y) = \frac{\rho(y|x) \cdot \rho(x)}{\rho(y)} \quad (4.1)$$

the likelihood $\rho(y|x)$ gives the measure of how good the parameters x are explaining the data.

Multiple methods have been proposed to solve for the inverse problem in atmospheric sciences, some are briefly outlined in section 1.3.3.2 with a comprehensive review provided by Kasibhatla et al. [2000]. Most of those methods use Gaussian probability density functions and linear models which give rise to the cost function of Equation 4.2 representing the mismatch between measured mole fractions and modeled mole fractions and the mismatch between prior and posterior emissions,

$$J = (\mathbf{y} - \mathbf{H}\mathbf{x})^T \mathbf{R}^{-1}(\mathbf{y} - \mathbf{H}\mathbf{x}) + (\mathbf{x} - \mathbf{x}_{prior})^T \mathbf{P}^{-1}(\mathbf{x} - \mathbf{x}_{prior}) \quad (4.2)$$

where \mathbf{H} is a linear model characterizing a change in mole fractions due to a change in emissions, \mathbf{P} is the prior emissions uncertainty and \mathbf{R} is the model measurement uncertainty.

Assuming linear model constitutes a significant limitation especially for highly varying trace constituents, in addition there is no way to include more uncertainties and requires the covariance matrix \mathbf{P} and \mathbf{R} to be well known.

4.2 Markov Chain Monte Carlo Method

4.2.1 Monte Carlo Integration

The problem of extracting useful information, moments, quantiles, highest posterior density regions for instance, from the posterior distribution Equation 4.1 can be expressed as a posterior expectation of a function of x [Gilks et al. 1996],

$$E[f(x)|y] = \frac{\int f(x)\rho(x) \cdot \rho(y|x) dx}{\rho(y)} \quad (4.3)$$

Monte Carlo integration evaluate the expectation of Equation 4.3 by drawing a set of random samples X_t , $t = 1, \dots, n$ from $\pi(x) = \rho(x)\rho(y|x)$ and then calculating,

$$E[f(X)] \approx \frac{1}{n} \sum_{t=1}^n f(X_t) \quad (4.4)$$

For independent sample points X_t the law of large numbers guarantees that the approximation can be made as accurate as needed by increasing the sample size n . It is not possible, however, to draw independent samples from typical posterior probability density functions encountered in atmospheric sciences due to the high dimension and often non-standard form.

The samples X_t are not required to be independent, however, [Gilks et al. 1996] as long as they are generated by a process drawing samples from $\pi(x)$ in correct proportion, this is usually achieved by drawing samples from a Markov Chain having $\pi(x)$ as its stationary distribution. A Markov Chain Monte Carlo integration is therefore a Monte Carlo integration drawing samples from a Markov Chain.

4.2.2 Markov Chains

A sequence of random numbers $X_0, X_1, \dots, X_{n-1}, X_n$ is a Markov Chain if the next state X_{n+1} is sampled from a distribution $P(X_{n+1}|X_n)$ which depends only on the current state of the sequence. The distribution $P(X_{n+1}|X_n)$ is called the *transition kernel*.

After sufficient number of iterations (*burn-in*), the chain will ‘forget’ its starting points X_0 and converge to a unique *stationary* distribution $\pi(\cdot)$ which does not depend on X_0 and n . Markov Chain Monte Carlo integration is, therefore, a Monte Carlo integration with samples taken from a Markov Chain whose stationary distribution is the target posterior distribution.

A Markov Chain is called a random walk if it satisfies,

$$X_{n+1} = X_n + \epsilon_n \tag{4.5}$$

Where ϵ_n is generated independently of X_0, X_1, \dots, X_n . The random walk is called *symmetric random walk* if the distribution of the ϵ_n is symmetric about zero.

4.2.3 The Metropolis-Hastings Algorithm

The Metropolis-Hastings (M-H) algorithm together with the Gibbs sampling are the most commonly used sampling techniques to construct markov chains whose stationary distributions are the posterior distribution. Here we focus on the M-H algorithm because the Gibbs sampler is a special case of M-H where proposal distributions are the posterior conditionals [Gilks et al. 1996]. The algorithm of M-H is presented in Algorithm 1.

The M-H algorithm starts by initializing the sample value for the random variable x , usually taken from the prior distribution of x , then for each iteration, a proposal sample x' is generated from the proposal distribution. The proposed sample is accepted with a probability α based upon how well the proposed sample is located within the joint posterior density.

Algorithm 1 Metropolis-Hastings algorithm

```
1: initialize  $x^{(0)} \sim q(x)$ 
2: for iteration  $i = 1, 2, \dots$  do
3:   Propose:  $x' \sim q(x^{(i)}|x^{(i-1)})$ 
4:   acceptance probability:
5:      $\alpha(x'|x^{(i-1)}) = \min \left\{ 1, \frac{q(x^{(i-1)}|x')\pi(x')}{q(x'|x^{(i-1)})\pi(x^{(i-1)})} \right\}$ 
6:    $u \sim U(0, 1)$ 
7:   if  $u < \alpha$  then
8:     Accept the proposal:  $x^{(i)} \leftarrow x'$ 
9:   else
10:    Reject the proposal:  $x^{(i)} \leftarrow x'$ 
11:   end if
12: end for
```

The random-walk M-H algorithm, which is the most common, adds a small perturbation to the current state of the chain $x' = x + Normal(0, \sigma)$ and then accepts or rejects the perturbed value. The acceptance ratio of this symmetric proposal distribution depends only on the joint posterior distribution because the terms $q(x'|x^{(i-1)})$ and $q(x^{(i-1)}|x')$ cancel each other in the acceptance probability.

The random-walk M-H algorithm approximates the stationary distribution $\pi(\cdot)$ by exploring the state-space in small steps, each corresponding to a sample in the Markov Chain. The form of the acceptance probability α ensures that high probability region of π are explored more often than the tail of the distribution.

4.3 Trans-Dimensional Markov Chain Monte Carlo Methods

During inverse estimation of surface fluxes of atmospheric trace constituents from observations, the spatial domain is represented as the spatial grids of the underlying chemical transport model. In practice, however, these grids need to be aggregated into fewer regions or basis functions that can reasonably be constrained by the number of available measurement sites.

The Metropolis-Hastings algorithm requires that the number of basis function, i.e. the dimension of the vector \mathbf{x} , be determined a priori. Subjective determination of the number of basis functions as well as their spatial delimitation leads to forced correlation of emissions within one region which may not exist in the true data and the assumption that the emissions in adjacent regions are uncorrelated. Fixing the number of basis functions results in aggregation errors when too few degrees of freedom are allowed to the model [Lunt et al.

2016] or spatial structure in the posterior fluxes estimate which does not exist in the true field when the number of basis function is too high.

Green [1995] has proposed the reversible-jump Markov Chain Monte Carlo (rJMCMC) which extends the Markov Chain Monte Carlo (MCMC) for a variable dimension state vector. This is achieved by including the basis functions representation in the state vector as outlined in section 4.3.1 and adjusting the proposal distribution to consider the change in dimension and adding the corresponding term in the acceptance ratio. The rJMCMC applies to all problems where the size of the state vector is unknown, the term TDMCMC is interchangeably used in geophysical science problems where the vector \mathbf{x} represents spatial (and temporal) dimensions.

Bodin et al. [2009] have applied the TDMCMC for the problem of seismic tomography. More recently Lunt et al. [2016] have demonstrated the use of TDMCMC in atmospheric inversion of long lived greenhouse gases. In this work we have used the method of Lunt et al. [2016].

For the trans-dimensional inversion, we need to include the number of unknown parameters k in the Bayes theorem Equation 4.1 and replace the state vector \mathbf{x} by \mathbf{m} which represents the emissions and their corresponding partitioning into basis functions, the exact form of \mathbf{m} is presented in the section 4.3.1,

$$\rho(\mathbf{m}|y, k) \propto \rho(y|\mathbf{m}, k) \cdot \rho(\mathbf{m}|k) \tag{4.6}$$

The general nature of MCMC methods allows us to introduce additional unknowns in the inversion, Ganesan et al. [2014] have shown that hierarchical Bayesian approaches that incorporates hyperparameters θ describing the uncertainties in the parameters of the prior distribution, model measurements uncertainties as well as correlations timescales lead to realistic emissions and associated uncertainties. The general form of the transdimensional, hierarchical Bayesian equation becomes [Lunt et al. 2016],

$$\rho(\mathbf{m}, \theta, k|y) \propto \rho(y|\mathbf{m}, \theta, k) \cdot \rho(\mathbf{m}|\theta, k) \cdot \rho(\mathbf{m}|k) \cdot \rho(k) \cdot \rho(\theta) \tag{4.7}$$

4.3.1 Basis functions

Similar to Bodin et al. [2009] and Lunt et al. [2016], we have used so-called voronoi tessellations to reduce the dimension of the emissions vector \mathbf{x} , but still allowing the flexibility to incorporate variable number of basis function in the inverse problem. Voronoi cells are constructed by assigning a number of points called nuclei (seeds, or generators) to the domain, each nuclei defines a region where any point within the region is closer to the region's nuclei than any other nuclei, the edge of each region is equidistant between the closest two nuclei

and perpendicular to the line connecting them. With voronoi tessellation, the size and shape of each basis function is conveniently presented by two values; the latitude and longitude of the region's nucleus.

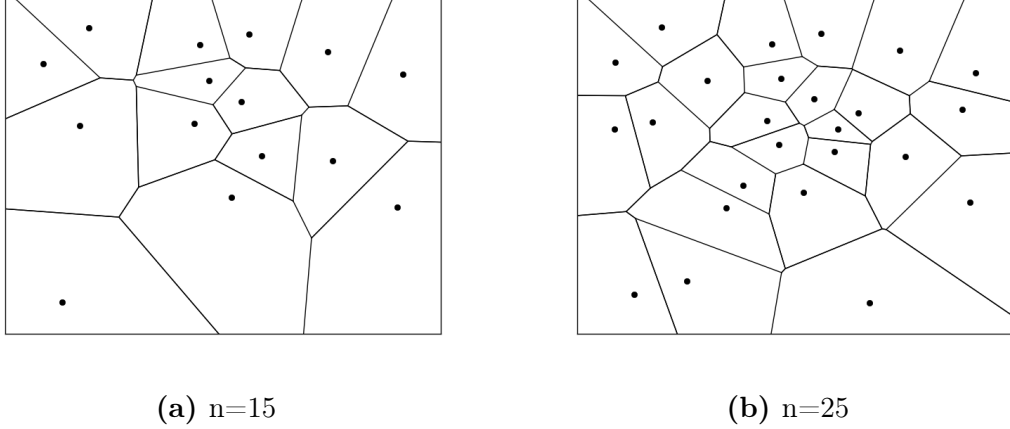


Figure 4.1: Examples of voronoi diagram for 15 nuclei (a) and 25 nuclei(b). Each nuclei (dots) defines a regions where each points within the region is closer to the region's nuclei than any other nuclei

In case of voronoi tessellation, the basis functions for the transdimensional inversion are represented by the configuration of the voronoi diagram c which represent the latitude and longitude of the voronoi nuclei and the corresponding value of emissions flux x :

$$m = (c, x) \tag{4.8}$$

For practical purpose, voronoi cells are restricted to the points of underlying grid cells which are closest to the cells nuclei in such a way that each grid cell can only belong to one voronoi cell.

4.3.2 Acceptance probability for the TDMCMC

The main difference between M-H algorithm and TDMCMC is the form of the acceptance probability, where the acceptance ratio of M-H methods becomes a special case for the most general form of TDMCMC presented in Equation 4.9,

$$U \leq (\text{prior ratio} \times \text{likelihood ratio} \times \text{proposal ratio} \times |\mathbf{J}|) \tag{4.9}$$

$$U \leq \left(\frac{\rho(m')}{\rho(m)} \times \frac{\rho(y'|m')}{\rho(y|m)} \times \frac{q(m|m')}{q(m'|m)} \times |\mathbf{J}| \right) \tag{4.10}$$

in the Equation 4.10, m' is a proposed update in the basis functions which can be a perturbation added to the value of the flux, or a change in dimension. The term $|\mathbf{J}|$ is the determinant of the Jacobian matrix of the transformation $m \rightarrow m'$, the Jacobian normalizes the difference in ‘volume’ between two spaces of different dimensions. For the transformations that do not change the dimension of m , the transformation matrix for the space component is the identity matrix and the corresponding determinant of the Jacobian matrix is $|\mathbf{J}| = 1$, this is the case for a fixed-dimension metropolis-hastings algorithm.

Bodin et al. [2009] have shown that for birth-death MCMC, which is the case for this work, when dimensional changes that allow only one more(less) increase (decrease) in the dimension size are considered, the determinant of the Jacobian matrix $|\mathbf{J}| = 1$ as well.

In following sections, we determine the form of the prior distribution, the likelihood function and the proposal distribution.

4.3.3 Prior distribution

The prior distribution for a variable number of unknowns parameters, k depends on both the basis functions m and k :

$$\rho(m) = \rho(m|k) \cdot \rho(k) \quad (4.11)$$

Where the basis functions m are expressed by Equation 4.8. Owing to the independence between the location of a voronoi cell c and the value of emission flux x , the term $\rho(m|k)$ can be separated into two terms,

$$\rho(m|k) = \rho(c|k) \cdot \rho(x|k) \quad (4.12)$$

the full prior distribution for the basis functions becomes,

$$\rho(m) = \rho(c|k) \cdot \rho(x|k) \cdot \rho(k) \quad (4.13)$$

We have assumed that the number of basis functions k , can take any integer value between a specified range k_{min} and k_{max} all numbers having equal probability (uniform distribution) between the range. The prior on the number of basis functions $\rho(k)$ is given by,

$$\rho(k) = \frac{1}{(k_{max} - k_{min})} \text{ if } k_{min} < k \leq k_{max}, 0 \text{ otherwise} \quad (4.14)$$

Similarly, assuming that voronoi nuclei can be position at any grid on the underlying grid cells, with equal probability. For $K = k_{latitude} \times k_{longitude}$ grid cells and k voronoi nuclei

there are $\frac{K!}{k!(K-k)!}$ possible configurations. Assuming equal probability for all grids cells, the prior for nuclei location is expressed by:

$$\rho(c|k) = \left[\frac{K!}{k!(K-k)!} \right]^{-1} \quad (4.15)$$

For any given basis function, a lognormal probability density function (PDF) for the prior emissions fluxes is assumed. The parameters of the lognormal PDF are themselves unknown parameters to solve for, following the hierarchical bayesian approach proposed by Ganesan et al. [2014], which is nicely incorporated in the TDMCMC. The lognormal PDF for prior emissions is given by:

$$\rho(x|k) = \frac{1}{x\sigma_x\sqrt{2\pi}} \cdot \exp\left(\frac{-(\ln x - \mu_x)^2}{2\sigma_x^2}\right) \quad (4.16)$$

The final form of the basis functions prior PDF (Equation 4.13) for the TDMCMC is:

$$\rho(m) = \left[\frac{K!}{k!(K-k)!} \right]^{-1} \cdot \frac{1}{(k_{max} - k_{min})} \cdot \frac{1}{x\sigma_x\sqrt{2\pi}} \cdot \exp\left(\frac{-(\ln x - \mu_x)^2}{2\sigma_x^2}\right) \quad (4.17)$$

if $k_{min} < k \leq k_{max}$, 0 otherwise

4.3.4 Likelihood function

The likelihood function gives a quantitative measures of how well the model m matches observed data. We have adopted the least-square misfit which quantifies how the simulated data Hx matches the observed data y ,

$$\rho(y|m, k) = \frac{1}{\sqrt{|\mathbf{R}|}2\pi} \cdot \exp\left(\frac{-\Phi(m)}{2}\right) \quad (4.18)$$

Where \mathbf{R} is the model-measurement covariance matrix and $\Phi(m)$ is the model data mismatch:

$$\phi(m) = (\mathbf{y} - \mathbf{H}\mathbf{m})^t \mathbf{R}^{-1} (\mathbf{y} - \mathbf{H}\mathbf{m}) \quad (4.19)$$

The model-measurement covariance matrix has further been decomposed in two hyper-parameters, one describing the model measurement uncertainty σ_y and the other being the correlation length between measurements τ . Specifically, the diagonal elements of \mathbf{R} are squares of σ_y , and the off-diagonal terms are given by Equation 4.20 [Ganesan et al. 2014], where r_{ij} is the covariance between measurements i and j , and $\Delta t_{i,j}$ is the time between measurements,

$$r_{ij} = \sqrt{r_{ii}} \cdot \sqrt{r_{jj}} \cdot \exp\left(\frac{-\Delta t_{i,j}}{\tau}\right) \quad (4.20)$$

4.3.5 Proposal distributions and acceptance probabilities

The proposal distribution is the only remaining term in the Equation 4.10 to derive the full mathematical expression of the acceptance probability for the transdimensional Markov Chain Monte Carlo. Unlike the Metropolis-Hastings algorithm (Algorithm 1), where the next iteration corresponds to the update in emission fluxes, there are six possible updates to move from the current state to the next in the hierarchical transdimensional MCMC, as listed below,

1. x update: randomly select and perturb one value of emissions flux like in M-H
2. θ_x update: randomly select and perturb one hyperparameter value related to emissions
3. θ_y update: randomly select and perturb one hyperparameter value related to observations
4. move: randomly select and move one voronoi nucleus location
5. birth: add one new voronoi nucleus at a random location
6. death: randomly select and remove one voronoi nucleus

and each of these six possible perturbations has its own form of acceptance probability which is a special case of Equation 4.10.

4.3.5.1 Emission update

Updating a value of emissions flux x for a basis function c takes the form of a Gaussian perturbation to the current value. The Gaussian perturbation being symmetric, the proposal ratio of Equation 4.10, $\frac{q(m|m')}{q(m'|m)} = 1$. The acceptance probability for emission flux update is the product of the prior ratio and likelihood ratio, considering the form of the prior given by Equation 4.17 and the likelihood function of Equation 4.18. The acceptance probability for the emission flux update is given by:

$$\alpha_{xupdate} = \min \left[1, \exp \left(\frac{-(\ln x'_i - \mu)^2}{2\sigma_x^2} + \frac{(\ln x_i - \mu)^2}{2\sigma_x^2} \right) \cdot \exp - \left(\frac{\Phi(m') - \Phi(m)}{2} \right) \right] \quad (4.21)$$

4.3.5.2 Emission hyperparameter update

A perturbation on hyperparameters acting on \mathbf{x} will only change the parameters of the lognormal distribution μ, σ and has no effect on the likelihood function. The acceptance probability simply becomes the prior ratio accounting for the change in the parameters of the lognormal distribution, so from Equation 4.17 we get,

$$\alpha_{x-hyper} = \min \left[1, \frac{\sigma_x}{\sigma'_x} \exp \left(\frac{-(\ln x - \mu')^2}{2\sigma_x'^2} + \frac{(\ln x_i - \mu)^2}{2\sigma_x^2} \right) \right] \quad (4.22)$$

It is important to point out that the hyperparameters of the emission PDF are not informed by the data, which guarantees the independence between of the form of prior from the data.

4.3.5.3 Observation hyperparameter update

A change in the hyperparameters acting on data θ_y will results in a change in the covariance matrix \mathbf{R} and, therefore, the likelihood function. The acceptance probability in this case is the likelihood ratio, from Equation 4.18 we obtain,

$$\alpha_{y-hyper} = \min \left[1, \exp \left(\frac{-(\Phi'(m) - \Phi(m))}{2} \right) \cdot \frac{|\mathbf{R}|}{|\mathbf{R}'|} \right] \quad (4.23)$$

4.3.5.4 Move step

A move update consists of selecting a random nucleus of the basis functions, perturbing its position with a Gaussian PDF centered at its current location but with the emission flux associated to the nucleus remaining unchanged. In this case, the proposal ratio can be written as,

$$\frac{q(m|m')}{q(m'|m)} = \frac{q(c|m')}{q(c'|m)} \cdot \frac{q(x|m')}{q(x'|m)} \quad (4.24)$$

The second term of the right hand side is unity because the flux value did not change, and in addition the first term is also unity because the position $c = c(x, y)$ has been perturbed by a symmetric distribution. The proposal ratio for a move update is, therefore, $\frac{q(m|m')}{q(m'|m)} = 1$. Similarly, the prior distribution does not change since the emission flux value does not change; The acceptance probability for the move update is the likelihood ratio:

$$\alpha_{move} = \min \left[1, \exp \left(\frac{-(\Phi(m') - \Phi(m))}{2} \right) \right] \quad (4.25)$$

4.3.5.5 Birth step

During a birth move, a vacant grid cell is selected randomly and assigned a new voronoi nucleus, subsequently, an emission value is assigned to the newly created voronoi cell by adding a Gaussian perturbation to the current emission flux value at the position of the new nucleus. Since the nucleus is placed independently from the new emission value, we can write

$$\frac{q(m|m')}{q(m'|m)} = \frac{q(c|m')}{q(c'|m)} \cdot \frac{q(x|m')}{q(x'|m)} \quad (4.26)$$

If the current state m has k number of voronoi cells, and K is the total number of model grids; there are $K - k$ possible locations of the new nucleus. The probability of birth at position c'_{k+1} is given by:

$$q(c'|m) = 1/(K - k) \quad (4.27)$$

If x_i is the emission at position c'_{k+1} , the probability of generating a new emission flux x'_{k+1} is given by,

$$q(x'|m) = \frac{1}{\sigma_b \sqrt{2\pi}} \exp\left(-\frac{(x'_{k+1} - x_k)^2}{2\sigma_b^2}\right) \quad (4.28)$$

where σ_b is the size of Gaussian perturbation from x_k . The proposal PDF for a birth process is therefore,

$$q(m'|m) = \frac{1}{(K - k)\sigma_b \sqrt{2\pi}} \exp\left(-\frac{(x'_{k+1} - x_k)^2}{2\sigma_b^2}\right) \quad (4.29)$$

For the reverse step of the birth, the probability of deleting a cell at position c'_{k+1} is

$$q(c|m') = 1/(k + 1) \quad (4.30)$$

and the probability of removing an emission flux when a cell is deleted is

$$q(x|m') = 1 \quad (4.31)$$

We finally get the proposal ratio for the birth step expressed as

$$\left[\frac{q(m|m')}{q(m'|m)}\right]_{birth} = \frac{\sqrt{2\pi}(K - k)}{k + 1} \cdot \sigma_b \cdot \exp\left(\frac{(x'_{k+1} - x_i)^2}{2\sigma_b^2}\right) \quad (4.32)$$

The acceptance probability for a birth process is computed by taking Equation 4.32, Equation 4.17 and Equation 4.18 into Equation 4.10,

$$\alpha_{birth} = \min \left[1, \frac{\sigma_b}{\sigma_x x'_{k+1}} \cdot \exp\left(\frac{(x'_{k+1} - x_i)^2}{2\sigma_b^2}\right) \cdot \exp\left(\frac{-(\ln(x'_{k+1}) - \mu)^2}{2\sigma_x^2}\right) \cdot \exp\left(-\frac{\Phi(m') - \Phi(m)}{2}\right) \right] \quad (4.33)$$

The terms corresponding to the underlying resolution grid K cancel each other in Equation 4.33. Which imply that one does not have to force the voronoi nuclei to the positions of underlying grid cells [Lunt et al. 2016] and can take any position in the domain.

4.3.5.6 Death step

The death process randomly selects a voronoi nucleus c_k and removes it along with the associated emission x_k . The remove point becomes part of another voronoi cell c_j with emission x_j . With similar reasoning to the birth step, the proposal ratio of the death step is given by,

$$\left[\frac{q(m|m')}{q(m'|m)} \right]_{death} = \frac{k}{\sigma_d \sqrt{2\pi} (K - k + 1)} \cdot \exp\left(-\frac{(x'_j - x_k)^2}{2\sigma_d^2} \right) \quad (4.34)$$

where σ_d is the size of the Gaussian perturbation of the reverse step(birth step). The acceptance probability for the death step is given by:

$$\alpha_{death} = \min \left[1, \frac{x'_k \sigma_x}{\sigma_{bd}} \cdot \exp\left(-\frac{(x'_j - x_k)^2}{2\sigma_{bd}^2} \right) \cdot \exp\left(-\frac{(\ln(x_k) - \mu)^2}{2\sigma_x^2} \right) \cdot \exp\left(-\frac{\Phi(m') - \Phi(m)}{2} \right) \right] \quad (4.35)$$

Algorithm 2 Reversible jump MCMC algorithm [Lunt et al. 2016]

```

1: initialize parameters  $x, c, \theta_x, \theta_y$ ,
2: for iteration  $i = 1, 2, \dots n$  do
3:    $r \leftarrow i \bmod 5$ 
4:   if  $r=0$  then
5:      $x'_i = x_i + N(0, \sigma_x)$  ▷ Emission update
6:   else if  $r=1$  then
7:      $\Theta'_i = \theta_i + N(0, \sigma_{theta})$  ▷ hyperparameter update
8:   else if  $r=2$  then
9:      $k' = k + 1$  ▷ form a new voronoi cell: birth
10:  else if  $r=3$  then
11:     $k' = k - 1$  ▷ Delete one voronoi cell: death
12:  else if  $r=4$  then
13:     $c'_i = c_i + N(0, \sigma_{move})$  ▷ move one voronoi cell: move step
14:  end if
15:   $\alpha \leftarrow (x', c', \theta', k')$  ▷ calculate acceptance ratio
16:   $u \leftarrow U(0, 1)$  ▷ calculate a random vale  $u \sim U(0, 1)$ 
17:  if  $\ln(\alpha) \geq \ln(U(0, 1))$  then
18:     $(x, c, \theta, k) = (x', c', \theta', k')$  ▷ accept
19:  end if
20:   $q \leftarrow i \bmod 100$ 
21:  if  $q = 0$  then Store  $(x, c, \theta, k)$  ▷ store every 100th iteration
22:  end if
23: end for

```

4.4 Implementation of the RJMCMC

4.4.1 List of parameters used in the inversion

We have applied the RJMCMC methodology outlined in the algorithm 2 to estimate methane and carbon dioxide emissions in Central and Eastern Africa. Values and range of parameters and hyper-parameters used for the inversion are listed in Table 4.1. We have stored every 100th iteration, the reported values are the median of the posterior distribution and the error bars are the 16th and 84th percentiles.

Table 4.1: List and values of parameters used in the inversion

parameter	Distr. type	starting value	range	stepsize
Emission scaling factors	Lognormal	$\mu = 1, \sigma = 2$	-	0.3
Hyper parameter of Lognormal mean	uniform	1	[0.8,1.6]	0.4
Hyper parameter of Lognormal standard deviation	uniform	2	[1,3]	0.4
Model-measurement mismatch: sigma-model	uniform	50	[1,100]	0.4
correlation timescale	uniform	12 hours	[1,120]	4
Number of basis functions	uniform	50	[5,600]	randomly add (birth) or remove (death) one
Frequency of calculation of each sigma-model value	constant	7 days	-	-
Number of iterations	constant	1 000 000	-	-
Burn-in: number of discarded initial iterations	constant	200 000	-	-
nsub: store every $nsub^{th}$ iteration	constant	100	-	-
stepsize for longitude move	constant	8.0	-	-
stepsize for latitude move	constant	5.0	-	-
stepsize for birth/death	constant	2.0	-	-

4.4.2 Data filtering using NAME model

NAME footprints were also used for data filtering. The local ratio, which is the fraction of NAME sensitivity footprints of the nine grid boxes surrounding the station to the total sensitivity of the NAME spatial domain, was used to detect and filter out time periods when measurements were overly influenced by local emissions. A high degree of local influence typically corresponds to times when the air is particularly stagnant and transport dominated by sub-grid scale processes that cannot be resolved by the model [Lunt et al. 2016]. We have used a local ratio threshold of 40% for this work.

Chapter 5

Data Presentation and Analysis

Mole fractions of carbon dioxide, methane and carbon monoxide have been measured by the Picarro G2401 from June 2015. In addition, black carbon with biomass burning fraction was measured by a seven-wavelengths dual spots Aethalometer from May 2015, weather data are measured by two weather stations. All available data and instruments are described in section 2.3. Here we present and analyze CO_2 , CH_4 , CO , black carbon and weather data from June 2015 to February 2017.

5.1 Time series of measured mole fractions and black carbon concentrations

Time series of carbon dioxide (Figure 5.1) exhibit enhanced concentrations of CO_2 during both dry seasons. The same enhanced concentrations are observed for carbon monoxide (Figure 5.3) and black carbon (Figure 5.4). Unlike other measured species, methane mixing ratios (Figure 5.2) did not show any significant enhancement during the long dry season (Jun-July-August) of 2015 and 2016.

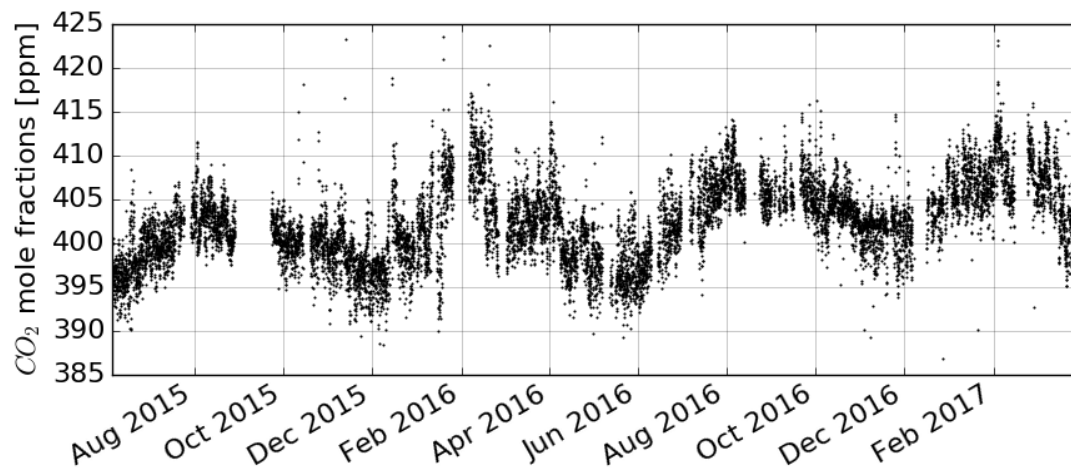


Figure 5.1: CO₂ time series for Mugogo station

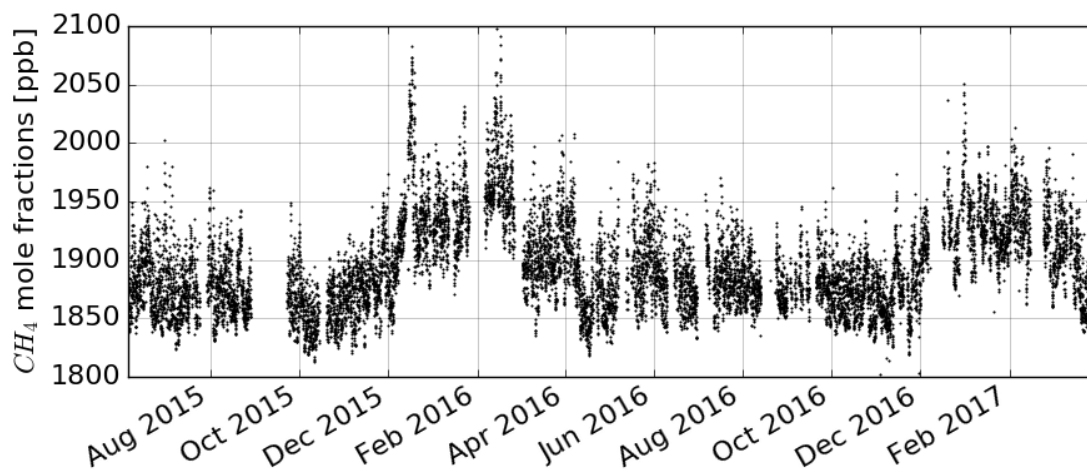


Figure 5.2: Time series of measured CH₄ mole fractions at Mugogo

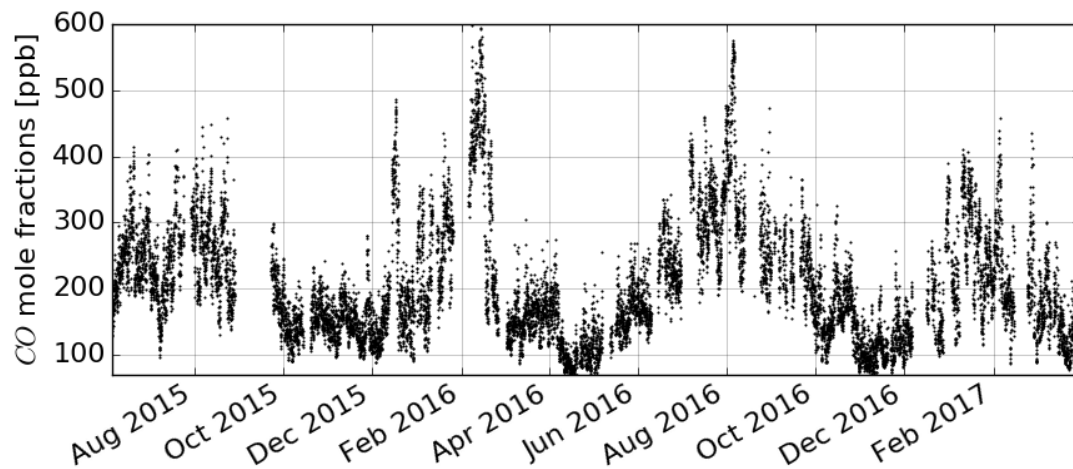


Figure 5.3: Time series of measured *CO* at Mugogo from June 2015 to February 2017

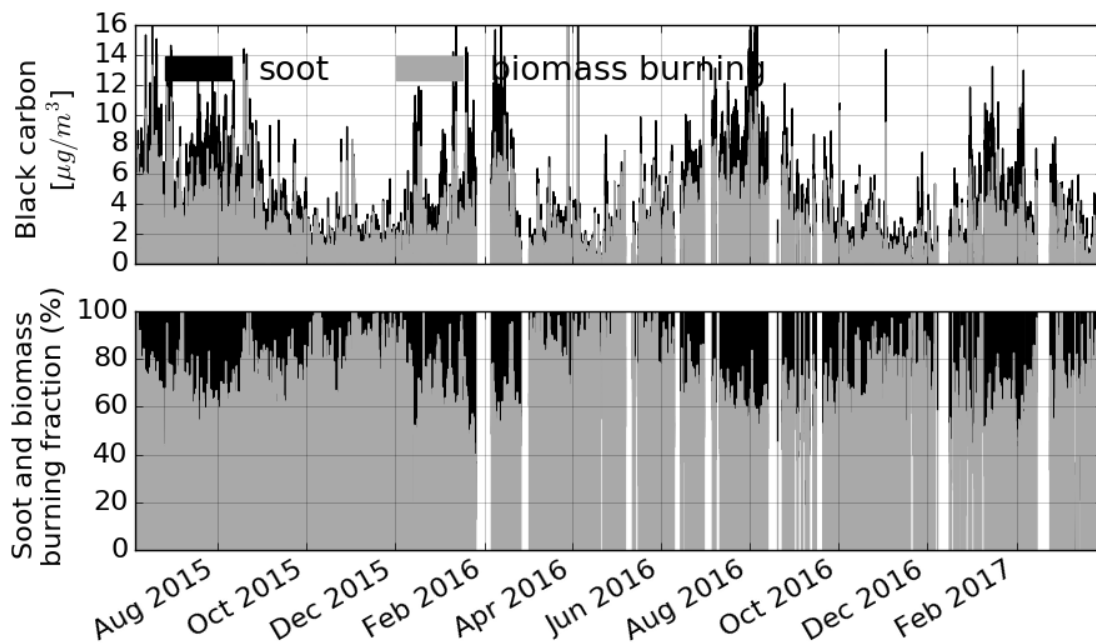


Figure 5.4: Hourly average black carbon indicating fossil fuel and biomass burning fraction

5.1.1 Seasonal cycles

5.1.1.1 Seasonal cycle of carbon dioxide, carbon monoxide and black carbon

Calculated footprints by the NAME model show that the station footprint is almost entirely located in the Northern Hemisphere in the short dry season (Dec-Jan-Feb) as shown in Figure 3.6 whereas the Figure 3.8 shows that the station is entirely influenced by the southern hemispheric air masses during the long dry season (Jun-Jul-Aug.). The Sun transitions from Northern to Southern Hemisphere in the Fall (Sept-Oct-Nov) and from Southern to Northern Hemisphere in Spring (Mar-Apr-May). The Sun transition sets up strong convection corresponding to the rain seasons, during which the station footprints extend to both hemispheres.

The location of the center of the ITCZ is classically determined from the precipitation field. In effort to locate the ITCZ from the UK Met office's unified model meteorological data, we followed Zagar et al. [2011] who characterized the ITCZ following the zero crossing of the meridional component of the wind. We found approximate locations of the ITCZ similar to what is reported in literature over the African continent [Nicholson 2009]. The surface pressure at sea level shown in Figure 5.5 also provided a better proxy for the ITCZ location compared to other potential indicators including the specific humidity and the vertical wind speed

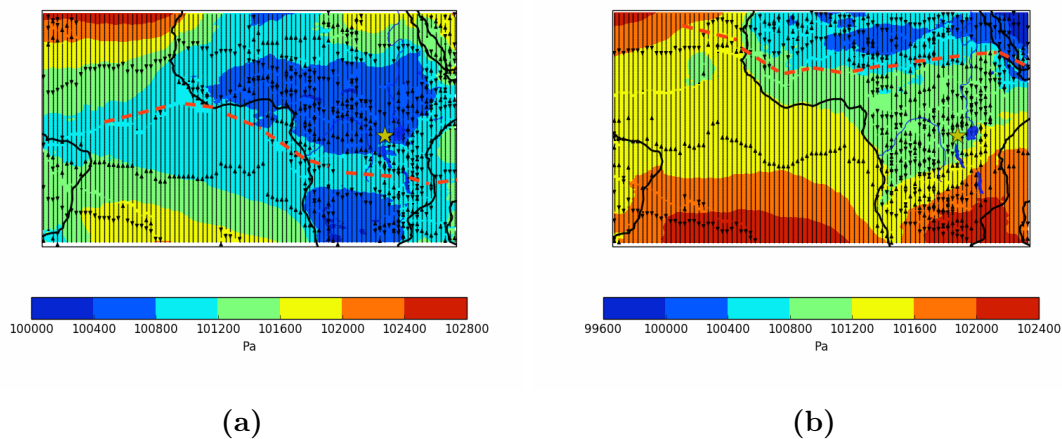
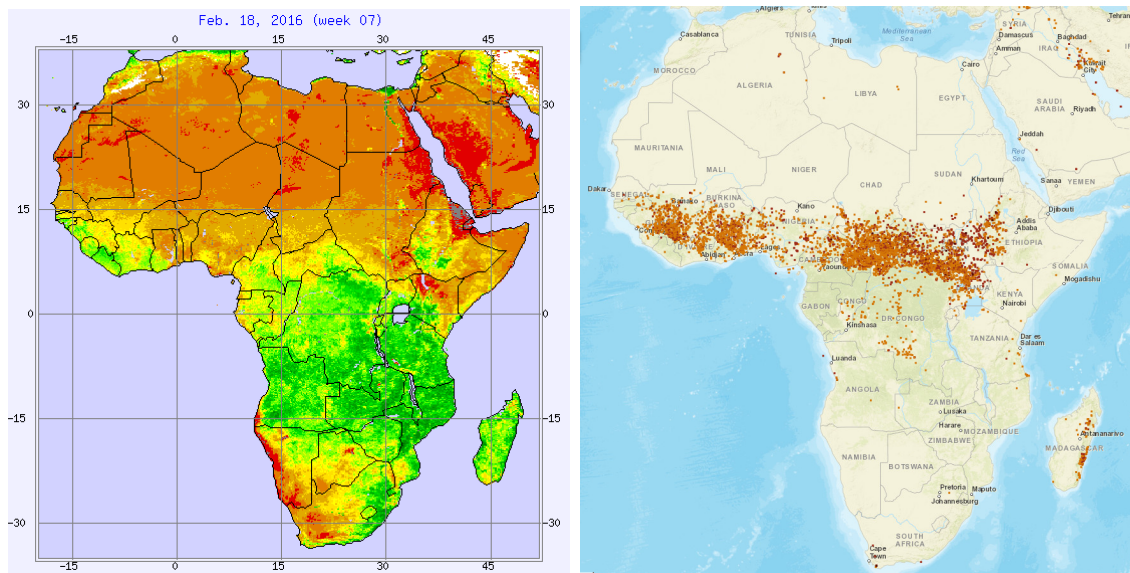


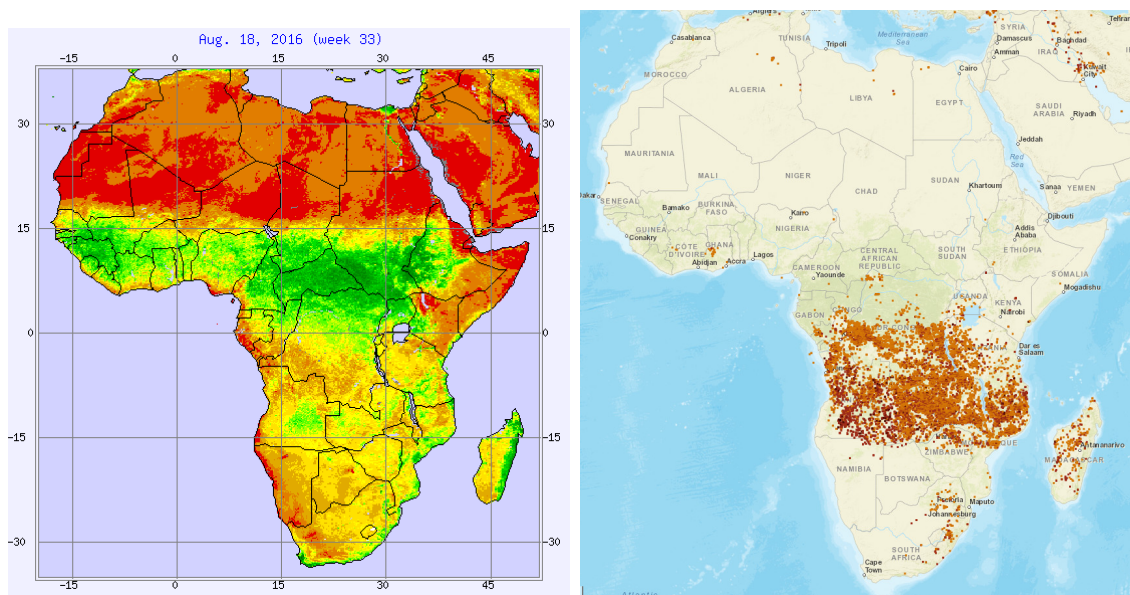
Figure 5.5: Boundary layer average meridional component of the wind speed overlaid to the surface pressure at sea level for February (a) and July (b). The approximate location of the ITCZ, highlighted by a broken red line, is the latitudinal band where the meridional wind changes the sign. We used the wind and pressure data from the UK met office's unified model meteorology, used for the modeling part of this work

During the short dry season of December-January-February, the Sun is over the Southern part of Africa, which leaves the Northern part very dry. The dryness results in a regional scale biomass burning with some due to people preparing their fields for the next growing season while other fires might be natural bush fires.



(a) Map of vegetation health index for February 2016 [NOAA STAR 2017] (b) Satellite observed open fires, February 2016 [UMD 2017]

Figure 5.6: Satellite observed vegetation health index (a) where greener color means healthier vegetation, and open fires (b) where each dot represents an open fire. Both maps are for February



(a) Map of vegetation health index for February 2016 [NOAA STAR 2017] (b) Satellite observed open fires, February 2016 [UMD 2017]

Figure 5.7: Satellite observed vegetation health index (a), greener color means healthier vegetation and open fires (b) each dot represents an open fire. Both maps are for August, 2016

Similarly, during the long dry season of June-July-August, the Sun is over the Northern part of Africa the Southern part becomes very dry due to lack of convection and hence precipitation, which results in region scale biomass burning. Figure 5.6 shows the map of vegetation health index for for February 2017 (Figure 5.6a) provided by NOAA Satellite Applications and Research (STAR) [NOAA STAR 2017] where a greener color represents healthier vegetation. The corresponding active fires detected by Visible Infrared Imaging Radiometer Suites (VIIRS) sensor aboard the Suomi National Polar-orbiting partnership (NPP) satellite are depicted in Figure 5.6b, fire maps were downloaded from the University of Maryland (UMD) website. [UMD 2017]. Figure 5.7 depicts the vegetation health index and fire maps for August.

Figure 5.6 and Figure 5.7 together with their corresponding footprints Figure 3.6 and Figure 3.8 suggest that the enhanced mixing ratios of CO_2 CO and black carbon concentration observed in both dry seasons result from regional scale biomass burning that occur in the Northern Africa during the short dry season and in the Southern Africa during the long dry season.

Figure 5.4 bottom panel, indicates that fossil fuel black carbon (soot) significantly contributes to the total black carbon measured at Mugogo especially during both dry seasons where its contribution can be in the 20–30% range. Possible sources of soot for Mugogo include the nearest, albeit small, town of Musanze located at 12 km from the station in the North-East direction. In the south-West there are Gisenyi in Rwanda and Goma in the Democratic Republic of Congo, located at 45 km from the station. There are also a number of small cities in Uganda, the major ones being Masaka and Kampala the capital city of Uganda both located in the North-East direction and 270 km and 380 km respectively. In the South East direction there is Kigali, the capital city of Rwanda, located at 70 km away.

The atmospheric lifetime of soot is generally assumed to be greater than 4.2 days [Jacobson 2010; Wang et al. 2014] with wet deposition as the main removal process. Considering the atmospheric lifetime of soot of 4 days and a modal wind speed of 3 m s^{-1} (Figure 5.15b) during the short dry season, it is evident that soot emitted from Kampala would be able to reach the station especially considering that there is much less rain during this season. Similarly, fossil fuel black carbon emitted from Kigali, the capital of Rwanda, and other major towns of Tanzania would be able to make it to the station during the dry season of June-July-August. Which explains the relatively higher fraction of soot measured at Mugogo station during the dry seasons.

5.1.1.2 Seasonal cycle of methane

Time series of measured methane mole fractions at Mugogo station (Figure 5.2) exhibit high methane mixing ratios during the December-January-February season. The average station footprint for this period (Figure 3.6) indicates that during this time of the year, the sta-

tion is largely influenced by air masses coming from the Northern hemisphere. Figure 5.8a and Figure 5.8b show the latitudinal distribution of monthly mean methane mole fractions calculated by NOAA from flask measurements for January 2008 and July 2008 respectively [GLOBALVIEW 2017], and latitudinal distributions of monthly mean CO_2 mole fractions (Figure 5.9) have been shown for comparison. A significant inter-hemispheric gradient exists for methane mixing ratios, and the gradient gets even stronger during the short dry season.

The enhanced methane mole fractions during the short dry season are, therefore, due to northern hemisphere air masses being advected to the station during this time of the year. Unlike CO_2 and CO whose seasonal cycles are largely driven by regional biomass burning, methane season cycles are mostly driven by shifting winds pattern around the year.

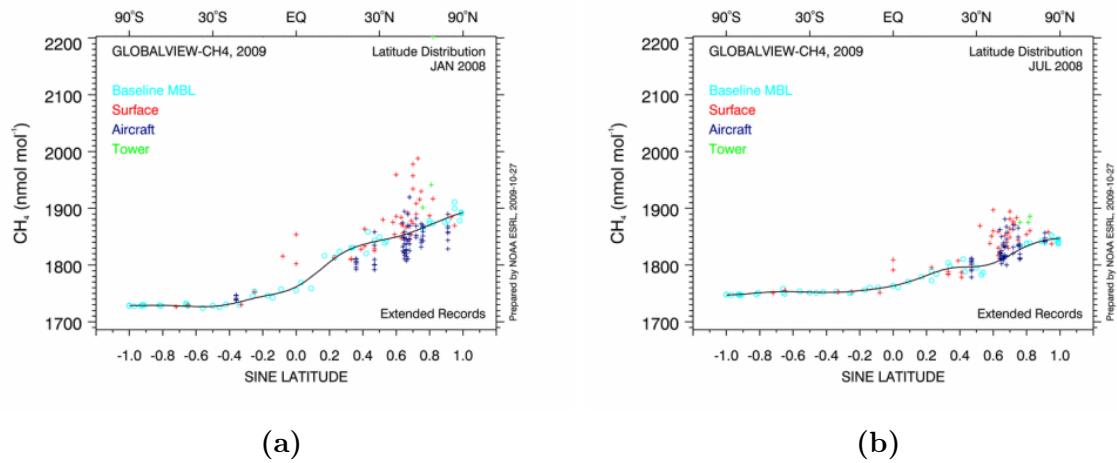


Figure 5.8: Latitudinal distribution of monthly mean mole fractions of CH_4 measured by NOAA for (a) January 2008 and (b) July 2008 [GLOBALVIEW 2017]. Cyan circles are baseline from marine boundary layer, red 'pluses' are surface measurements, blue 'pluses' are aircraft measurements and a smooth curve is fitted to the marine boundary layer measurements

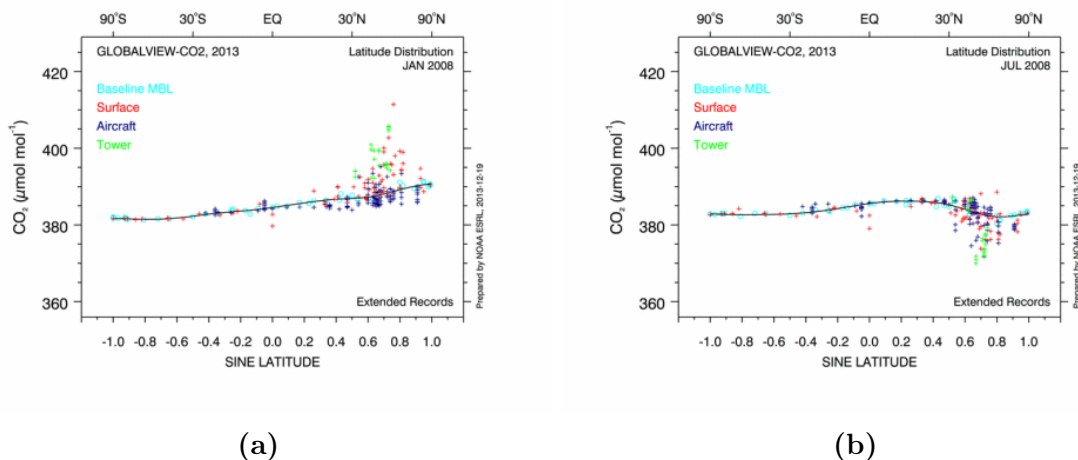
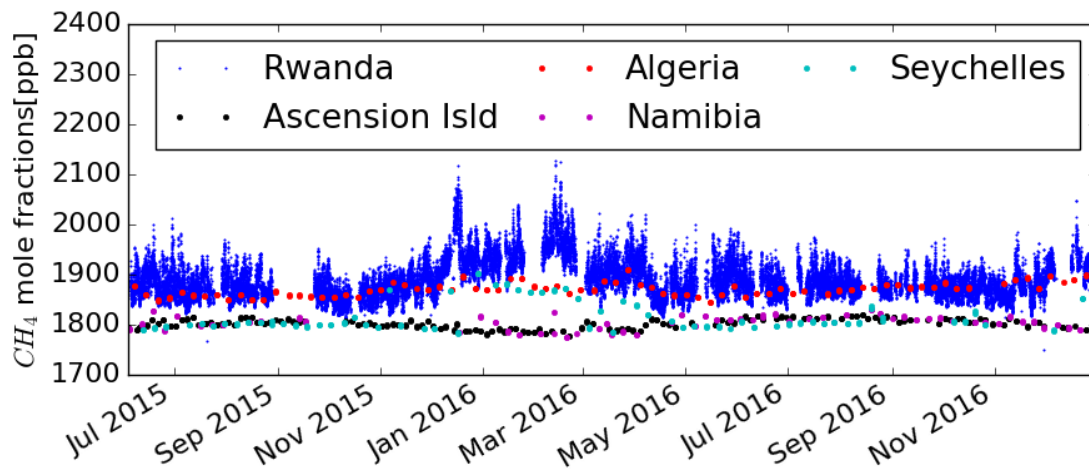
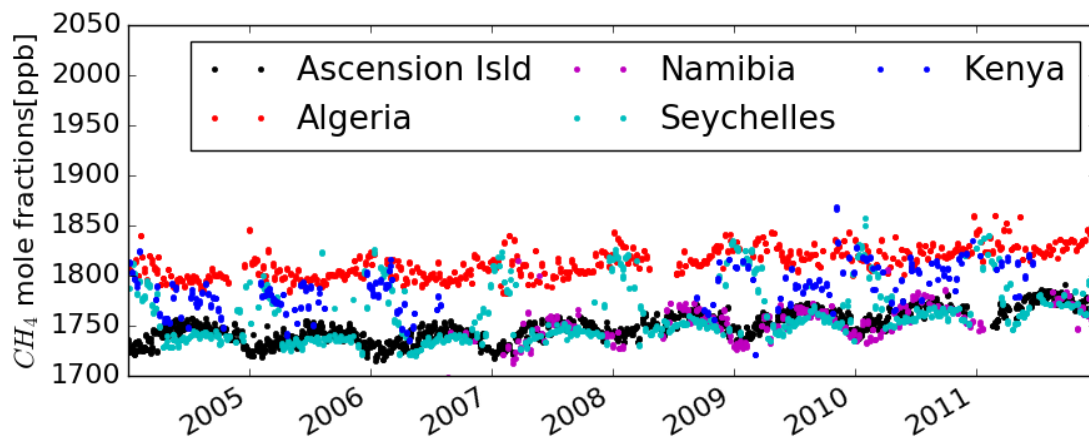


Figure 5.9: Latitudinal distribution of monthly mean mole fractions of CO_2 measured by NOAA for (a) January 2008 and (b) July 2008 [GLOBALVIEW 2017]. Cyan circles are baseline from marine boundary layer, red 'pluses' are surface measurements, blue 'pluses' are aircraft measurements and a smooth curve is fitted to the marine boundary layer measurements

We have plotted the recently released NOAA flask data from stations that are closest to Mugogo station, those are Mahe Island in the Seychelles, Assekrem station in Algeria, the Ascension Island (UK) station and the Gobabeb station in Namibia (Figure 5.10a). We have also plotted (Figure 5.10b) the same stations and the Mt. Kenya station for the period of 2004 to 2011 when the Mt. Kenya station was operating, where the map of Figure 5.11a shows the location of those stations. Both the Seychelles station and the Mt. Kenya station have the same season cycle as Mt. Mugogo station, but the Ascension island, which is in the same equatorial belt, does not exhibit the mole fractions enhancement around February. Figure 5.11b demonstrates that Mugogo station, the Mount Kenya station and the Seychelles station are located between the two seasonal extremes of the ITCZ and, therefore, are seasonally exposed to air masses from both hemispheres, while the Ascension Island station always receives air masses from the southern Hemisphere.



(a)



(b)

Figure 5.10: Time series of closest NOAA measurement sites for our measurement period (a) and for the data used in CarbonTracker-CH4 (b)

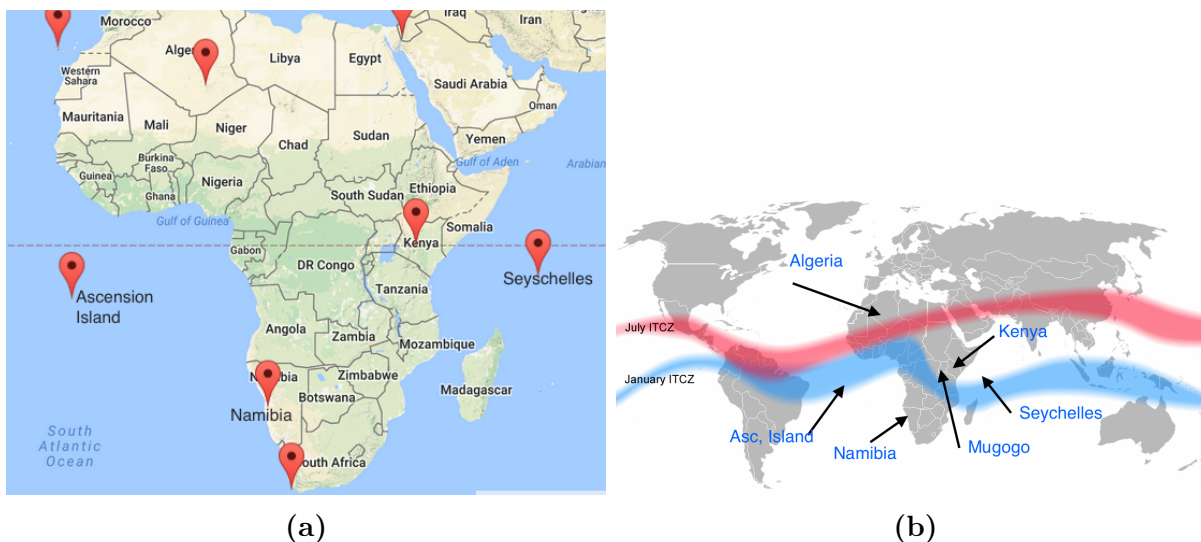


Figure 5.11: (a) Location of NOAA sites that are closest to Mugogo station <https://www.esrl.noaa.gov/gmd/ccgg/carbontracker/observations.php>. (b) Approximate location of the ITCZ in January and July (source: Wikipedia) with approximate locations of the closest NOAA stations

5.2 Diurnal cycles of CO_2 and CH_4

Carbon dioxide measured at Mugogo station exhibits a daily cycle, with low values of mole fractions observed during the day due to ecosystem uptake and high values observed during the night as shown in Figure 5.12. Unlike CO_2 , methane increases during the day and decreases during the night (Figure 5.13). Possible explanation for methane diurnal cycle at Mugogo would involve the dynamic of the mixing layer; if Mugogo summit is mostly in the mixing layer during the day and above the planetary boundary layer during the night, the measurement could be largely influenced by local sources during the day while measurement would represent a lower regional background during the night. Possible local sources and their expected influence on diurnal cycle of methane are enumerated below:

Wetland emissions: Mugogo is surrounded by wetlands located in the valleys. As wetland methane emissions increase with temperature, [Cui et al. 2015; MacDonald et al. 1998] we would expect methane emissions to peak in the afternoon, this is consisted with observed diurnal cycle of methane mole fractions at Mugogo

Fossil fuel emissions: As detailed in section 5.4.4, methane mixing ratios increase for winds coming from the South-East direction, so this points to possible fossil fuel emission from Kigali, the capital city of Rwanda.

Lake Kivu emissions: Lake Kivu located at about 40 km in the South West of Mugogo is known to contain large amount of CH_4 (65 km^3) and carbon dioxide (256 km^3) at

0°C and 1 atm [Pasche et al. 2011]. Gas emissions from lakes have been shown to be enhanced at night due to cooler surface water setting up convection and bubbling. Methane emitted overnight from lake Kivu would accumulate in the boundary layer and contributed to the high mole fractions observed at Mugogo in the morning as the planetary boundary layer breaks up. Polar plots of Figure 5.27 show increased methane mole fractions for winds coming from the South West of the station, which correspond to the location of Lake Kivu, in February, March, May and September. Given the amount of methane dissolved in the lake, one would expect CH_4 fluxes from the lake to be a significant driver of CH_4 mole fractions measured at Mugogo. Fluxes from the lake are likely limited by the mountain chain formally know as the Congo-Nile divide which extends from South to North between the station and the lake, with summit altitude equal or higher than mount Mugogo summit.

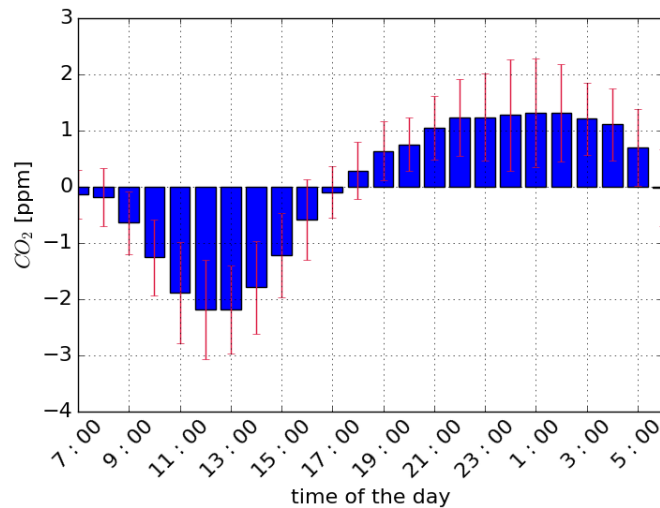


Figure 5.12: Average diurnal cycle of CO_2 at Mugogo. Values are difference from the mean and error bars are the range of monthly means

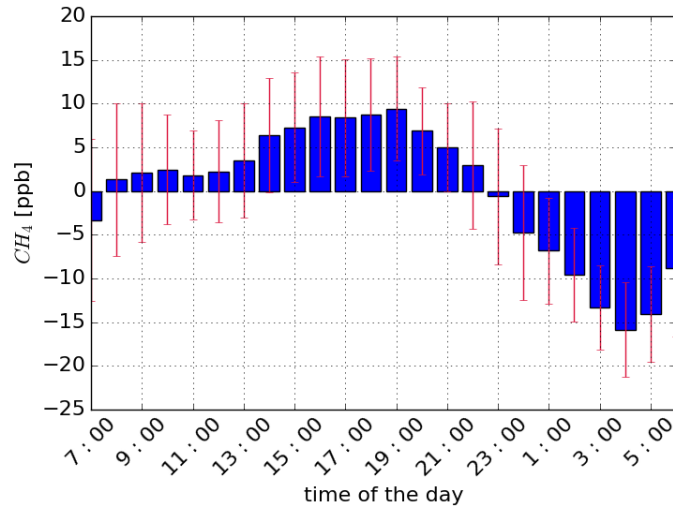


Figure 5.13: Average diurnal cycle of methane mixing ratios. Values are difference from the mean and error bars are the range of monthly values

5.3 Weather data

Mount Mugogo is located in the North West part of Rwanda which is significantly cooler and receives more precipitation than the rest of the country. Figure 5.14 shows that the daily maximum temperature was slightly higher in February and March while the coolest temperature close to freezing were measured in the long rain season (March-April-May). The wettest months are March, April and May while the driest months were July, August and September.

Lights winds are observed around the year with a modal wind speed in the $2\text{--}4\text{ m s}^{-1}$ range as shown in Figure 5.15b, Figure 5.16b Figure 5.17b and Figure 5.18b. The highest wind speed observed were around 11 m s^{-1} and were observed in the rain seasons.

Unlike wind speed which vary very little around a year, wind directions have a clear seasonal shift, and Figure 5.15a points out that Easterlies and North-East winds dominate the short dry season, as expected from this equatorial location during the Northern Winter. During this short dry season, strongest winds in the $6\text{--}8\text{ m s}^{-1}$ range, blow from North-East and West North West, although not very frequent.

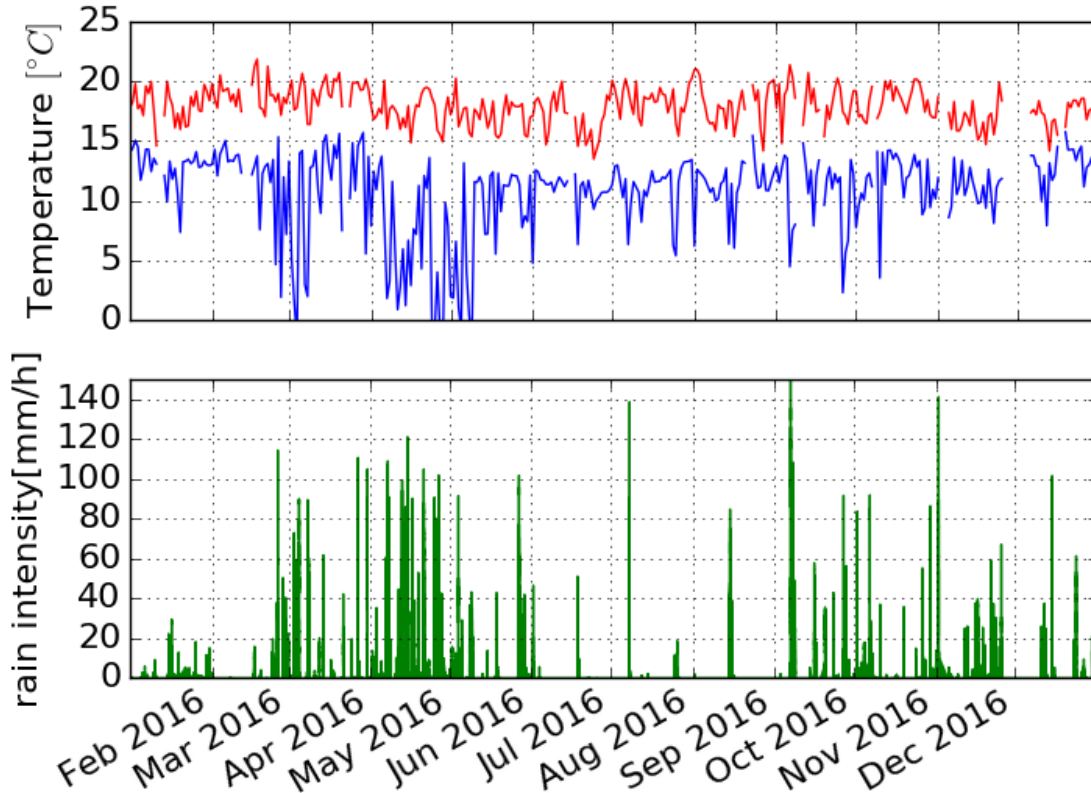


Figure 5.14: Measured daily minimum temperature (blue), daily maximum temperature (red) and precipitation intensity (bottom panel) at Mugogo

In the long rain season (March-April-May) winds shift to Southerlies and South West winds (Figure 5.16a). During this season also winds get stronger with high wind speeds of $8\text{--}10\text{ ms}^{-1}$ primarily blowing from the South, with some coming from the South West.

The winds direction do not change a lot from the long rain season to the dry season. Still, Figure 5.17a shows increased wind component from the South East direction and reduced Easterlies compared to the previous season. In addition, the highest wind speeds observed are lower and there is no preferred direction for higher wind speed.

During the short rain season, Mugogo station sees winds blowing from a wider area ranging from the South South East to North East. With higher wind blowing from South South East, South East and North East.

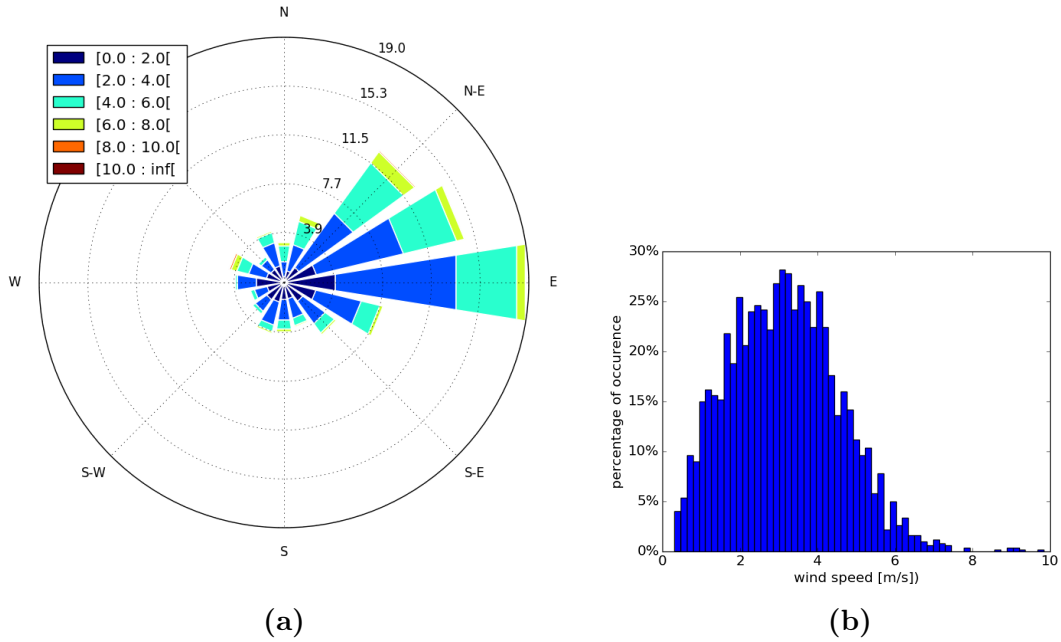


Figure 5.15: Wind rose (a) and wind speed frequency(b) for the short dry season of December-January-February

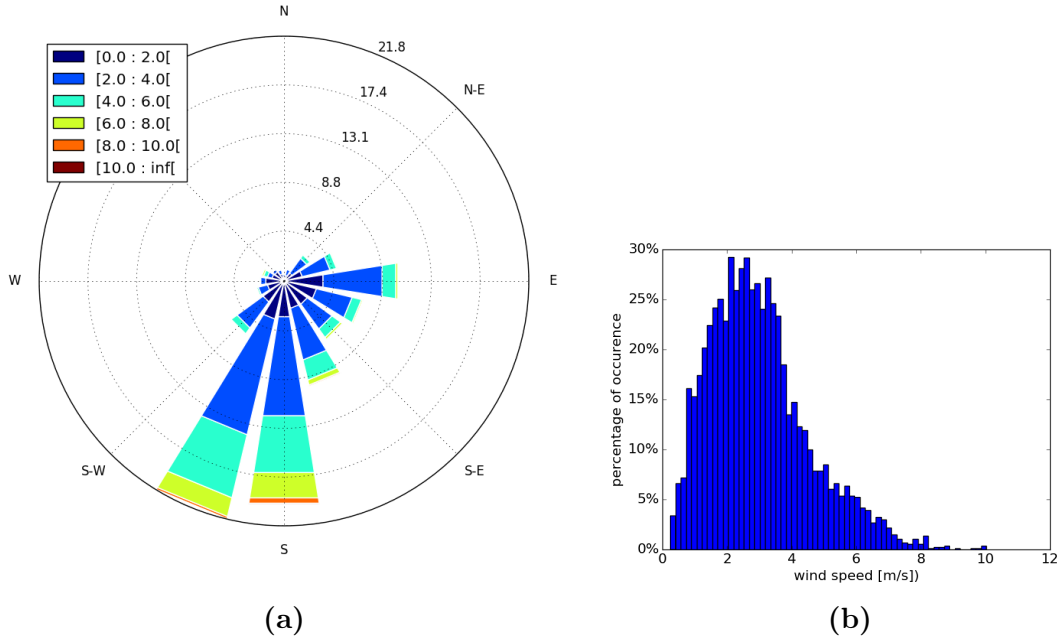


Figure 5.16: Wind rose (a) and wind speed frequency (b) for the long rain season (Mar-Apr-May)

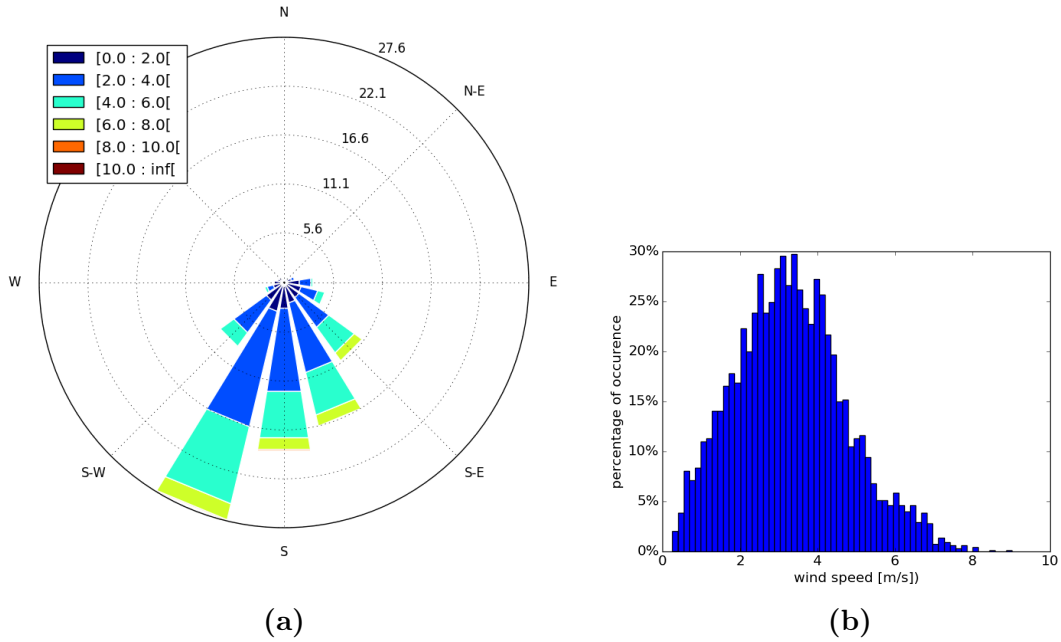


Figure 5.17: Wind roses (a) and wind speed frequency (b) for the long dry season (Jun-Jul-Aug)

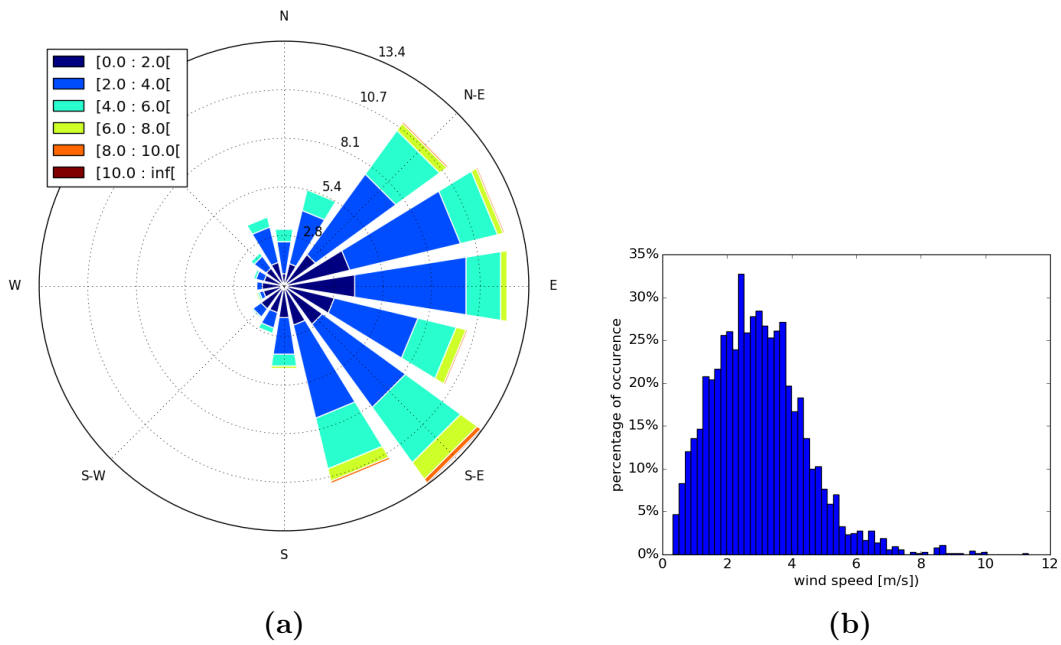


Figure 5.18: Wind rose (a) and wind speed frequency (b) for the short rain season (Sept-Oct-Nov.)

5.4 Correlations between species

In this section we seek to find possible correlations between measured mole fractions of CO_2 , CH_4 , CO and BC concentration which indicates common or co-located sources.

5.4.1 Mixing ratio correlations between black carbon and carbon monoxide

We have already found in section 5.1.1.1 and 5.1.1.2 that carbon monoxide and BC have the same seasonal distribution largely due to regional bush fires and fossil fuel burning from nearest towns. In addition, Figure 5.19 illustrates that most major pollution events seen in black carbon concentration time series are also found in CO mole fractions time series. More quantitatively, Figure 5.20a, Figure 5.21a and Figure 5.21b indicate that carbon monoxide mole fractions and BC concentration are well correlated most of the year with coefficients of determination R^2 of 78% and 71% in the dry seasons and 64% in the short rain season. However, there is no correlation between CO and BC in the long rain season as seen in Figure 5.20b. The lack of correlation between CO and BC in the long rain season, and relatively weak correlation in the short rain season points out to substantial wet removal of black carbon particles before they make it to the station.

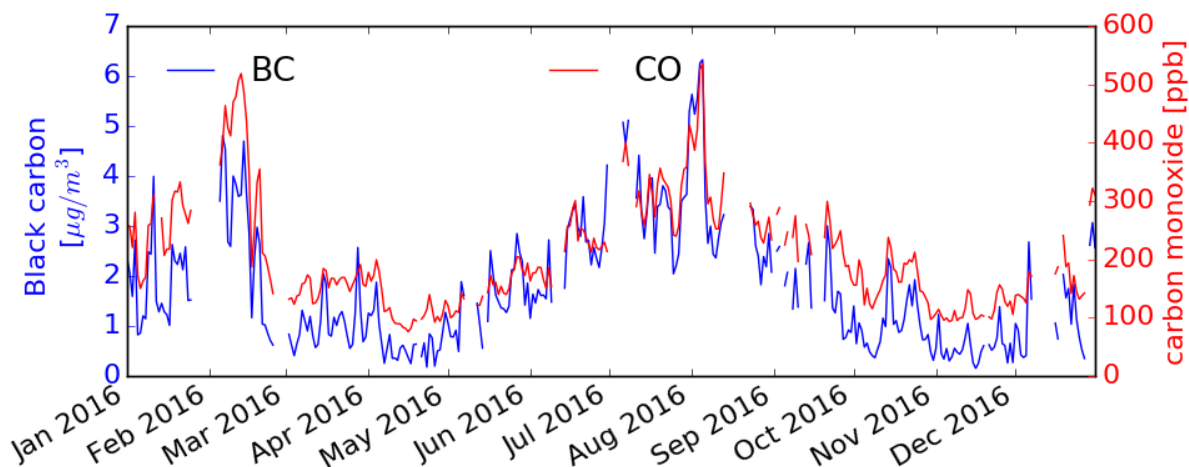


Figure 5.19: Daily mean carbon monoxide (blue) and black carbon (red) for 2016

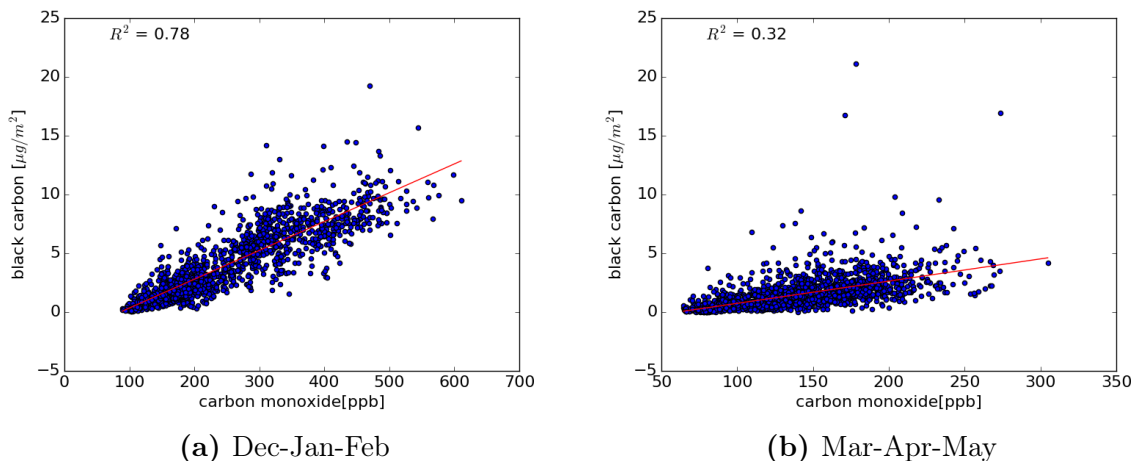


Figure 5.20: Scatter plots for CO and BC for the short dry season (DJF) and the long rain season (MAM)

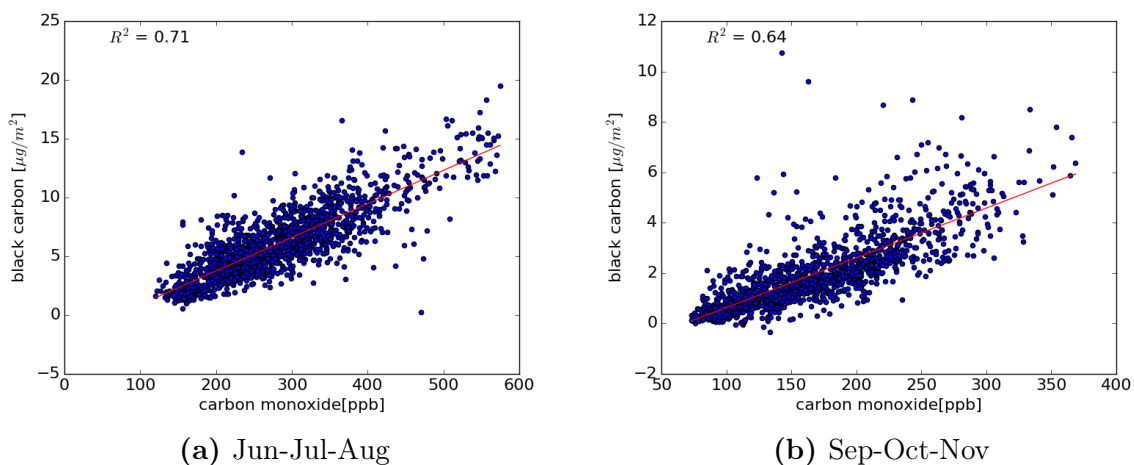


Figure 5.21: Scatter plots for CO and BC for the long dry season (JJA) and the short rain season (SON)

5.4.2 Correlation between carbon monoxide and methane mole fractions

During the short dry season, as can be seen in Figure 5.22a, there is no significant correlation between CH_4 mole fractions and CO . This is a period of the year when air masses with higher methane concentrations are advected from the Northern Hemisphere. Measured methane mole fractions are likely to change due to the wind speed and direction, while CO depends on regional biomass burning as well as local sources.

Figure 5.22b indicates that CH_4 mole fraction and CO mole fractions are correlated during the long rain season. This correlation points to a possible common source for CO and CH_4 during this period of the year, and more investigation would be needed to tell apart the relative contribution between local biomass burning and fossil fuel emissions from nearby towns, which are both possible common source of CO and CH_4 .

There is no correlation between methane mole fractions and carbon monoxide mole fractions during both the long dry season and the short rain season, as highlighted in Figure 5.23a and Figure 5.23b. During this time carbon monoxide mole fractions are enhanced by regional scale biomass burning while methane mole fractions stay relatively low compared to the February maximum.

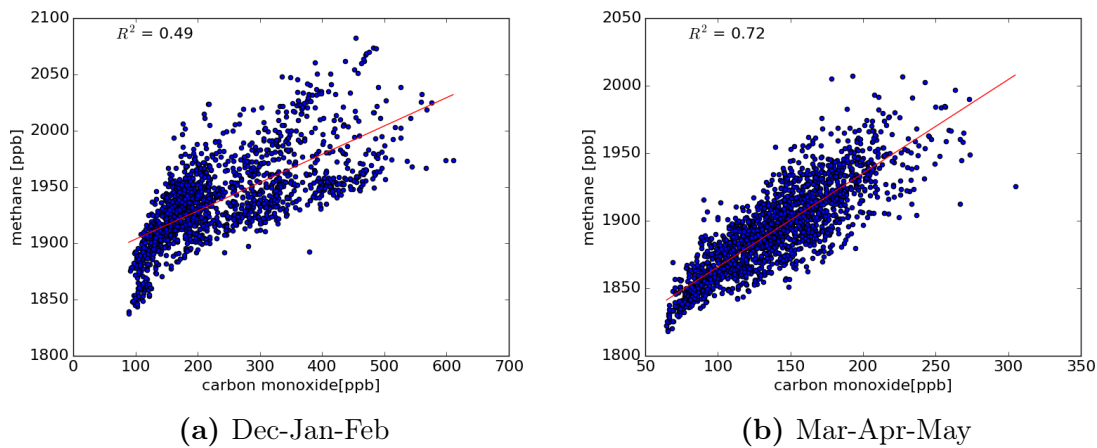


Figure 5.22: Correlation between carbon monoxide and methane mixing ratio for the short dry season and the long rain season

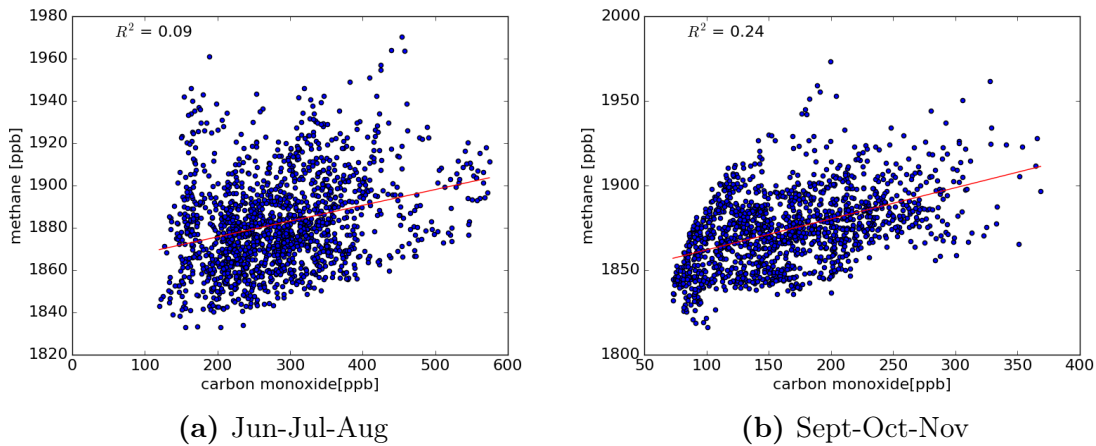


Figure 5.23: Correlation between carbon monoxide and methane mixing ratio for the long dry season and the short rain season

5.4.3 Correlation between carbon monoxide and carbon dioxide mole fractions

Correlation between CO_2 and CO mole fractions are shown in Figure 5.24a, Figure 5.24b, Figure 5.25a and Figure 5.25b for the four seasons. The coefficient of determination directly follows the scale of regional biomass burning. There is no correlation at all during the long rain season, a period when the regional biomass burning is minimum, and the largest coefficient of determination is observed in the long dry season, a period where regional biomass burning is at its maximum. Intermediate values for the coefficient of determination are found in the short rain season and the short dry season, but still the short dry season has higher coefficient of determination than the short rain season.

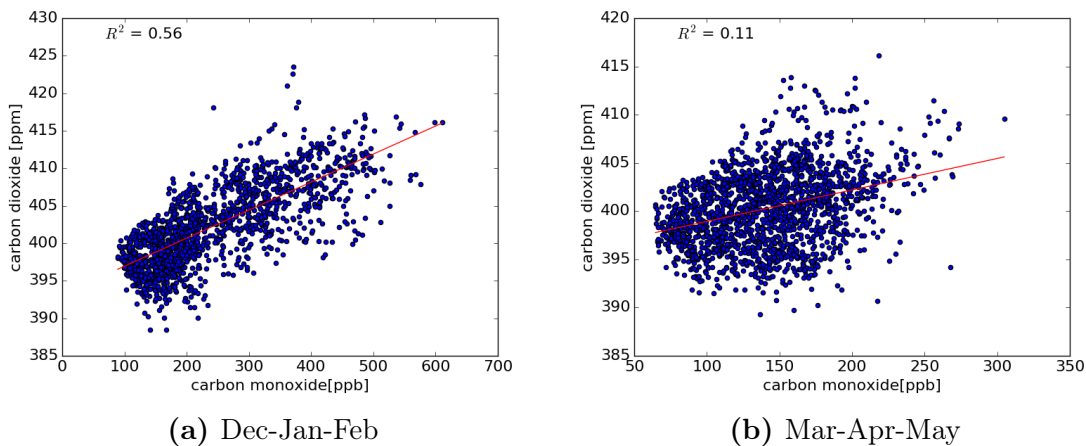
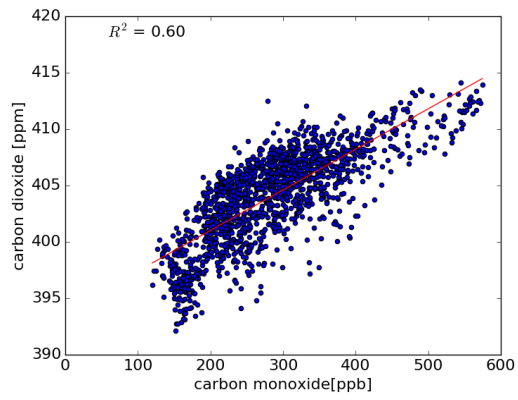
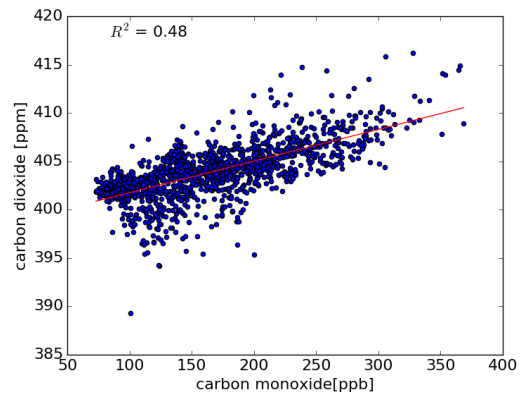


Figure 5.24: Correlation between carbon monoxide and carbon dioxide mixing ratio for the short dry season and the long rain season



(a) Jun-Jul-Aug



(b) Sept-Oct-Nov

Figure 5.25: Correlation between carbon monoxide and carbon dioxide mixing ratio for the long dry season and the short rain season

5.4.4 Methane mole fractions dependence on wind direction

A methane rose plot for the year 2016 is shown in Figure 5.26 which is overlaid to a map illustrating the location of lake Kivu and the city of Kigali. The rose plot shows the frequency of wind direction with color code representing methane mole fractions, with a purpose to identify the most likely direction that high/low values of methane mole fractions were coming from.

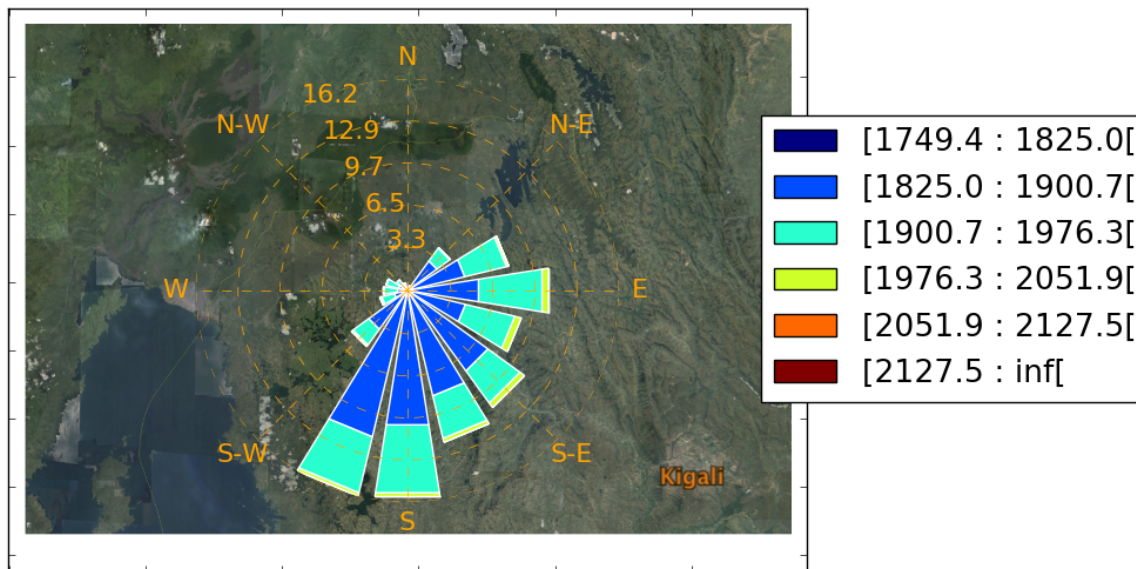


Figure 5.26: Methane rose plot showing the wind direction frequency color-coded with methane mole fractions for 2016. The rose plots is overlaid on a map showing the location of lake Kivu and the city of Kigali

From Figure 5.26, we expect that Kigali city fossil fuel emissions would come from the South East direction, while possible emissions from lake Kivu would come from the South West direction.

Monthly rose plots of methane mole fractions are presented in Figure 5.27. The rose plots emphasizes the seasonal cycle of methane, already investigated in section 5.1.1.2, where highest mole fractions are measured in February whereas lowest are observed around October. On top of the background concentrations which are set by the seasonal cycle, one can identify, in some months, the directions from which methane mole fractions were consistently high.

Mole fractions enhancement from lake Kivu emissions are observed for the winds blowing from the South West and South South West directions, those enhancement are visible for

the months of February, March, May, July and September.

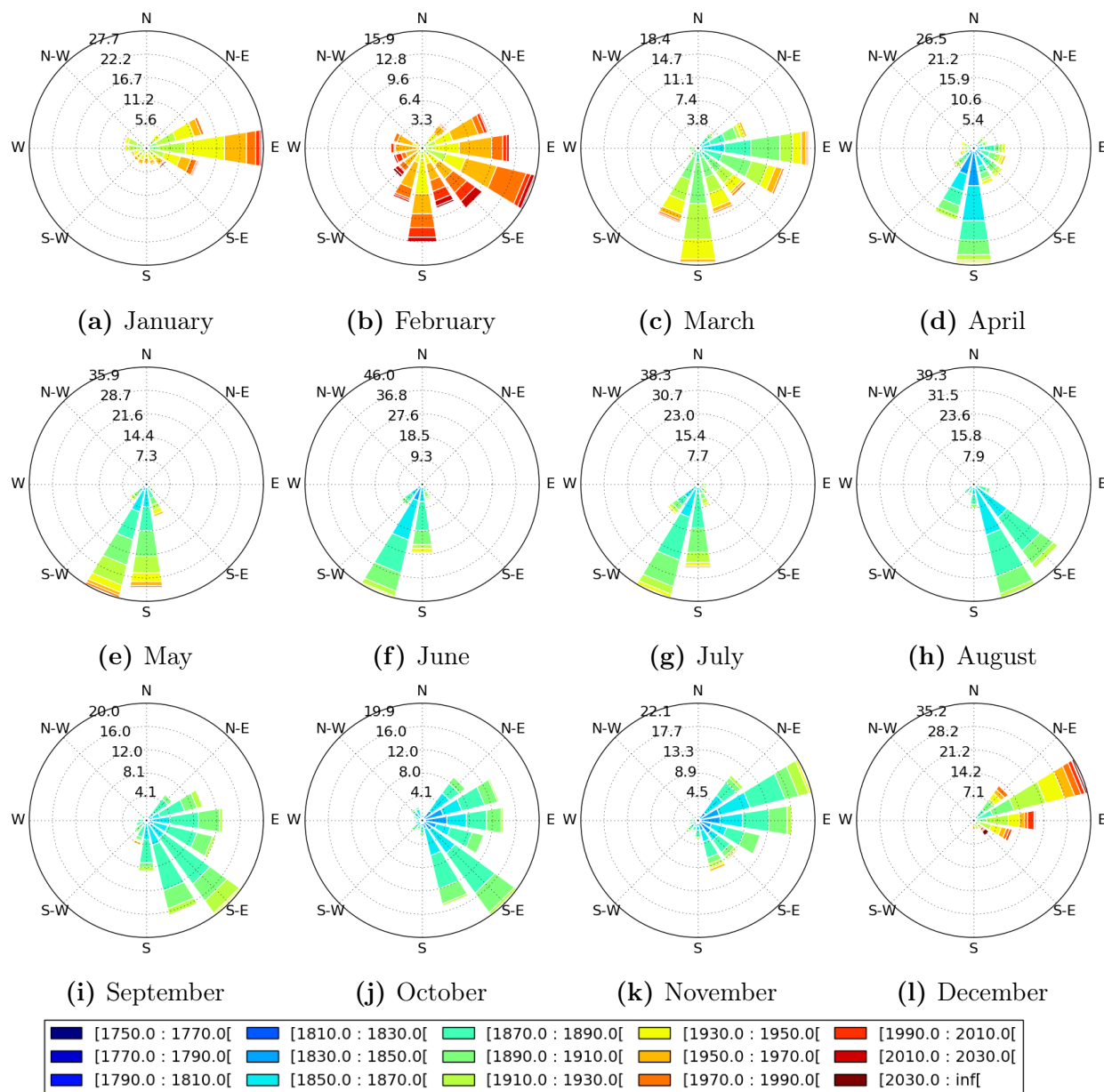


Figure 5.27: Methane rose plots showing the wind direction frequency color-coded with methane mole fractions.

Emissions from the city of Kigali also were likely to enhance the baseline methane concentrations from the South East and South South East directions, and those enhancements occurred in January, February, March, September, October and December.

A significant contribution from South of our station is also observed in February, March, May, June and July. The South direction corresponds to the settlements near the station as well as agricultural fields. The enhancement from the Southern direction is likely to be due to emissions from agricultural activity in the direct vicinity of the station.

5.4.5 Carbon dioxide mole fractions dependence on wind direction

Rose plots of carbon dioxide, shown in Figure 5.28, exhibit a seasonal cycle where high mole fractions are observed in February and August as discussed in section 5.1.1.1.

Unlike methane, carbon dioxide mole fractions are equally distributed from all directions. This is due to the fact that CO_2 has varied sources and sinks including household cooking, open burning, transportation, plant photosynthesis and respiration etc. These sources are likely to be found in all directions from the station.

A stronger mole fractions enhancement from the South West direction and the East North East direction is observed in February. Those directions correspond to the location of lake Kivu and the nearby town of Musanze respectively.

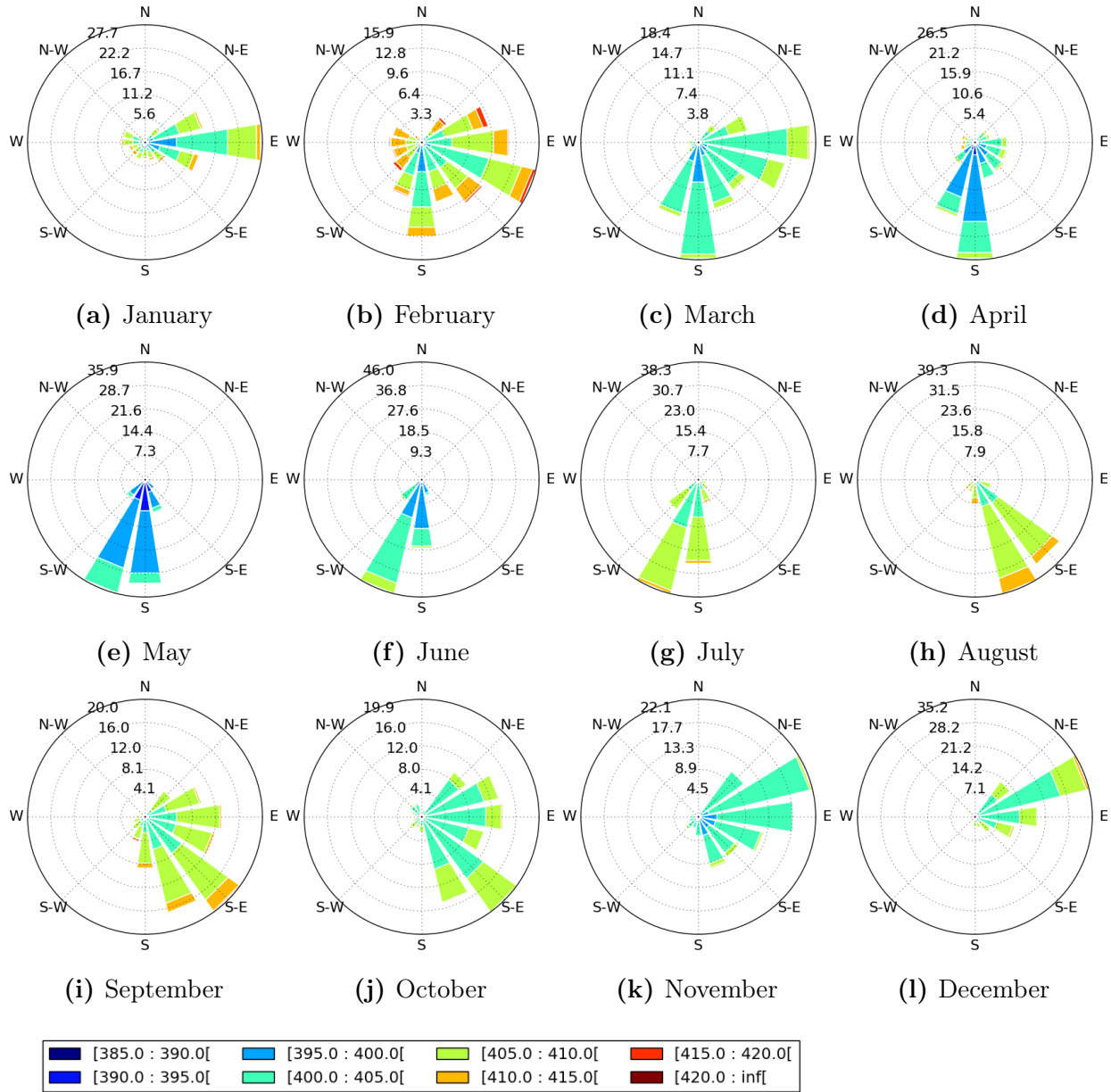


Figure 5.28: Carbon dioxide rose plots showing the wind direction frequency color-coded with carbon dioxide mole fractions.

Chapter 6

Methane inversion

Measured mole fractions of methane and calculated NAME sensitivity maps were used within the RJMCMC framework to optimally estimate methane emissions in Eastern and Central Africa. Here we describe the prior emissions used in the inversion, the inversion domain and the boundary conditions and methane inversion results.

6.1 Inversion prior

“Current observation networks are sufficient to quantify global annual radiative forcing and constrain global emission rates (with knowledge of loss rates), but they are not sufficient for accurately estimating regional scale emissions and how they are changing with time” - IPCC:WGI [2013, AR5, p.165]

Our specific goal was to start from the best available estimate of global methane emission fluxes, and use it as our prior and update regional emissions fluxes from our measured data. In this regard, we have used assimilated methane emissions provided by the global methane budget [Peters, Jacobson, et al. 2007; CarbonTracker-CH4 2010].

6.1.1 CarbonTracker-CH4

CarbonTracker-CH4 is a data assimilation system for CH_4 provided by the National Oceanic and Atmospheric Administration (NOAA). Corresponding data assimilation systems for CO_2 are available for different time periods, the latest being Carbon Tracker 2016.

CarbonTracker-CH4 has different modules for each component of the methane cycle, transport and chemistry.

Transport module: The chemistry and transport in Carbon tracker are simulated by the two-way nested global chemistry-transport zoom model, Tracer Model, version 5 (TM5) [Krol et al. 2005]. The model separately simulates advection, deep and shallow convection and vertical diffusion in the planetary boundary layer and free troposphere.

TM5 was driven by the meteorology from European Center for Medium range Weather Forecast (ECMWF) with 91 vertical levels and at a global resolution of $3^\circ \times 2^\circ$ and a nested regional grid of $1^\circ \times 1^\circ$ over North America.

Fossil Fuel Module: CarbonTracker-CH₄ used the prior emissions from Emissions Database for Global Atmospheric Research, EDGAR 3.2FT2000 [EDGAR 2005], which is 1×1 degree grid estimates for fugitive emissions from coal, oil and gas production. The database is based on emissions inventories by country and sector.

Agriculture and Waste module: CarbonTracker-CH₄ uses EDGAR 3.2FT2000 emission inventory for prior emissions for rice agriculture, enteric fermentation, animal waste management, wastewater and landfills.

Fire module: The fire module used in the CarbonTracker-CH₄ uses the Global Fire Emission Database (GFED). The GFED uses the Carnegie-Ames Stanford Approach (CASA) biogeochemical model [Potter et al. 1993] to estimate the carbon fuel in various biomass types. The GFED calculates the burned area from the Moderate Resolution Imaging Spectroradiometer (MODIS) satellite active fire counts combined with vegetation cover information. The burned area are then fed into the CASA biospheric model to calculate prior estimates of emissions from fires.

Natural sources: Wetlands, which are regions that are permanently or seasonally water logged, are the largest natural source of atmospheric methane. The CarbonTracker-CH₄ uses as prior the estimates of Bergamaschi, Frankenberg, et al. [2007], which is an inverse study estimating methane surface fluxes from SCIAMACHY satellite observations.

The prior for the termites and wild animal methane emissions for CarbonTracker were based on Houweling et al. [1999] and Sanderson [1996] and the methane loss by oxidation in soil was based on study by Ridgwell et al. [1999]. Emissions maps for February and July are shown in Figure 6.1, each high emission spot in the map corresponds to a wetland region.

Observations: CarbonTracker-CH₄ uses surface observations from NOAA ESRL Cooperative Global Air Sampling Network. These are flask samples which are collected once a week or once in two weeks and are sent to the NOAA laboratory where they are analyzed. In addition to flask samples, CarbonTracker-CH₄ included measurements from tall towers in Canada operated by Environment Canada (EC). Figure 5.11a shows the observations sites used in CarbonTracker-CH₄ that are closest to our inversion domain. To the East there are Mount Kenya whose record has a lot of missing data (Figure 5.10b) and the Seychelles, in the North direction there is the site of Assekrem in Algeria, the Ascension Island site is in the West direction and Gobabeb, Namibia in the Southern direction. All those sites are outside of our inversion domain and, as shown in Figure 5.10, only the Mahe Island site in the Seychelles and the Mount Kenya sites capture the seasonal cycle that we see at Mugogo. In addition, low frequency,

flask samples are well suited to capture large scale and long-term trends but cannot detect regional scales and high frequency variability in mole fractions that are needed to constrain regional emissions.

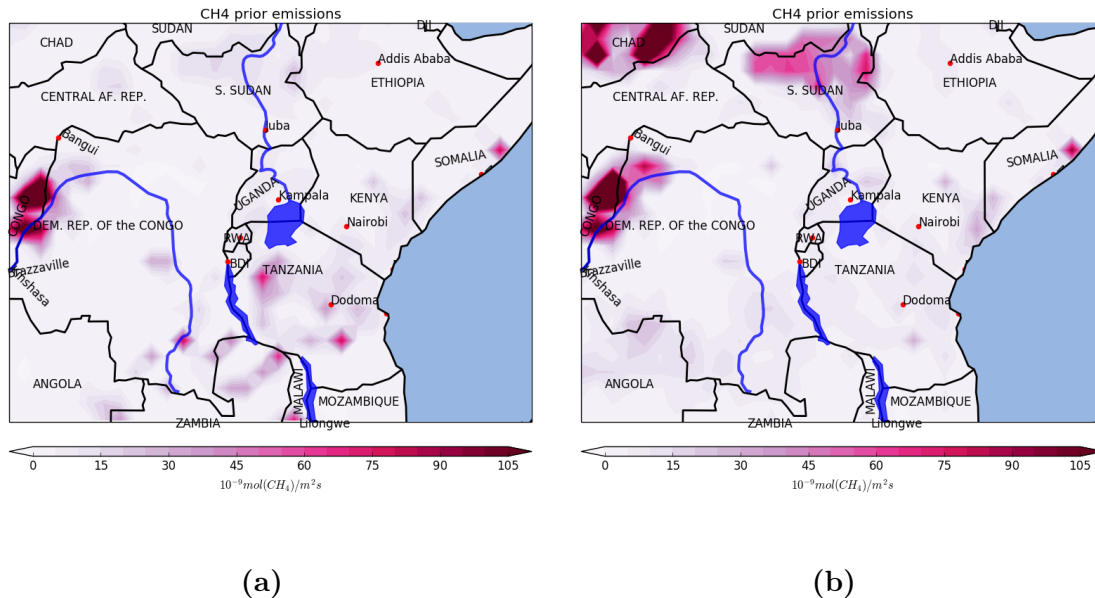


Figure 6.1: Prior emissions of methane from CarbonTracker-CH₄, for February (a) and July(b).

6.2 Inversion setup

6.2.1 Inversion domain and sub-domain

The NAME model was run for the domain extending from -40.0 to 18.0 degrees North latitude and -15.0 to 55.0 degrees East longitude. The domain is shown in Figure 6.2 made up by all five colored boxes. The TDMCMC inversion was run for a much smaller sub-domain, illustrated by the center blue box in Figure 6.2, while the outer orange, yellow, light blue and red regions of Figure 6.2 were considered fixed regions and solved for using the usual Metropolis-Hastings algorithm. Solving the TDMCMC for a sub-domain greatly improve the computational efficiency of the inversion, and is justified by the fact that the magnitude of the sensitivities decreases with the distance from the measurement site, and the model is not expected to resolve finer spacial details in the far field region of the domain.

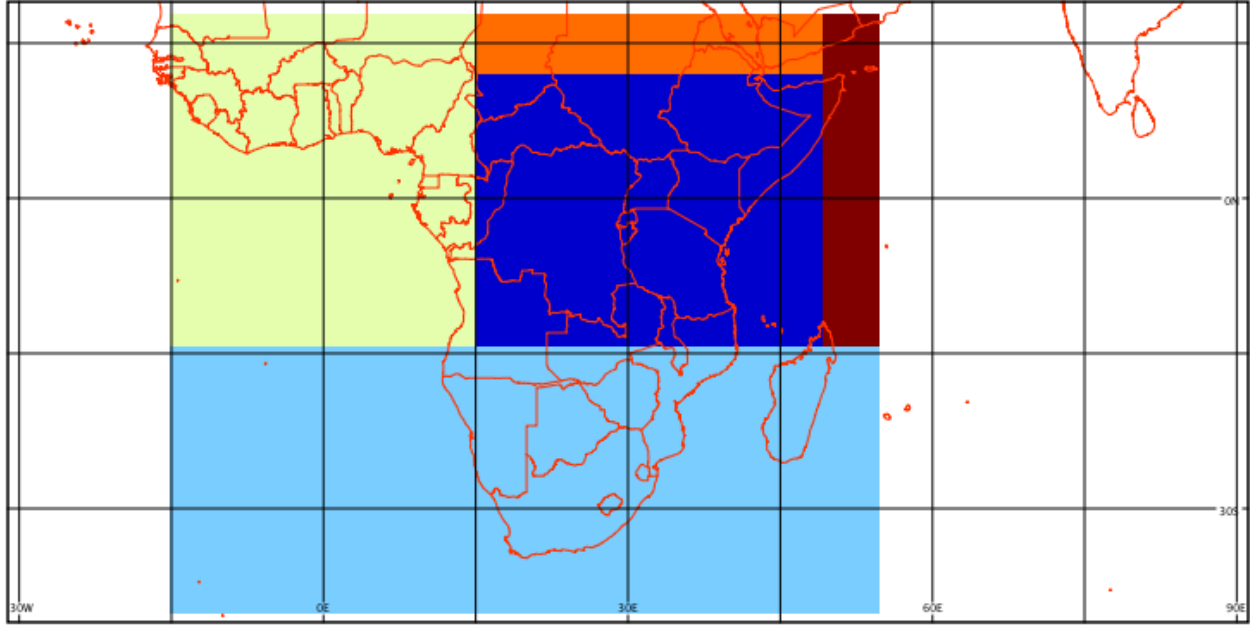


Figure 6.2: NAME domain and subdomain used for inversion, the transdimensional inversion was done in the center blue box, while the fixed-dimension MCMC was used for the outer boxes

6.2.2 Boundary Conditions

The CarbonTracker-CH₄ provides assimilated mole fractions of CH₄ at 3-hourly and $3^\circ \times 2^\circ$ resolution. However, the most recent methane mole fractions are available for year 2010. To estimate the boundary conditions for 2016, we have taken advantage of NOAA flask sampling sites which are located close to the edge of inversion domain in each direction, as shown in Figure 5.11a. We then sliced a vertical cross section from the CarbonTracker-CH₄ mole fractions along each of the four boundaries of the inversion domain, for each site, the cross section was scaled up by the ratio of monthly mean mole fractions measured at the site in 2016 divided by the monthly mean mole fractions measured at the same site in 2010. The scaling factors were found between 1.015–1.035 and are shown in the bottom panel of Figure 6.3, while the top panel shows the monthly mean values for 2010 and 2016.

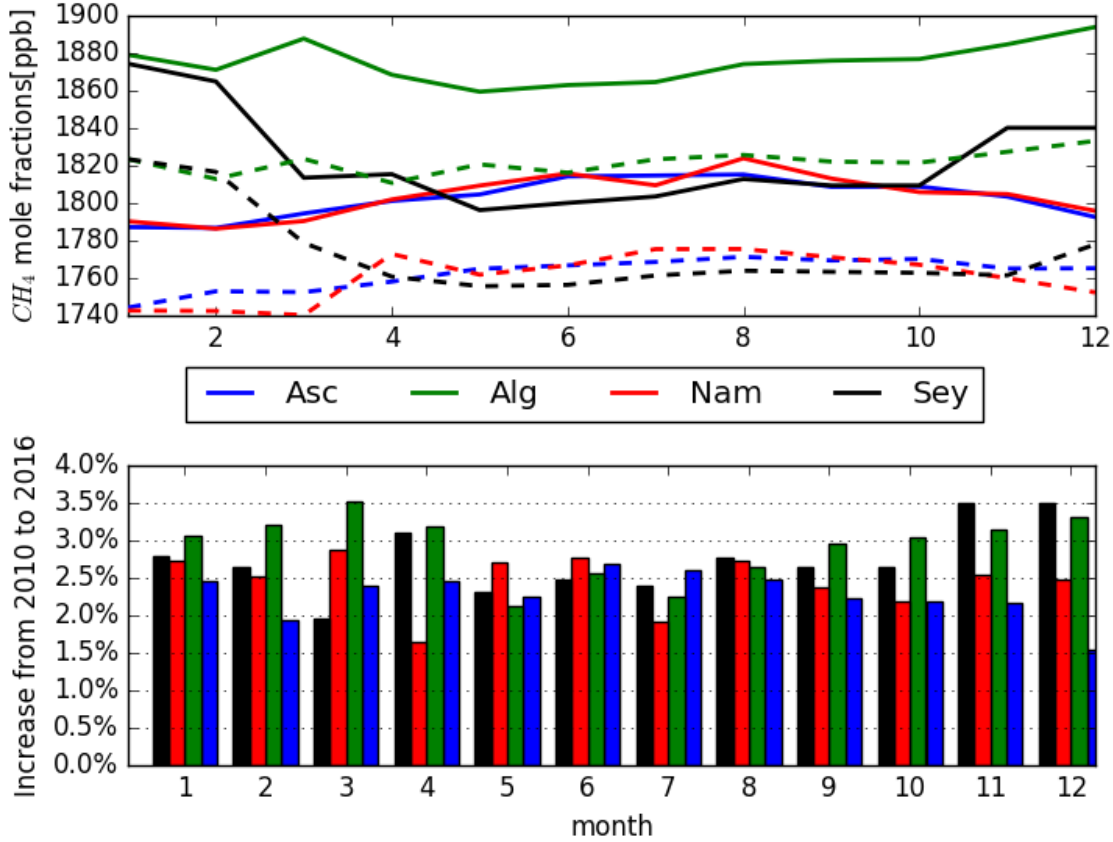


Figure 6.3: Top panel: Monthly mean mole fractions measured at the stations close to the edge of the inversion domain for 2016 (strait line) and 2010 (broken line). **bottom panel:** Ratios of monthly mean mole fractions measured in 2016 over those measured in 2010, the ratios where used to scales the boundary mole fractions. The color scale apply to both panels

6.2.3 Inversion parameters

We have carried out a TDMCMC inversion where the basis functions were allowed to vary between $k_{min} = 5$ and $k_{max} = 600$ according to Equation 4.14. Prior emissions scaling factors were assumed to follow a lognormal distribution (Equation 4.16) of location parameter $\mu_x = 1.0$ and scale parameter $\sigma_x = 2.0$, which corresponds to prescribing a $2\text{-}\sigma$ uncertainty of 200%. The parameters μ_x and σ_x were allowed to vary following a uniform distribution $0.8 \leq \mu_x \leq 1.6$ and $1.0 \leq \sigma_x \leq 3.0$. The model-measurements uncertainties, were allowed to vary between 1–100 ppb with a starting value of 50 ppb. The model-measurement uncertainties represent various uncertainties associated with the instrument and the model simulation of mole fraction, these include structural uncertainties within the model, representation errors and aggregation errors. Each simulation was run for 1 200 000 iterations with the first 200 000 iterations discarded as burn-in. Table 4.1 provides a more complete list of parameters.

6.3 CH_4 inversion results

In this section we present some of the results of methane inversion, while the rest of results have been put in the appendix A.

6.3.1 Uncertainty reduction maps

The air masses coming to the measurement site often originate from a specific direction depending on the direction and the speed of the wind, and the calculated lagrangian footprints tend to localize in specific regions of the inversion subdomain. Regions to which the measurement site is the most sensitive get the highest uncertainty reduction while region with less sensitivity to measurements have posterior emission fluxes close to prior emissions. The sensitivity is proportional to the product of the footprint and the emission flux as shown in the equation of the likelihood function (Equation 4.19).

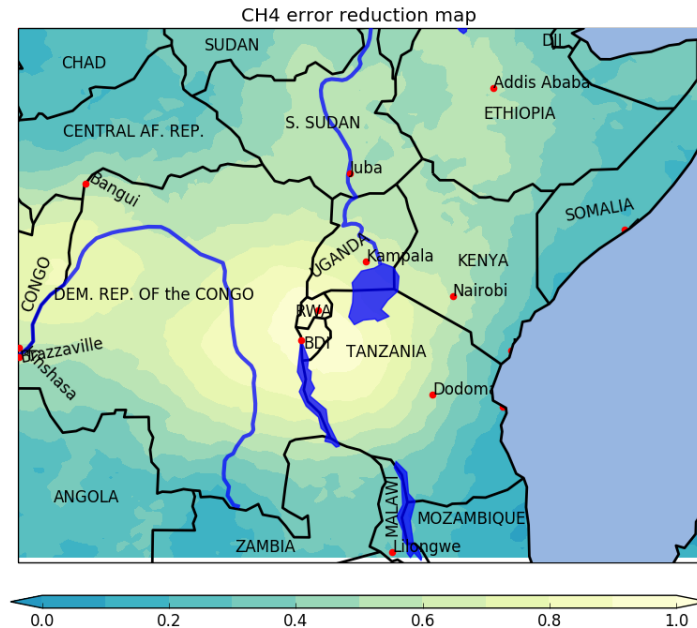


Figure 6.4: Uncertainty reduction map for February 2016

Figure 6.4 presents the uncertainty reduction maps for February 2016. The normalized uncertainty reduction map is the ratio of the 90th percentile ranges of the posterior to the

prior, expressed as:

$$uncertainty_reduction = 1 - \frac{90\%ile\ range\ posterior}{90\%ile\ range\ prior} \quad (6.1)$$

The prior uncertainty was obtained by running the inversion without observations, which results in the prior but with the uncertainty reflecting all sources of uncertainty in the inversion system.

6.3.2 Posterior emission maps

We show in Figure 6.5, the prior methane emissions for February 2016 (Figure 6.5a) and the corresponding posterior emissions fluxes (Figure 6.5b). The posterior emissions are less than the prior emissions in the inversion sub-domain, this suggest that the prior was an overestimate.

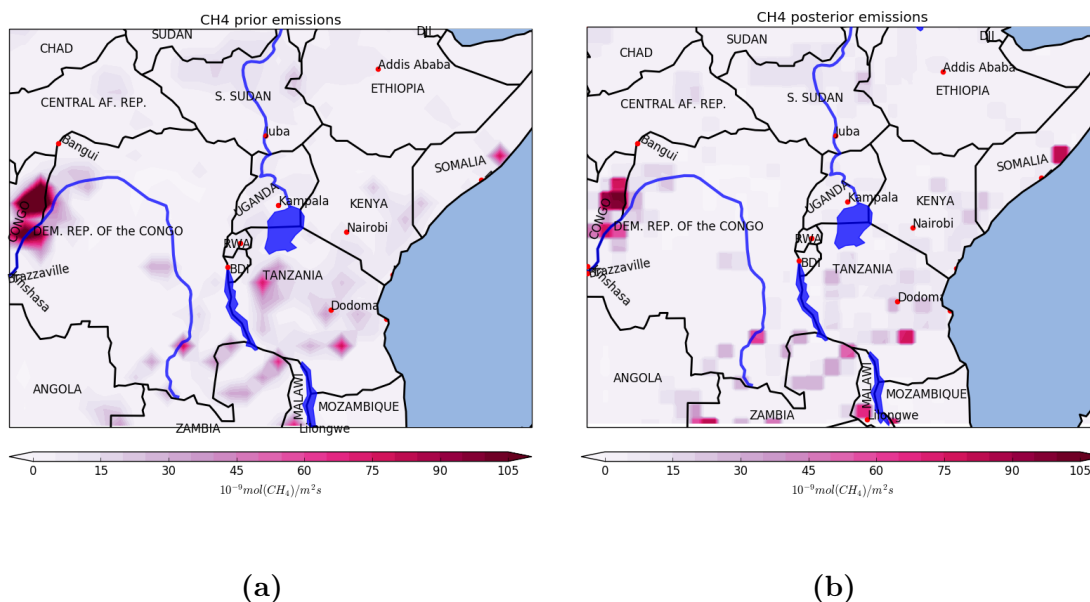


Figure 6.5: CH_4 prior (a) and posterior (b) emission fluxes for February 2016

6.3.3 Scaling factors and country totals

Scaling factors, which are the ratio of the posterior over the prior emissions are shown in Figure 6.6a. A scaling factor greater than 1 indicates that the posterior was increased from the prior. Our inversion for February 2016 results in general reduction of prior emissions. Bar plots of prior and posterior country totals for February 2016 are presented in Figure 6.6b,

Rwanda, Burundi, Tanzania and the Democratic Republic of the Congo saw the largest decrease in the posterior national total emissions.

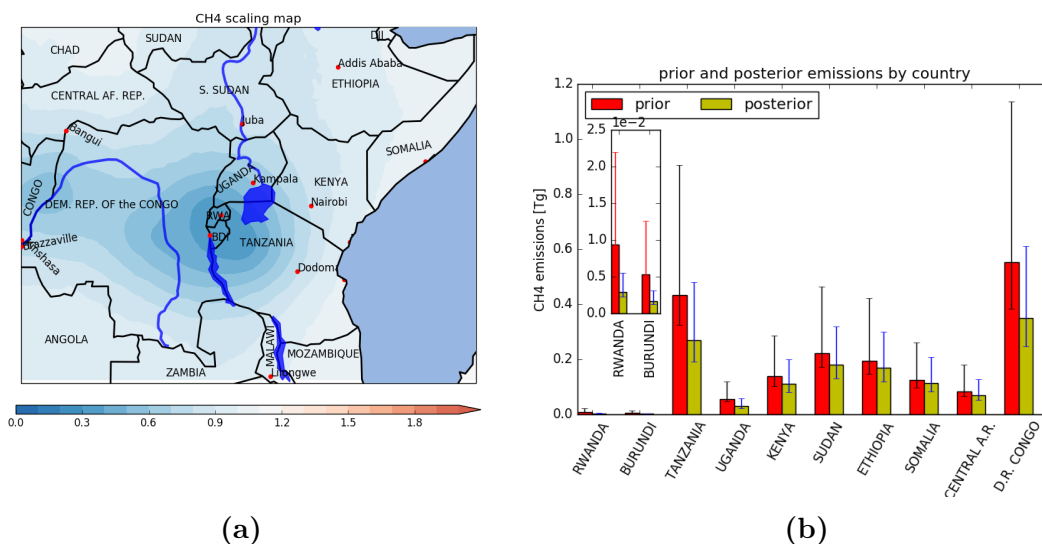


Figure 6.6: Prior scaling maps(a) and countries emissions totals (b) for February 2016

6.3.4 Forward run with optimized methane emissions

We present, in Figure 6.7 and Figure 6.8, the time series comparing the mole fractions modeled with prior and posterior emission to observations. We also include the prior and posterior baseline contribution to modeled mole fractions which result from the emissions coming from the boundaries of the inversion subdomain and the regions outside the inversion subdomain (Figure 6.2).

The modeled mole fractions accurately reproduce observations measured at Mt. Mugogo. The figures reveal that modeled mole fractions using prior emissions are higher than observed mole fractions at Mt. Mugogo, but, as illustrated in both figures, most of the increase happens from the baseline. This is an interesting finding because we previously found that emissions from the inversion regions were overestimated, but also suggest that the baseline contribution, which are emissions away from the inversion subdomain, should be increased in order to explain measurements at Mt. Mugogo. Furthermore, by estimating a reduction in estimated regional emissions and suggesting an increase in emissions outside the region, we expect little or no change to the global budget of methane.

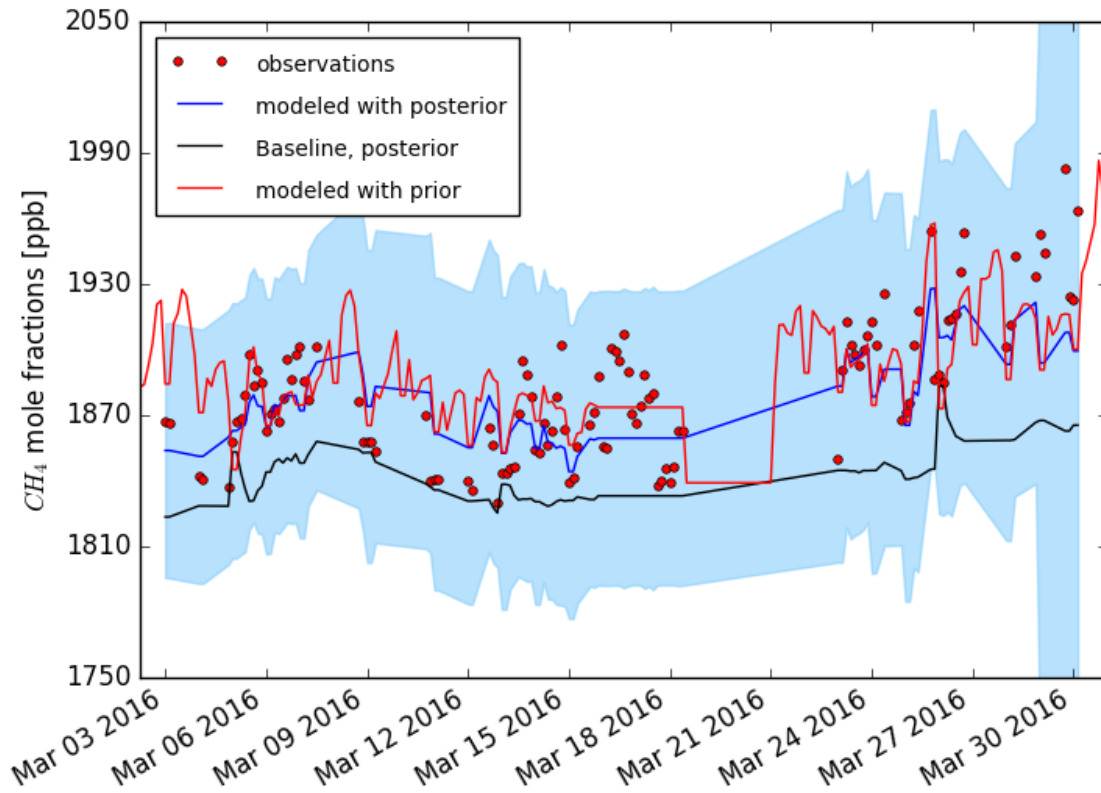


Figure 6.7: time series of optimized mole fractions (blue curve) compared to observations (red dots) and the modeled observation with prior emissions (red) with the prior (magenta) and posterior (black) baseline contribution to modeled mole fractions, for March 2016

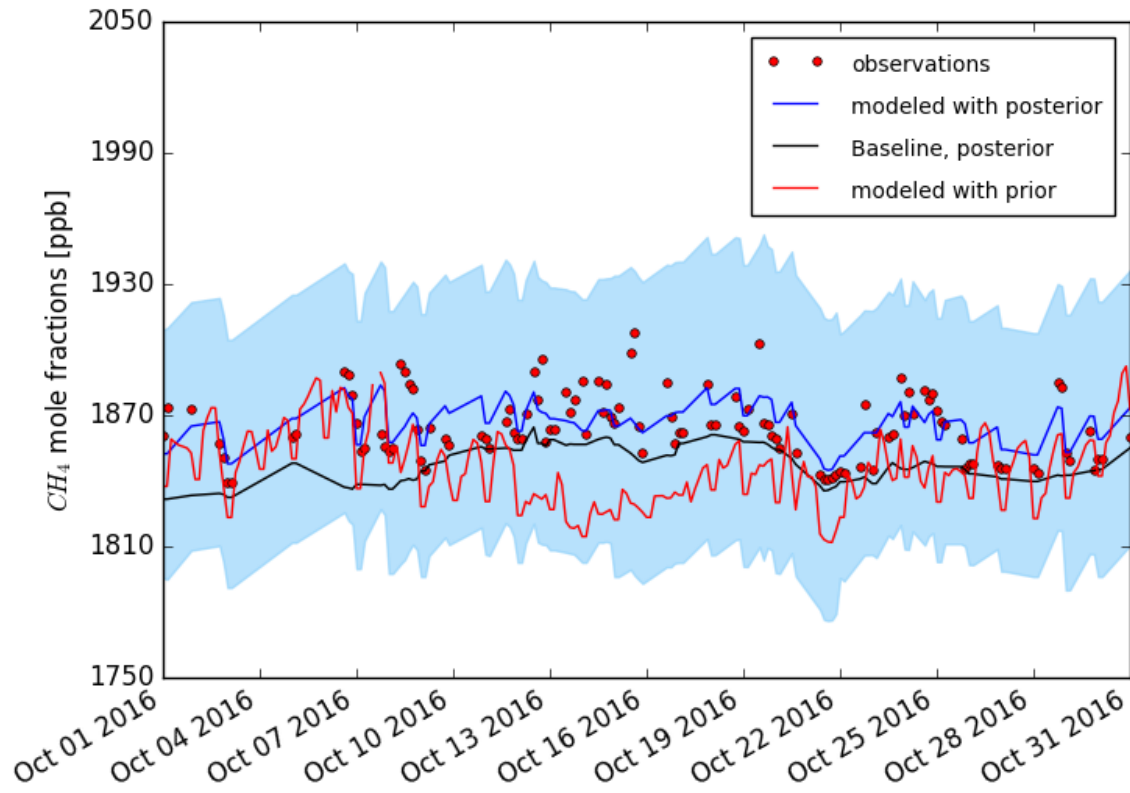


Figure 6.8: time series of optimized mole fractions (blue curve) compared to observations (red dots) and the modeled observation with prior emissions (red) with the prior (magenta) and posterior (black) baseline contribution to modeled mole fractions, for October 2016

6.3.5 Summary of methane inversion results

The Central and East African region emitted methane in the range of 1–4 Tg each month (Figure 6.9). High methane emissions were observed in December and January and in May and June, periods which correspond to the transition from the wet season to the dry season. Maximum methane emissions in May and January suggest that the water table in wetlands was transition from flooded to dry, which is optimal for methane production. Overall the total methane source from the inversion domain was 24.13 Tg (16.3–33.81 Tg) of CH_4 , a change from a prior of 25.84 Tg (15.17–53.13 Tg) of CH_4 , this is a small decrease but with 80 % uncertainty reduction.

National totals for the year 2016 are shown in Figure 6.10, the Democratic Republic of the Congo, Sudan and Tanzania were the highest methane emitters in 2016, while Rwanda and Burundi were the lowest emitters, owing to their small area.

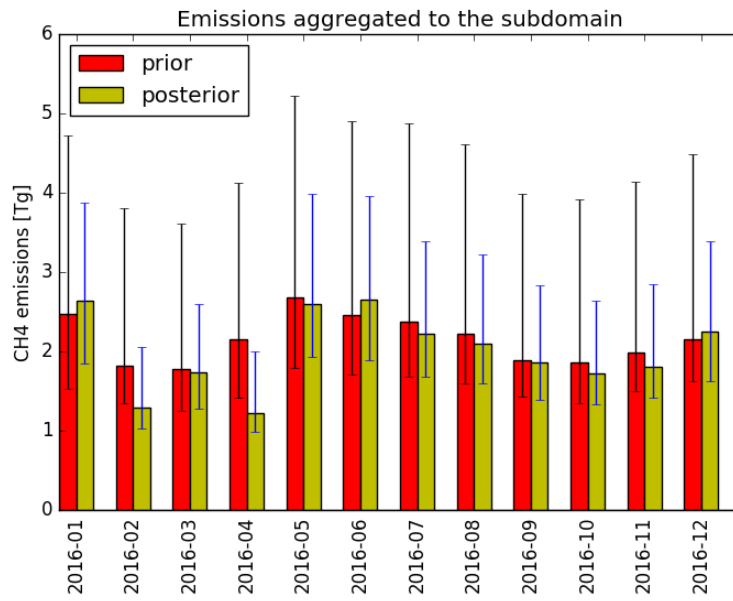


Figure 6.9: Prior and posterior monthly emissions fluxes of methane (Tg/month) estimated for the entire inversion subdomain

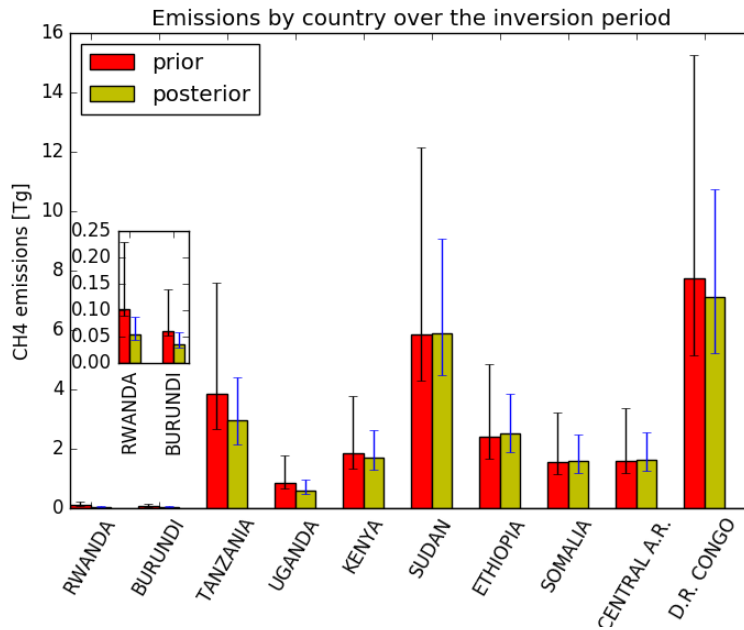


Figure 6.10: Country's prior and posterior emissions estimated for the year 2016

Chapter 7

Carbon dioxide inversion

Optimized mole fractions of carbon dioxide are estimated using the NAME model footprints and the RJMCMC methodology. This chapter outlines the prior and boundary conditions used in the inversion, the inversion setup and parameters and the inversion results.

7.1 Inversion prior

We have used CarbonTracker-CO₂, version CT2016 [Peters, Jacobson, et al. 2007, with updated documentation at <https://www.esrl.noaa.gov/gmd/ccgg/carbontracker/index.php>] emissions and mole fractions as prior and boundary conditions for the CO₂ inversion.

Terrestrial biosphere module: Carbon Tracker CO₂ version 2016 (CT2016) uses the CASA biogeochemical model to calculate carbon fluxes using input from weather models and satellite observed Normalized difference Vegetation Index (NDVI) to track plant phenology. CASA model provides monthly mean Net Primary Production (NPP) and heterotrophic respiration (R_H), NPP is the difference in photosynthetic carbon uptake, named the Gross Primary Production (GPP), and the metabolic respiration, also called the autotrophic respiration (R_A). The monthly mean Net Ecosystem Exchange (NEE) is calculated as the algebraic sum of NPP and R_H , $NEE = NPP + R_H$, carbon uptake by terrestrial biosphere is considered negative. Following the method of Olsen et al. [2004], CT2016 further downscale the monthly mean NPP and R_H calculated by CASA model to diurnal cycle by transforming NPP and R_H to GPP and total ecosystem respiration (R_E), $R_E = R_A + R_H$ where GPP is modeled as a linear function of incoming surface solar radiation and R_E as a function of near-surface temperature.

Fire emission module: The CT2016 uses the Fourth-generation Global Fire Emission Database (GFED4.1) [Giglio et al. 2013] and the Global Fire Emission Database from NASA Carbon Monitoring System (GFED_CMS). The GFED4.1 uses the ECMWF and emissions are modeled at 3-hourly interval, while the GFED_CMS uses the Modern-Era Retrospective Analysis for Research and Application (MERRA)

meteorology and emissions are available at daily resolution. Both modules use the satellite derived fire counts and vegetation cover to estimate the burned area which is then fed into the CASA model to estimate carbon dioxide emissions from fire.

Fossil fuel module: CT2016 uses two fossil fuel emissions datasets; the “Miller” dataset and the Open-source Data Inventory of Anthropogenic CO_2 (ODIAC) dataset. The Miller fossil fuel dataset extrapolates to 2016 the annual global and country totals from the Carbon Dioxide Information Analysis Center (CDIAC) [Boden et al. 2013] which extends through 2010. The extrapolation applies a percentage change for each fuel type (solid, liquid and gas) following the 2016 British Petroleum (BP) Statistical Review of World Energy for 2011–2015 [BP 2016]. The country totals are further mapped into a $1^\circ \times 1^\circ$ grid following the spacial patterns of the EDGAR database. The ODIAC fossil fuel emission uses the 2016 version of CDIAC [Boden et al. 2016] which extends up to 2013 which is then extrapolated to 2016 in the same way as the Miller dataset. Unlike the Miller dataset, The ODIAC country totals are mapped into a $1^\circ \times 1^\circ$ following the geographical location of power plants, provided by the Carbon Monitoring and Action (CARMA) and the remaining fossil fuel emissions were distributed using the nightly image collected by the U. S. Airforce Defense Meteorological Satellite Project (DMSP), while aviation emissions were mapped using flight tracks adapted from the UK Global Aircraft Emissions data project for climate change impacts evaluation (AERO2k) air emission inventory.

Oceans module: First guess air-sea exchanges for CT2016 data assimilation were taken from the climatology of direct measurement of CO_2 partial pressure in surface waters $p - CO_2$ provided by Takahashi et al. [2009], in addition, ocean inversion fluxes from Jacobson et al. [2007] were also used in order to estimate the uncertainty in the inversion.

Atmospheric transport and observations: Carbon Tracker CO_2 , version 2016 uses TM5 model and surface observations from NOAA ESRL Cooperative Global Air Sampling Network which have been already introduced in section 6.1.1.

7.1.1 Inversion domain and boundary conditions

Similar to the methane inversion, NAME model was run for the spatial domain -40 to 18 latitude North and -15 to 55 longitude East. The TDMCMC inversion sub-domain was bounded by -14.3 and 12.2 latitude and 15.3 and 49.4 longitude. For boundary conditions we have used the gridded mole fractions provided by the near real-time Carbon Tracker, version 2016. For CO_2 inversion, the model-data mismatch was set to be uniformly distributed between 1–20 ppm, while other parameters where the same as the CH_4 inversion that were presented in section 6.2.3 and Table 4.1.

7.1.2 Modeling the diurnal cycle of CO_2

Biogenic fluxes of CO_2 to the atmosphere are largely composed by the photosynthetic CO_2 uptake by plants also termed the Gross Primary Production (GPP), the release of CO_2 due to metabolic respiration of living plants also called the autotrophic respiration (R_A) and the release of CO_2 due to decomposition of organic matter in soil, the heterotrophic respiration (R_H). From the atmospheric measurement perspective, we see the net algebraic sum of all those fluxes, the Net Ecosystem Exchange (NEE). The NEE is a relatively small value with a global total of a few petagrams of carbon per year compared to the individual fluxes of about 120 PgC per year in both ways [Carbon Tracker 2016].

Our NAME setup only allowed time-integrated (30 day) footprints to be stored. Therefore, the impact of sub-monthly variations in flux on modeled mole fractions was not included in our simulation. Given that CO_2 flux has very large diurnal cycle, it is likely that its omission from our setup will lead to biases. In future, this will be corrected by storing time-resolved NAME footprints.

To partially mitigate this shortcoming of our model setup, we have used the daily average fluxes and boundary conditions as proxy for the anthropogenic CO_2 fluxes plus the Net Ecosystem Exchange, which is, in fact, what drives the trend in measured mole fractions at given location. The CO_2 inversion could be improved by using the time-resolving footprints.

7.2 CO_2 inversion results

Results for carbon dioxide inversion for each month of 2016 can be found in the appendix B. Here we show sample results and highlight major findings.

7.2.1 Uncertainty reduction map and footprints

Figure 7.1 shows the uncertainty reduction map for carbon dioxide for February 2016 and the corresponding footprint. The equation of the likelihood function (equation 4.19) indicates that the sensitivity is proportional to the product of the footprint and the emission flux. We, therefore, see high sensitivity to the measurements in the regions of high values of the footprints or in the regions of high emission fluxes. During February 2016, the measurements were most sensitive to emissions from Tanzania and the Democratic republic of the Congo and significantly sensitive to emissions from Kenya, Uganda and Somalia.

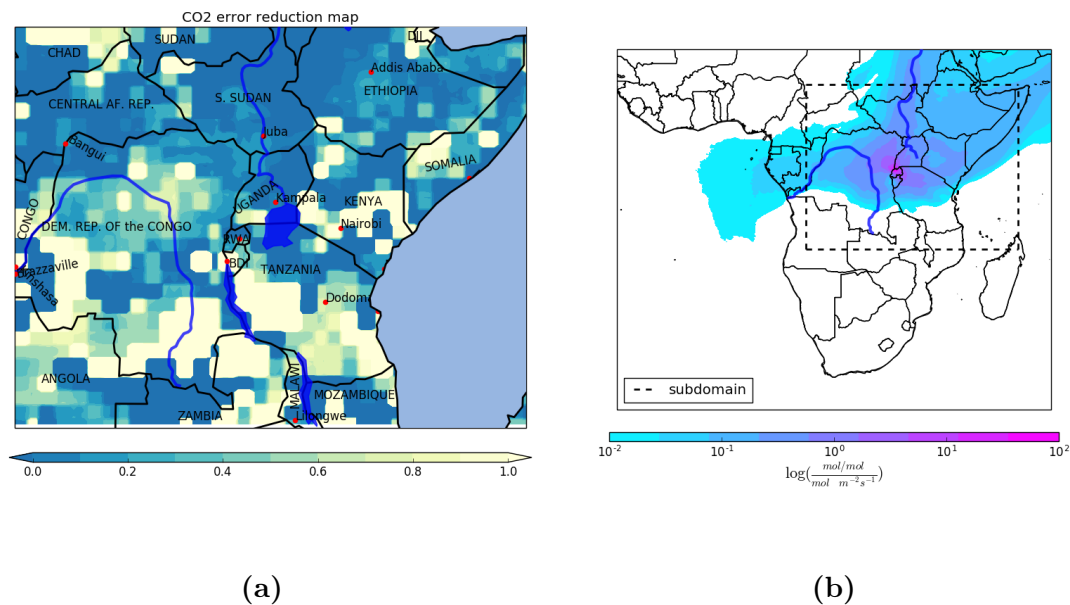
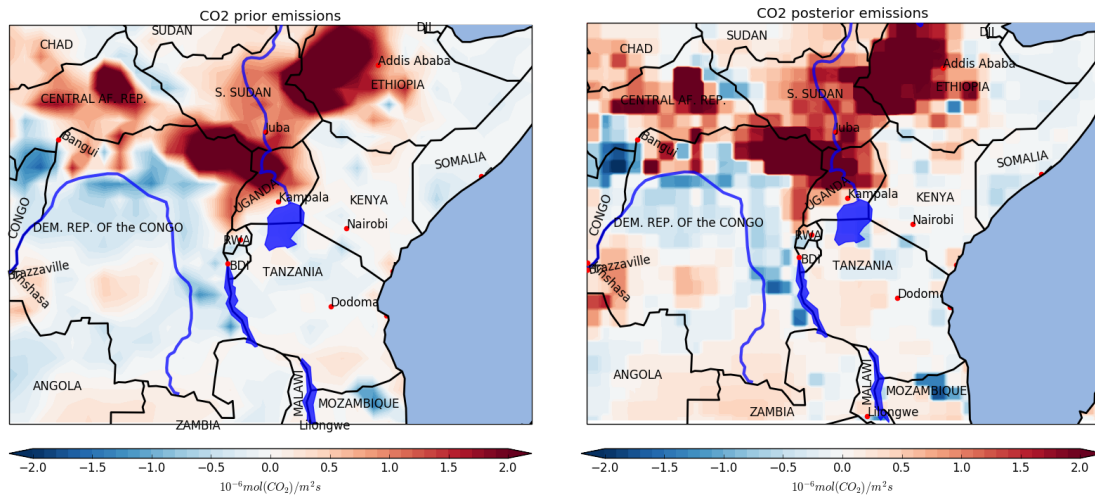


Figure 7.1: Uncertainty reduction map (a) and footprint (note the log scale) (b) for February 2016. The extent of the map in (a) is highlighted with a broken line in the footprint map

7.2.2 Prior and posterior emissions

CO_2 prior and posterior emissions in Eastern and central Africa are largely driven by biogenic emissions. The northern part of the inversion subdomain which includes northern Democratic Republic of Congo, Central African Republic, Southern Chad, South Sudan, South of the Republic of Sudan (North Sudan), and Ethiopia are a net source of atmospheric CO_2 during the short dry season, mostly due to biomass burning and reduced photosynthesis. During this time, the central part of the inversion sub-domain was a net sink of CO_2 to the atmosphere. Figure 7.2 illustrates that the posterior emissions have the same spatial emission distribution as the prior with a significant source of CO_2 in the northern part of Central Africa.



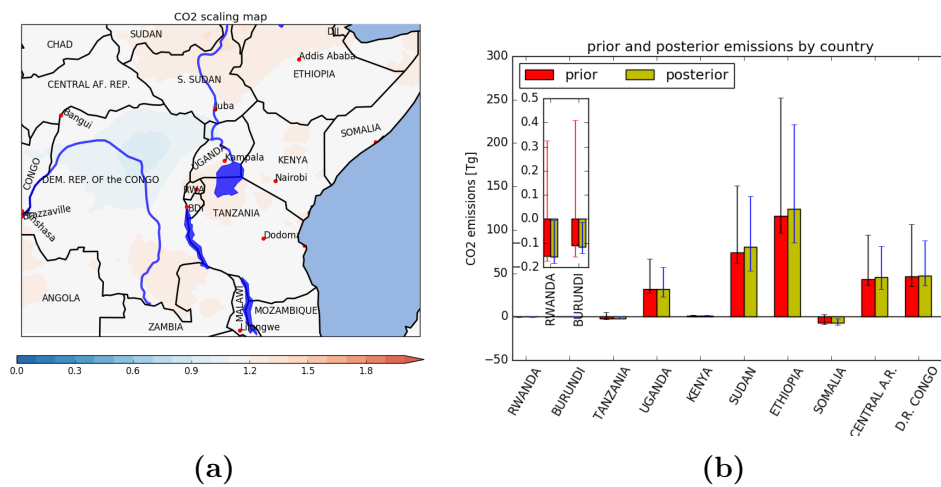
(a)

(b)

Figure 7.2: CO_2 prior (a) and posterior (b) emissions for February 2016

7.2.3 Emissions scaling factors and country totals

Ethiopia and South Sudan (Figure 7.3b) were the largest net source of CO_2 in February 2016. The posterior emissions were slightly higher than the prior emissions for those two countries. The map of posterior over prior emissions (Figure 7.3a) points to increased emissions with respect to the prior along the southern boundary of the inversion sub-domain which is part of Angola and Zambia and reduced prior emissions in the central Democratic Republic of the Congo



(a)

(b)

Figure 7.3: Prior scaling maps (a) and countries emissions totals (b) for February 2016

7.2.4 Forward run with optimized CO_2 emissions

Time series of observed mole fractions of CO_2 , modeled mole fractions with prior and posterior emissions as well as the modeled baseline are depicted in Figure 7.4 for March 2016 and Figure 7.5 for October 2016. The large variability in modeled mole fractions is due to lack of sufficient observations to constrain the inversion because we have used only daily averages. During March and October the net contribution of the inversion subdomain to the measured mole fractions was so small that most of variability in the measured mole fractions were due to the contribution from the boundaries.

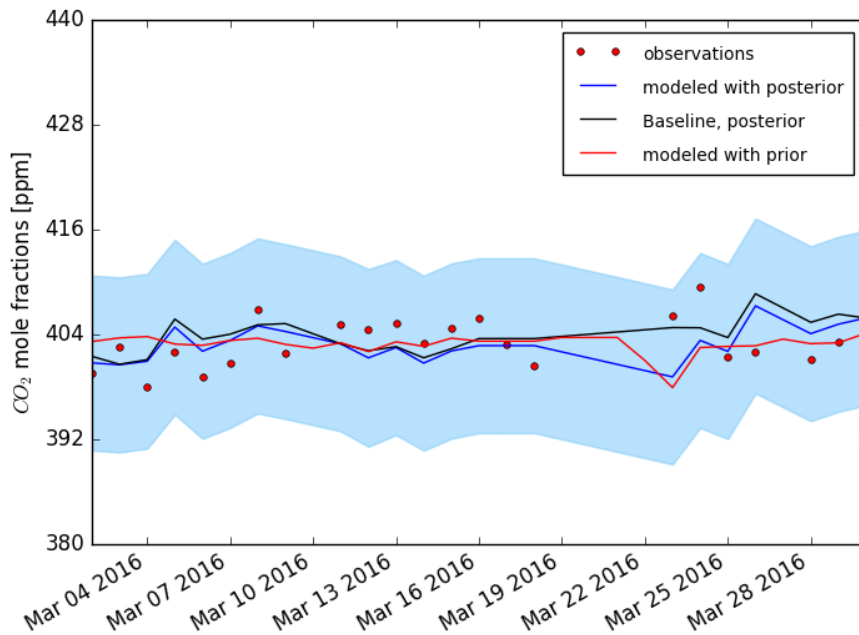


Figure 7.4: time series of optimized mole fractions (blue curve) compared to observations (red dots) and the modeled observation with prior emissions (red) with the posterior baseline (black) contribution to modeled mole fractions, for March 2016

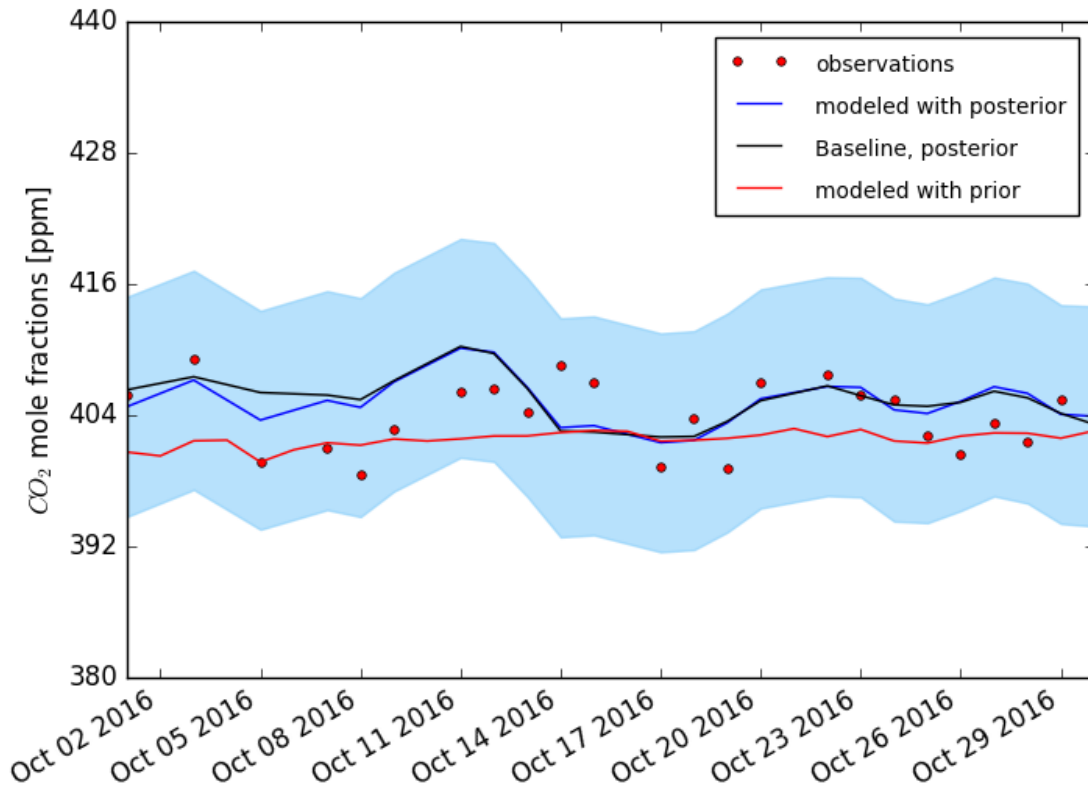


Figure 7.5: time series of optimized mole fractions (blue curve) compared to observations (red dots) and the modeled observation with prior emissions (red) with the posterior baseline (black) contribution to modeled mole fractions, for October 2016

7.2.5 Summary of CO_2 inversion

The Eastern and Central African region was a net source of 139.77 Tg of CO_2 (147.54 Tg prior) during the year 2016. Figure 7.6 indicates that the Democratic Republic of Congo was the largest net source of CO_2 with a net emission of 325.3 Tg of CO_2 while South Sudan was the single largest net sink of CO_2 whose magnitude was estimated to -213.4 Tg of CO_2 .

Figure 7.7 points out that the inversion subdomain was a net sink of CO_2 in May, June, August, September and October, and a net source the rest of the year. Whether a country is a net source or sink of CO_2 largely depends on seasonal cycle of precipitations; most countries in northern part of the domain (Central African Republic, South Sudan, Ethiopia, Uganda) are a net sink of CO_2 around August, September and October. Countries in the more southern part of the inversion domain (D. R. Congo, Rwanda, Tanzania) are net CO_2 source during northern Summer because precipitations are localized more to the North following

ITCZ and the South part is under intense biomass burning.

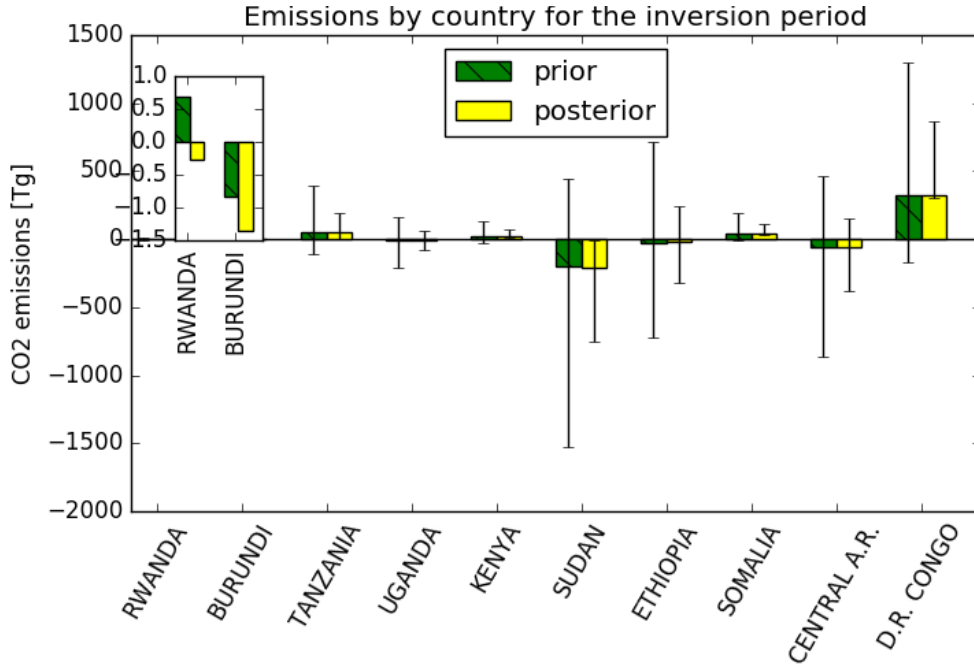


Figure 7.6: Net prior and posterior CO_2 emissions fluxes by country for 2016

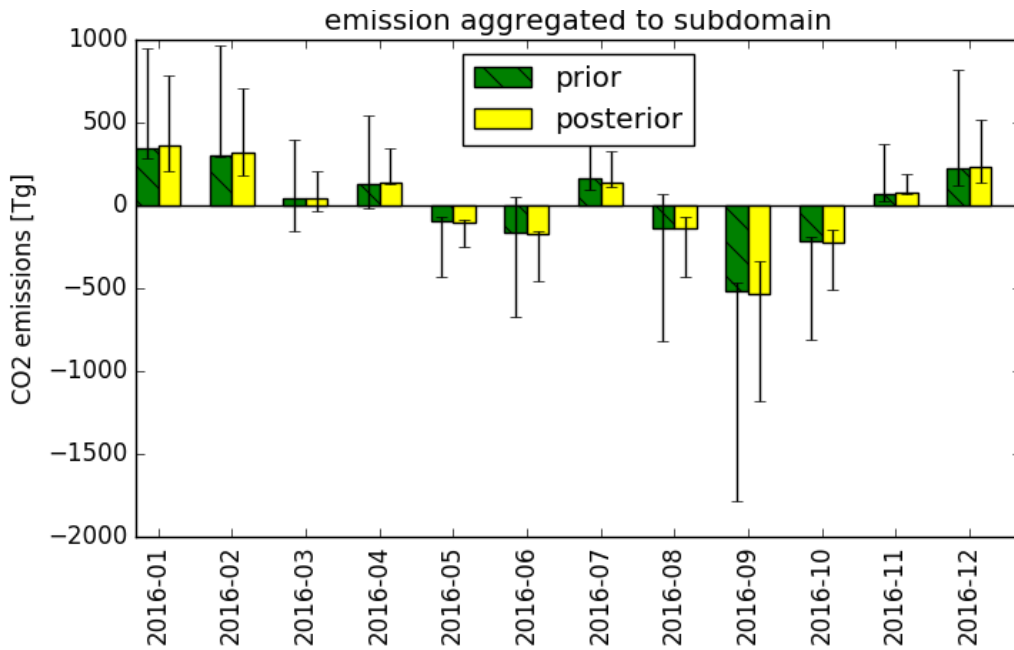


Figure 7.7: Net prior and posterior CO_2 monthly emissions fluxes within the inversion subdomain

Conclusions and way forward

Conclusions

We have set up a high frequency greenhouse gases monitoring station in the Volcanic region of North West Rwanda at Mount Mugogo, which is the first and, currently, the only one in tropical Africa. The station currently measures carbon dioxide, methane, nitrous oxide, black carbon, ozone and meteorological parameters. The Advanced Global Atmospheric Gases Experiment (AGAGE), which the station is part now of, regularly performs intercomparisons between AGAGE data and other networks, especially the National Oceanic and Atmospheric Administration (NOAA), Global Monitoring Division. The data that is being measured at Mt. Mugogo has, therefore, internationally recognized calibrations standards and protocols; this is what makes it useful for global and regional inverse studies and calibration of remotely sensed measurements among others.

Time series of measured atmospheric mole fractions of carbon dioxide exhibit a seasonal cycle, with significant enhancements observed around February and August, the short and long dry seasons respectively. Observed enhancements of CO_2 mole fractions, which corresponds to increased black carbon and carbon monoxide concentrations, are caused by regional scale biomass burning which happens seasonally in Northern parts of Central Africa in December, January and February, and in Central to Southern Africa during June, July and August.

Time series of atmospheric mole fractions of methane indicate increased methane concentration during the short dry season of December-January-February, but not in the long dry season. We propose that the methane increase in the short dry season is due to advection of methane-rich Northern Hemisphere air masses to Mount Mugogo during the seasonal shift of the inter tropical convergence zone.

Inverse estimation of surface fluxes of methane have found that the region was a source of 41.54 Tg of CH_4 during the year 2016, a 60 % increase from the prior emissions of 25.84 Tg. Highest regional emissions were found in May, October and November. A significant fraction of emissions were coming from Northern parts of the inversion domain Africa, namely, South Sudan, Ethiopia and Somalia. The Democratic Republic of Congo and Tanzania were also the highest emitter in Central Africa while Rwanda and Burundi have smallest methane

emissions.

We have found that Eastern and Central Africa was a net source of CO_2 during 2016 with an estimated amount of 147–477 Tg of CO_2 . With the Highest emissions happening in December-January-February a time when large scales biomass burning occur in the Northern regions of inversion domain. Likewise, the region is a net sink of CO_2 during the time when the Northern regions are in the rain season.

The estimated fluxes constitute additional data for comparison and cross-checking global inversion studies, calibration of ecosystem models and for regional emissions verification.

Limitations and future research

Mount Mugogo is a good location for regional scale research. Given the quality of instruments and the increasing number of parameters that are measured at Mt. Mugogo, it would serve better the science and policy community if it were relocated to a more remote location where pollution from nearby sources is minimal. Mount Karisimbi, an extinct volcano 20 km away from Mugogo, has been proposed as a potential global site that would significantly improve the quality of the data and increase the geographical extent of the station footprint.

Prescribed meteorological parameters can be a major source of uncertainty in inverse studies, because the current computational resources would not allow us to perturb the four-dimensional field of meteorological parameters within a chemistry transport models. The uncertainty in wind speed and directions in chemistry transport model is expected to be larger in Africa due to scarcity of meteorological observations that feed into global numerical weather prediction models. An assessment of common reanalysis meteorology as they compare to actual observations in a large domain in Africa would provide some insight to the magnitude of the uncertainty.

A more complete regional study would incorporate nearest measurements from NOAA flask stations and satellite column observations. This was not possible for our work which was a near “real-time” measurements and inversion, while scientific measurements tend to come within a one year time lag. This work can be completed and extended by incorporating all available observations within the region.

Carbon dioxide inversion can be improved by using footprints that store time information. This would allow the NAME model to accurately capture the diurnal cycle of carbon dioxide, allowing to run the inversion at a higher frequency (few hours) than the daily average we have used for this work.

Appendices

A CH_4 Inversion results

A.1 Results for January 2016

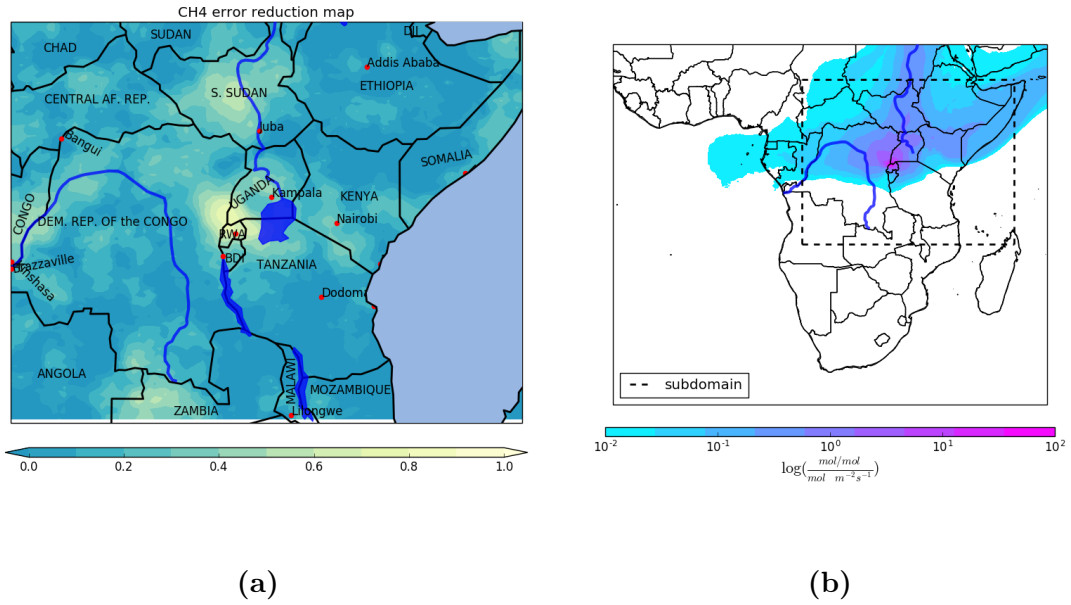


Figure A.1: Error reduction map (a) and footprint (note the log scale) (b) for January 2016. The extent of the map in (a) is highlighted with a broken line in the footprint map

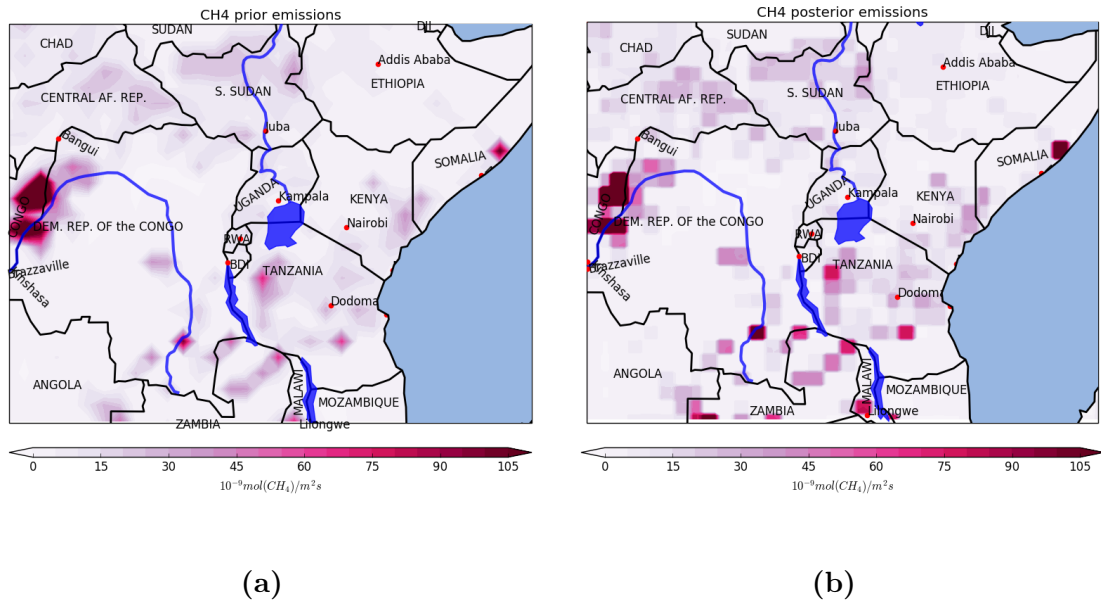
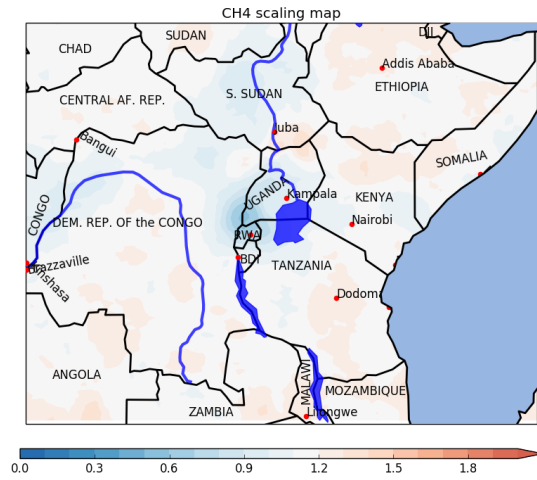
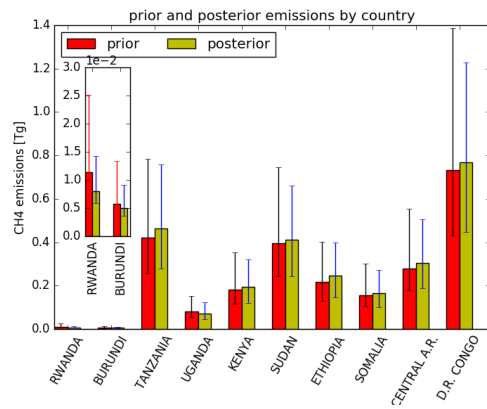


Figure A.2: CH_4 prior (a) and posterior (b) emissions for January 2016



(a)



(b)

Figure A.3: Prior scaling maps(a) and countries emissions totals(b) for January 2016

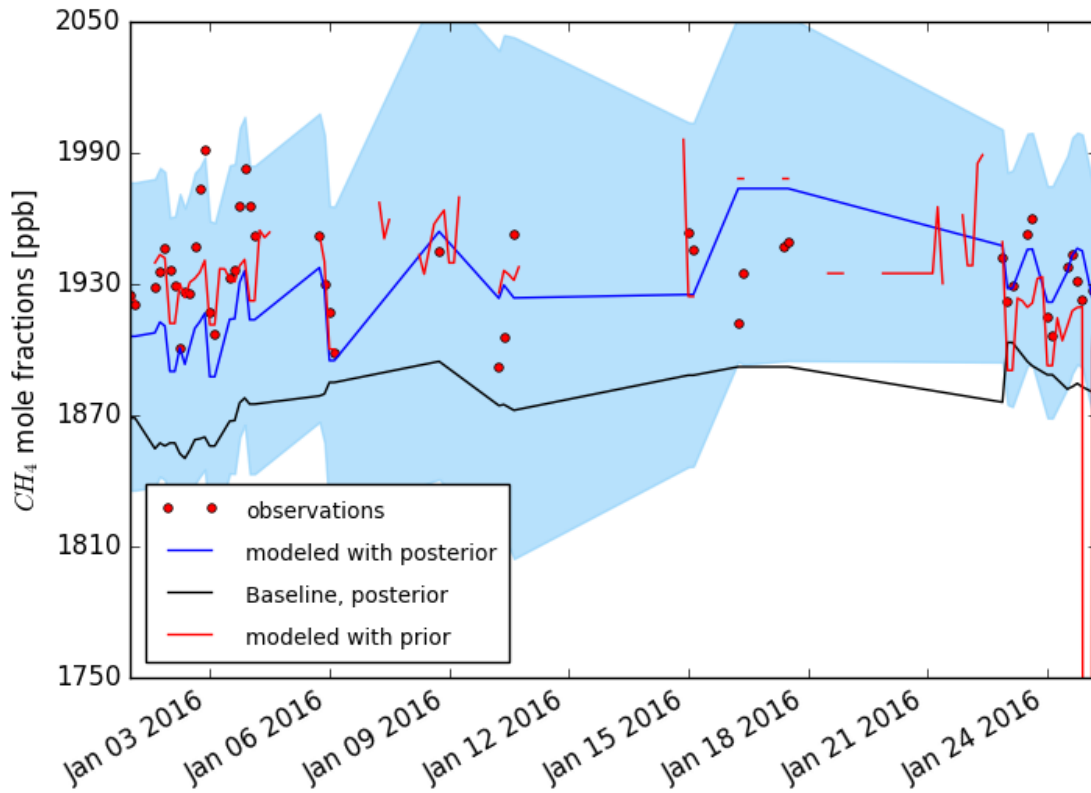


Figure A.4: Time series of optimized mole fractions (blue curve) compared to observations (red dots) and the modeled observation with prior emissions (red) with the prior (magenta) and posterior (black) baseline contribution to modeled mole fractions, for January 2016

A.2 Results for February 2016

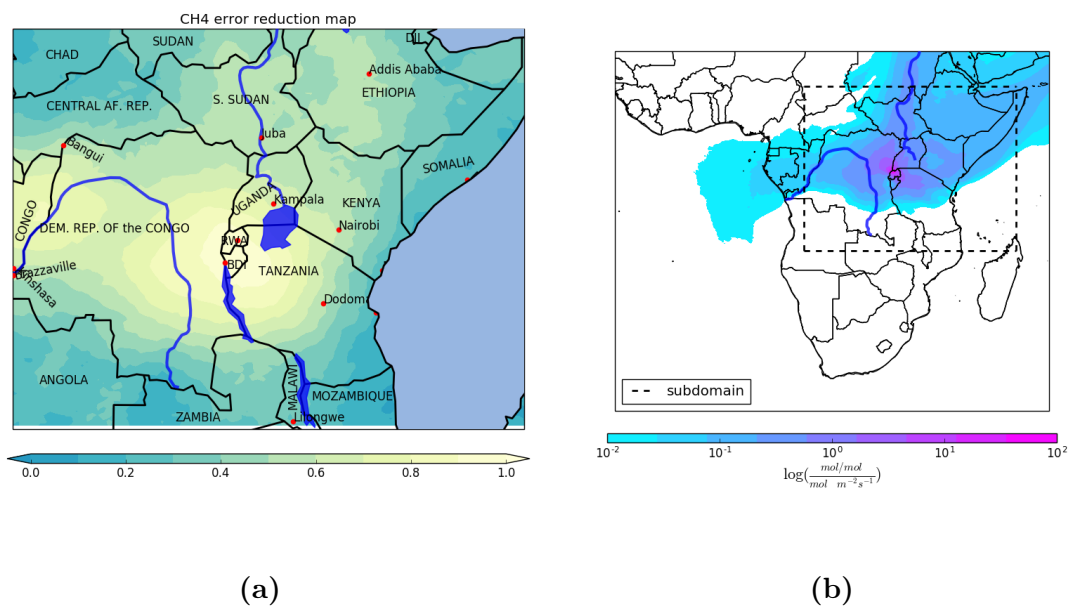


Figure A.5: Error reduction map (a) and footprint (note the log scale) (b) for February 2016. The extent of the map in (a) is highlighted with a broken line in the footprint map

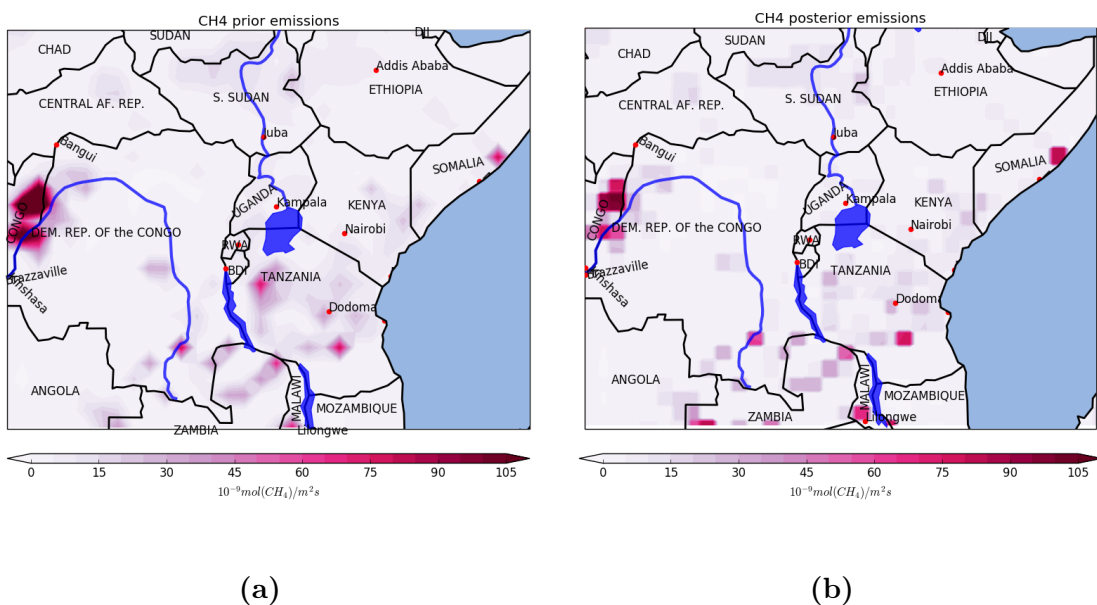
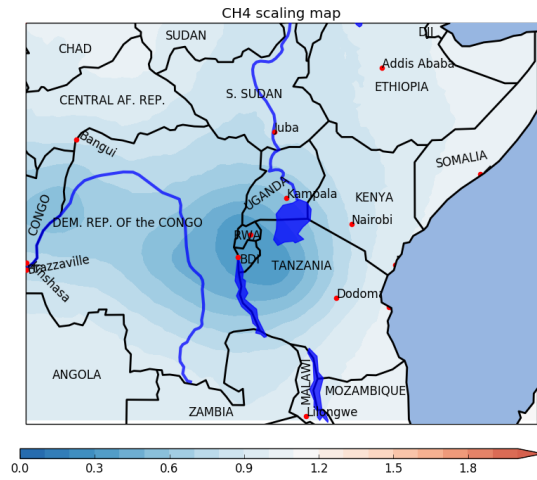
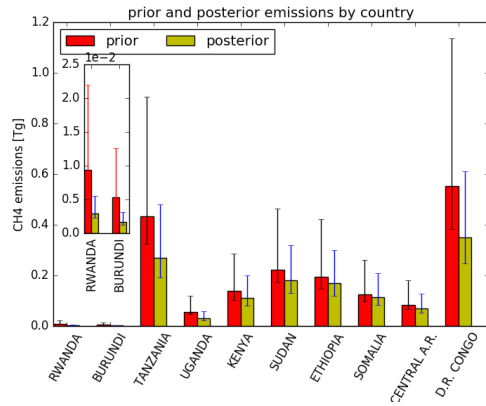


Figure A.6: CH_4 prior (a) and posterior (b) emissions for February 2016



(a)



(b)

Figure A.7: Prior scaling maps(a) and countries emissions totals(b) for February 2016

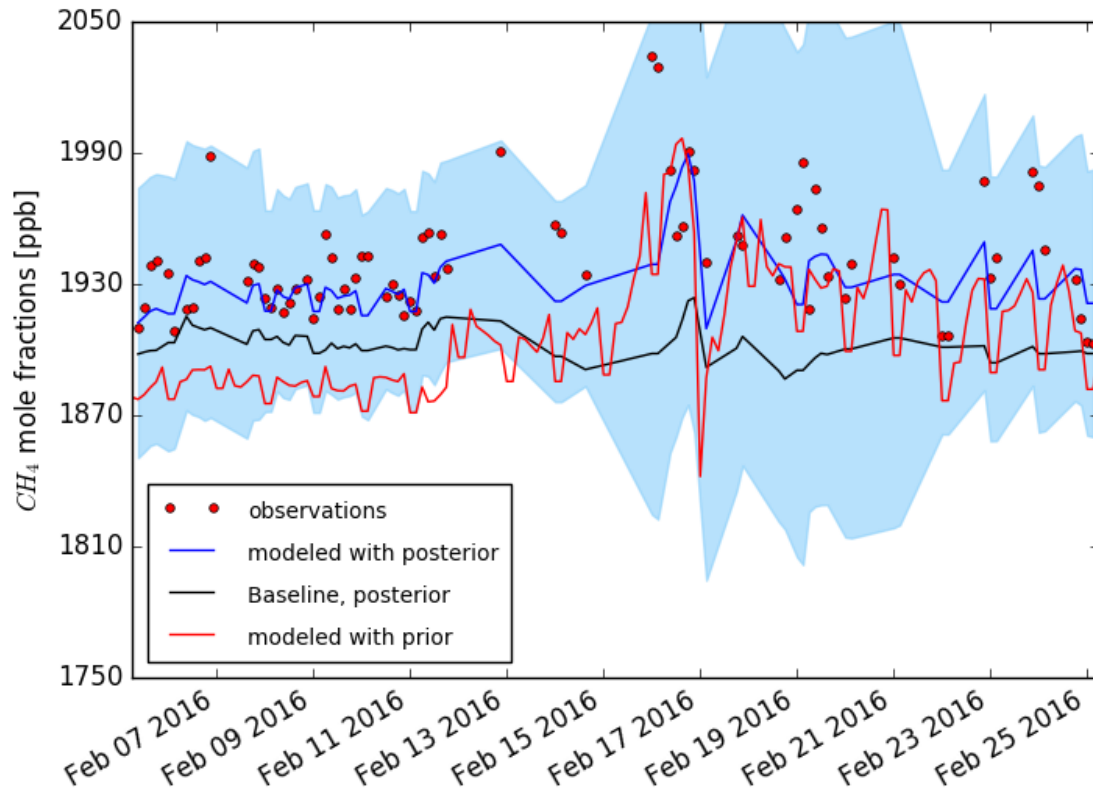


Figure A.8: Time series of optimized mole fractions (blue curve) compared to observations (red dots) and the modeled observation with prior emissions (red) with the prior (magenta) and posterior (black) baseline contribution to modeled mole fractions, for February 2016

A.3 Results for March 2016

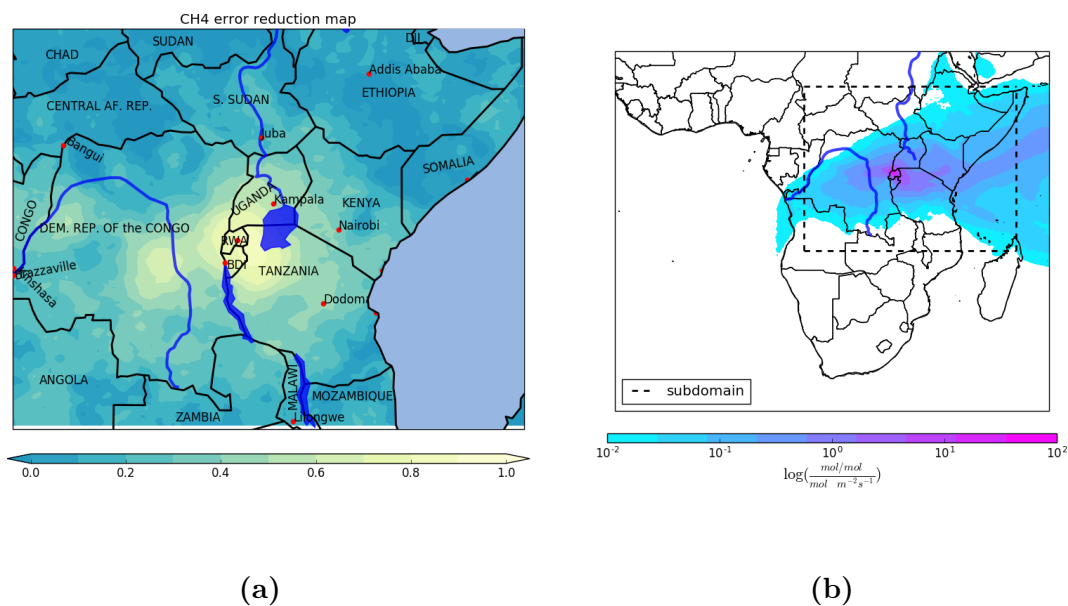


Figure A.9: Error reduction map (a) and footprint (note the log scale) (b) for March 2016. The extent of the map in (a) is highlighted with a broken line in the footprint map

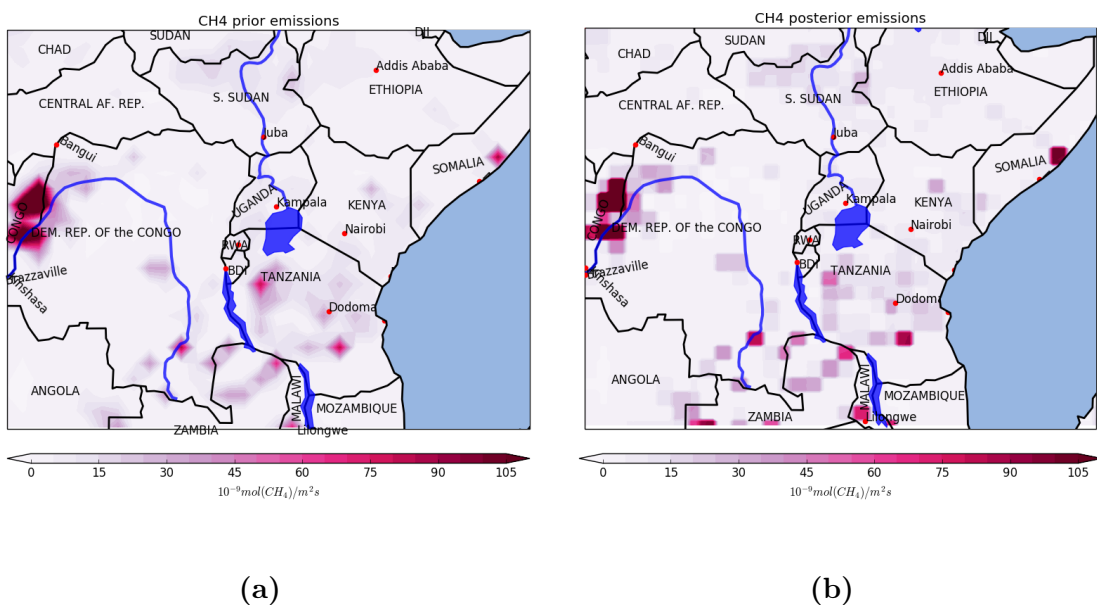
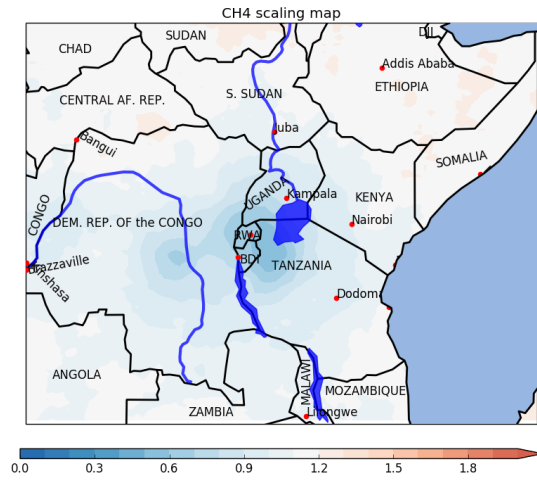
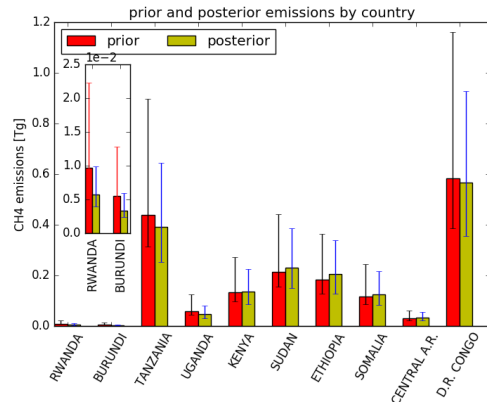


Figure A.10: CH_4 prior (a) and posterior (b) emissions for March 2016



(a)



(b)

Figure A.11: Prior scaling maps(a) and countries emissions totals(b) for March 2016

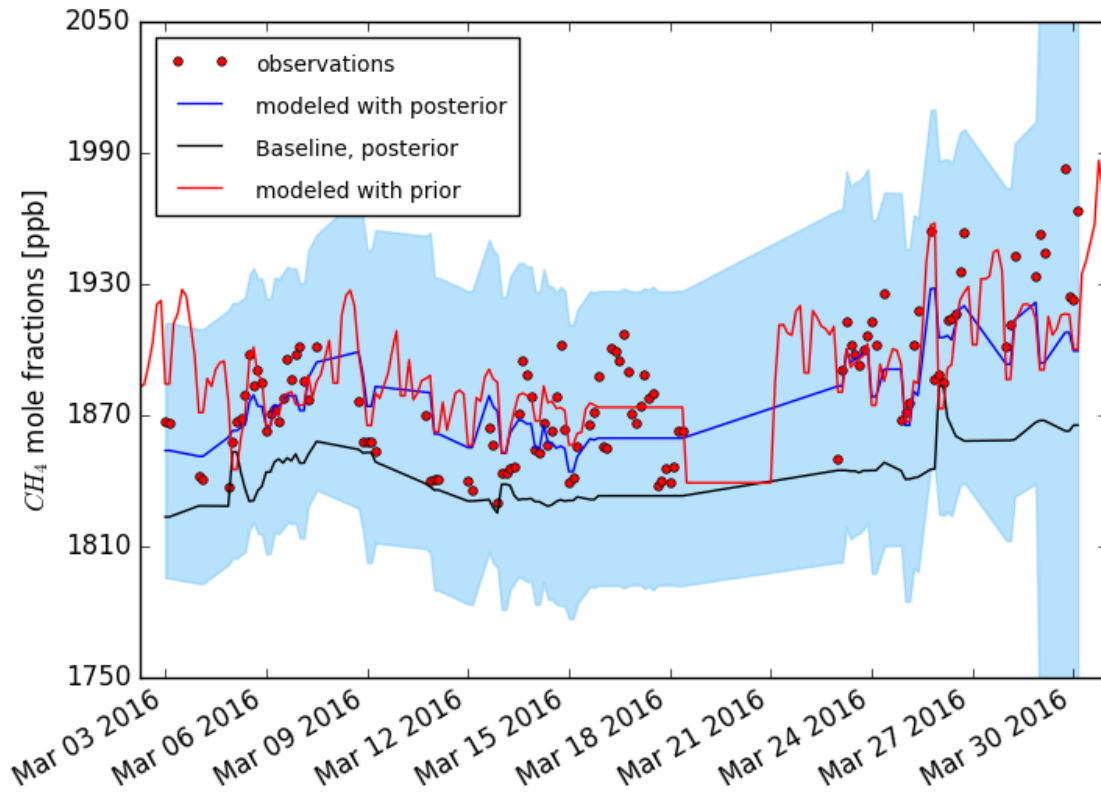


Figure A.12: Time series of optimized mole fractions (blue curve) compared to observations (red dots) and the modeled observation with prior emissions (red) with the prior (magenta) and posterior (black) baseline contribution to modeled mole fractions, for March 2016

A.4 Results for April 2016

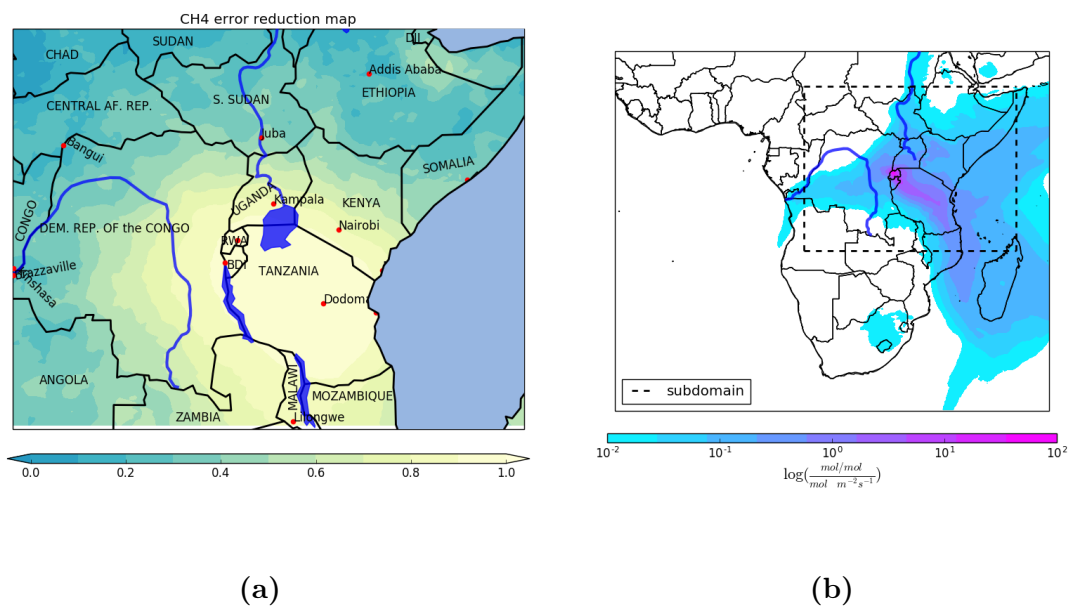


Figure A.13: Error reduction map (a) and footprint (note the log scale) (b) for April 2016. The extent of the map in (a) is highlighted with a broken line in the footprint map

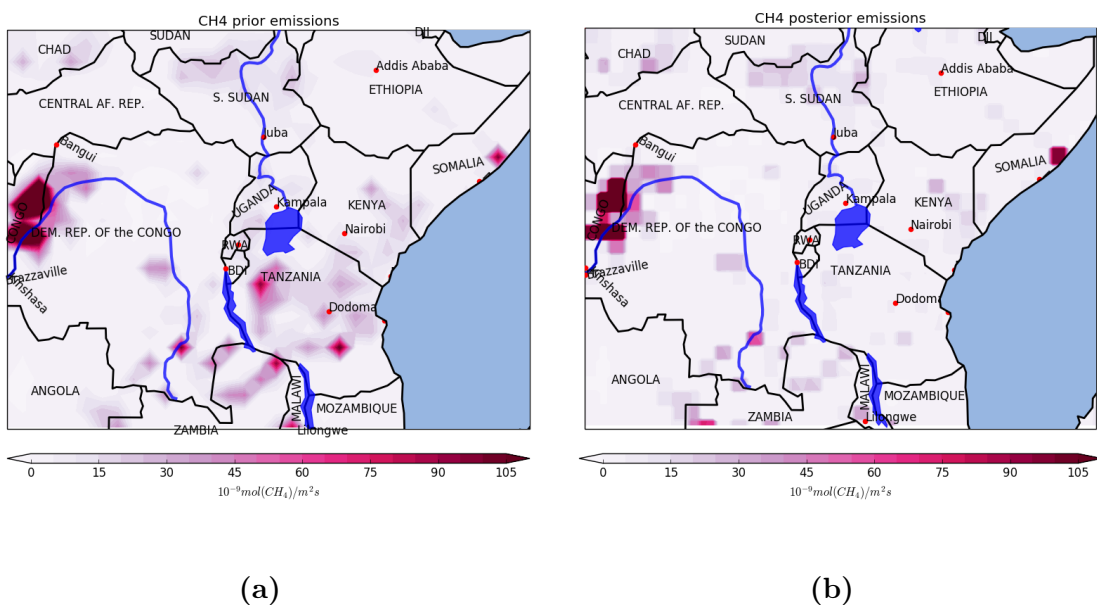
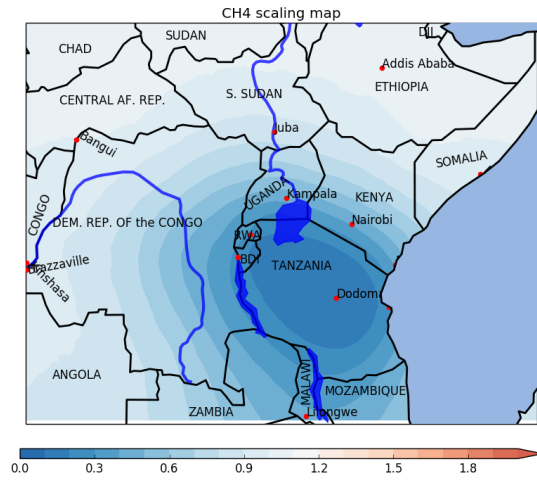
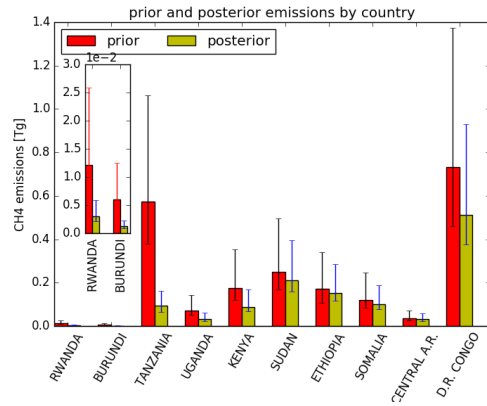


Figure A.14: CH_4 prior (a) and posterior (b) emissions for April 2016



(a)



(b)

Figure A.15: Prior scaling maps(a) and countries emissions totals(b) for April 2016

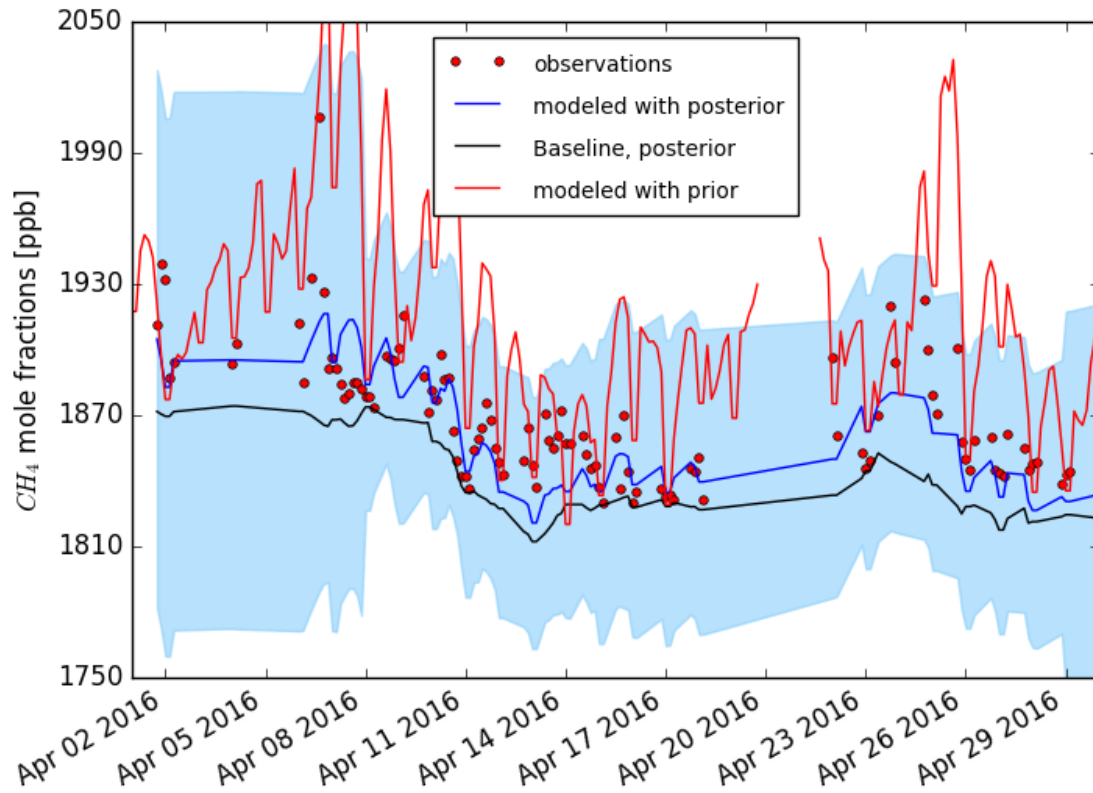


Figure A.16: Time series of optimized mole fractions (blue curve) compared to observations (red dots) and the modeled observation with prior emissions (red) with the prior (magenta) and posterior (black) baseline contribution to modeled mole fractions, for April 2016

A.5 Results for May 2016

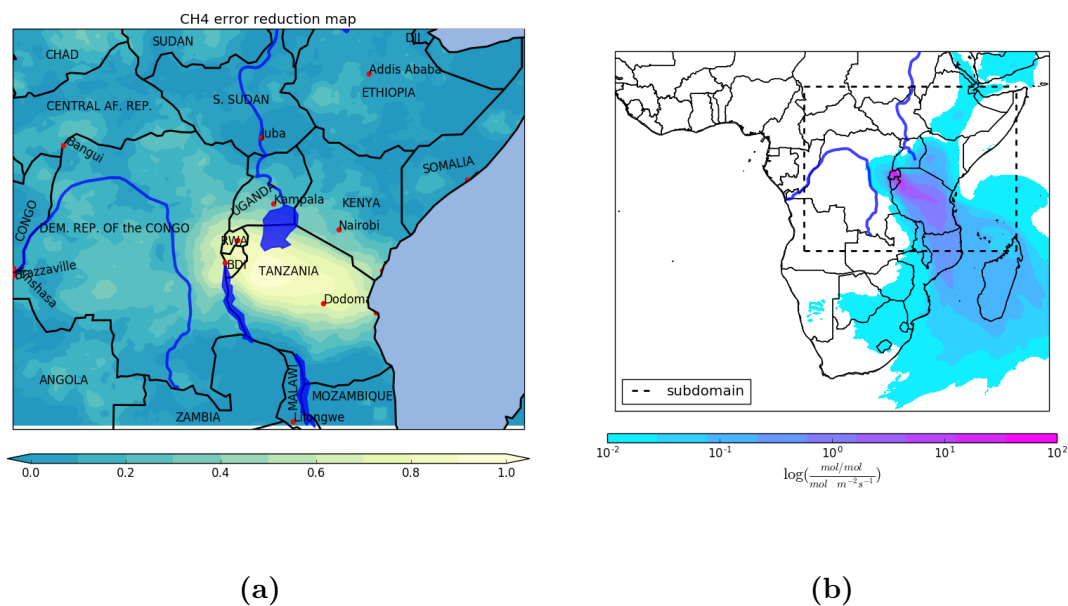


Figure A.17: Error reduction map (a) and footprint (note the log scale) (b) for May 2016. The extent of the map in (a) is highlighted with a broken line in the footprint map

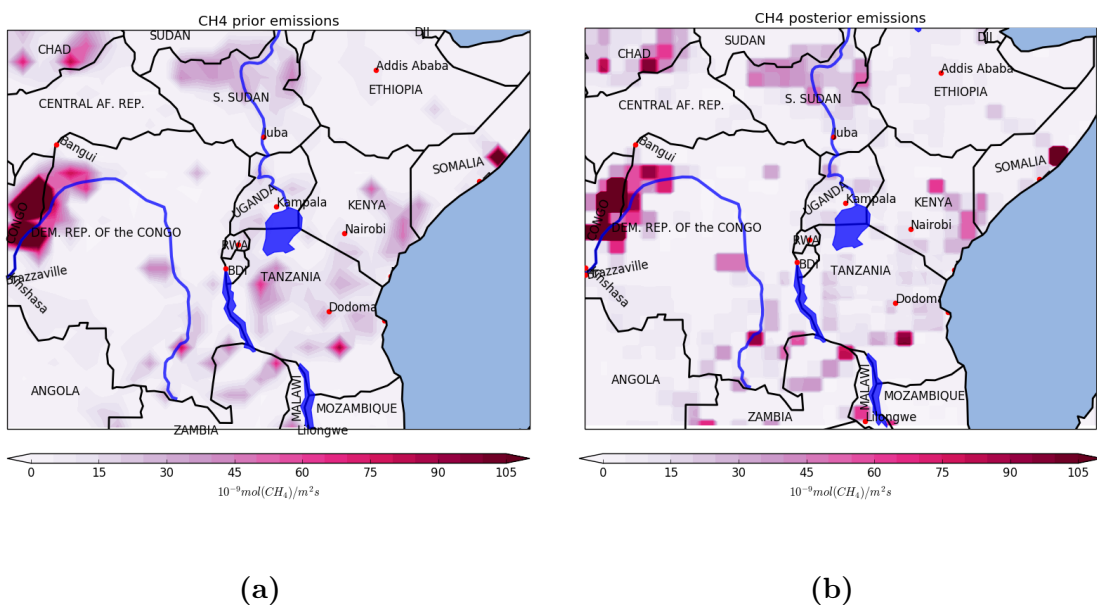
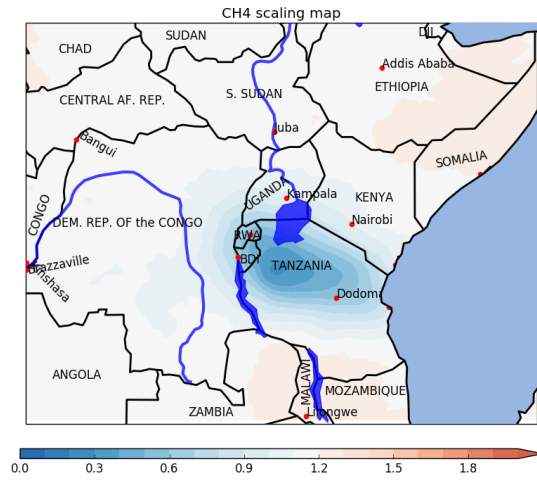
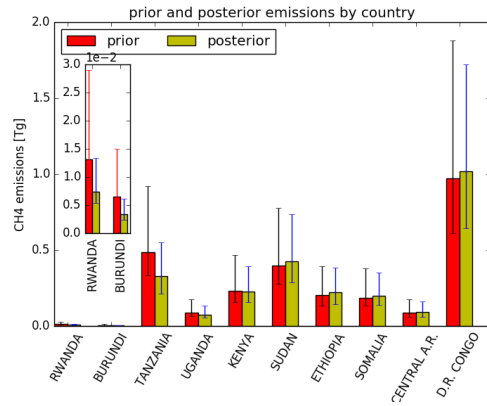


Figure A.18: CH_4 prior (a) and posterior (b) emissions for May 2016



(a)



(b)

Figure A.19: Prior scaling maps(a) and countries emissions totals(b) for May 2016

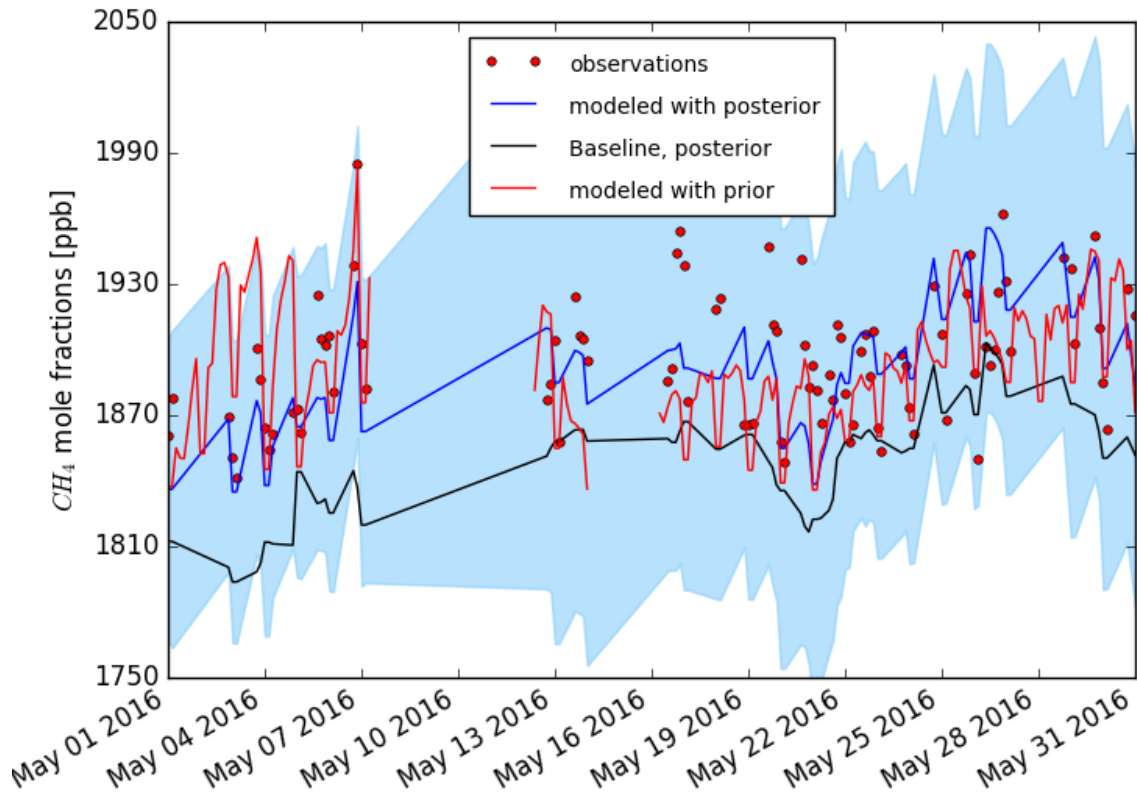


Figure A.20: Time series of optimized mole fractions (blue curve) compared to observations (red dots) and the modeled observation with prior emissions (red) with the prior (magenta) and posterior (black) baseline contribution to modeled mole fractions, for May 2016

A.6 Results for June 2016

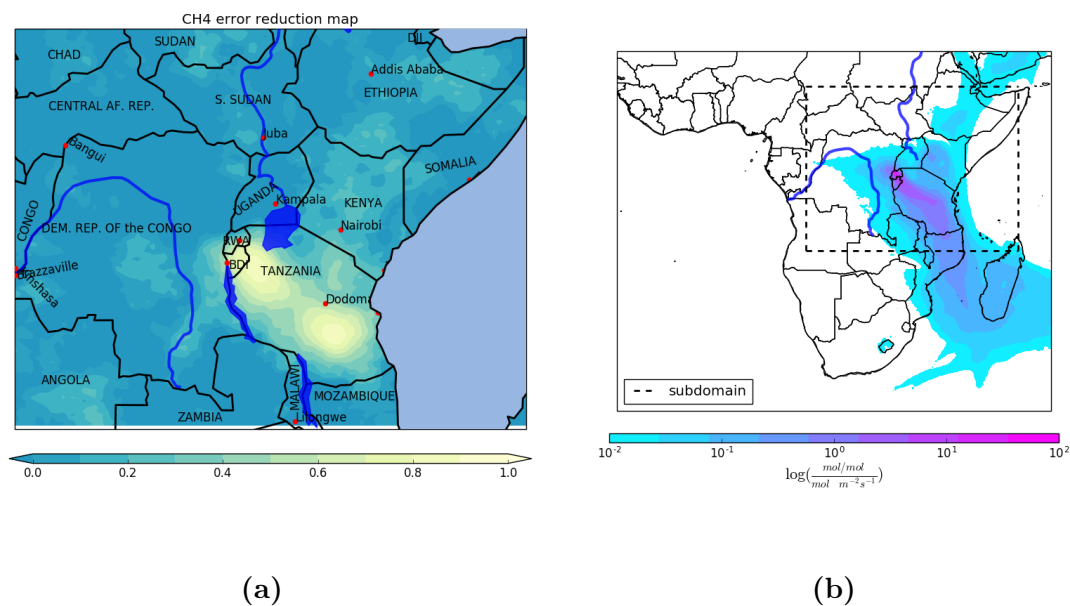


Figure A.21: Error reduction map (a) and footprint (note the log scale) (b) for June 2016. The extent of the map in (a) is highlighted with a broken line in the footprint map

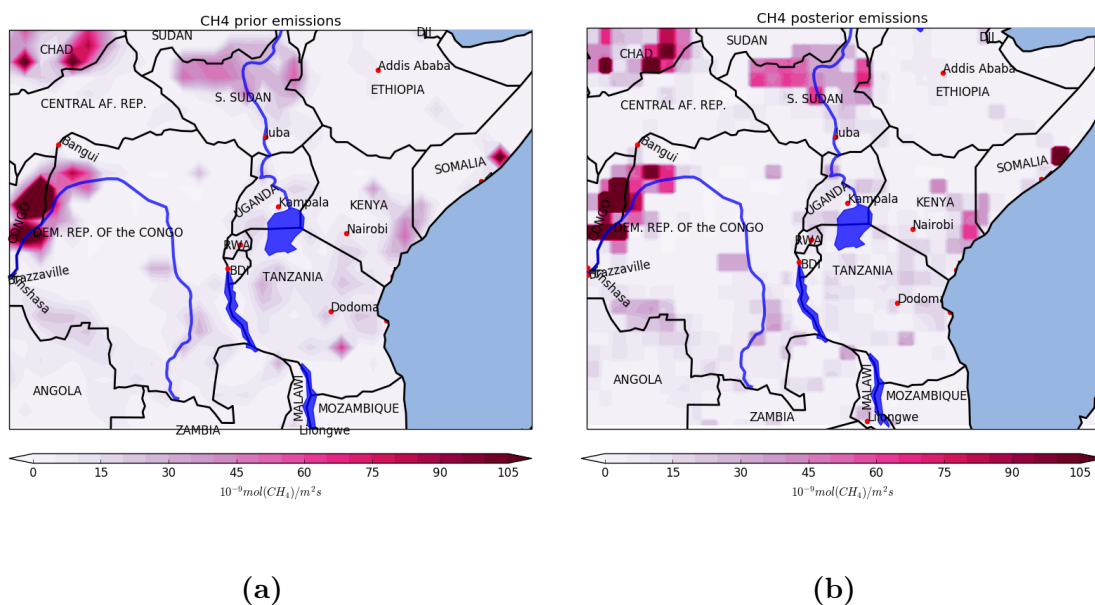
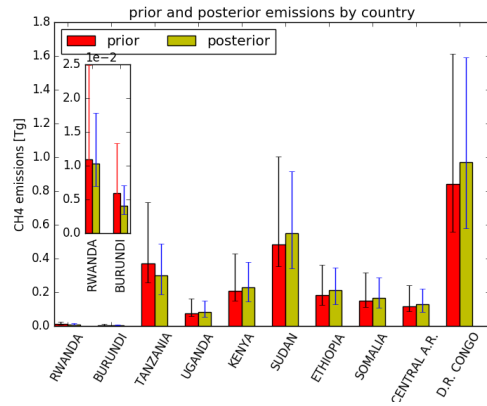
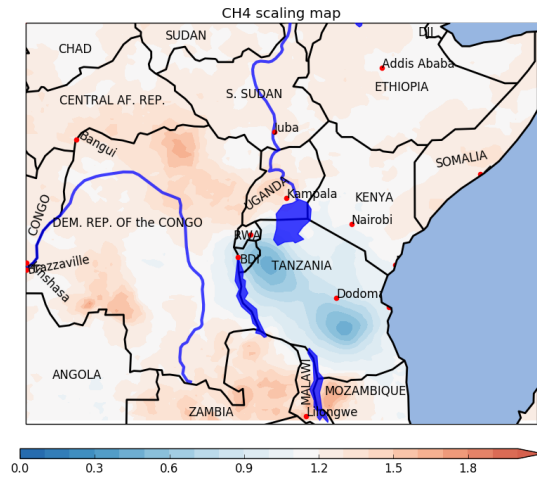


Figure A.22: CH_4 prior (a) and posterior (b) emissions for June 2016



(a)

(b)

Figure A.23: Prior scaling maps(a) and countries emissions totals(b) for June 2016

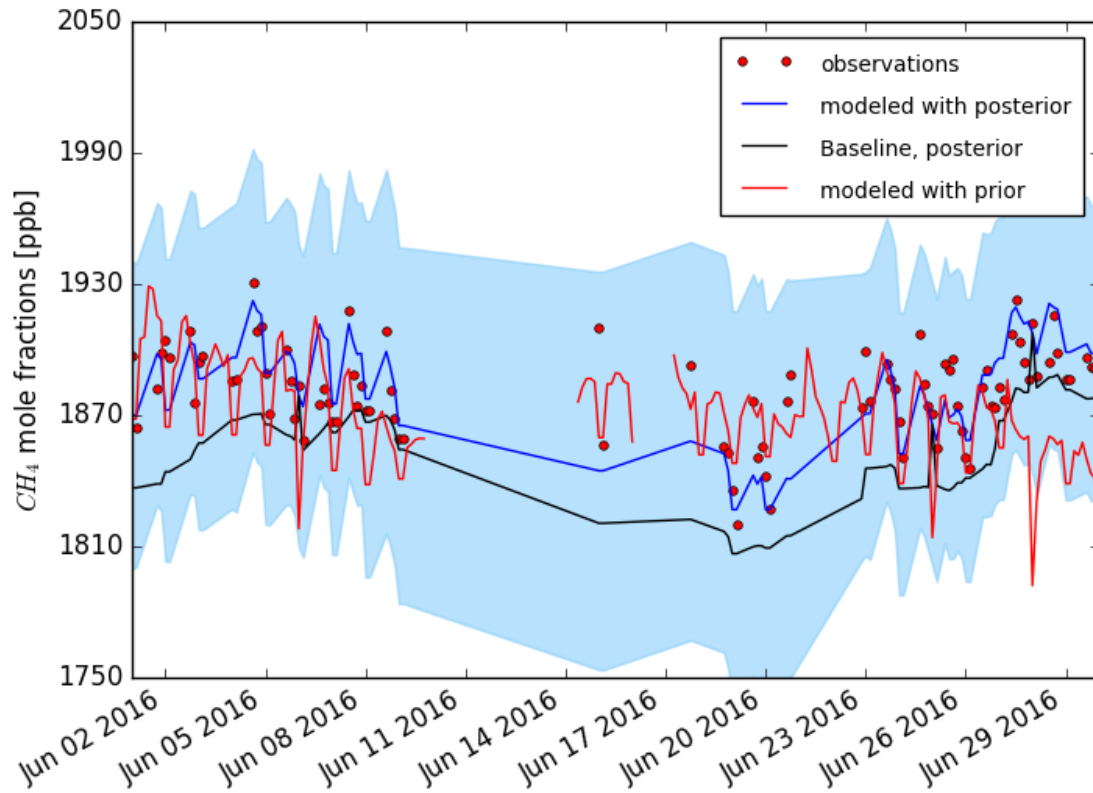


Figure A.24: Time series of optimized mole fractions (blue curve) compared to observations (red dots) and the modeled observation with prior emissions (red) with the prior (magenta) and posterior (black) baseline contribution to modeled mole fractions, for June 2016

A.7 Results for July 2016

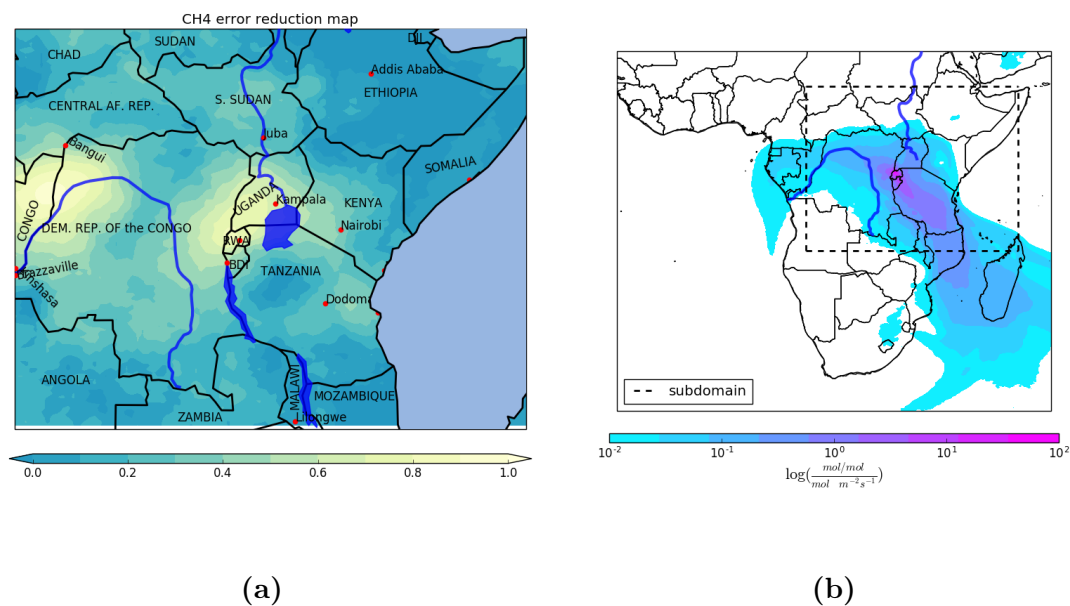


Figure A.25: Error reduction map (a) and footprint (note the log scale) (b) for July 2016. The extent of the map in (a) is highlighted with a broken line in the footprint map

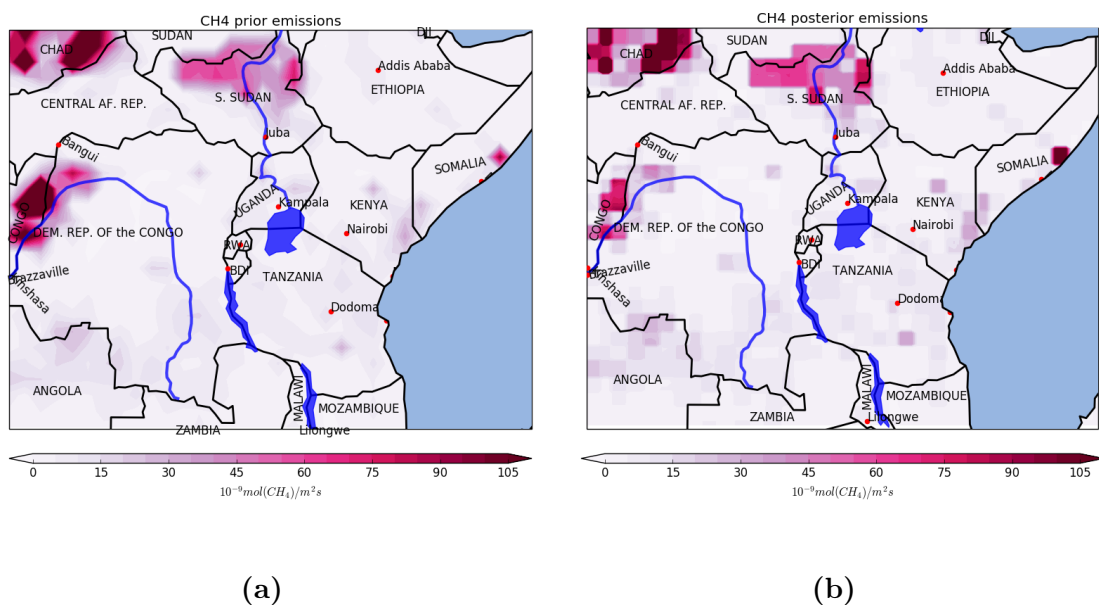
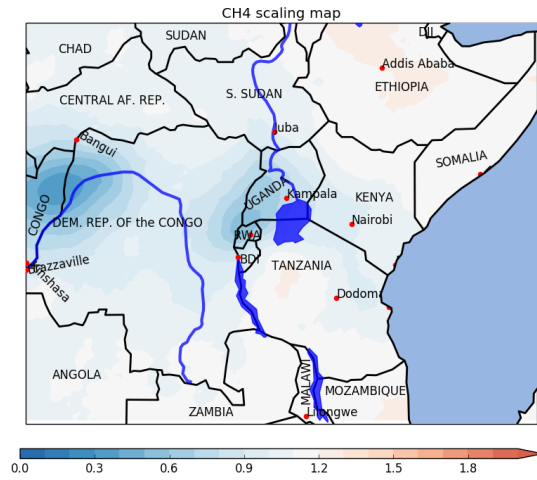
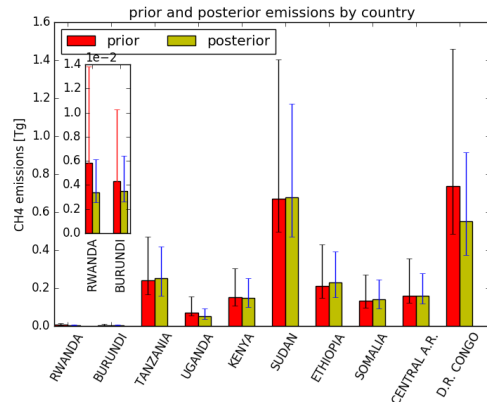


Figure A.26: CH_4 prior (a) and posterior (b) emissions for July 2016



(a)



(b)

Figure A.27: Prior scaling maps(a) and countries emissions totals(b) for July 2016

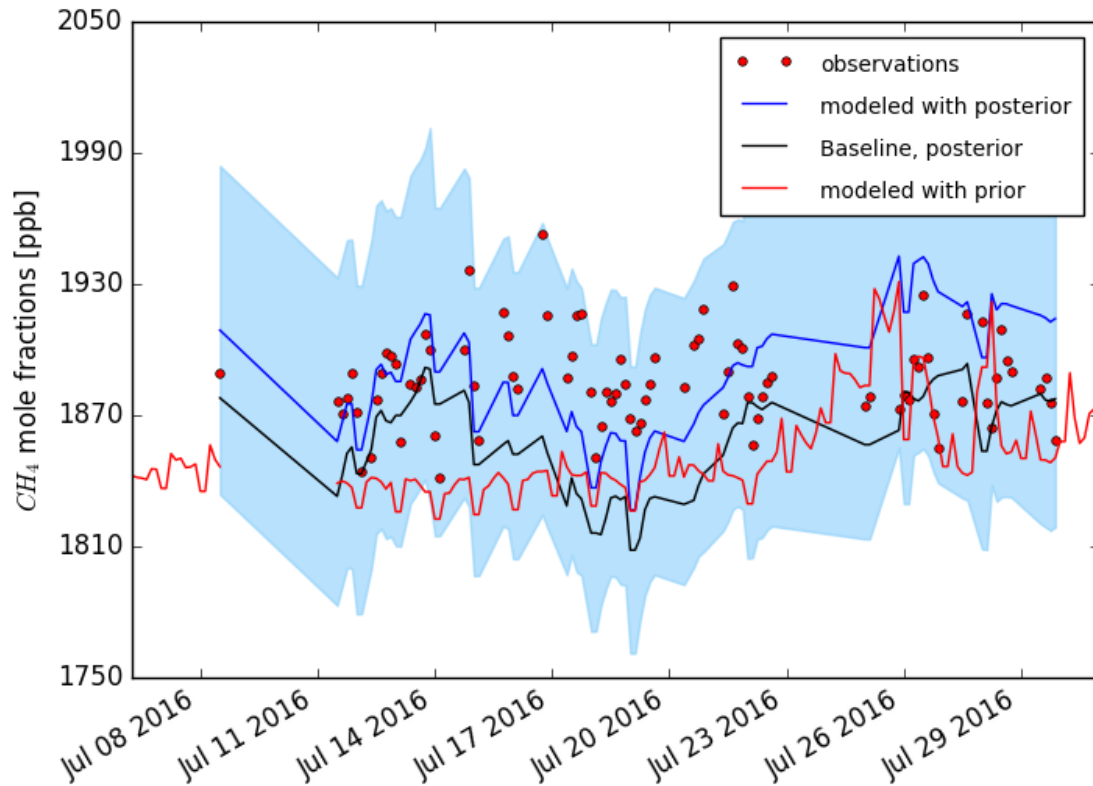


Figure A.28: Time series of optimized mole fractions (blue curve) compared to observations (red dots) and the modeled observation with prior emissions (red) with the prior (magenta) and posterior (black) baseline contribution to modeled mole fractions, for July 2016

A.8 Results for August 2016

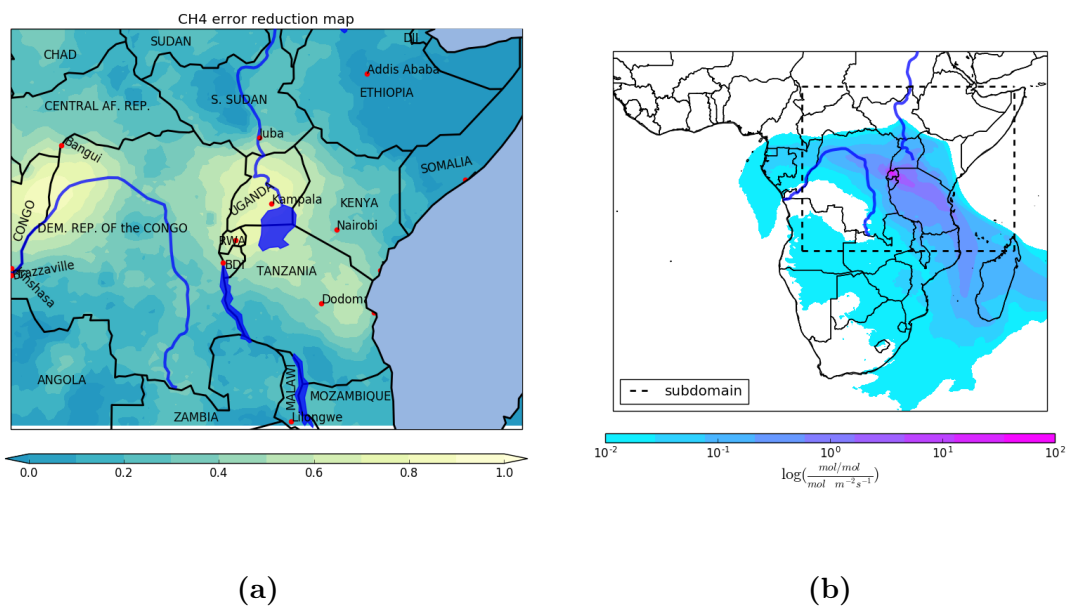


Figure A.29: Error reduction map (a) and footprint (note the log scale) (b) for August 2016. The extent of the map in (a) is highlighted with a broken line in the footprint map

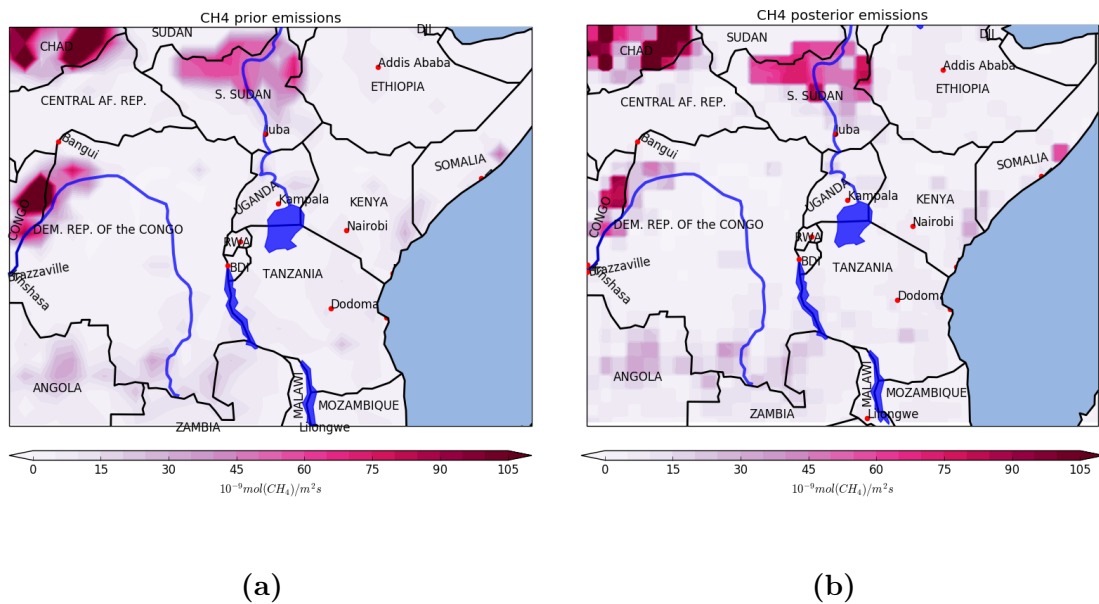
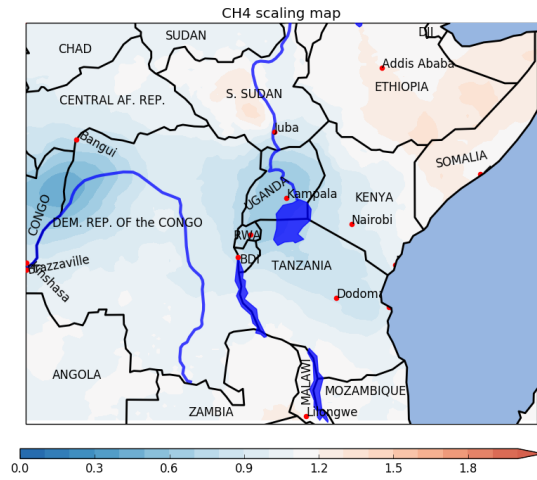
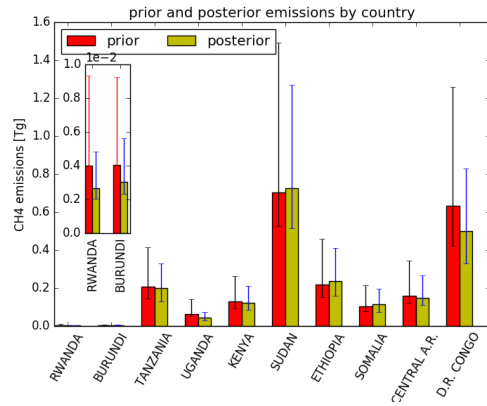


Figure A.30: CH_4 prior (a) and posterior (b) emissions for August 2016



(a)



(b)

Figure A.31: Prior scaling maps(a) and countries emissions totals(b) for August 2016

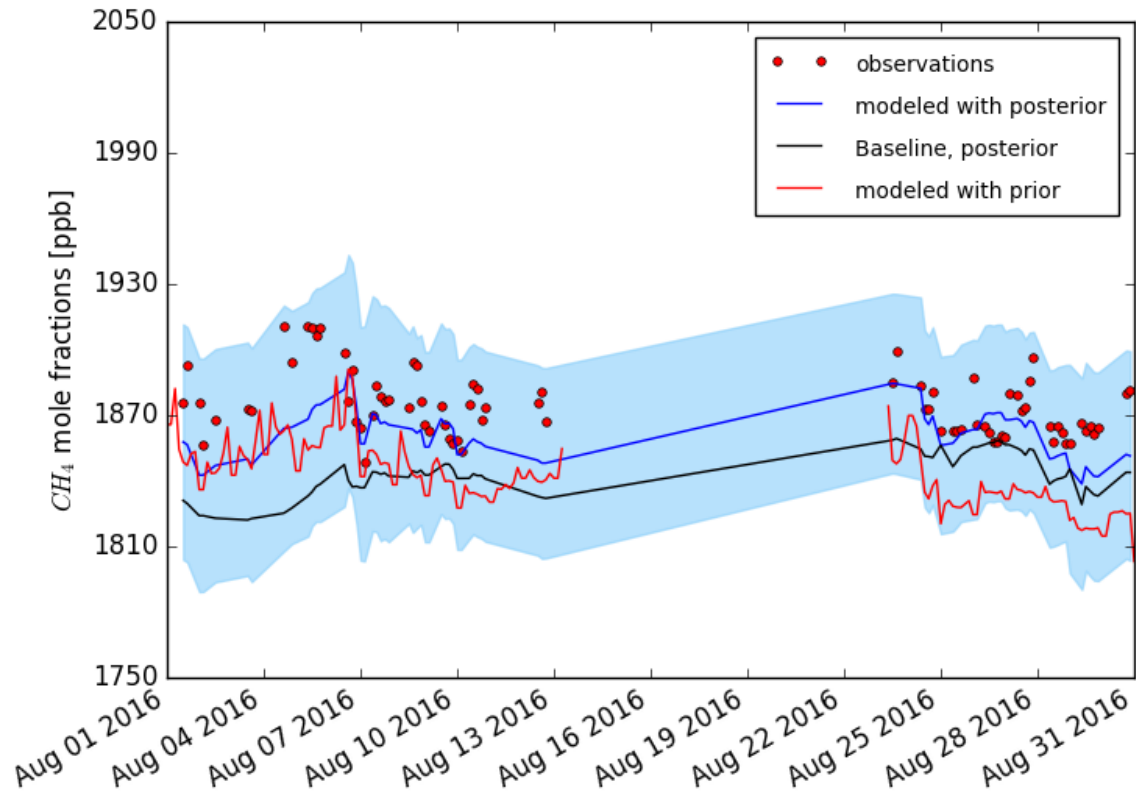


Figure A.32: Time series of optimized mole fractions (blue curve) compared to observations (red dots) and the modeled observation with prior emissions (red) with the prior (magenta) and posterior (black) baseline contribution to modeled mole fractions, for August 2016

A.9 Results for September 2016

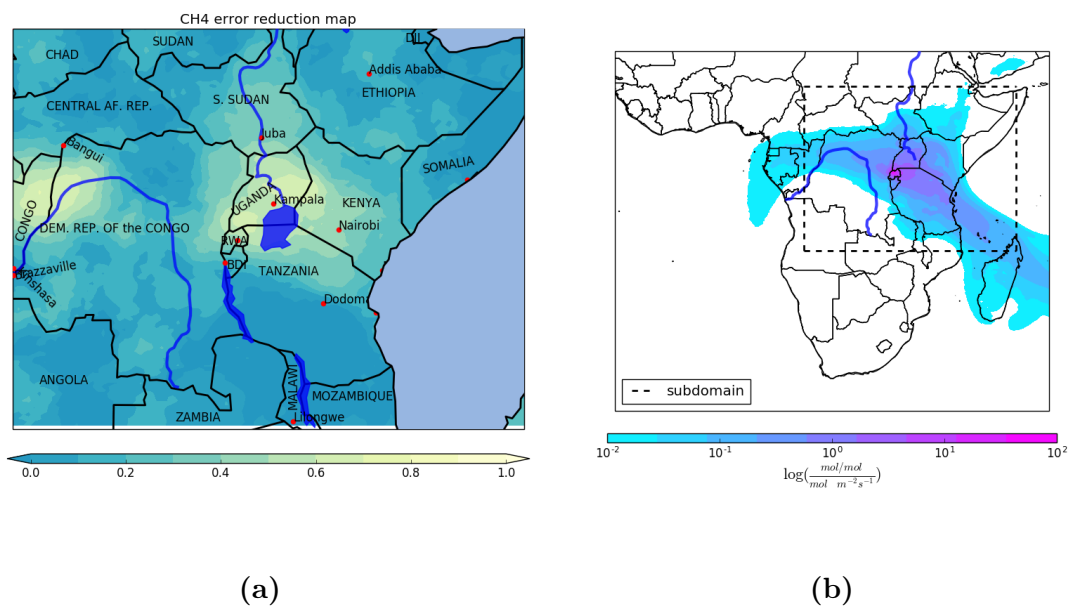


Figure A.33: Error reduction map (a) and footprint (note the log scale) (b) for September 2016. The extent of the map in (a) is highlighted with a broken line in the footprint map

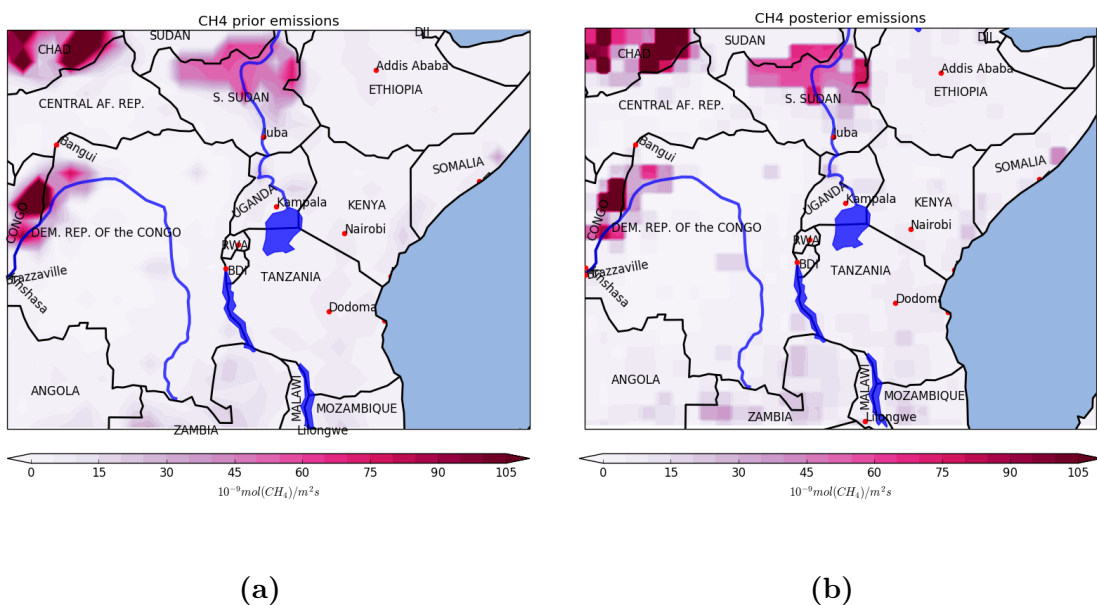
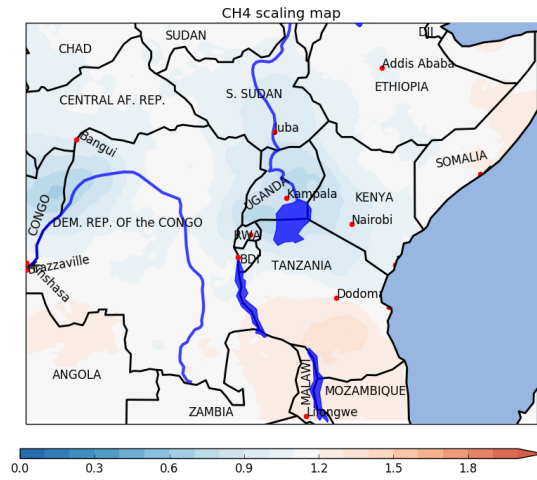
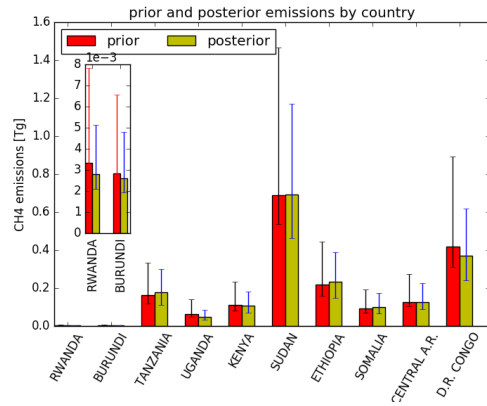


Figure A.34: CH_4 prior (a) and posterior (b) emissions for September 2016



(a)



(b)

Figure A.35: Prior scaling maps(a) and countries emissions totals(b) for September 2016

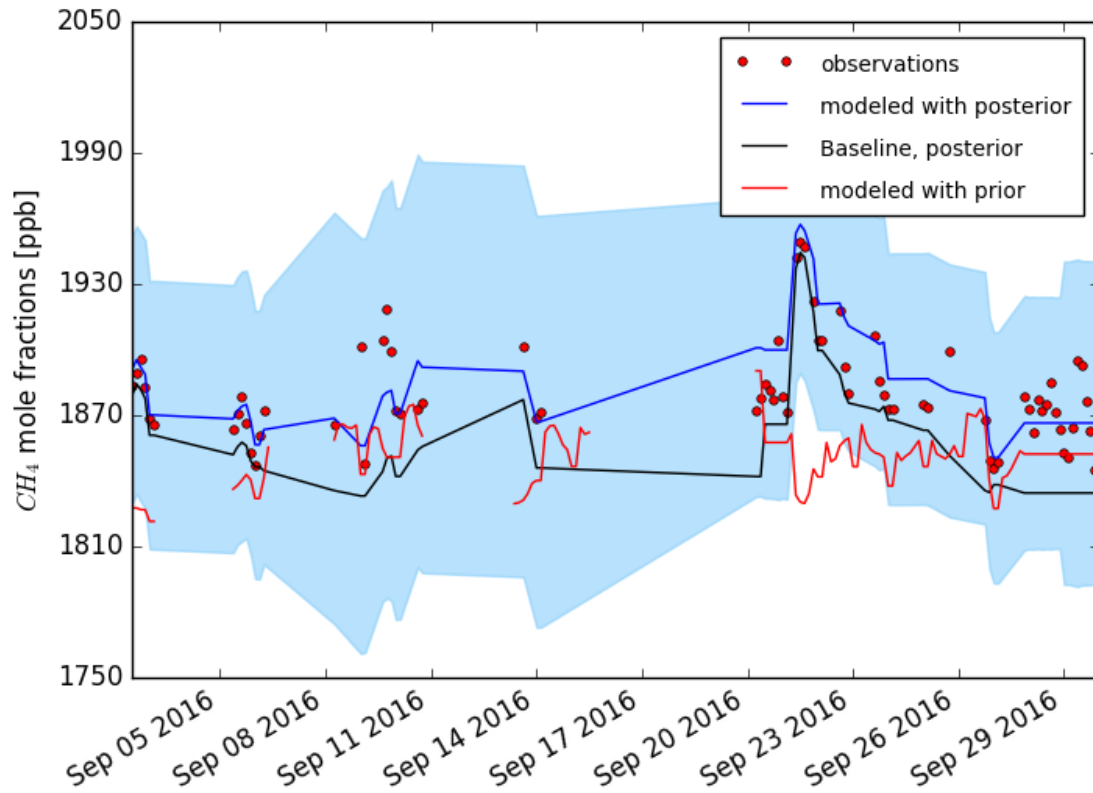


Figure A.36: Time series of optimized mole fractions (blue curve) compared to observations (red dots) and the modeled observation with prior emissions (red) with the prior (magenta) and posterior (black) baseline contribution to modeled mole fractions, for September 2016

A.10 Results for October 2016

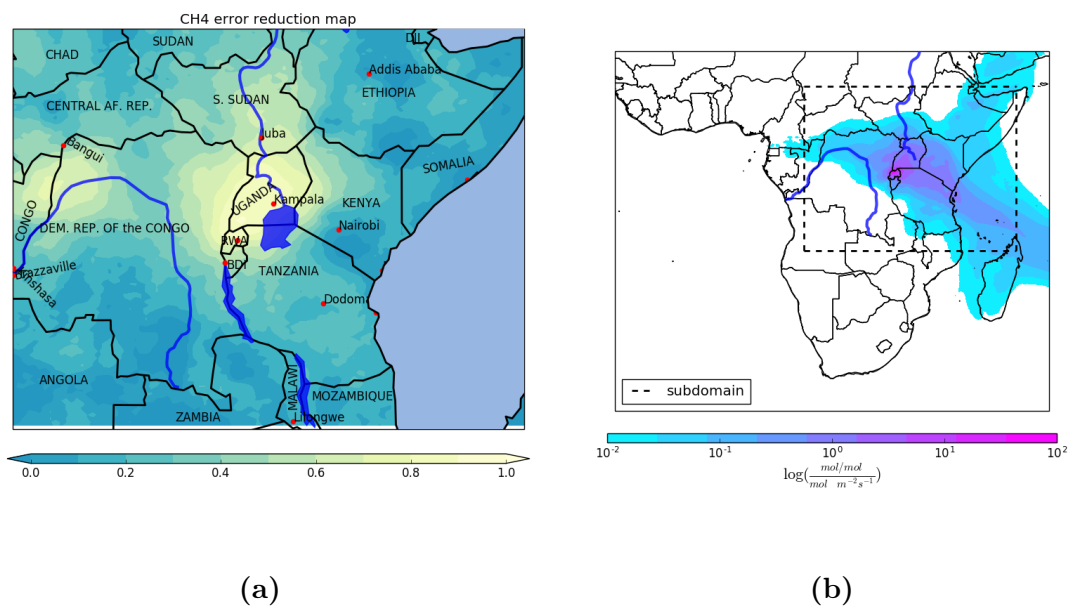


Figure A.37: Error reduction map (a) and footprint (note the log scale) (b) for October 2016. The extent of the map in (a) is highlighted with a broken line in the footprint map

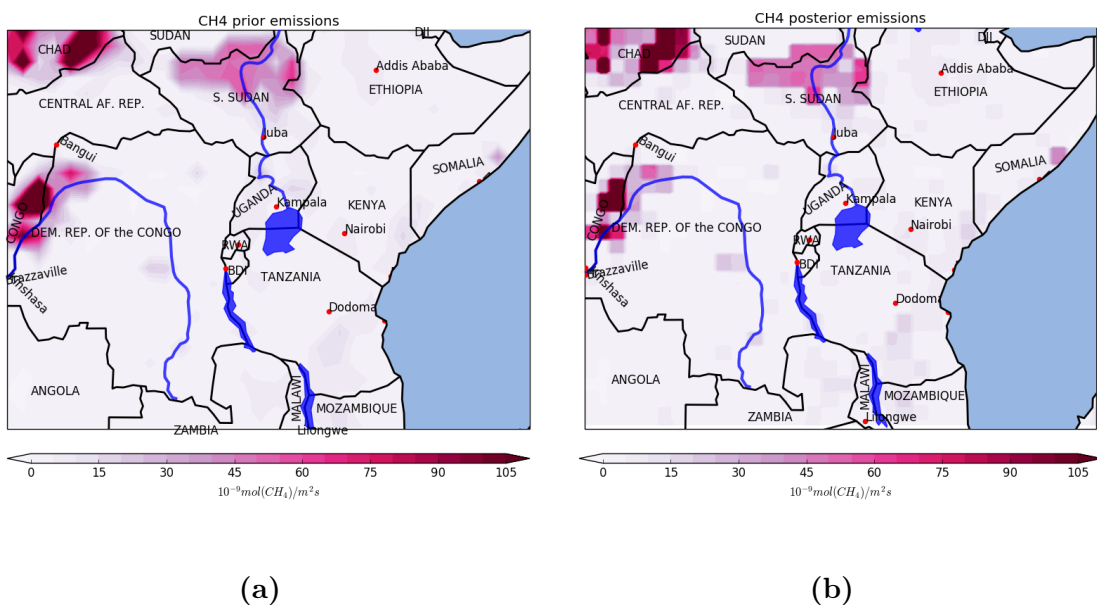
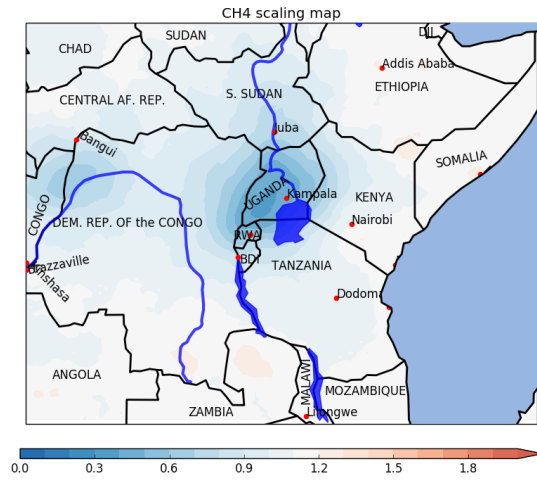
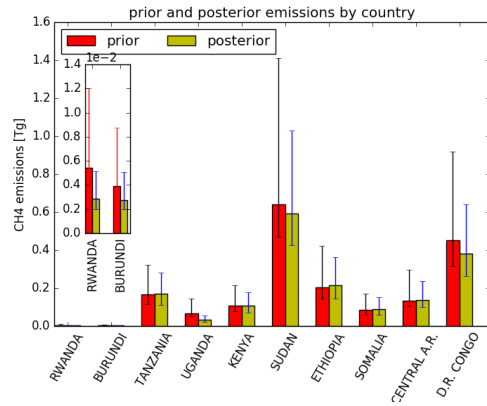


Figure A.38: CH_4 prior (a) and posterior (b) emissions for October 2016



(a)



(b)

Figure A.39: Prior scaling maps(a) and countries emissions totals(b) for October 2016

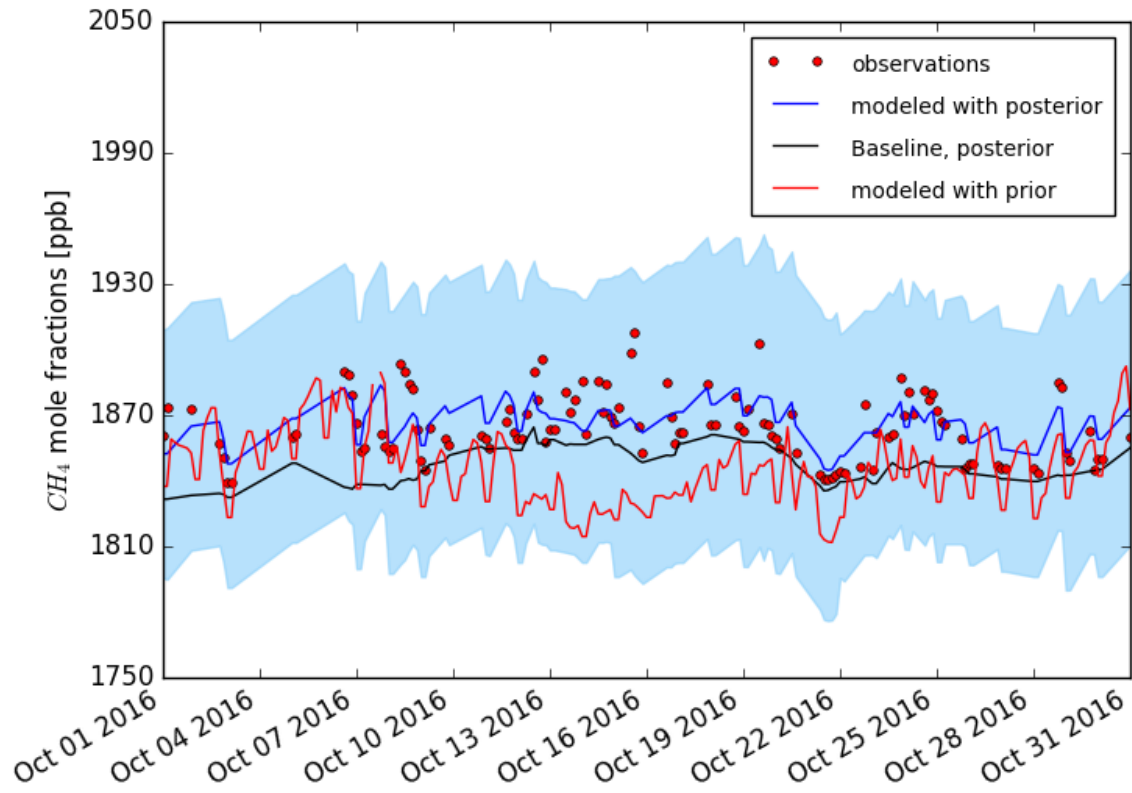


Figure A.40: Time series of optimized mole fractions (blue curve) compared to observations (red dots) and the modeled observation with prior emissions (red) with the prior (magenta) and posterior (black) baseline contribution to modeled mole fractions, for October 2016

A.11 Results for November 2016

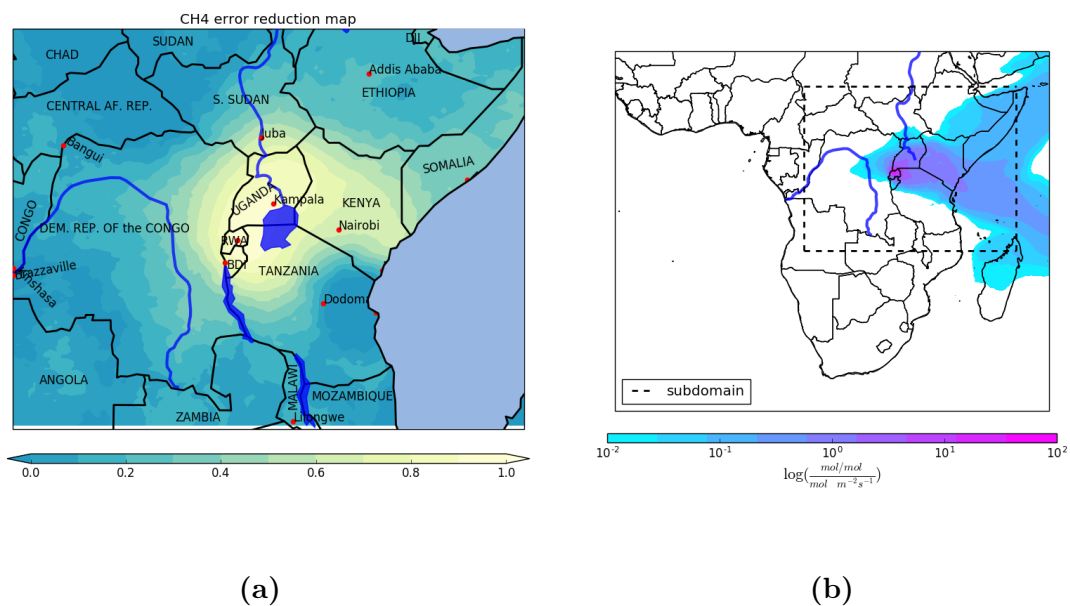


Figure A.41: Error reduction map (a) and footprint (note the log scale) (b) for November 2016. The extent of the map in (a) is highlighted with a broken line in the footprint map

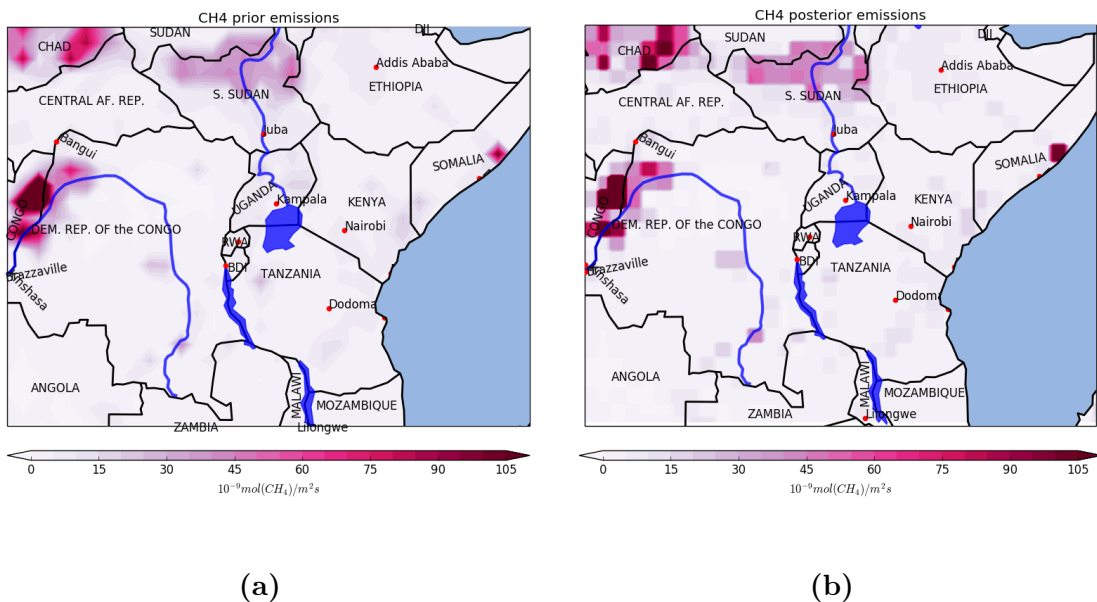
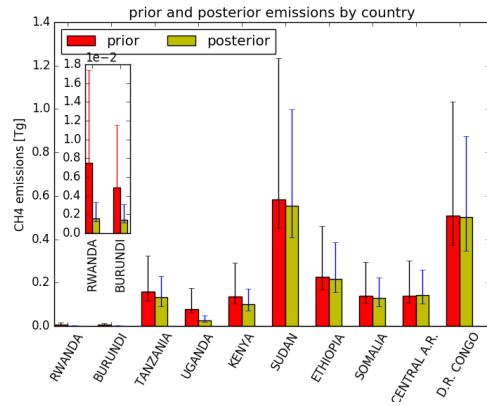
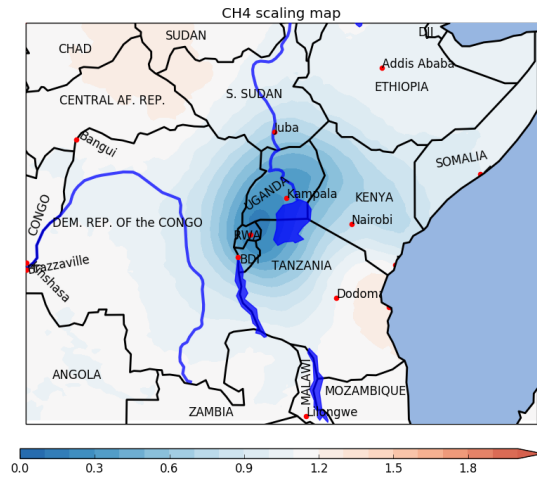


Figure A.42: CH_4 prior (a) and posterior (b) emissions for November 2016



(a)

(b)

Figure A.43: Prior scaling maps(a) and countries emissions totals(b) for November 2016

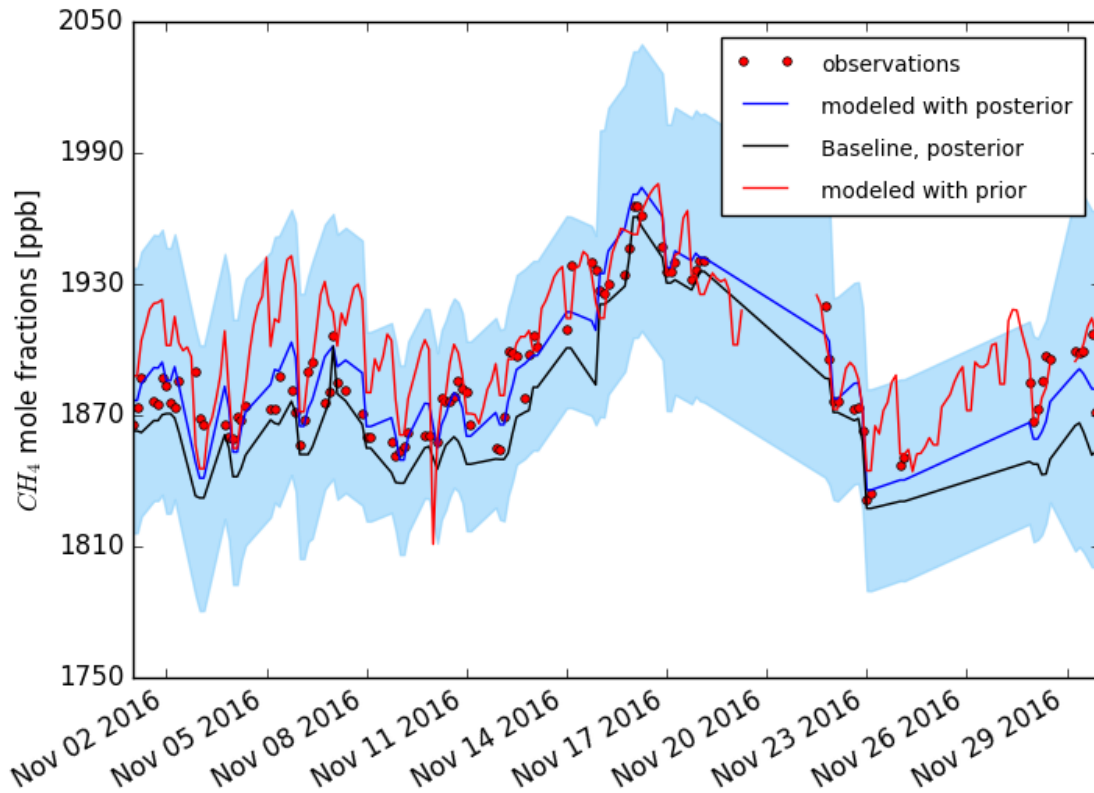


Figure A.44: Time series of optimized mole fractions (blue curve) compared to observations (red dots) and the modeled observation with prior emissions (red) with the prior (magenta) and posterior (black) baseline contribution to modeled mole fractions, for November 2016

A.12 Results for December 2016

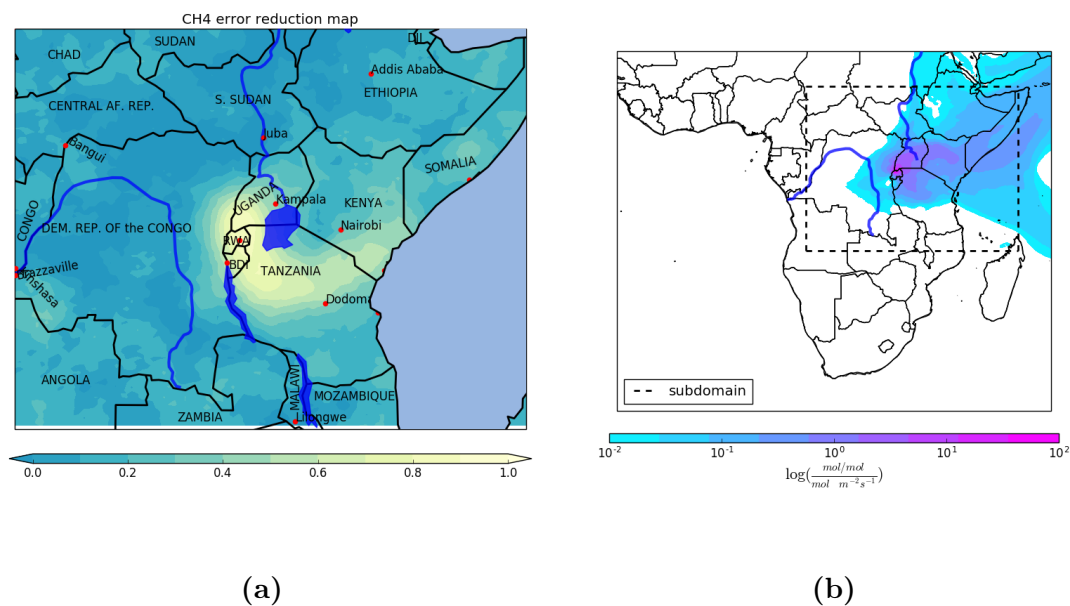


Figure A.45: Error reduction map (a) and footprint (note the log scale) (b) for December 2016. The extent of the map in (a) is highlighted with a broken line in the footprint map

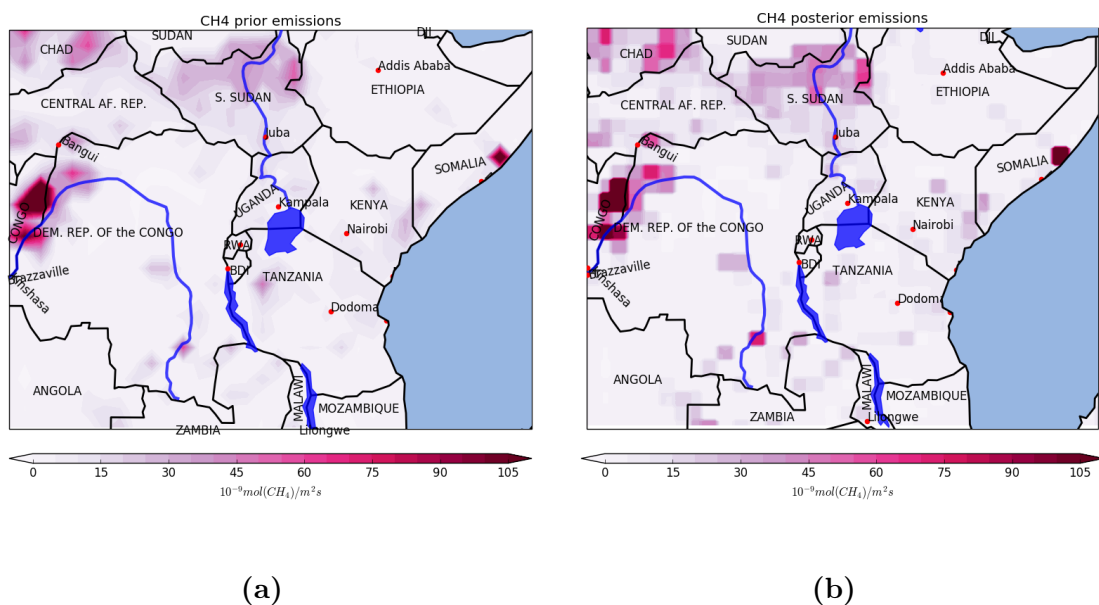
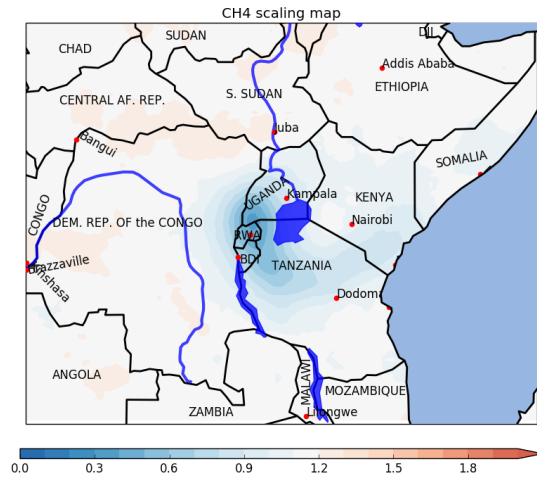
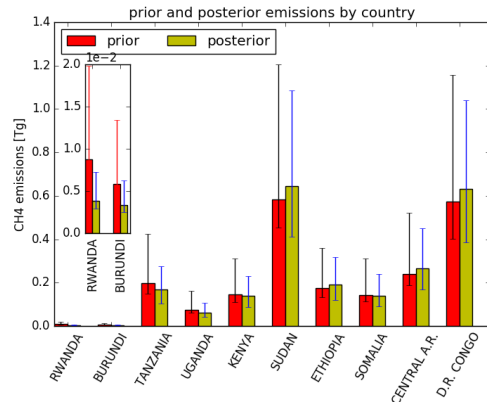


Figure A.46: CH_4 prior (a) and posterior (b) emissions for December 2016



(a)



(b)

Figure A.47: Prior scaling maps(a) and countries emissions totals(b) for December 2016

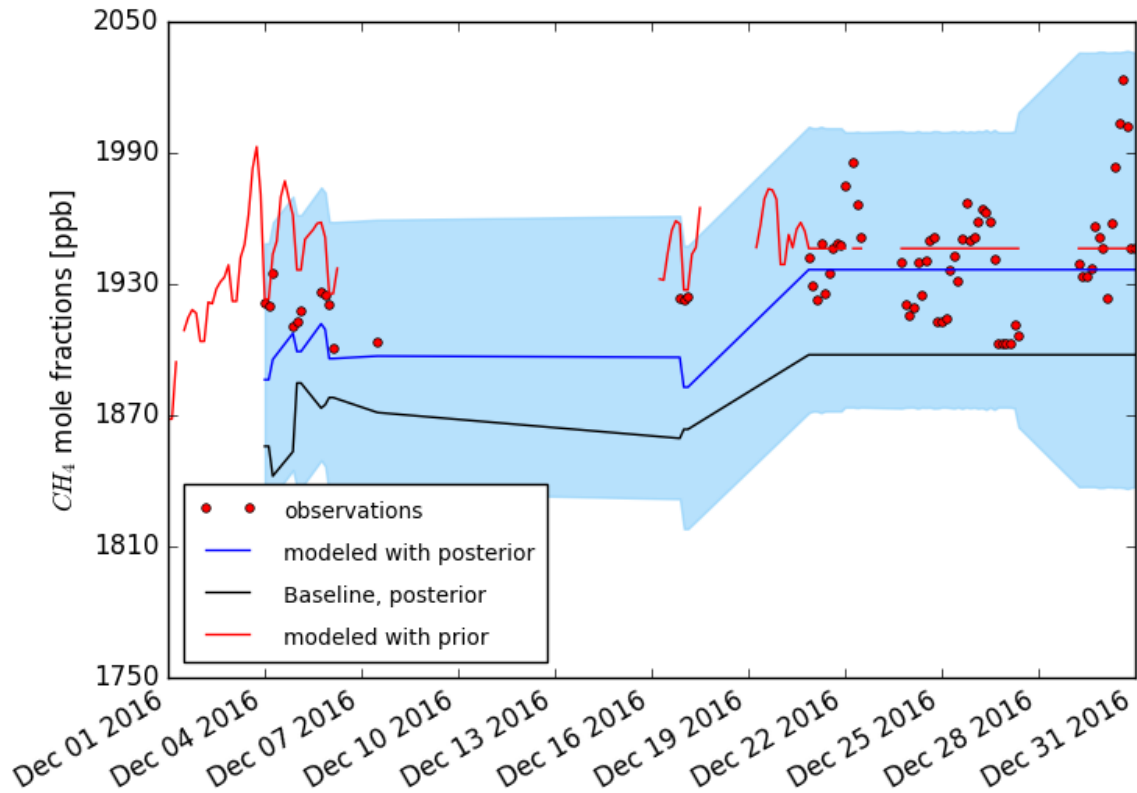


Figure A.48: Time series of optimized mole fractions (blue curve) compared to observations (red dots) and the modeled observation with prior emissions (red) with the prior (magenta) and posterior (black) baseline contribution to modeled mole fractions, for December 2016

B CO_2 Inversion results

B.1 Results for January 2016

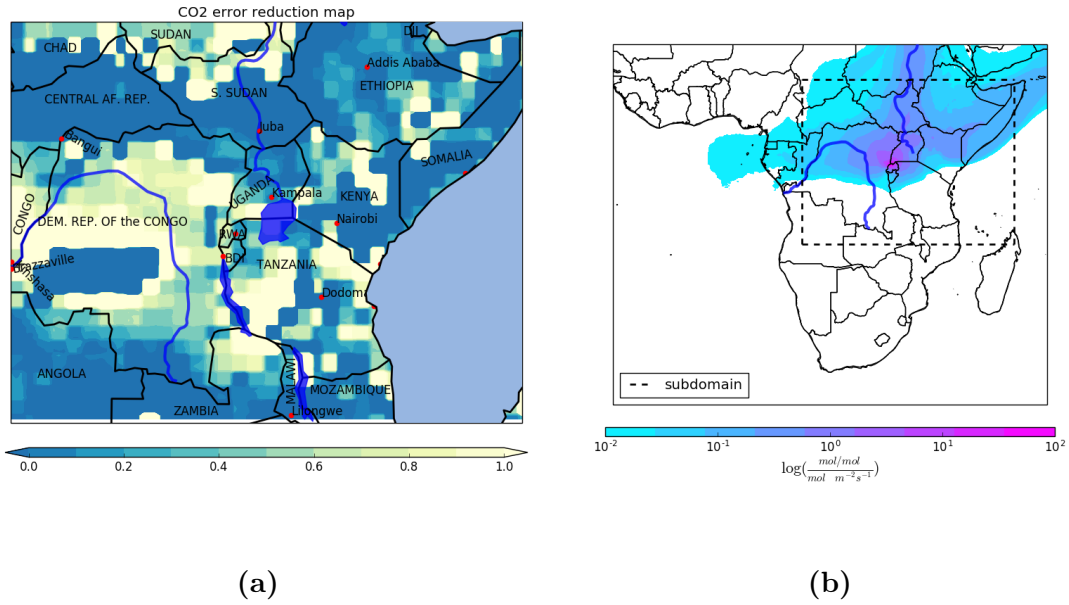


Figure B.49: Error reduction map (a) and footprint (note the log scale) (b) for January 2016. The extent of the map in (a) is highlighted with a broken line in the footprint map

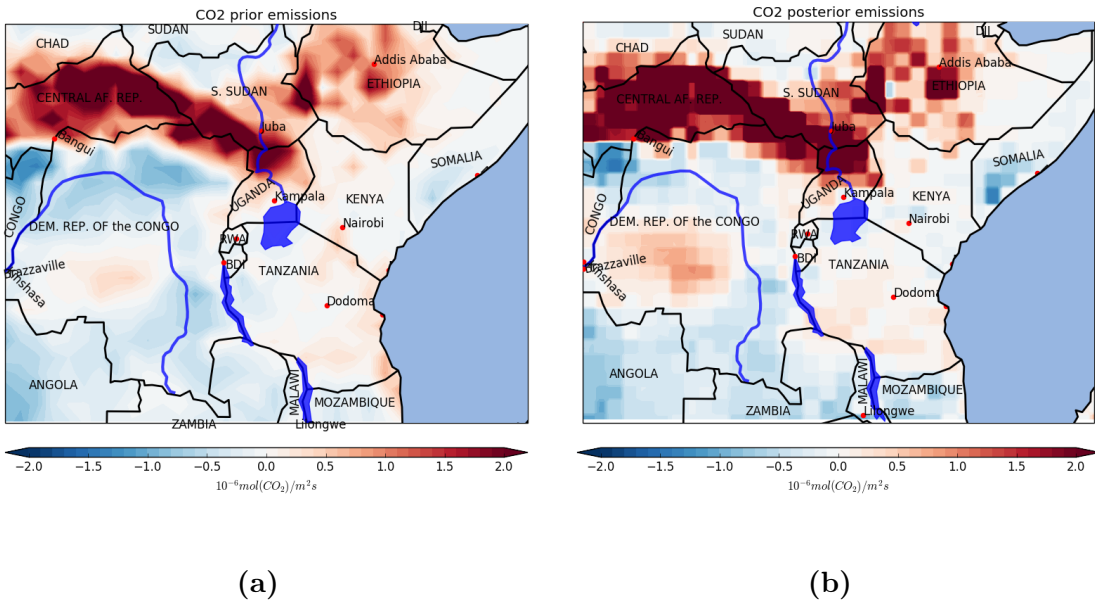
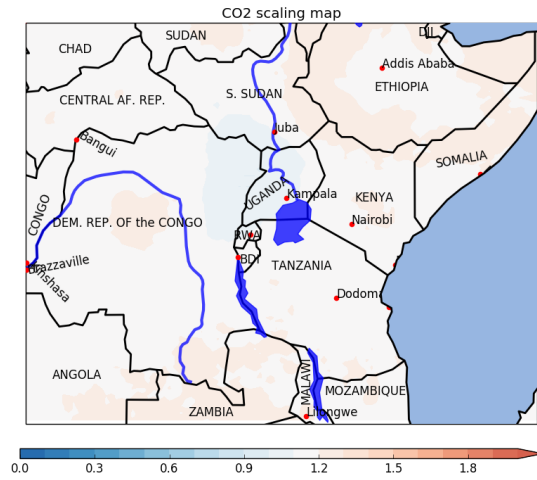
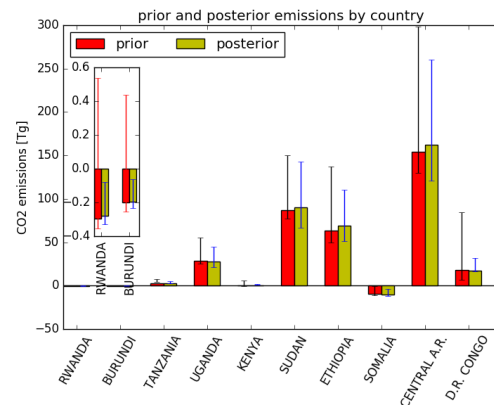


Figure B.50: CO_2 prior (a) and posterior (b) emissions for January 2016



(a)



(b)

Figure B.51: Prior scaling maps(a) and countries emissions totals (b) for January 2016

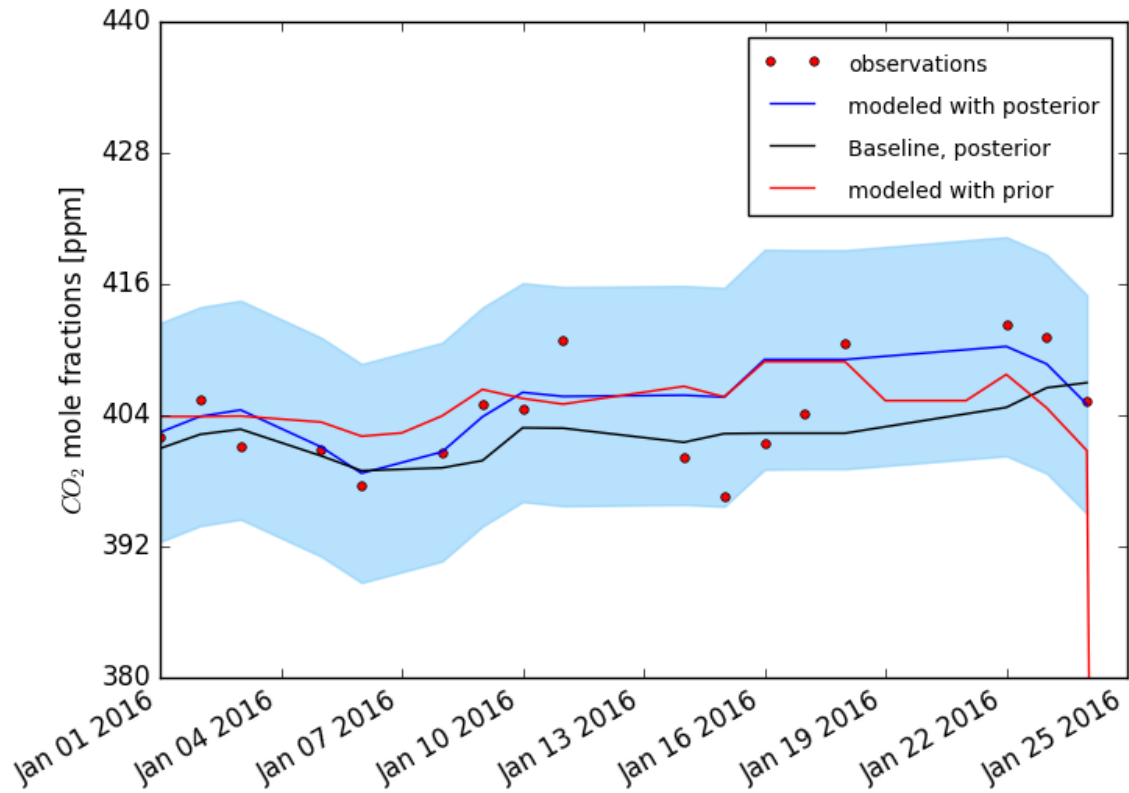


Figure B.52: Time series of optimized mole fractions (blue curve) compared to observations (red dots) and the modeled observation with prior emissions (red) with the prior (magenta) and posterior (black) baseline contribution to modeled mole fractions, for January 2016

B.2 Results for February 2016

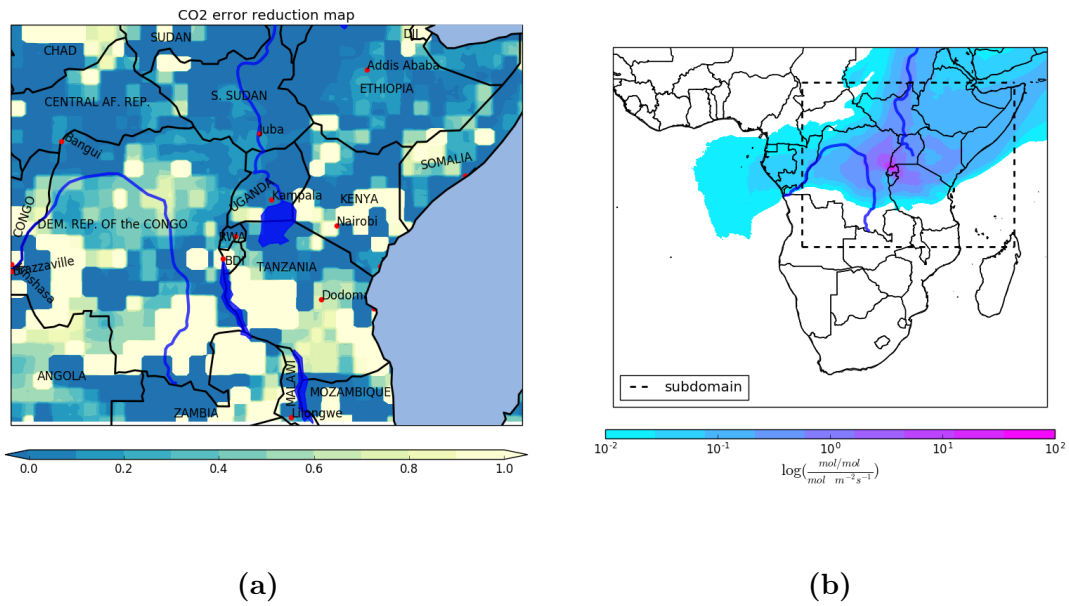


Figure B.53: Error reduction map (a) and footprint (note the log scale) (b) for February 2016. The extent of the map in (a) is highlighted with a broken line in the footprint map

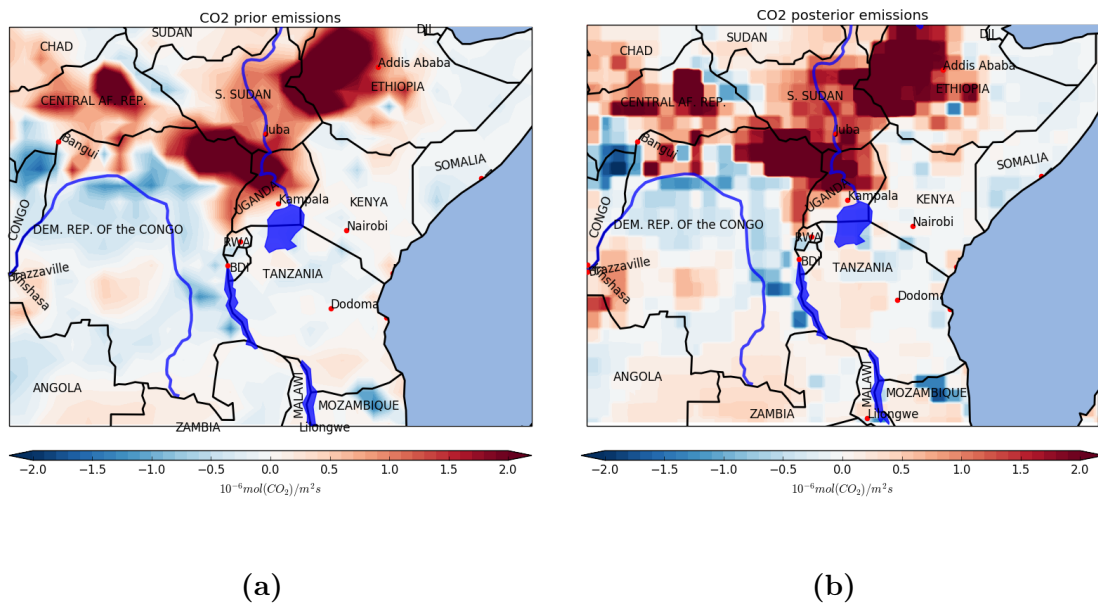
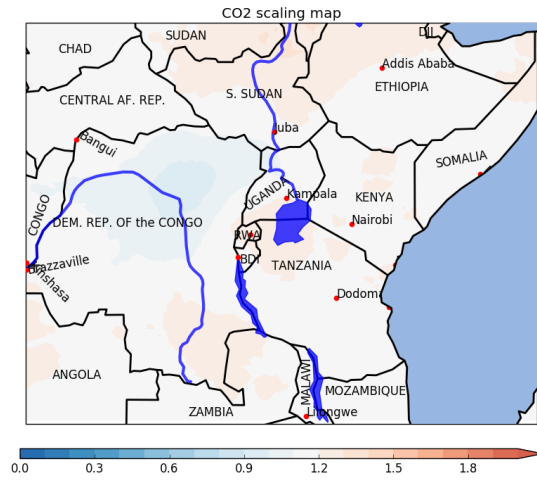
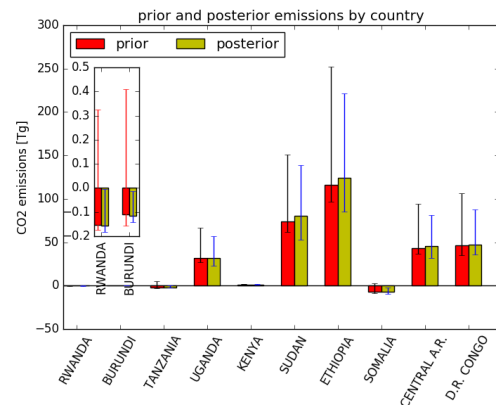


Figure B.54: CO_2 prior (a) and posterior (b) emissions for February 2016



(a)



(b)

Figure B.55: Prior scaling maps(a) and countries emissions totals (b) for February 2016

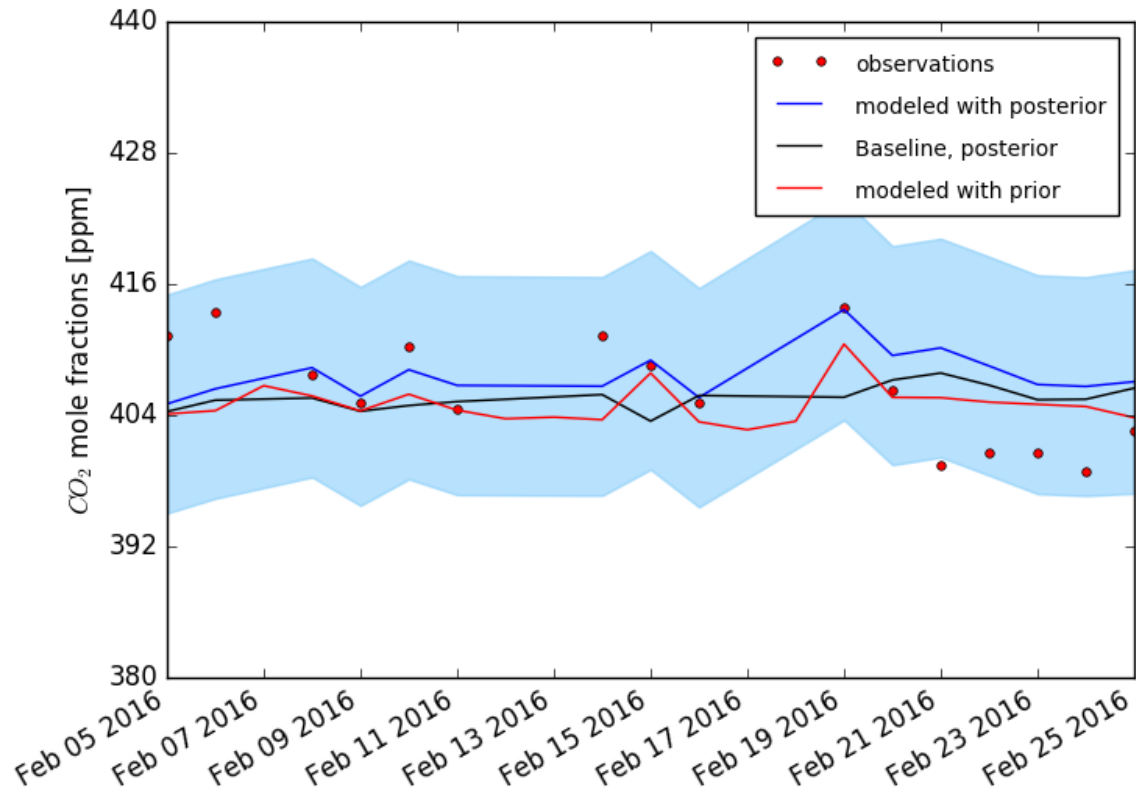


Figure B.56: Time series of optimized mole fractions (blue curve) compared to observations (red dots) and the modeled observation with prior emissions (red) with the prior (magenta) and posterior (black) baseline contribution to modeled mole fractions, for February 2016

B.3 Results for March 2016

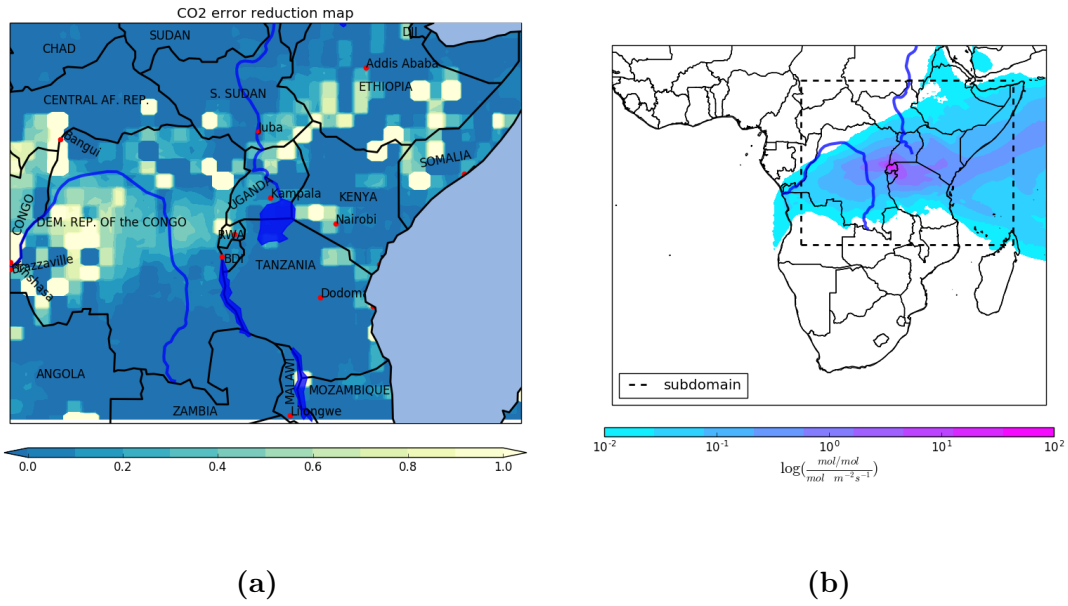


Figure B.57: Error reduction map (a) and footprint (note the log scale) (b) for March 2016. The extent of the map in (a) is highlighted with a broken line in the footprint map

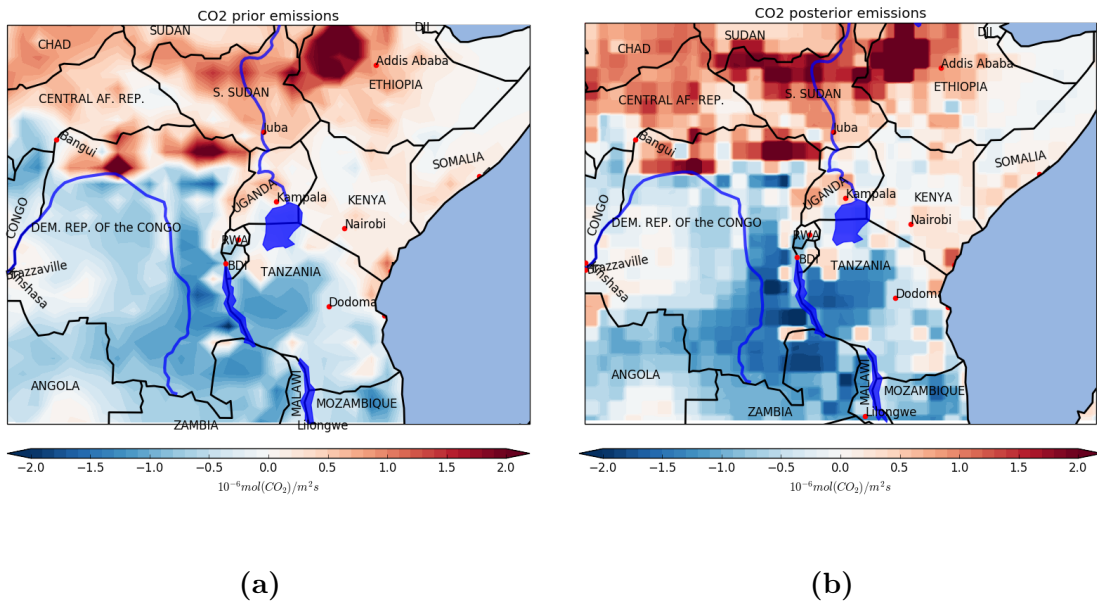
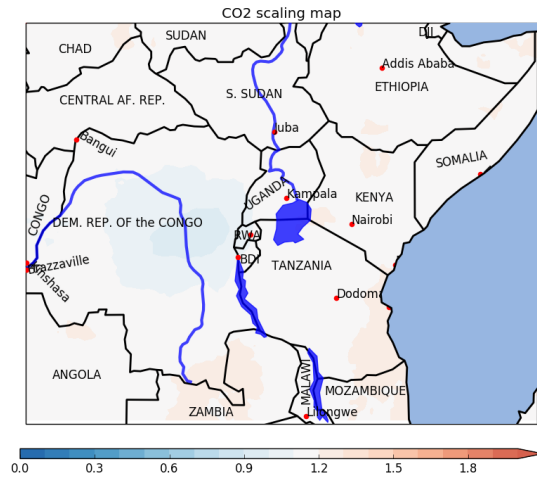
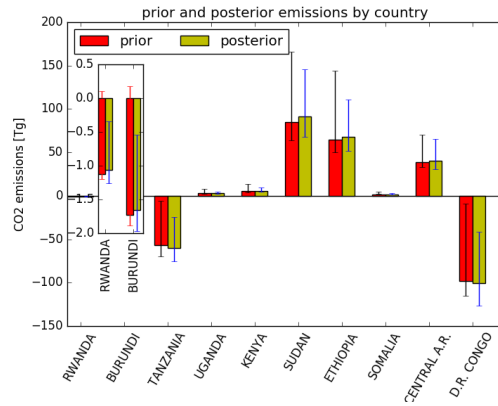


Figure B.58: CO_2 prior (a) and posterior (b) emissions for March 2016



(a)



(b)

Figure B.59: Prior scaling maps(a) and countries emissions totals (b) for March 2016

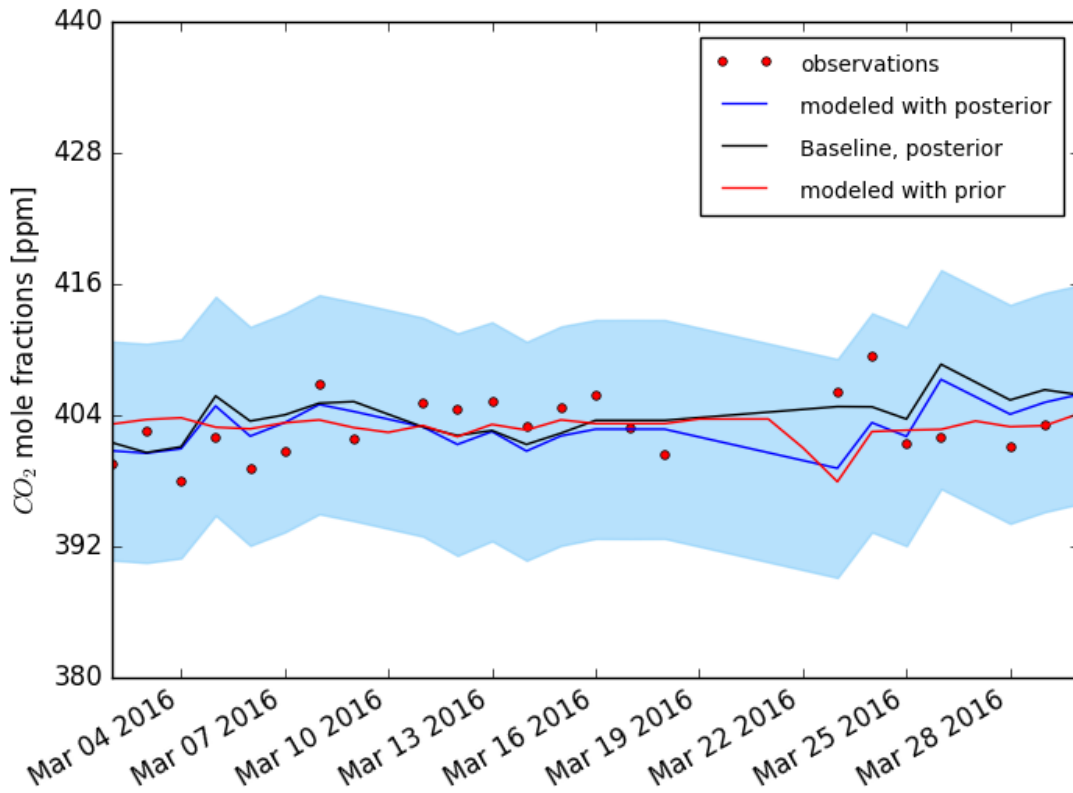


Figure B.60: Time series of optimized mole fractions (blue curve) compared to observations (red dots) and the modeled observation with prior emissions (red) with the prior (magenta) and posterior (black) baseline contribution to modeled mole fractions, for March 2016

B.4 Results for April 2016

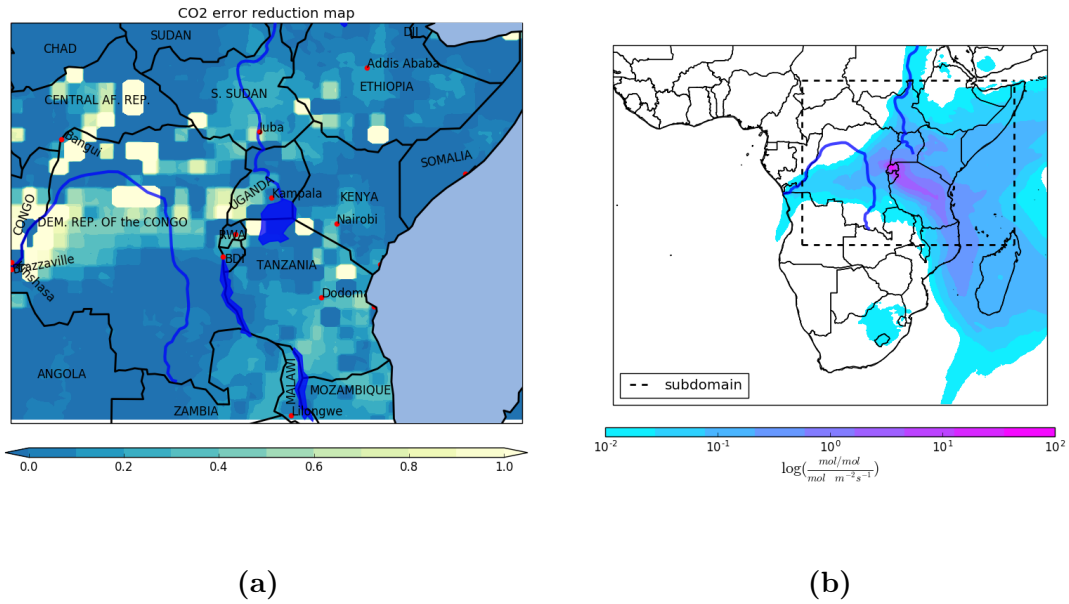


Figure B.61: Error reduction map (a) and footprint (note the log scale) (b) for April 2016. The extent of the map in (a) is highlighted with a broken line in the footprint map

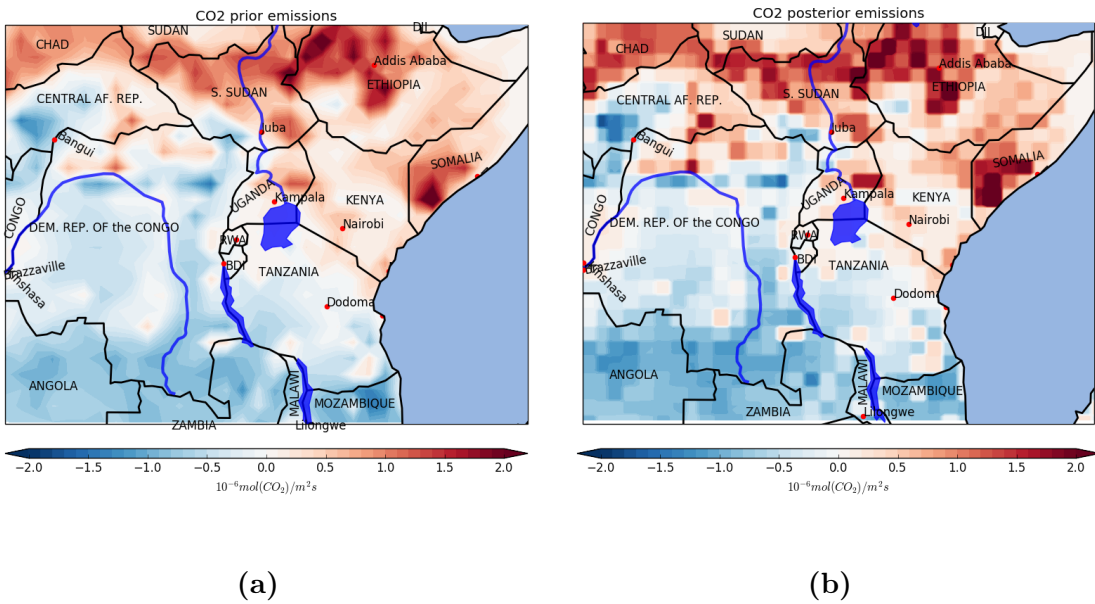
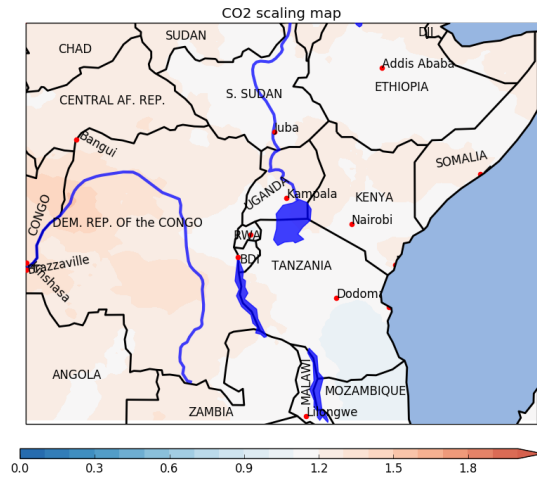
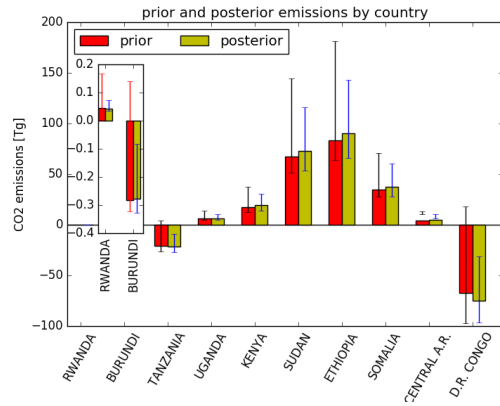


Figure B.62: CO_2 prior (a) and posterior (b) emissions for April 2016



(a)



(b)

Figure B.63: Prior scaling maps(a) and countries emissions totals (b) for April 2016

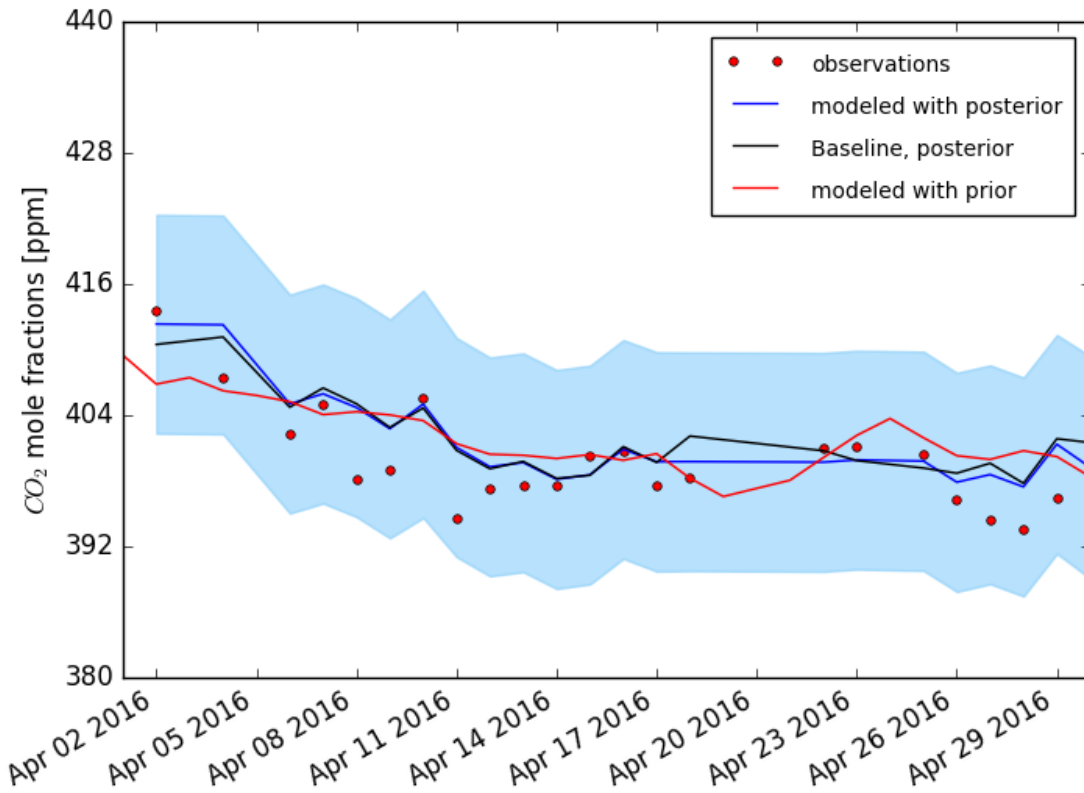


Figure B.64: Time series of optimized mole fractions (blue curve) compared to observations (red dots) and the modeled observation with prior emissions (red) with the prior (magenta) and posterior (black) baseline contribution to modeled mole fractions, for April 2016

B.5 Results for May 2016

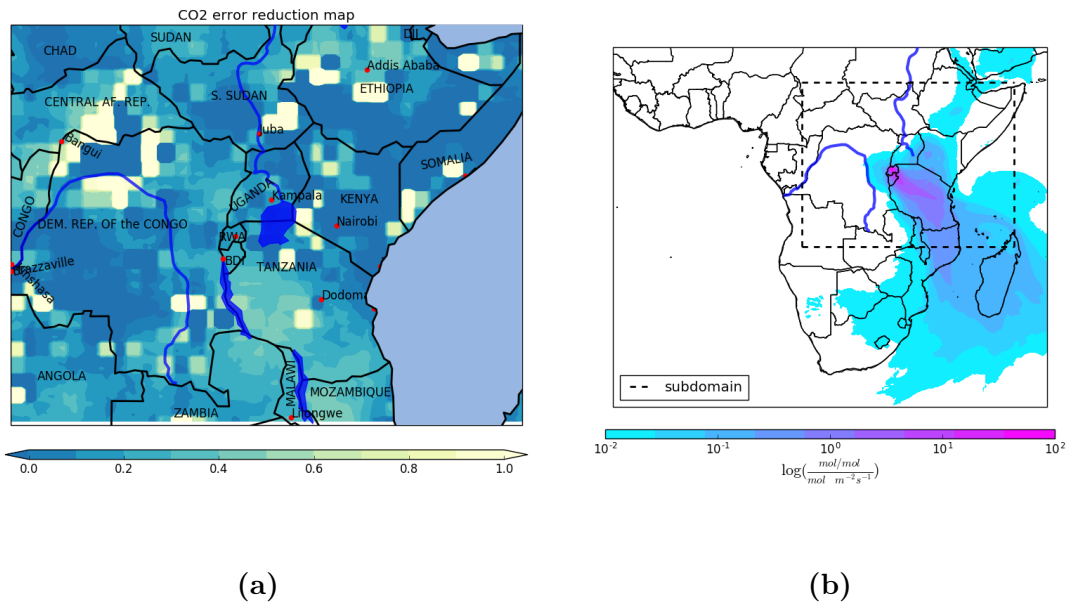


Figure B.65: Error reduction map (a) and footprint (note the log scale) (b) for May 2016. The extent of the map in (a) is highlighted with a broken line in the footprint map

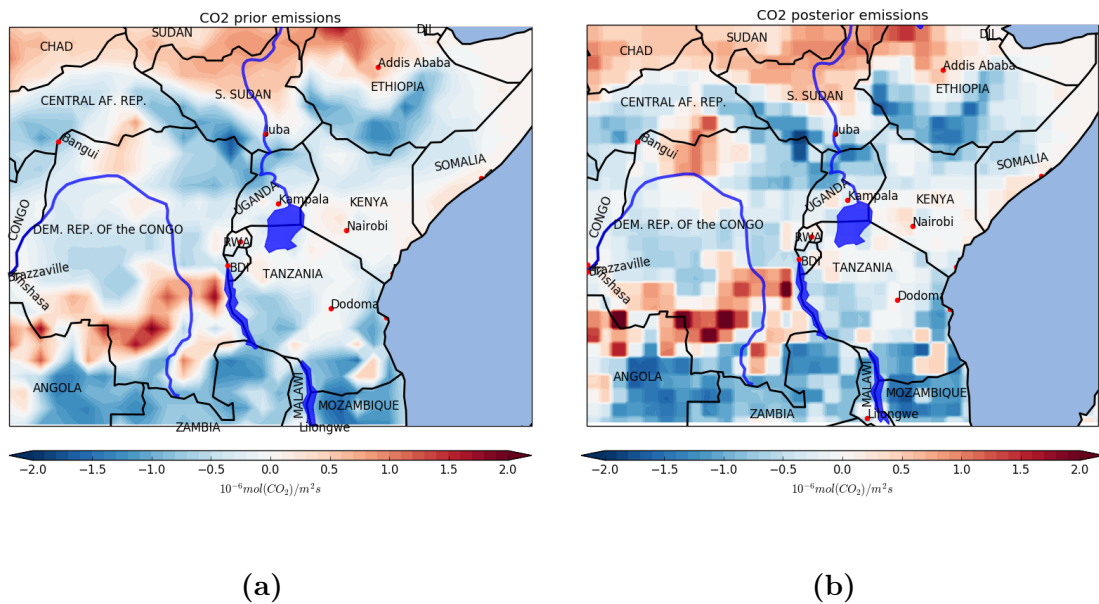
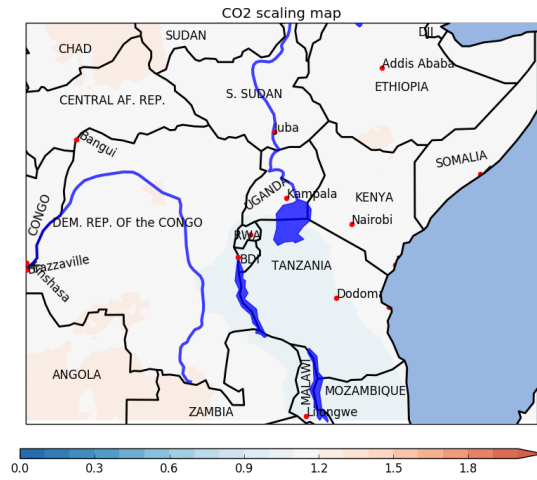
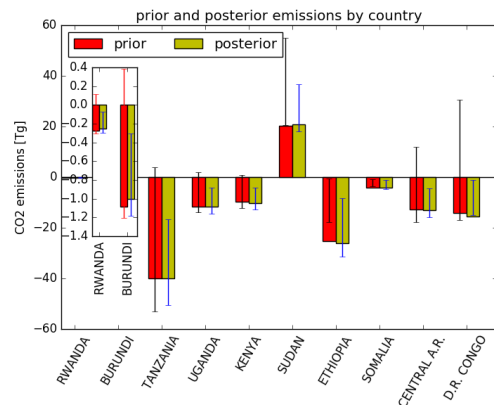


Figure B.66: CO_2 prior (a) and posterior (b) emissions for May 2016



(a)



(b)

Figure B.67: Prior scaling maps(a) and countries emissions totals (b) for May 2016

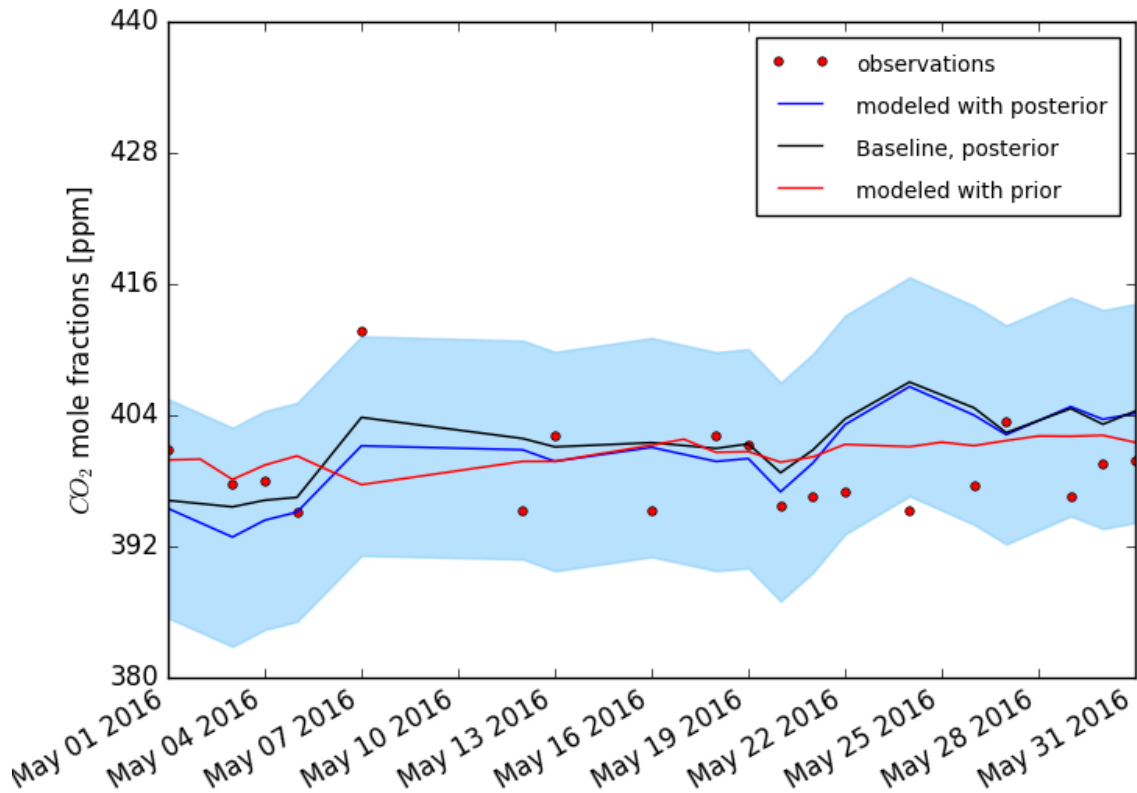


Figure B.68: Time series of optimized mole fractions (blue curve) compared to observations (red dots) and the modeled observation with prior emissions (red) with the prior (magenta) and posterior (black) baseline contribution to modeled mole fractions, for May 2016

B.6 Results for June 2016

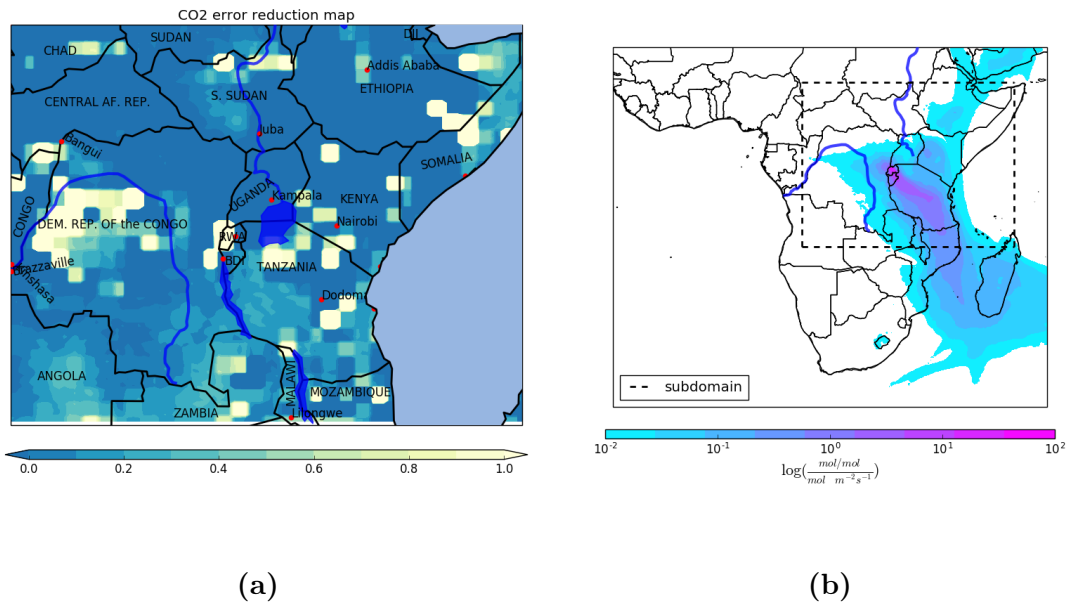


Figure B.69: Error reduction map (a) and footprint (note the log scale) (b) for June 2016. The extent of the map in (a) is highlighted with a broken line in the footprint map

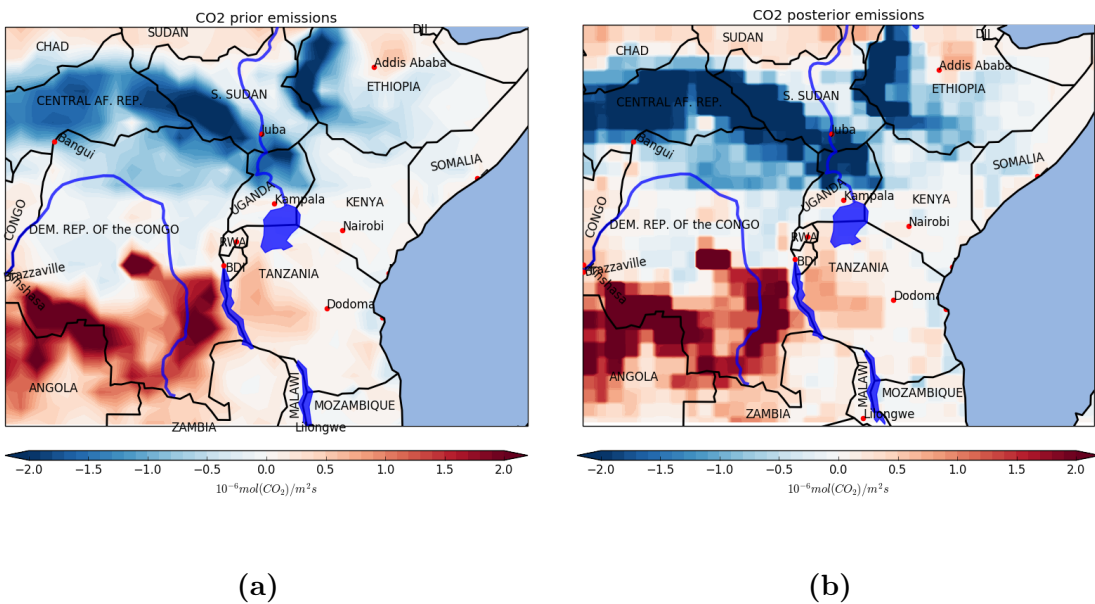
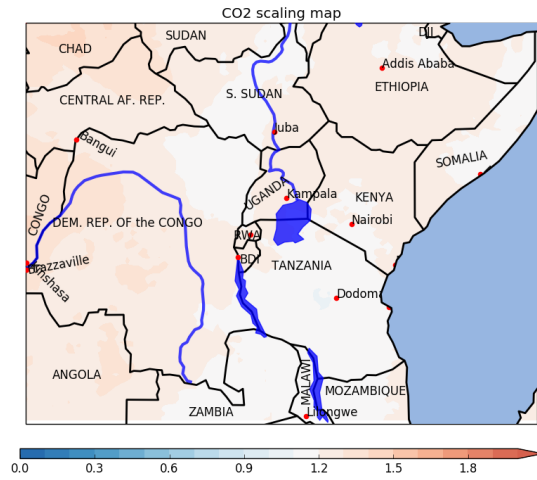
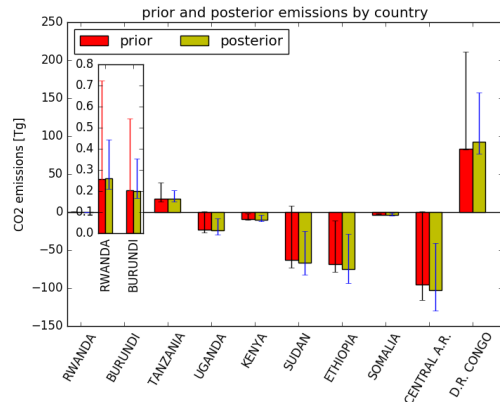


Figure B.70: CO_2 prior (a) and posterior (b) emissions for June 2016



(a)



(b)

Figure B.71: Prior scaling maps(a) and countries emissions totals (b) for June 2016

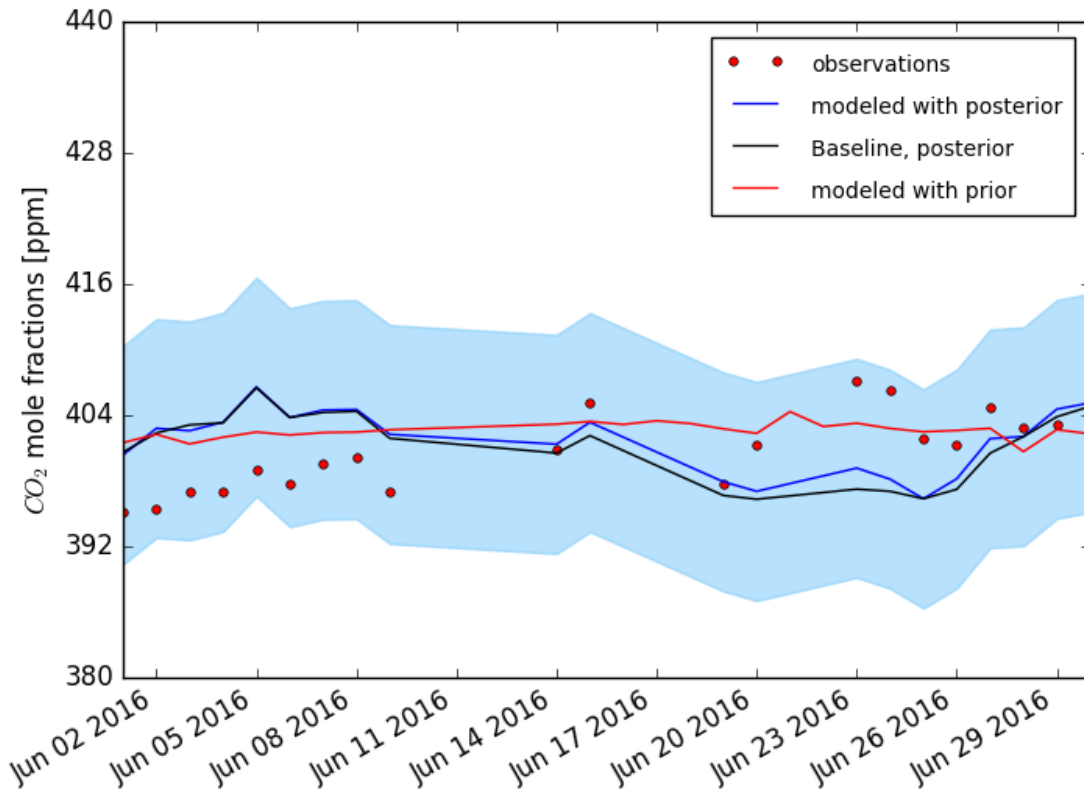


Figure B.72: Time series of optimized mole fractions (blue curve) compared to observations (red dots) and the modeled observation with prior emissions (red) with the prior (magenta) and posterior (black) baseline contribution to modeled mole fractions, for June 2016

B.7 Results for July 2016

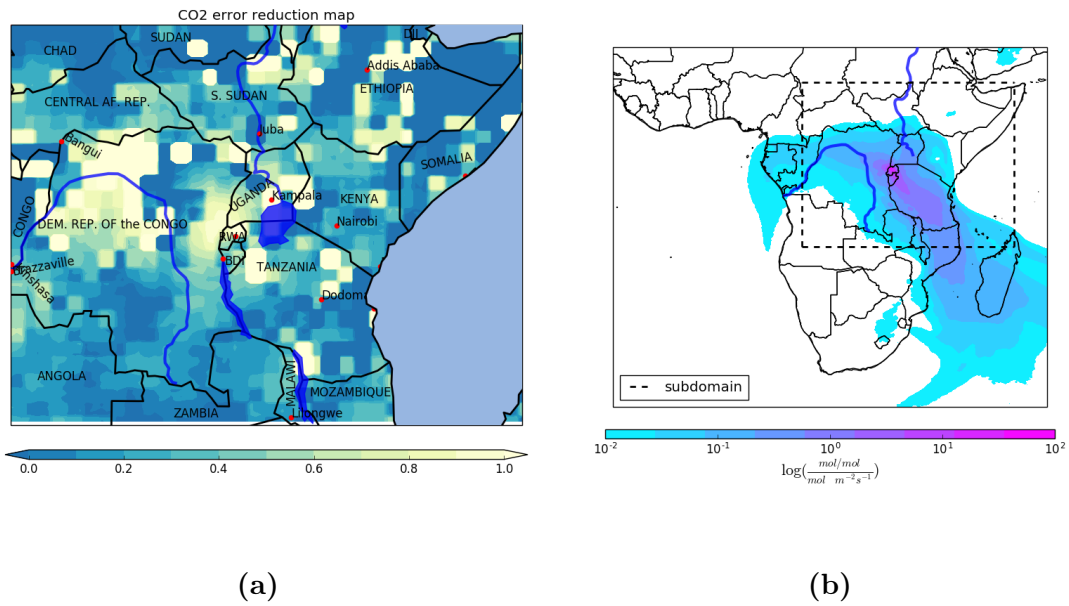


Figure B.73: Error reduction map (a) and footprint (note the log scale) (b) for July 2016. The extent of the map in (a) is highlighted with a broken line in the footprint map

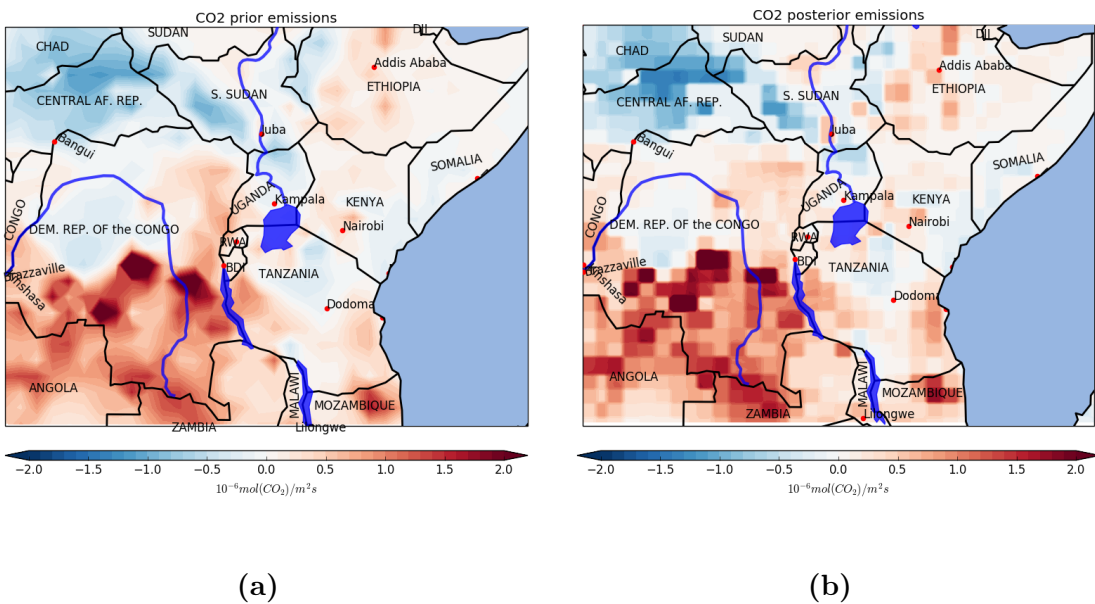
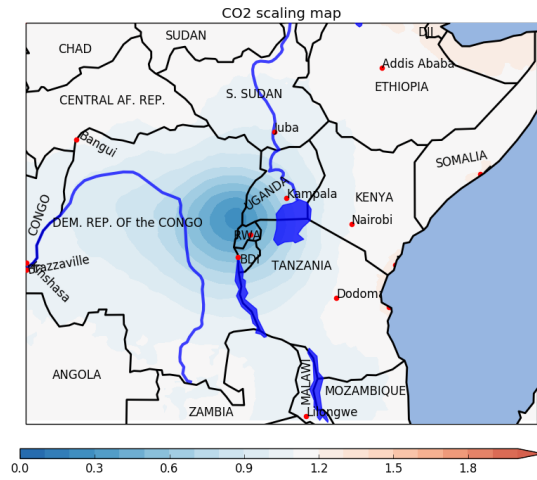
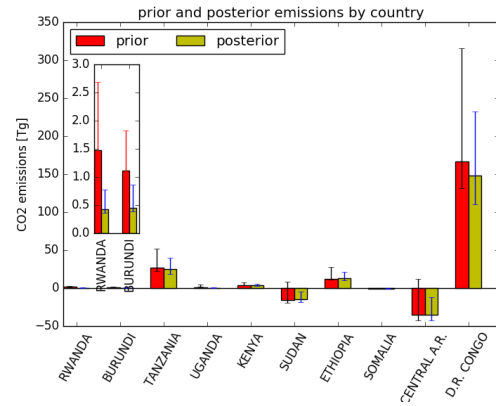


Figure B.74: CO_2 prior (a) and posterior (b) emissions for July 2016



(a)



(b)

Figure B.75: Prior scaling maps(a) and countries emissions totals (b) for July 2016

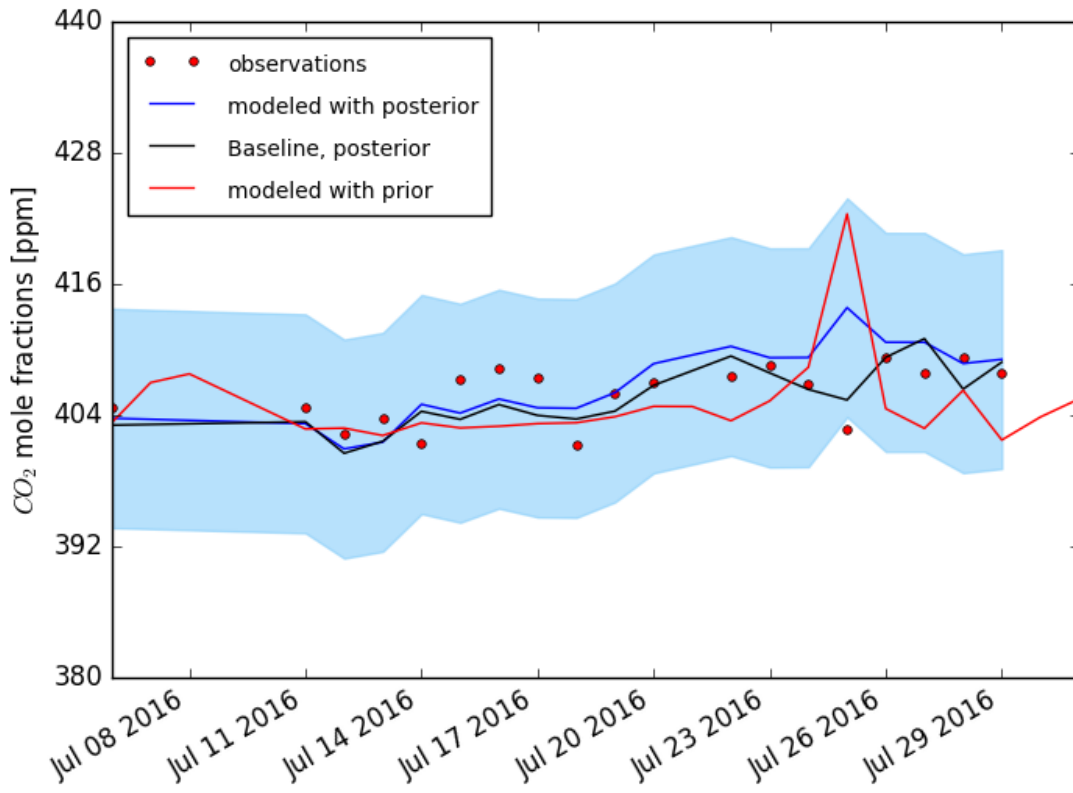


Figure B.76: Time series of optimized mole fractions (blue curve) compared to observations (red dots) and the modeled observation with prior emissions (red) with the prior (magenta) and posterior (black) baseline contribution to modeled mole fractions, for July 2016

B.8 Results for August 2016

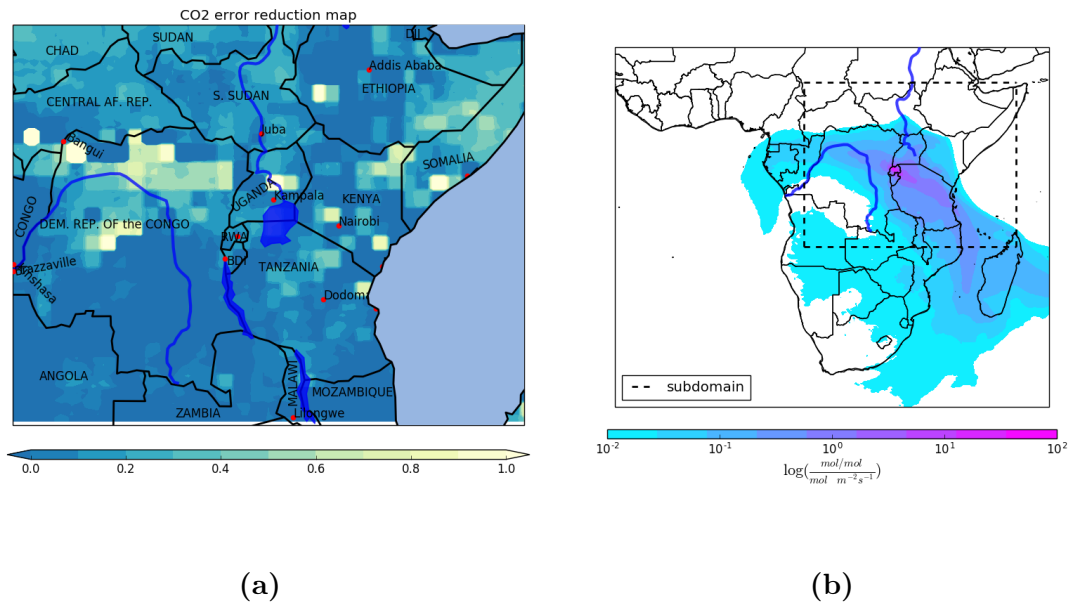


Figure B.77: Error reduction map (a) and footprint (note the log scale) (b) for August 2016. The extent of the map in (a) is highlighted with a broken line in the footprint map

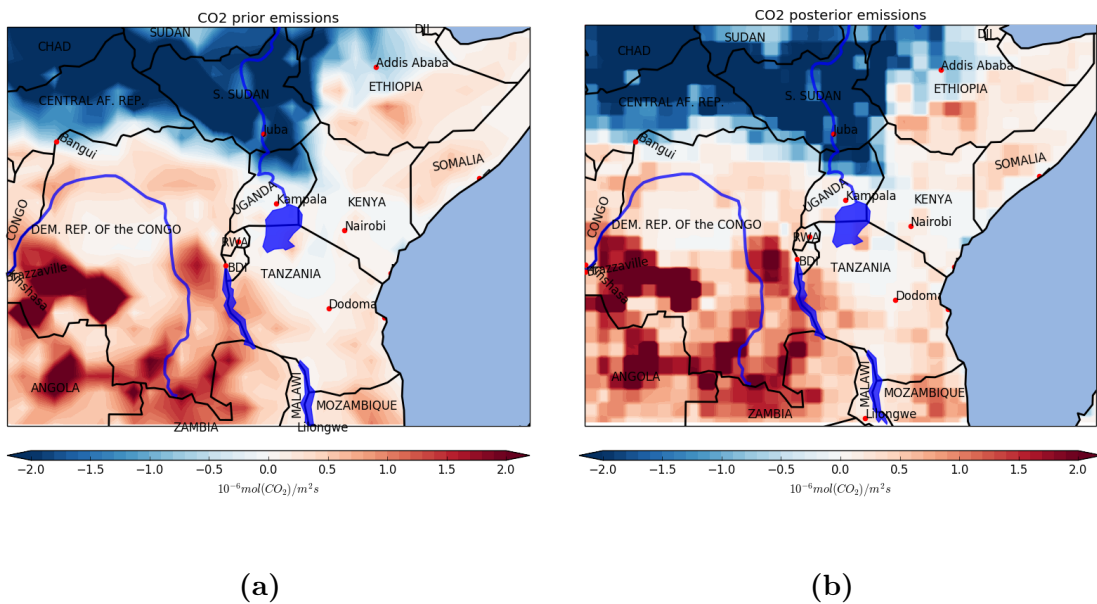
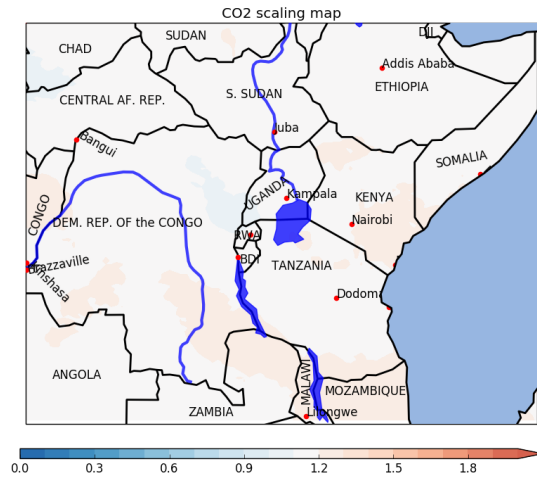
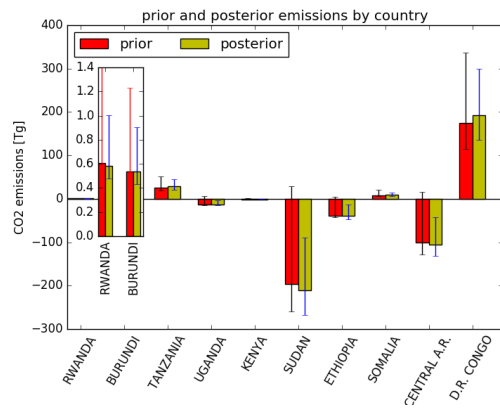


Figure B.78: CO_2 prior (a) and posterior (b) emissions for August 2016



(a)



(b)

Figure B.79: Prior scaling maps(a) and countries emissions totals (b) for August 2016

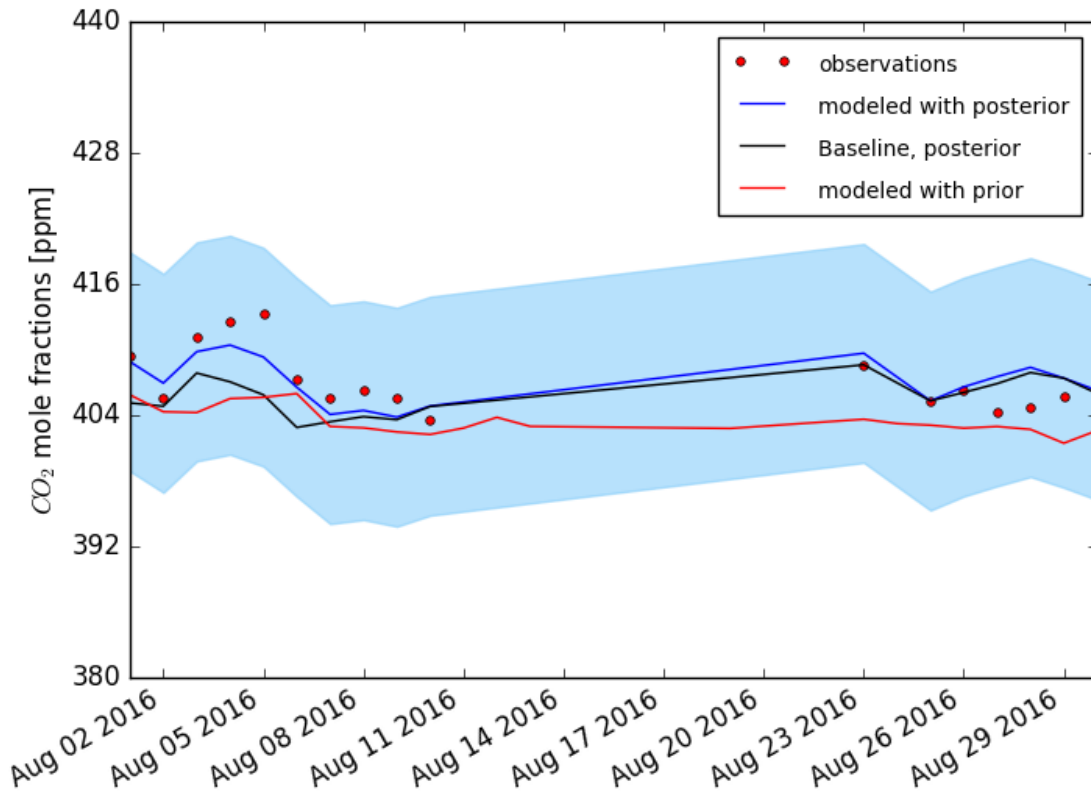


Figure B.80: Time series of optimized mole fractions (blue curve) compared to observations (red dots) and the modeled observation with prior emissions (red) with the prior (magenta) and posterior (black) baseline contribution to modeled mole fractions, for August 2016

B.9 Results for September 2016

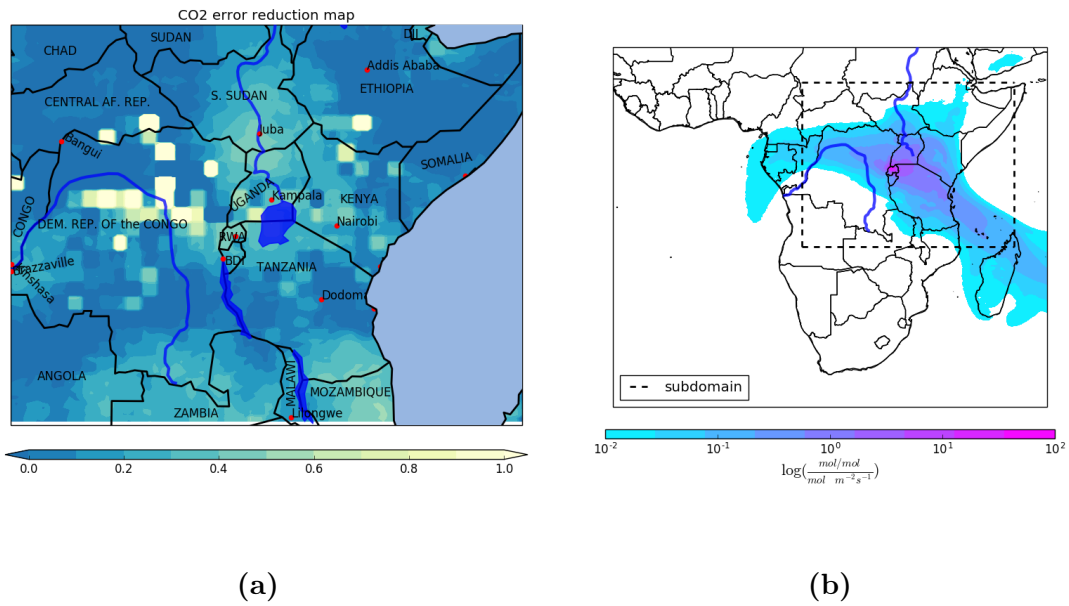


Figure B.81: Error reduction map (a) and footprint (note the log scale) (b) for September 2016. The extent of the map in (a) is highlighted with a broken line in the footprint map

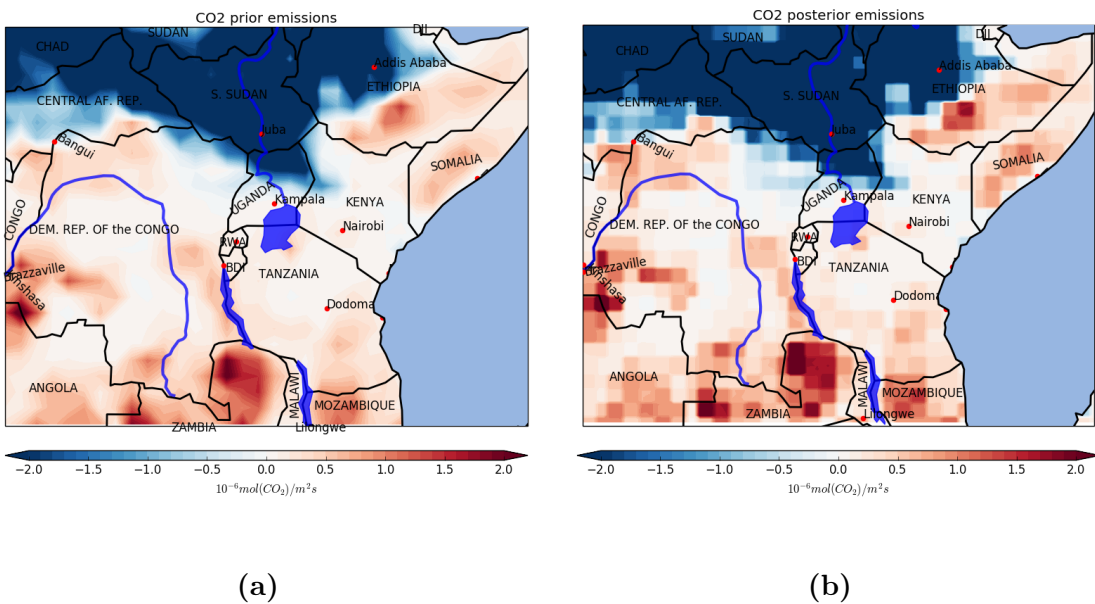
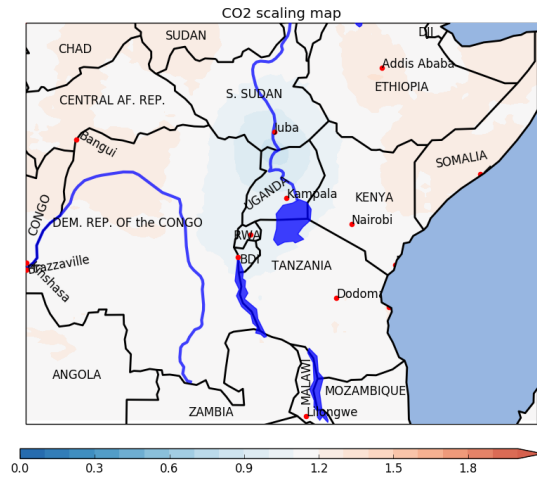
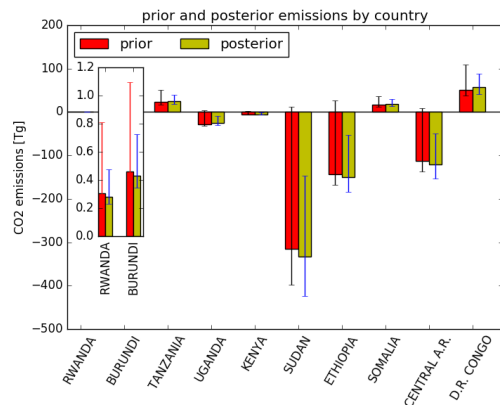


Figure B.82: CO_2 prior (a) and posterior (b) emissions for September 2016



(a)



(b)

Figure B.83: Prior scaling maps(a) and countries emissions totals (b) for September 2016

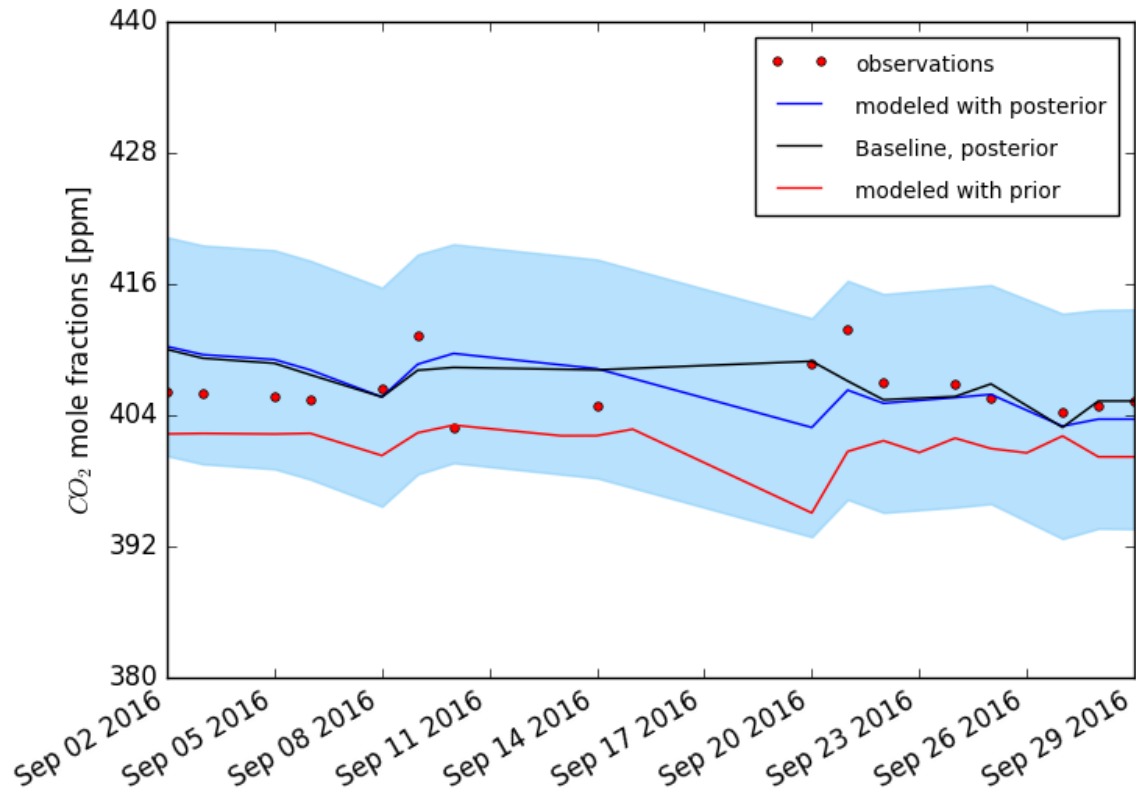


Figure B.84: Time series of optimized mole fractions (blue curve) compared to observations (red dots) and the modeled observation with prior emissions (red) with the prior (magenta) and posterior (black) baseline contribution to modeled mole fractions, for September 2016

B.10 Results for October 2016

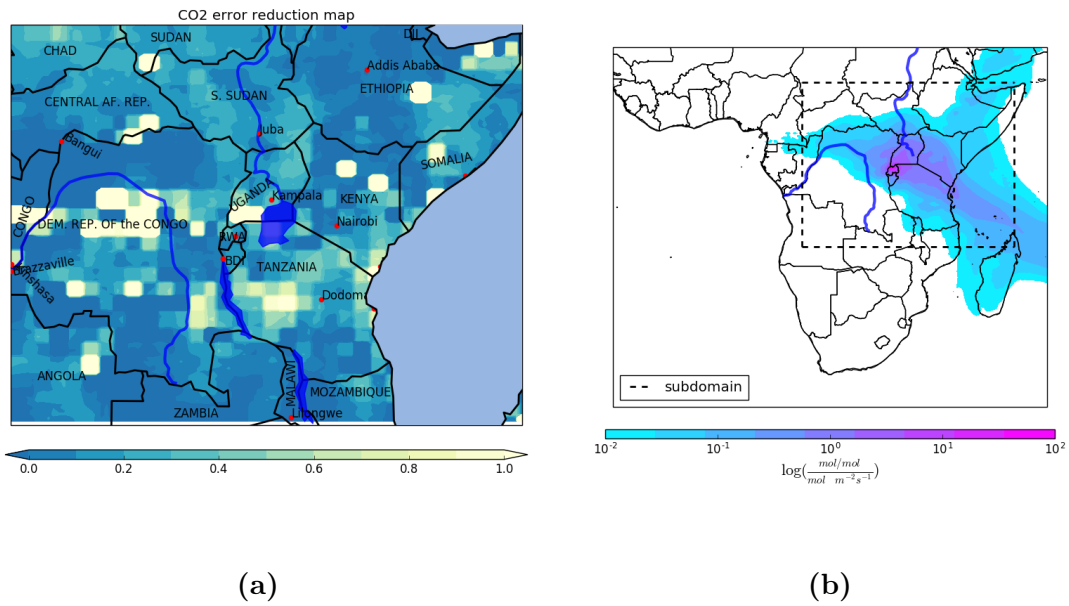


Figure B.85: Error reduction map (a) and footprint (note the log scale) (b) for October 2016. The extent of the map in (a) is highlighted with a broken line in the footprint map

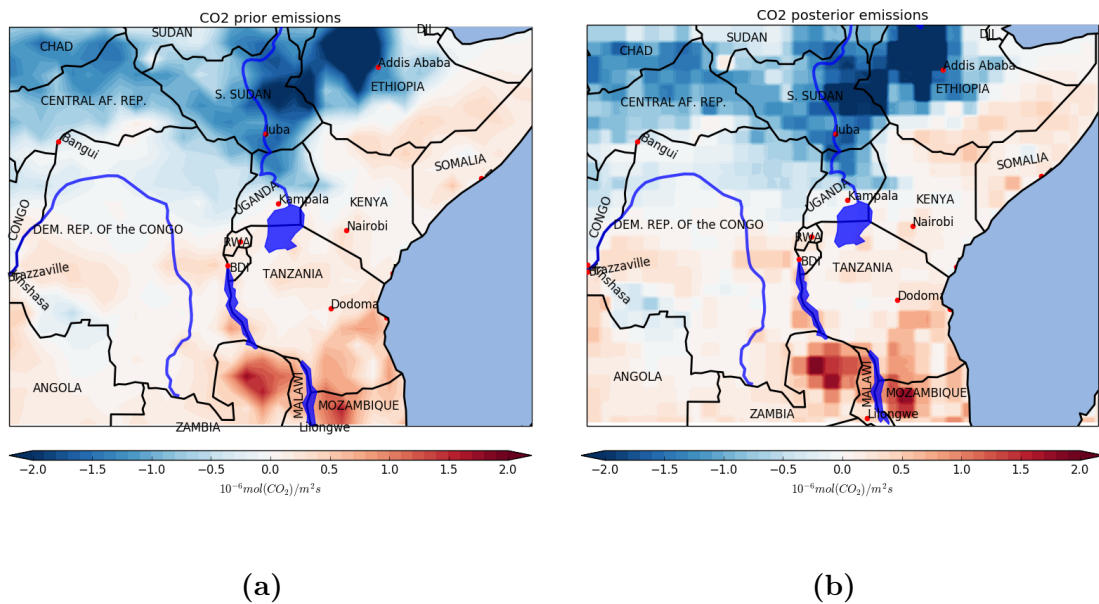
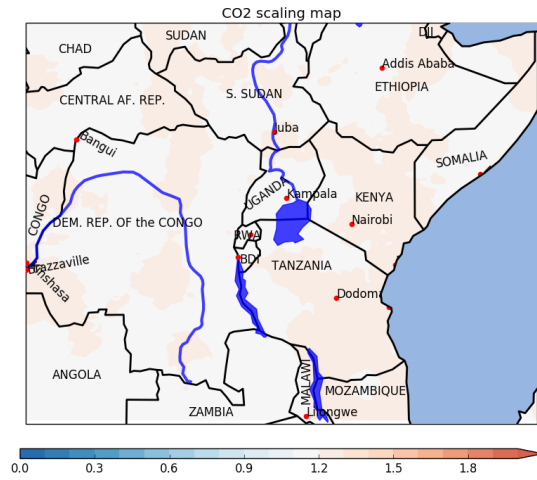
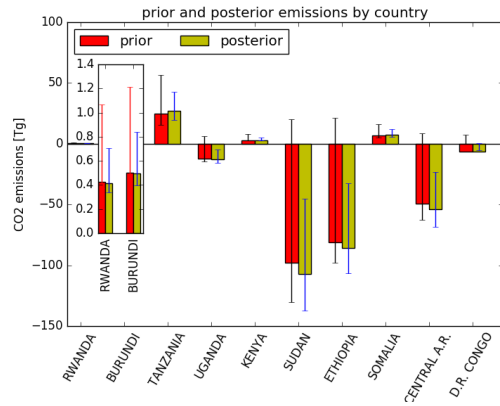


Figure B.86: CO_2 prior (a) and posterior (b) emissions for October 2016



(a)



(b)

Figure B.87: Prior scaling maps(a) and countries emissions totals (b) for October 2016

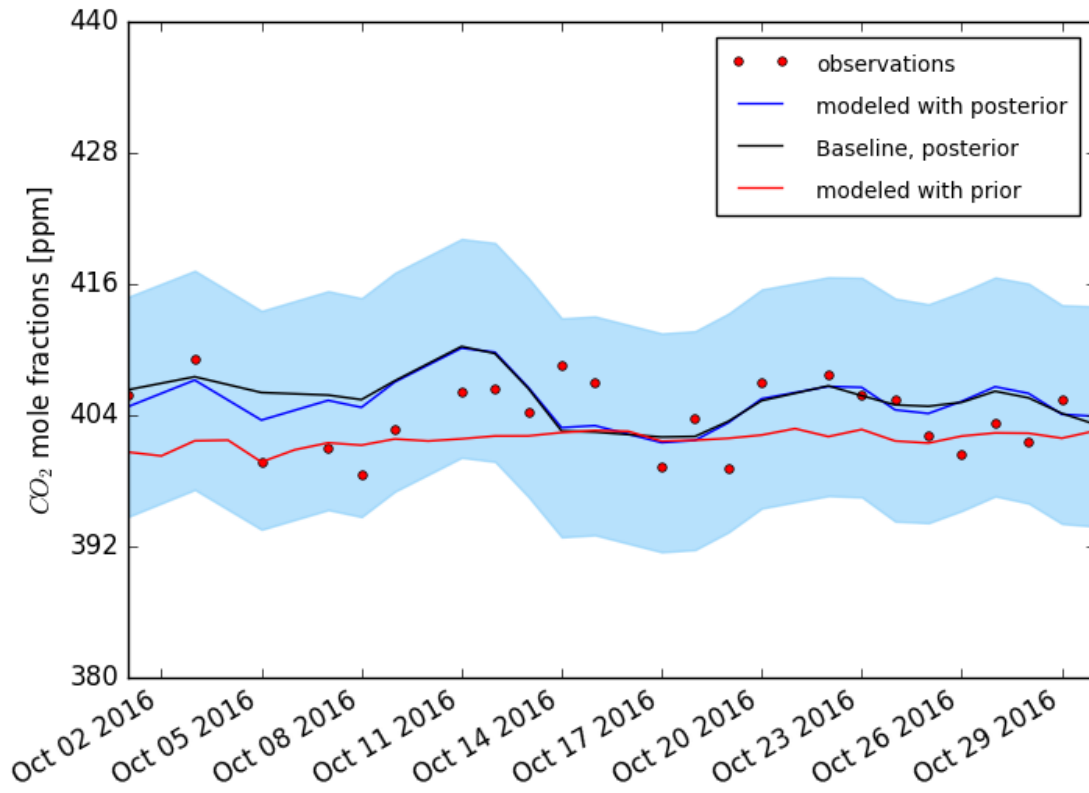


Figure B.88: Time series of optimized mole fractions (blue curve) compared to observations (red dots) and the modeled observation with prior emissions (red) with the prior (magenta) and posterior (black) baseline contribution to modeled mole fractions, for October 2016

B.11 Results for November 2016

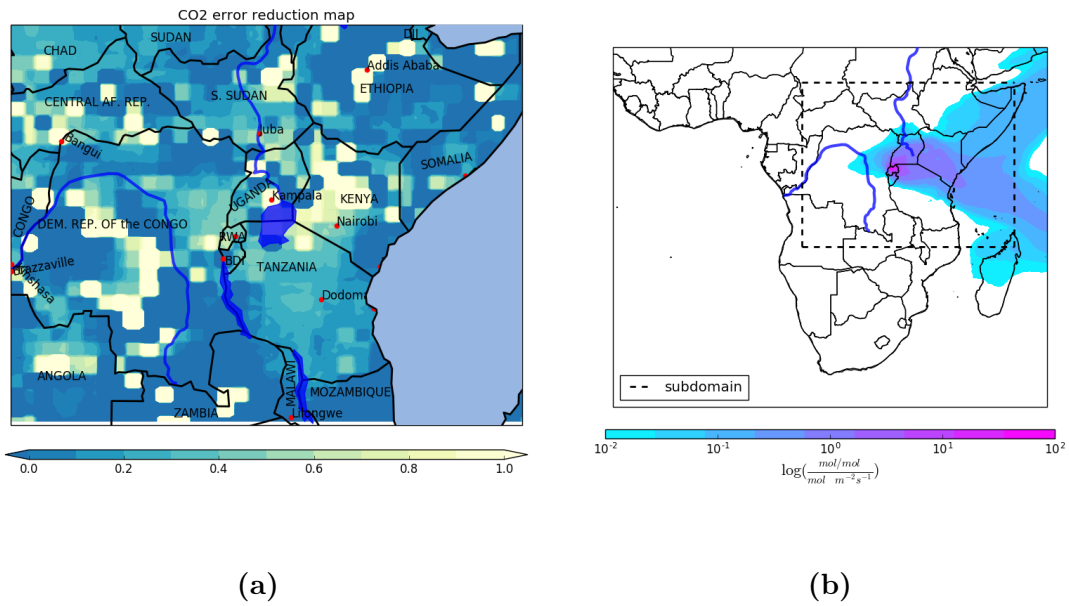


Figure B.89: Error reduction map (a) and footprint (note the log scale) (b) for November 2016. The extent of the map in (a) is highlighted with a broken line in the footprint map

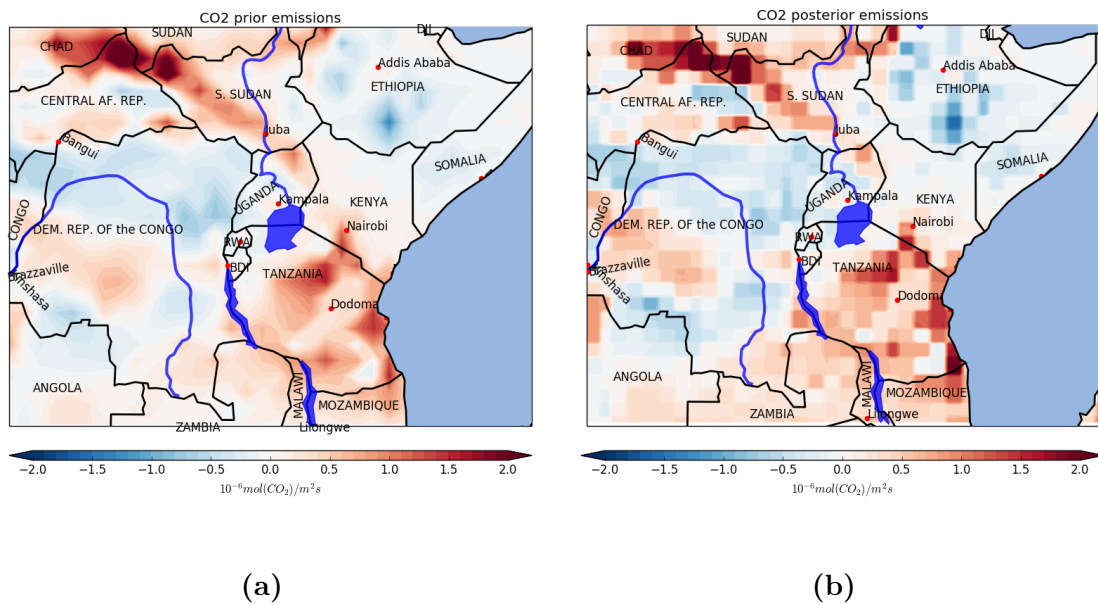
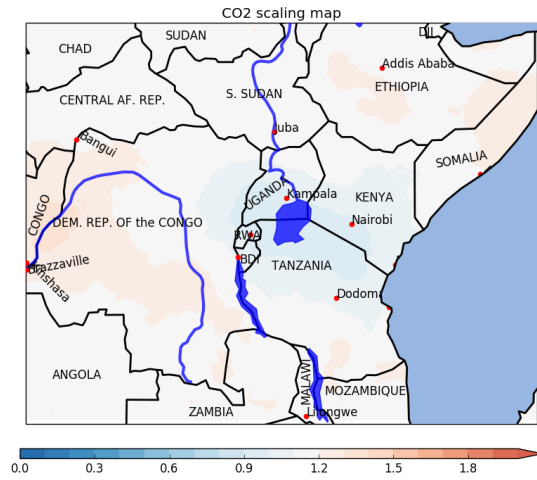
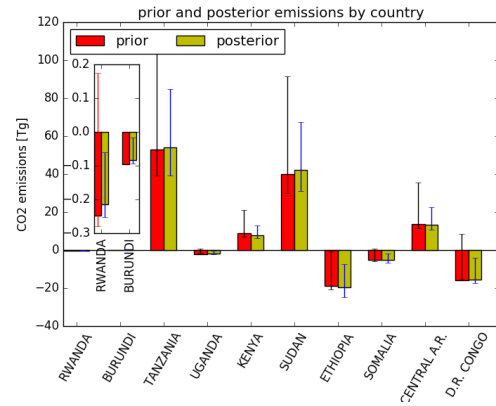


Figure B.90: CO_2 prior (a) and posterior (b) emissions for November 2016



(a)



(b)

Figure B.91: Prior scaling maps(a) and countries emissions totals (b) for November 2016

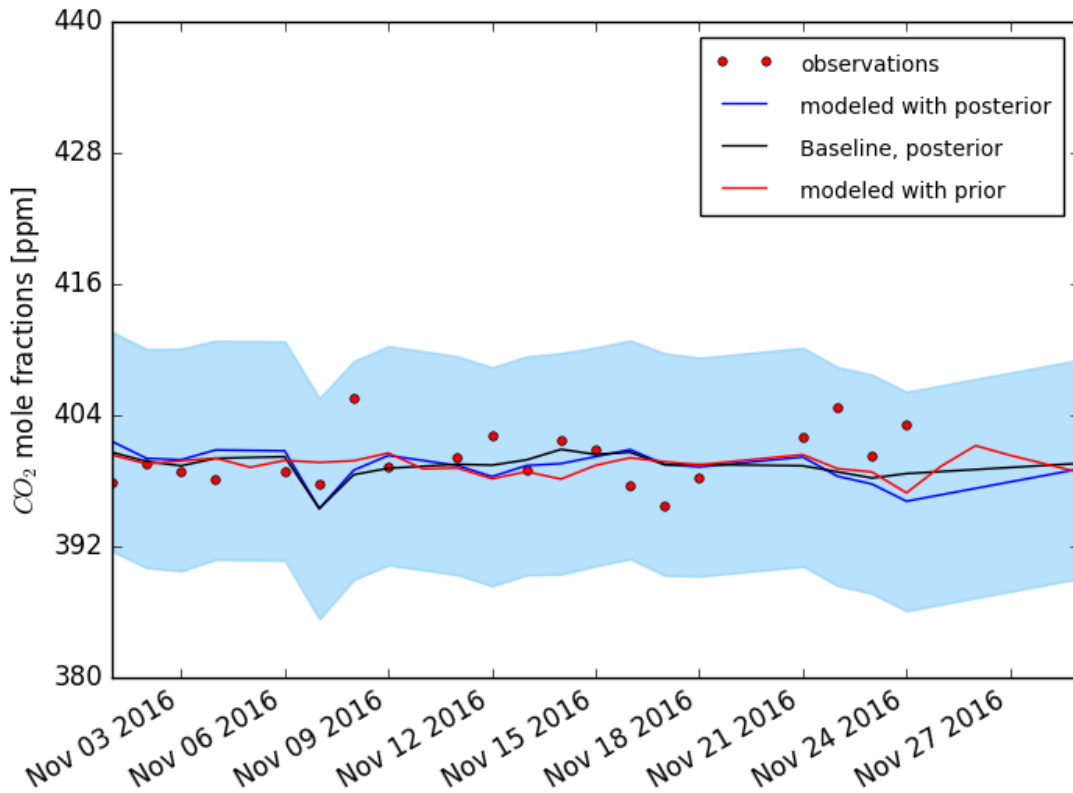


Figure B.92: Time series of optimized mole fractions (blue curve) compared to observations (red dots) and the modeled observation with prior emissions (red) with the prior (magenta) and posterior (black) baseline contribution to modeled mole fractions, for November 2016

B.12 Results for December 2016

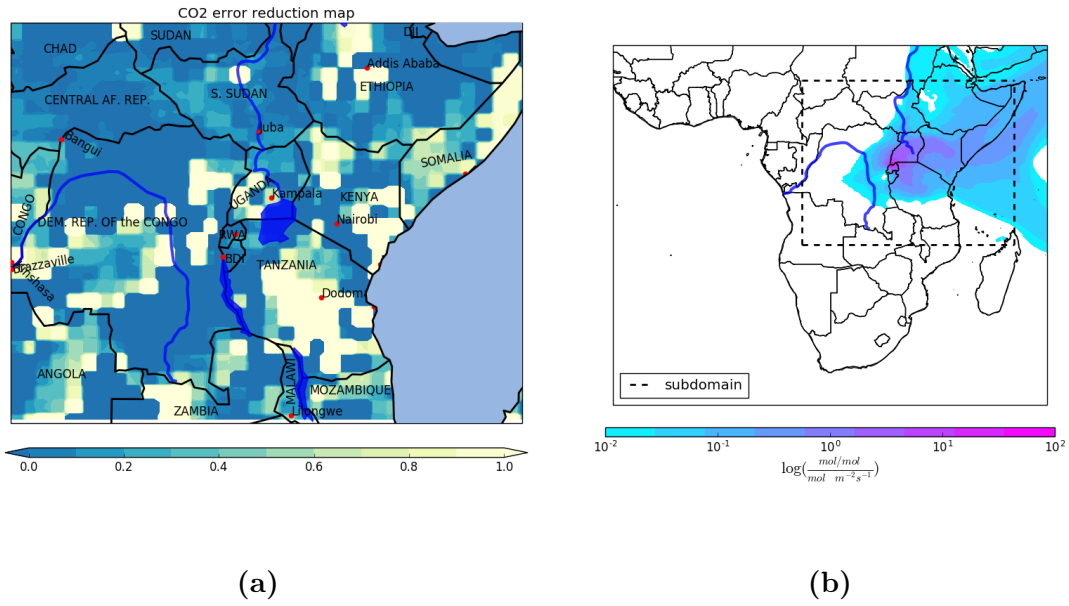


Figure B.93: Error reduction map (a) and footprint (note the log scale) (b) for December 2016. The extent of the map in (a) is highlighted with a broken line in the footprint map

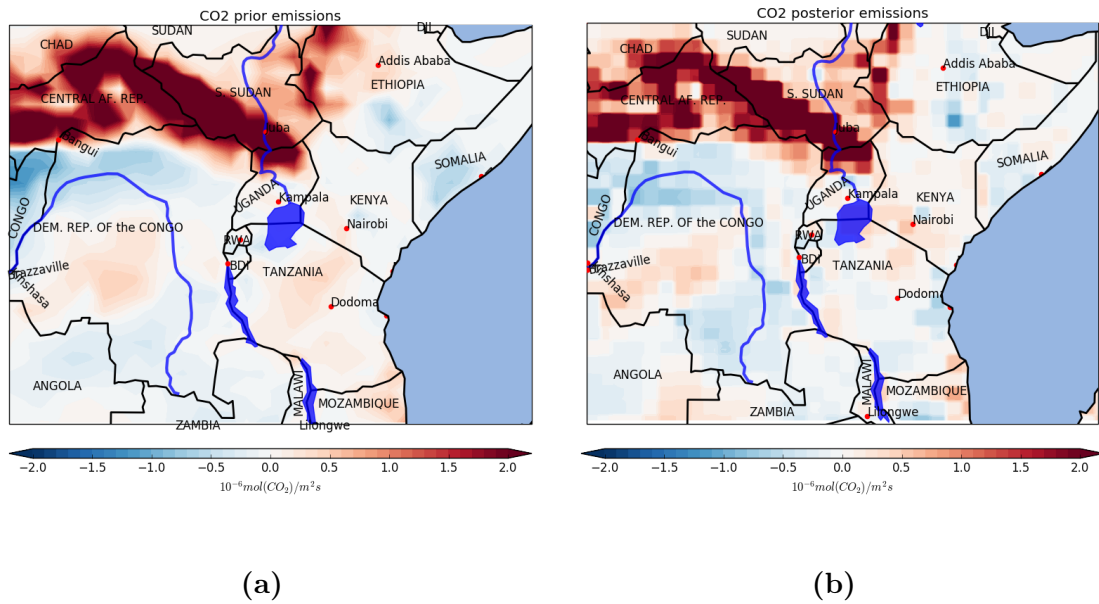
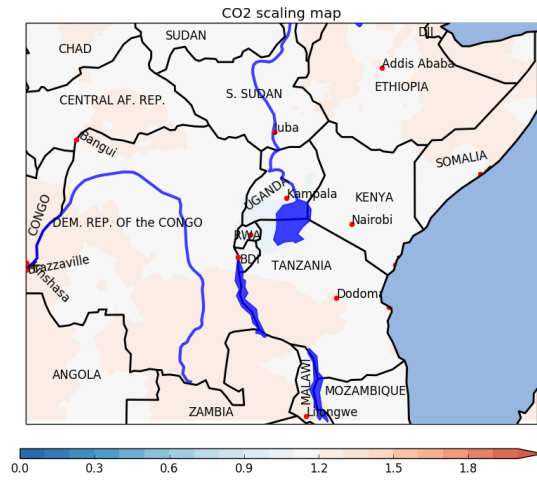
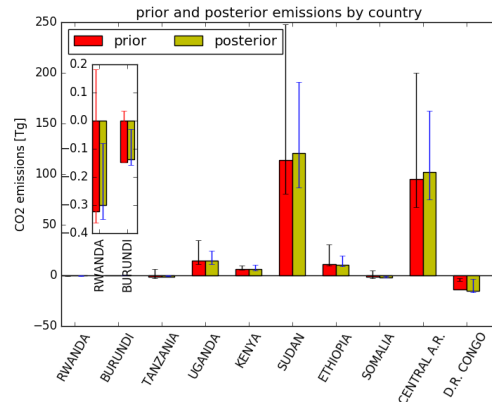


Figure B.94: CO_2 prior (a) and posterior (b) emissions for December 2016



(a)



(b)

Figure B.95: Prior scaling maps(a) and countries emissions totals (b) for December 2016

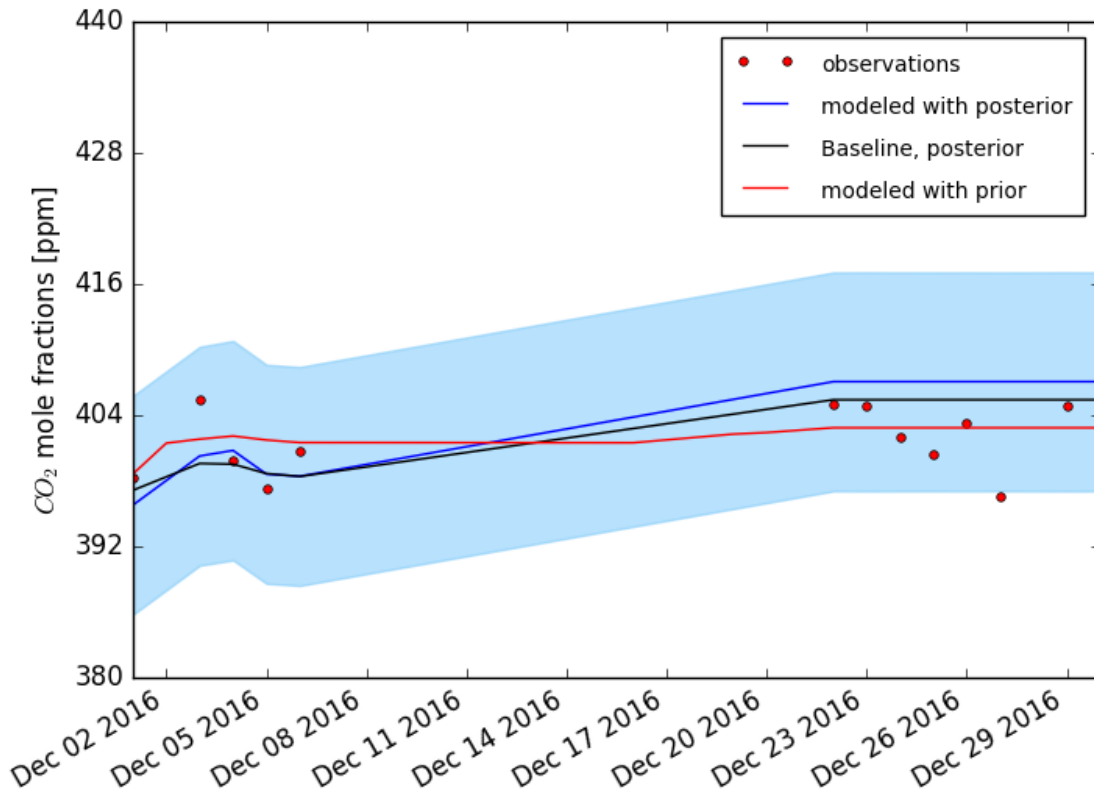


Figure B.96: Time series of optimized mole fractions (blue curve) compared to observations (red dots) and the modeled observation with prior emissions (red) with the prior (magenta) and posterior (black) baseline contribution to modeled mole fractions, for December 2016

Bibliography

- Andrews A. E., Kofler J. D., Trudeau M. E., Williams J. C., et al. (2014). “CO₂, CO, and CH₄ measurements from tall towers in the NOAA Earth System Research Laboratory’s Global Greenhouse Gas Reference Network: instrumentation, uncertainty analysis, and recommendations for future high-accuracy greenhouse gas monitoring efforts.” *Atmospheric Measurement Techniques* **7.2**, pp. 647–687 (cited on page 29).
- Ballantyne A. P., Alden C. B., Miller J. B., Tans P. P., et al. (2012). “Increase in observed net carbon dioxide uptake by land and oceans during the past 50 years.” *Nature* **488**.7409, pp. 70–73 (cited on page 19).
- Bergamaschi P., Frankenberg C., Meirink J. F., Krol M., et al. (2007). “Satellite cartography of atmospheric methane from SCIAMACHY on board ENVISAT: 2. Evaluation based on inverse model simulations.” *Journal of Geophysical Research: Atmospheres* **112**.D2. D02304, n/a–n/a (cited on page 89).
- Bergamaschi P., Houweling S., Segers a., Krol M., et al. (2013). “Atmospheric CH₄ in the first decade of the 21st century: Inverse modeling analysis using SCIAMACHY satellite retrievals and NOAA surface measurements.” *Journal of Geophysical Research: Atmospheres* **118**.13, pp. 7350–7369 (cited on pages 16, 23).
- Bergamaschi P., Krol M., Dentener F., Vermeulen A., et al. (2005). “Inverse modelling of national and European CH₄ emissions using the atmospheric zoom model TM5.” *Atmospheric Chemistry and Physics* **5**, pp. 2431–2460 (cited on page 13).
- Boden T. A., Marland G., and Andres R. J. (2013). *Global, Regional and National Fossil-Fuel CO₂ Emissions*. Carbon Dioxide Information Analysis Center, Oak ridge National Laboratory, US Department of Energy, Oak Ridge, Tenn. U.S.A (cited on page 100).
- Boden T. A., Marland G., and Andres R. J. (2016). *Global, Regional and National Fossil-Fuel CO₂ Emissions*. Carbon Dioxide Information Analysis Center, Oak ridge National Laboratory, US Department of Energy, Oak Ridge, Tenn. U.S.A (cited on page 100).
- Bodin Thomas and Sambridge Malcolm (2009). “Seismic tomography with the reversible jump algorithm.” *Geophysical Journal International* **178**.3, pp. 1411–1436 (cited on pages 55, 57).

- Bousquet P, Ciais P, Miller J B, Dlugokencky E J, et al. (2006). “Contribution of anthropogenic and natural sources to atmospheric methane variability.” *Nature* **443**.7110, pp. 439–43 (cited on page 20).
- Bousquet P., Ringeval B., Pison I., Dlugokencky E. J., et al. (2011). “Source attribution of the changes in atmospheric methane for 2006-2008.” *Atmospheric Chemistry and Physics* **11**.8, pp. 3689–3700 (cited on page 15).
- BP (2016). *BP Statistical Review of World Energy*. URL: <https://www.bp.com/content/dam/bp/pdf/energy-economics/statistical-review-2016/bp-statistical-review-of-world-energy-2016-full-report.pdf> (visited on 05/12/2017) (cited on page 100).
- Bruhweiler L M P, Michalak A M, Peters W, Baker D F, et al. (2005). “An improved Kalman Smoother for atmospheric inversions.” *Atmospheric Chemistry and Physics* **5**, pp. 2691–2702 (cited on page 23).
- Burgers G., Leeuwen P. V., and Evensen G. (1998). “Analysis scheme in the ensemble kalman filter.” *Mon. Weather Rev.* **126**, pp. 1719–1724 (cited on page 23).
- Carbon Tracker (2016). *Carbon Tracker CO2, version 2016*. URL: <https://www.esrl.noaa.gov/gmd/ccgg/carbontracker/index.php>] (visited on 05/15/2017) (cited on page 101).
- CarbonTracker-CH4 (2010). *CarbonTracker-Ch4*. URL: <http://www.esrl.noaa.gov/gmd/ccgg/carbontracker-ch4/> (visited on 05/15/2017) (cited on page 88).
- Chen Yu-Han and Prinn Ronald G. (2006). “Estimation of atmospheric methane emissions between 1996 and 2001 using a three-dimensional global chemical transport model.” *Journal of Geophysical Research* **111**.D10, p. D10307 (cited on pages 20, 22).
- Chui C. and Chen G. (1991). *Kalman Filtering With Real Time Application*. 2nd. New York: Springer (cited on page 23).
- Crosson E.R. (2008). “A cavity ring-down analyzer for measuring atmospheric levels of methane, carbon dioxide, and water vapor.” *Applied Physics B* **92**.3, pp. 403–408 (cited on page 29).
- Cui M, Ma A., Qi H., Zhuang X., et al. (2015). “Warmer temperature accelerates methane emissions from the Zoige wetland on the Tibetan Plateau without changing methanogenic community composition.” *Scientific Reports* **5**, p. 11616 (cited on page 73).
- Dlugokencky E. J., Bruhweiler L., White J. W. C., Emmons L. K., et al. (2009). “Observational constraints on recent increases in the atmospheric CH4 burden.” *Geophysical Research Letters* **36**.18, p. L18803 (cited on page 15).
- Dlugokencky Edward J, Nisbet Euan G, Fisher Rebecca, and Lowry David (2011). “Global atmospheric methane: budget, changes and dangers.” *Philosophical transactions. Series*

- A, Mathematical, physical, and engineering sciences* **369**.1943, pp. 2058–72 (cited on pages 13–15, 17, 19–21).
- EDGAR (2005). *Emission Database fo Glabal Atmospheric Research*. URL: <http://themasites.pbl.nl/tridion/en/themasites/edgar/index.html> (visited on 05/12/2017) (cited on page 89).
- Fraser a., Palmer P. I., Feng L., Boesch H., et al. (2013). “Estimating regional methane surface fluxes: the relative importance of surface and GOSAT mole fraction measurements.” *Atmospheric Chemistry and Physics* **13**.11, pp. 5697–5713 (cited on page 16).
- Ganesan A. (2013). *Quantifying Emissions of Greenhouse Gases From South Asia Through a Targeted Measurement Campaign*. PhD Thesis, M.I.T (cited on page 43).
- Ganesan A. L., Rigby M., Zammit-Mangion A., Manning A. J., et al. (2014). “Characterization of uncertainties in atmospheric trace gas inversions using hierarchical Bayesian methods.” *Atmospheric Chemistry and Physics* **14**.8, pp. 3855–3864 (cited on pages 55, 58).
- GAW (November, 2013). *World Data Central for Greenhouse Gases*. <http://ds.data.jma.go.jp/gmd/wdcgg/wdcgg.html> (cited on pages 15, 16).
- Giglio Louis, Randerson James T., and Werf Guido R. van der (2013). “Analysis of daily, monthly, and annual burned area using the fourth-generation global fire emissions database (GFED4).” *Journal of Geophysical Research: Biogeosciences* **118**.1, pp. 317–328 (cited on page 99).
- Gilks W. R., Richardson S., and Spiegelhalter D. J., eds. (1996). *Markov Chain Monte Carlo in Practice*. Chapman & Hall/CRC, p. 486 (cited on pages 52, 53).
- Global Carbon Project(2013) Methane budget and trends (2013). <http://www.globalcarbonproject.org/methanebudget> (cited on pages 19, 20).
- GLOBALVIEW (2017). *GLOBALVIEW data products*. URL: <https://www.esrl.noaa.gov/gmd/ccgg/globalview/index.html> (visited on 05/15/2017) (cited on pages 70, 71).
- GOSAT Project (2013). http://www.gosat.nies.go.jp/index_e.html (cited on page 17).
- Green Peter J. (1995). “Reversible jump Markov chain Monte Carlo computation and Bayesian model determination.” *Biometrika* **82**.4, pp. 711–732. eprint: /oup/backfile/content_public/journal/biomet/82/4/10.1093/biomet/82.4.711/2/82-4-711.pdf (cited on page 55).
- Houghton R. a., House J. I., Pongratz J., Werf G. R. van der, et al. (2012). “Carbon emissions from land use and land-cover change.” *Biogeosciences* **9**.12, pp. 5125–5142 (cited on pages 15, 19).

- Houweling Sander, Kaminski Thomas, Dentener Frank, Lelieveld Jos, et al. (1999). “Inverse modeling of methane sources and sinks using the adjoint of a global transport model.” *Journal of Geophysical Research: Atmospheres* **104**.D21, pp. 26137–26160 (cited on page 89).
- IPCC (2006). *IPCC Guidelines for National Greenhouse Gas Inventories, Prepared by the National Greenhouse Gas Inventories Programme*. Ed. by H. S. Eggleston, L. Buendia, K. Miwa, T. Ngara, et al. Hayama: IGES (cited on page 21).
- IPCC:WGI (2013). *Working Group I contribution to the IPCC 5th Assessment Report Climate Change 2013: The Physical Science Basis*. Ed. by Thomas Stocker, Qin Dahe, Gian-Kasper Plattner, Lisa Alexander, et al. UNEP, p. 2216 (cited on pages 13, 14, 18–20, 88).
- Jacobson Mark Z. (2010). “Short-term effects of controlling fossil-fuel soot, biofuel soot and gases, and methane on climate, Arctic ice, and air pollution health.” *Journal of Geophysical Research: Atmospheres* **115**.D14. D14209, p. D14209 (cited on page 69).
- Jacobson, Mikaloff Fletcher Sara E., Gruber Nicolas, Sarmiento Jorge L., et al. (2007). “A joint atmosphere-ocean inversion for surface fluxes of carbon dioxide: 1. Methods and global-scale fluxes.” *Global Biogeochemical Cycles* **21**.1. GB1019, n/a–n/a (cited on page 100).
- Kalman R E (1960). “A New Approach to Linear Filtering and Prediction Problems.” *Journal of Basic Engineering* **82**.Series D, pp. 35–45 (cited on page 22).
- Kasibhatla P., Heimann M., Rayner P., Mahowald N., et al., eds. (2000). *Inverse Methods in global biogeochemical cycles*. American Geophysical Union, p. 114 (cited on page 52).
- Kirschke Stefanie, Bousquet Philippe, Ciais Philippe, Sauniois Marielle, et al. (2013). “Three decades of global methane sources and sinks.” *Nature Geoscience* **6**.10, pp. 813–823 (cited on pages 19–22).
- Kort Eric a., Eluszkiewicz Janusz, Stephens Britton B., Miller John B., et al. (2008). “Emissions of CH₄ and N₂O over the United States and Canada based on a receptor-oriented modeling framework and COBRA-NA atmospheric observations.” *Geophysical Research Letters* **35**.18, p. L18808 (cited on page 13).
- Krol M., Houweling S., Bregman B., Broek M. van den, et al. (2005). “The two-way nested global chemistry-transport zoom model TM5: algorithm and applications.” *Atmospheric Chemistry and Physics* **5**.2, pp. 417–432 (cited on page 88).
- Le Quéré Corinne, Raupach Michael R., Canadell Josep G., Marland et al. Gregg, et al. (2009). “Trends in the sources and sinks of carbon dioxide.” *Nature Geoscience* **2**.12, pp. 831–836 (cited on page 13).
- Lunt M. F., Rigby M., Ganesan A. L., and Manning A. J. (2016). “Estimation of trace gas fluxes with objectively determined basis functions using reversible-jump Markov chain

- Monte Carlo.” *Geoscientific Model Development* **9.9**, pp. 3213–3229 (cited on pages 54, 55, 61–63).
- MacDonald J. A., Fowler D., Hargreaves K. J., Skiba U., et al. (1998). “Methane emission rates from a northern wetland; response to temperature, water table and transport.” *Atmospheric Environment* **32.19**, pp. 3219–3227 (cited on page 73).
- Maksyutov S., Takagi H., Valsala V. K., Saito M., et al. (2013). “Regional CO₂ flux estimates for 2009–2010 based on GOSAT and ground-based CO₂ observations.” *Atmospheric Chemistry and Physics* **13.18**, pp. 9351–9373 (cited on pages 16, 22).
- Manning A. J., O’Doherty S., Jones A. R., Simmonds P. G., et al. (2011). “Estimating UK methane and nitrous oxide emissions from 1990 to 2007 using an inversion modeling approach.” *Journal of Geophysical Research: Atmospheres* **116.D2**. D02305 (cited on page 44).
- Marzouk Youssef M., Najm Habib N., and Rahn Larry a. (2007). “Stochastic spectral methods for efficient Bayesian solution of inverse problems.” *Journal of Computational Physics* **224.2**, pp. 560–586 (cited on page 22).
- McSweeney Robert (2011). *Rwanda’s climate: Observation and Projections*. Tech. rep. Kigali: University of OXFORD, p. 44 (cited on page 24).
- Mendelsohn J., Jarvis A., Robertson T., and Nyiratuza M. (2016). *Rwanda: The Measure of a Land*. Ed. by Vital Signs. Vital Signs, p. 60 (cited on page 24).
- Miller S. M., Michalak a. M., and Levi P. J. (2013). “Atmospheric inverse modeling with known physical bounds: an example from trace gas emissions.” *Geoscientific Model Development Discussions* **6.3**, pp. 4531–4562 (cited on pages 22, 23).
- Montzka S a, Krol M, Dlugokencky E, Hall B, et al. (2011). “Small interannual variability of global atmospheric hydroxyl.” *Science (New York, N.Y.)* **331.6013**, pp. 67–9 (cited on page 20).
- Morino I., Uchino O., Inoue M., Yoshida Y., et al. (2011). “Preliminary validation of column-averaged volume mixing ratios of carbon dioxide and methane retrieved from GOSAT short-wavelength infrared spectra.” *Atmospheric Measurement Techniques* **4.6**, pp. 1061–1076 (cited on pages 16, 17).
- Morrison N. L. and Webster H. N. (2005). “An Assessment of Turbulence Profiles in Rural and Urban Environments Using Local Measurements and Numerical Weather Prediction Results.” *Boundary-Layer Meteorology* **115.2**, pp. 223–239 (cited on page 41).
- Nicholson Sharon E (2009). “A revised picture of the structure of the monsoonj and land ITCZ over West Africa.” *Climate Dynamics* **32**, pp. 1155–1171 (cited on page 67).
- Nisbet Euan and Weiss Ray (2010). “Atmospheric science. Top-down versus bottom-up.” *Science (New York, N.Y.)* **328.5983**, pp. 1241–3 (cited on pages 13, 14).

- NOAA STAR (2017). *START- global vegetation health products*. URL: https://www.star.nesdis.noaa.gov/smcd/emb/vci/VH/vh_browse.php (visited on 07/12/2017) (cited on pages 68, 69).
- NOAA/ESRL/GMD (November, 2013). *Mount Kenya Station*. <http://www.esrl.noaa.gov/gmd/dv/site/site.php?code=MKN> (cited on page 15).
- Olsen Seth C. and Randerson James T. (2004). “Differences between surface and column atmospheric CO₂ and implications for carbon cycle research.” *Journal of Geophysical Research: Atmospheres* **109**.D2. D02301, n/a–n/a (cited on page 99).
- Pasche Natacha, Schmid Martin, Vazquez Francisco, Schubert Carsten J., et al. (2011). “Methane sources and sinks in Lake Kivu.” *Journal of Geophysical Research: Biogeosciences* **116**.G3. G03006, n/a–n/a (cited on page 74).
- Peter Salameh (2016). *GCWERKS*. URL: <http://gcwerks.com/> (visited on 07/12/2017) (cited on page 38).
- Peters Glen P., Andrew Robbie M., Boden Tom, Canadell Josep G., et al. (2013). “The challenge to keep global warming below 2C.” *Nature Climate Change* **3**.1, pp. 4–6 (cited on pages 13, 14).
- Peters, Jacobson A. R., Sweeney C., Andrews A. E., et al. (2007). “An atmospheric perspective of North American carbon dioxide exchange: CarbonTracker.” *PNAS* **104**.48, pp. 18925–18930 (cited on pages 88, 99).
- Picarro (2016). http://www.picarro.com/technology/cavity_ring_down_spectroscopy (cited on page 29).
- Potter Christopher S., Randerson James T., Field Christopher B., Matson Pamela A., et al. (1993). “Terrestrial ecosystem production: A process model based on global satellite and surface data.” *Global Biogeochemical Cycles* **7**.4, pp. 811–841 (cited on page 89).
- Prinn R. G. (2000). “Measurement equation for trace chemicals in fluids and solution of its inverse, in Inverse Methods in Global Biogeochemical Cycles.” *Geophysical Monograph* **114**. American Geophysical Union. Ed. by P. Kasibhatla, M. Heimann, P. Rayner, N. Mahowald, et al., pp. 3–18 (cited on page 13).
- Prinn R. G., Huang L. Sun, Panday A., Potter K., et al. (2011). *Rwanda Climate Observatory Project: Site Evaluations and Recommendations, Proposed Instruments, and Implementation Strategy*. Tech. rep. Center for Global Change Science Report, MIT (cited on page 25).
- Prinn R. G., Weiss R. F., Fraser P. J., Simmonds P. G., et al. (2000). “A history of chemically and radiatively important gases in air deduced from ALE/GAGE/AGAGE.” *Journal of Geophysical Research* **105**.D14, p. 17751 (cited on page 18).

- Raupach Michael R, Marland Gregg, Ciais Philippe, Le Quéré Corinne, et al. (2007). “Global and regional drivers of accelerating CO₂ emissions.” *Proceedings of the National Academy of Sciences of the United States of America* **104**.24, pp. 10288–93 (cited on page 13).
- Rella C. W., Chen H., Andrews A. E., Filges A., et al. (2013). “High accuracy measurements of dry mole fractions of carbon dioxide and methane in humid air.” *Atmospheric Measurement Techniques* **6**.3, pp. 837–860 (cited on pages 29, 30).
- Ridgwell Andy J., Marshall Stewart J., and Gregson Keith (1999). “Consumption of atmospheric methane by soils: A process-based model.” *Global Biogeochemical Cycles* **13**.1, pp. 59–70 (cited on page 89).
- Rigby M., Prinn R. G., Fraser P. J., Simmonds P. G., et al. (2008). “Renewed growth of atmospheric methane.” *Geophysical Research Letters* **35**.22, p. L22805 (cited on pages 15, 20, 22).
- Saikawa E., Schlosser C. A., and Prinn R. G. (2013). “Global modeling of soil nitrous oxide emissions from natural processes.” *Global Biogeochemical Cycles* **27**.August, pp. 1–18 (cited on page 22).
- Sanderson M. G. (1996). “Biomass of termites and their emissions of methane and carbon dioxide: A global database.” *Global Biogeochemical Cycles* **10**.4, pp. 543–557 (cited on page 89).
- Sandradewi Jisca, Prevot Andre S. H., Szidat Sonke, Perron Nolwenn, et al. (2008). “Using Aerosol Light Absorption Measurements for the Quantitative Determination of Wood Burning and Traffic Emission Contributions to Particulate Matter.” *Environmental Science and Technology* **42**.9. PMID: 18522112, pp. 3316–3323. eprint: <http://dx.doi.org/10.1021/es702253m> (cited on page 39).
- Simpson Isobel J, Sulbaek Andersen Mads P, Meinardi Simone, Bruhwiler Lori, et al. (2012). “Long-term decline of global atmospheric ethane concentrations and implications for methane.” *Nature* **488**.7412, pp. 490–4 (cited on page 20).
- Takahashi Taro, Sutherland Stewart C., Wanninkhof Rik, Sweeney Colm, et al. (2009). “Climatological mean and decadal change in surface ocean pCO₂, and net sea–air CO₂ flux over the global oceans.” *Deep Sea Research Part II: Topical Studies in Oceanography* **56**.8. Surface Ocean CO₂ Variability and Vulnerabilities, pp. 554–577 (cited on page 100).
- UMD (2017). *VIIRS active fires global map*. URL: <http://viirsfire.geog.umd.edu/map/viirsMap.php> (visited on 05/21/2017) (cited on pages 68, 69).
- Vital Signs (2016). *Explore Atlas Rwanda*. URL: <http://rwanda.vitalsigns.org/explore-atlas-rwanda> (visited on 07/10/2017) (cited on page 24).
- Wang Qiaoqiao, Jacob Daniel J., Spackman J. Ryan, Perring Anne E., et al. (2014). “Global budget and radiative forcing of black carbon aerosol: Constraints from pole–to–pole

- (HIPPO) observations across the Pacific.” *Journal of Geophysical Research: Atmospheres* **119**.1. 2013JD020824, pp. 195–206 (cited on page 69).
- Weiss Ray F and Prinn Ronald G (2011). “Quantifying greenhouse-gas emissions from atmospheric measurements: a critical reality check for climate legislation.” *Philosophical transactions. Series A, Mathematical, physical, and engineering sciences* **369**.1943, pp. 1925–42 (cited on page 13).
- Welp L. R., Keeling R. F., Weiss R. F., Paplawsky W., et al. (2013). “Design and performance of a Nafion dryer for continuous operation at CO₂ and CH₄ air monitoring sites.” *Atmospheric Measurement Techniques* **6**.5, pp. 1217–1226 (cited on page 31).
- WMO (2011). *Report of the 15th WMO/IAEA Meeting of Experts on Carbon Dioxide, Other Green-house Gases, and Related Tracers Measurement Techniques, 7–10 September 2009, GAW report No. 194, WMO TD No. 1553*. URL: https://www.wmo.int/pages/prog/arep/gaw/documents/GAW_194_WMO_TD_1553_web.pdf (visited on 06/15/2017) (cited on page 30).
- Wunch Debra, Toon Geoffrey C, Blavier Jean-François L, Washenfelder Rebecca a, et al. (2011). “The total carbon column observing network.” *Philosophical transactions. Series A, Mathematical, physical, and engineering sciences* **369**.1943, pp. 2087–112 (cited on page 17).
- Yoshida Y., Kikuchi N., and Yokota T. (2012). “On-orbit radiometric calibration of SWIR bands of TANSO-FTS onboard GOSAT.” *Atmospheric Measurement Techniques* **5**.10, pp. 2515–2523 (cited on page 17).
- Yver Kwok C., Laurent O., Guemri A., Philippon C., et al. (2015). “Comprehensive laboratory and field testing of cavity ring-down spectroscopy analyzers measuring H₂O, CO₂, CH₄ and CO.” *Atmospheric Measurement Techniques* **8**.9, pp. 3867–3892 (cited on pages 29, 30, 34).
- Zagar N., Skok G., and Tribbia J. (2011). “Climatology of the ITCZ derived from ERA Interim reanalyses.” *Journal of Geophysical Research: Atmospheres* **116**.D15. D15103, n/a–n/a (cited on page 67).